The OH/IR star population in the Galactic center

by

Loránt Olivér Sjouwerman

Technical Report No. 316

Submitted to the School of Electrical and Computer Engineering
Chalmers University of Technology
in Partial Fulfilment of the Requirements for the Degree of
Doctor of Philosophy

Department of Radio and Space Science
School of Electrical and Computer Engineering
Chalmers University of Technology

Göteborg, Sweden
August 1997

ISBN 91-7197-535-7
ISSN 0346-718X

PRINTED BY
KOMPENDIET-GÖTEBORG
1997

FOR
CHALMERS TEKNISKA HÖGSKOLA
DEPARTMENT OF RADIO AND SPACE SCIENCE
WITH ONSALA SPACE OBSERVATORY

Abstract

The OH/IR stars, and M-type Mira variables, that form the topic of this thesis are in two important ways distinct from OH/IR stars found elsewhere in the Galaxy. Their location in the central few tens of parsecs of the Galactic center allows one to study the dynamics of the Galaxy on that scale, and to investigate a population of evolved stars with a high metal abundance.

The results presented here contribute to both areas; by investigating the possibility to determine proper motions of the stars (and thus individual stellar orbits), as well as by obtaining and analysing a new sample of OH/IR stars. All conclusions are drawn from interferometric observations of molecular maser line emission from the circumstellar envelope surrounding these stars.

In the innermost parts of the Galaxy accurate positions for OH/IR stars, necessary to measure their proper motions, cannot be determined from the easily detectable OH maser emission because of interstellar scattering. SiO masers are better suited. And after a survey for candidate OH/IR stars that have SiO or H_2O masers, it is shown that it is difficult, but indeed possible to determine milli-arcsecond accurate stellar positions relative to Sgr A*, the alleged dynamical center of the Galaxy. In the future, proper motions for OH/IR stars with SiO masers can be determined with VLBI techniques, and will be helpful in retrieving the mass-distribution in, and around the Galactic center.

With massive molecular clouds present, the Galactic center is expected to be a site for massive star formation. However, one should be careful to associate H_2O masers with such regions. Some H_2O masers should be ascribed to OH/IR stars or M-type Mira variables instead.

Much effort has been put in the search for more, faint OH/IR stars in the 1612 MHz OH maser line. A significant contribution is given to the statistical description of Galactic center OH/IR stars, both in kinematical as well as in intrinsic properties. More than 50 previously unknown OH/IR stars were detected in the central 40 parsec, most of them confirmed by the two different OH maser surveys described here. As the distance to the OH/IR stars is almost the same and relatively well known, and because the sample is relatively well studied at infrared wavelengths, the new sample forms a good base to study, for example, the mass-loss mechanism responsible for turning OH/IR stars into planetary nebulae.

A first analysis of intrinsic properties reveals that many OH/IR stars in the Galactic center were formed more than a Giga-year ago in a period of enhanced star formation, possibly a starburst; a striking conclusion that can only be drawn from OH/IR stars because they form the only traceable population older than a few 100 Mega-year in the Galactic center.

Sammanfattning

De OH/IR-stjärnor och M-typ Mira variabler vilka berörs i denna avhandling, skiljer sig på två viktiga punkter från de OH/IR-stjärnor man finner på andra ställen i Vintergatan. Deras placering i de mest centrala tiotals parsec i Vintergatans centrum tillåter studier av Vintergatans dynamik i denna skala, och även att en population av stjärnor med hög metallhalt kan undersökas.

Resultaten som presenteras här ger bidrag till båda dessa områden: genom att undersöka möjligheten att bestämma stjärnornas egenrörelser (och därmed enskilda stjärnbanor), samt genom att söka efter och analysera ett nytt urval av OH/IR-stjärnor. Alla slutledningar kommer från interferometriska observationer av molekylär linjeemission från områden runt omkring stjärnorna.

För att kunna bestämma egenrörelser krävs exakta positioner för OH/IR-stjärnorna. I de innersta delarna av Vintergatans centrum kan detta inte erhållas från OH-masrar, pga interstellär spridning. SiO-masrar är mer lämpade, och genom en sökning efter lämpliga OH/IR-stjärnor som har SiO- eller H_2O-masrar, kan vi se att det trots allt är möjligt att med millibågsekunders noggrannhet bestämma stjärnpositioner relativt Sgr A*, Vintergatans påstådda dynamiska centrum. I framtiden kommer egenrörelserna hos OH/IR-stjärnor att bestämmas med VLBI-teknik, och detta kommer att bli ett viktigt hjälpmedel för att erhålla massfördelningen i och runt omkring Vintergatans centrum.

Närvaron av massiva molekylära moln, medför att Vintergatans centrum förväntas vara en plats för massiv stjärnbildning. Men man bör vara försiktig med att assosciera H_2O-masrar med dessa områden. Vissa H_2O-masrar skall istället sammanlänkas med OH/IR-stjärnor eller M-typ Mira variabler.

Mycket tid har ägnats åt att söka efter svagare OH/IR-stjärnor vid 1612 MHz OH-maserlinjen. Ett viktigt tillskott ges till den statistiska beskrivningen av OH/IR-stjärnor i Vintergatans centrala delar, både av såväl kinematiska som fysiska egenskaper. Mer än 50 förut okända OH/IR-stjärnor detekterades i de mest centrala 40 parsec, de flesta av dem bekräftade genom de två olika eftersökningarna beskrivna här. Eftersom avståndet till OH/IR-stjärnorna är i princip detsamma, och relativt välkänt, och eftersom urvalet är relativt väl studerat vid infraröda våglängder, bildar det nya urvalet en god grund för studier av till exempel massförlustmekanismen vilken ansvarar för transformationen av OH/IR-stjärnor till planetariska nebulosor.

En första analys av fysiska egenskaper visar att många OH/IR-stjärnor i Vintergatans centrum bildades för mer än en miljard år sedan, i en period av ökad stjärnbildning; en anmärkningsvärd slutsats som endast kan dras från OH/IR-stjärnor eftersom de utgör den enda spårbara populationen i Vintergatans centrum, vilken är äldre än några få hundra miljoner år.

Samenvatting

De OH/IR sterren en M-type Mira variabelen, onderwerp van dit proefschrift, onderscheiden zich in twee belangrijke aspecten van OH/IR sterren in andere delen van de Melkweg. Hun plaats in de centrale tiental parsec van de Melkweg laat toe zowel de dynamica van de Melkweg op deze schaal, als ook een populatie geëvolueerde sterren met een hoog metaal gehalte te bestuderen.

De hier gepresenteerde resultaten dragen bij aan beide gebieden; een haalbaarheidsstudie van het bepalen van eigenbewegingen (en dus individuele banen), alsmede de verwerving en bestudering van een nieuwe verzameling OH/IR sterren. Alle conclusies zijn getrokken van interferometrische waarnemingen van moleculaire maserlijnstraling afkomstig uit het omhulsel van deze sterren.

Nauwkeurige posities voor OH/IR sterren in de binnenste delen van de Melkweg, nodig voor het bepalen van hun eigenbewegingen, kunnen door verstrooiing niet gemeten worden via de OH maser straling. Straling van SiO masers is beter geschikt, maar moeilijk meetbaar. Na een inventarisatie van OH/IR sterren die SiO of H_2O masers bezitten, is het wel degelijk mogelijk gebleken om milliboogseconde nauwkeurige posities te bepalen ten opzichte van het vermeende dynamische centrum, Sgr A*. In de toekomst kunnen met VLBI technieken eigenbewegingen van OH/IR sterren met SiO masers bepaald worden. Dit zal helpen in de bepaling van de massaverdeling in en rond het Melkwegcentrum.

Door de aanwezigheid van zware moleculaire wolken is het centrum van de Melkweg een logische plaats voor de vorming van sterren. Echter, men moet voorzichtig zijn H_2O masers aan zulke gebieden toe te schrijven. Sommige H_2O masers ontstaan namelijk in OH/IR sterren of M-type Mira variabelen.

Veel werk is besteed aan een speurtocht naar meer zwakke OH/IR sterren in de 1612 MHz OH maserlijn. Een significante bijdrage is geleverd aan de statistische beschrijving van OH/IR sterren in het Melkwegcentrum, zowel in bewegins-, als in intrinsieke eigenschappen. Meer dan 50 voorheen ongeziene OH/IR sterren zijn gedetecteerd in de binnenste 40 parsec, de meeste in meerdere OH maser zoektochten. Omdat de afstand tot de OH/IR sterren bijna gelijk en redelijk nauwkeurig bekend is, en omdat de sterren in het algemeen in het infrarood bestudeerd zijn, vormt de nieuwe verzameling een goed uitgangspunt om het mechanisme van massaverlies te bestuderen, verantwoordelijk voor de transformatie van een OH/IR ster naar een planetaire nevel.

Een eerste analyse van intrinsieke eigenschappen toont dat veel OH/IR sterren in het Melkwegcentrum gevormd zijn in een periode van uitgebreide stervorming, meer dan een miljard jaar geleden; een opmerkelijke conclusie die alleen getrokken kan worden met behulp van OH/IR sterren, omdat zij de enige zichtbare sterren ouder dan een paar honderd miljoen jaar in het centrum zijn.

Voor wie het allemaal net iets te lang duurde:
Wil Saladin († 17 december 1995) en Jan Hondema († 5 april 1996).

YOUR GREATNESS

LIES IN IMAGINATION

— SPHERE —

Preface

Since the discovery in the late 1960's of objects that are now known as OH/IR stars, both Onsala and Leiden have carried out surveys to find OH/IR stars in order to use them to study the structure of the Milky Way galaxy. A long tradition of investigating the nature of, and the use of OH/IR stars for dynamical purposes, started seriously in Onsala with Johansson (1979), and in Leiden with Baud (1978). Without the intention to neglect the efforts made on the southern hemisphere, and the many publications covering overall Galactic structure and the intrinsic nature of OH/IR stars themselves, the collaboration between Onsala and Leiden resulted particularly in publications, in which structure and dynamics of the central part of our Galaxy are discussed. As a matter of fact, the institute of the principal investigators switched by two from Leiden to Onsala and back again: Baud (1978), Habing (1983), Winnberg (1985), Lindqvist (1991), Van Langevelde (1992) and still continuing with Sevenster (1997). Given the long tradition of collaboration, it is not a big surprise to see the collaboration and tradition being extended and merged into this mixed Onsala and Leiden PhD project; the first half started with course work in Leiden, the finish will be to defend this thesis in, and – unintentionally – bringing back the principal investigators institute to Onsala.

Although, and because the projects guiding principle *for me* has been to find the black hole in the Galactic center, we could not avoid, nor neglect to look beyond this 'simple' question. Such questions usually require to answer more difficult questions in advance; questions that may, or may not be answered by the most renown experts. It particularly holds for a region as the Galactic center, where, without exception, all fields of astronomy meet. I just hope that we have taken the proper excursions, trying to answer some of the questions to get closer to our goal. Goals, questions and excursions that made, and still make this project into one I have never regretted starting, after that completely unexpected telephone call in the spring of 1992.

References

Baud B. 1978, PhD thesis, Leiden University
Habing H.J., Olnon F.M., Winnberg A., Matthews H.E., Baud B. 1983, A&A 128, 230
Johansson L.E.B. 1979, PhD thesis, Chalmers University of Technology
Lindqvist M. 1991, PhD thesis, Chalmers University of Technology
Sevenster M.N. 1997, PhD thesis, Leiden University, *in preparation*
Van Langevelde H.J. 1992, PhD thesis, Leiden University
Winnberg A., Baud B., Matthews H.E., Habing H.J., Olnon F.M. 1985, ApJ 291, L45

This thesis presents work carried out as a joint Onsala-Leiden project and contains the following papers; they will be referred to as chapters in the text:

Chapter 2: Paper A,
Appeared in *The Astrophysical Journal, Vol 461, page L41*
OH counterparts for H_2O masers in the Galactic center: evolved stars instead of signs of star formation
L.O. Sjouwerman & H.J. van Langevelde

Chapter 3: Paper B,
In preparation for *Astronomy & Astrophysics*
Detection of 22 GHz H_2O and 43 GHz SiO maser emission in Galactic center OH/IR stars and in the G−0.13−0.08 molecular cloud
L.O. Sjouwerman, M. Lindqvist, H.J. van Langevelde & P.J. Diamond

Chapter 4: Paper C,
In preparation for *Astronomy & Astrophysics*
Stellar positions from SiO masers in the Galactic center
L.O. Sjouwerman, H.J. van Langevelde & P.J. Diamond

Chapter 5: Paper D,
Accepted by *Astronomy & Astrophysics Supplement Series*
A new sample of OH/IR stars in the Galactic center
L.O. Sjouwerman, H.J. van Langevelde, A. Winnberg & H.J. Habing

Chapter 6: Paper E,
In preparation for *Astronomy & Astrophysics Letters*
OH/IR stars as signposts for ancient and future starburst activity in the Galactic center
L.O. Sjouwerman, H.J. Habing, M. Lindqvist, H.J. van Langevelde & A. Winnberg

Chapter 7: Paper F,
In preparation for *Astronomy & Astrophysics*
OH maser properties of OH/IR stars in the Galactic center
and which probably will be co-authored by M. Lindqvist, A. Winnberg, H.J. van Langevelde, H.J. Habing and/or J.A.D.L. Blommaert

Contents

Chapter 1

Background and Main Points to the research papers

1.1 Introduction

The main purpose of this thesis has been to find conclusive dynamical evidence for the existence of a massive black hole – more generally, the mass distribution – in the Galactic center (from now on abbreviated as GC), by using the line-of-sight motion of OH/IR stars (see below). A previous study by M. Lindqvist (PhD thesis in 1991) revealed that OH/IR stars are excellent probes to investigate the dynamics of the inner 100 parsec (1 pc = 206265 AU = 3×10^{16} m) of the GC. However, his survey did not yield the necessary number of OH/IR stars close to the black hole candidate Sgr A* for a good statistical analysis. Therefore, one of the objectives of this thesis was to obtain a good statistical sample of OH/IR stars from a sensitive survey in the inner 10 pc of Sgr A* (Chapter 5, Paper D). About fifty previously unknown OH/IR stars are found additionally, but unfortunately, the number of objects within 10 pc of Sgr A* after this survey is still very small.

The advent of new instruments, in particular the VLBA (the Very Long Baseline Array), theoretically opened perspectives to also measure proper motions of the OH/IR stars. In addition to the projected sky-coordinates and only the line-of-sight velocity vector, the full three dimensional velocity vector can be measured. One is in principle able to measure five of the six coordinates of the phase-space, with only the exact distance missing. Given this new possibility, a test to observe accurate positions of OH/IR stars is also included as part of this thesis (Chapters 3 and 4, Papers B and C). It is shown, that a project to determine proper motions of the OH/IR stars is actually possible, but laborious and observing time consuming.

The other Chapters (2, 6 and 7, Papers A, E and F) deal with results of the surveys. First, commenting on the interpretation of H_2O masers and infrared extinction curves in the GC, then a discussion of the peculiar distribution of expansion velocities ($v_{\rm exp}$) of the OH/IR stars in the GC, and finally an analysis of other properties of the GC OH/IR star sample. A dynamical analysis – the starting point for this thesis – is however not yet completed, and therefore not included.

1.1.1 OH/IR stars

A short description of an OH/IR star, is that of an average star ($\sim$ 1 to 7 solar masses, $M_\odot$) in a short-lived stage ($\sim 10^5$ yr) of ending its long life of stable nuclear fusion and transforming into a planetary nebula by expelling its envelope. When the central star has built up a degenerate core of oxygen and carbon, the energy is produced in hydrogen (and helium) shell burning, which in turn drives out the surrounding hydrogen to form a star of giant dimensions. The star is on the asymptotic giant branch (AGB) of the Hertzsprung-Russell diagram. The cool temperature in the outer part of the envelope allows dust to form, which in combination with the radiation pressure, low gravitational force and possibly shocks created by the stellar pulsation cycle, result in high mass-loss (of $10^{-6} \lesssim \dot{M} \lesssim 10^{-4}$ $M_\odot$ yr^{-1}).

The stars with the lower mass-loss rates can be observed optically as M-type Mira variables; a high mass-loss obscures the star totally at visible wavelengths. The absorbed energy is re-radiated as infrared radiation by the obscuring circumstellar matter. The expanding circumstellar envelopes form excellent environments for sustaining masers – in particular the 1612 MHz maser line of the OH molecule. Self-evidently, OH/IR stars have these OH masers. In the following, unless clearly stated otherwise, I shall include the M-type Miras – the optically visible OH/IR stars – in the OH/IR stars.

The OH/IR stars turn out to be excellent probes to study Galactic structure. The bright 1612 MHz OH masers can be observed all over the Galaxy (and beyond), and are easily recognisable. The radial velocity is obtained directly at the detection, and positions and occasionally distances can be determined. Most stars ($\sim$ 1 to 7 $M_\odot$) go through this phase, meaning that samples of OH/IR stars generally contain stars of different age (etc). Galactic populations, dynamics, and evolution, and the physical properties of OH/IR stars of different samples can be studied. And perhaps we can learn about the mass distribution of the Galaxy, and e.g. the mass-loss mechanism in AGB stars by studying different samples. Amongst others, I find the OH/IR star reviews by Habing (1993; 1996) most enlightening.

1.1.2 Galactic center

The OH/IR stars studied here are located at the GC, for which we use a distance of 8 kpc (Reid 1993). The GC is a peculiar environment, combining a large stellar density, numerous dense molecular clouds and enigmatic phenomena. To understand these phenomena, we want to see what is happening. However, this is prevented by the large interstellar extinction ($A_V > 25$ magnitudes) and the crowding and confusion of individual objects. Here, the OH/IR stars turn out to be very useful. Not only because the Galaxy is (mostly) transparent at 1612 MHz – so one can detect each object at its intrinsic intensity level –, but also because at each time only a fraction of all stars will be in the OH/IR star phase – limiting the confusion between individual detections.

A previous study by M. Lindqvist (1991) revealed indeed that the OH/IR stars form a sub-sample of the stars seen in the K-band (2.2 μm), and with 134 objects in a square degree very well identifiable individually. An attempt to measure the central mass distribution was only partly successful because of an insufficient number of objects close (< 10 pc) to the center. This lack was the main justification for starting this PhD project (Chapter 5); to find "the Black Hole" and to measure its mass. Very interesting were Lindqvist's findings of statistically different groups, divided according to $v_{\rm exp}$. An old, dispersed group can be distinguished from more recently formed, strongly rotating group. I will come back to that in Chapter 6, by discussing a third component.

With accumulating evidence for a tri-axial bulge or 'bar' in our Galaxy, it is likely that simple axi-symmetric models (e.g. the one used by Lindqvist et al. 1992b) do not describe the central mass concentration accurately. In Chapter 6 it is suggested that one can actually deduce the existence of the bar from the high-velocity OH/IR stars (also in combination with infalling gas).

The GC, in terms of stellar population, molecular environment, tri-axial bulge or bar, and energetic phenomena, is excellently reviewed by Genzel et al. (1994), Morris & Serabyn (1996), Blitz et al. (1993) and Mezger et al. (1996).

1.2 Main points

This thesis can be summarised by the following main points:

1.2.1 Chapter 2

Appeared in the *The Astrophysical Journal, Vol. 461, L41*

This paper concerns a quick response on two papers, that each are using an H_2O maser as a signpost for recent massive star formation in the GC. One of the arguments used for a star formation region, was that the list of Lindqvist et al. (1992a) did not show any OH maser counterpart. Before the final results of our survey were completed, we felt that we had to comment on this paper by showing our OH maser detection. It clearly classifies this H_2O maser source as an genuine AGB source.

The difficulty encountered by the interstellar extinction in IR measurements, can be illustrated with the case of OH359.956−0,050, the second source discussed and also known as GCIRS 24. This source has been found as an H_2O maser, first reported by Levine et al. (1995), who also performed near-IR measurements. From this and an adopted extinction law, they conclude the maser emission originates from a supergiant (bolometric magnitude $-7.6 \leq M_{\rm bol} \leq -8.1$, or 80,000–130,000 solar luminosities, $L_\odot$) of mass 12 $M_\odot$ and age 10^7 year. Our group has detected the object as an OH maser, indicating it is surrounded by a circumstellar shell (which means that there is less foreground extinction). With their infrared measurements and extinction law, we come to an AGB star with $-4.9 \leq M_{\rm bol} \leq -5.3$ or 7,000–10,000 $L_\odot$, mass 2 $M_\odot$ and age 10^9 year. These are completely different, but valid (!) conclusions within the given near-IR measurements. It gets even more complicated when Blum et al. (1996) with near-IR measurements, consistent with Levine et al. (1995), for the same source derive: AGB nature, $M_{\rm bol} \approx -6.4$, mass $\approx$ 5 $M_\odot$ and age 10^8 year, etc. Clearly, near-IR measurements alone are not sufficient to distinguish between supergiant and AGB star, and also requires a better understanding of the interstellar extinction to allow a proper correction before a reliable luminosity can be calculated.

1.2.1.a Main points of Paper A

1. H_2O masers by them selves are not proper tracers for star formation in the GC

2. Interstellar extinction correction remains a major problem in the GC

3. There are two extra (previously unknown) OH/IR stars with H_2O masers

1.2.2 Chapter 3

In this paper we investigate the occurrence of H_2O and SiO maser emission in a selection of OH/IR stars based on the list of Lindqvist et al. (1992a). Main goal is to find candidates for studying the proper motions of some of them, to obtain information about the orbits of the stars. Several authors have argued for a bar or tri-axial bulge for our Galaxy, and this should be reflected in the orbits of OH/IR stars. Unfortunately, the quality of the data sets is not very good, limiting further physical analysis. But we have reached our goal by increasing the number of candidate stars for future proper motion measurements from 15 to 46. Serendipitously we have found a number of additional H_2O masers in the core of the molecular cloud G−0.13−0.08, which we cautiously relate to massive star formation.

1.2.2.a Main points of Paper B

1. Purpose is to find proper motion candidates; from 15 we now have 46
2. A detection of 36 H_2O masers and 18 SiO masers in AGB stars and 10 H_2O masers by chance (non-AGB)
3. G−0.13−0.08 has many structured water masers; we confirm 2 previously known H_2O masers, confirm one of our own detections, and add 5 non-confirmed ones
4. High resolution H_2O maser spectra for OH359.956−0,050 clearly supports our view of an AGB nature (Chapter 2)

1.2.3 Chapter 4

We further continue with our first attempts to actually do the aforementioned measurements, i.e. to measure an accurate position for some of the SiO masers with VLBI techniques. The successful measurement is very difficult and depends strongly on the weather, but is possible with milli-arcsecond accuracy.

1.2.3.a Main points of Paper C

1. Measuring accurate positions for SiO masers in OH/IR stars in the GC, and with Sgr A* as phase and position reference is possible with the VLBA (including phased VLA), but difficult

2. 43 GHz phase referencing needs cycle times of 20+20 sec, and the VLA for sensitivity and short baselines

3. The input position catalogue must be very accurate

1.2.4 Chapter 5

Accepted by the *Astronomy & Astrophysics Supplement Series*

A chapter in which we describe the surveys for OH maser emission in the central 50 parsecs. Two methods are described; by adding up existing data (Fig. 1.1), and by just observing with higher sensitivity. The first method uses existing VLA data sets from Van Langevelde et al. (1993), observed for several epochs during 3 years time and therefore generally covering one to two full periods of the OH/IR stars in the field of view. However, the field of view is not exactly centered on the position, nor the velocity of the center of the Galaxy: the black hole candidate Sgr A*. Therefore, and equally important, also to include an equal sensitive search for high-velocity OH/IR stars, we made a deep, sensitive observation with the ATCA. The results are comparable, although a clear difference can be seen in the averaged fluxes of the VLA monitor data and the snapshot ATCA data when one considers the same stars (Chapter 7). Maybe not surprisingly, the weaker OH masers that the whole survey revealed, are in no other way different from the stronger OH masering stars; not in spatial nor in kinematic properties, and we quietly suggest the physical properties do not differ significantly either (which for the "old sample" is investigated in Lindqvist et al. – in preparation). In dealing with such large data sets, a simple way of searching the data cubes is also mentioned. By plotting the OH maser spectra already several interesting sources have been found (with symmetric quadruple masers, for example) that may help to resolve the physical mechanism in mass-loss for these stars and thereby linking the mass-loss for AGB stars to the mass-loss in (proto) planetary nebulae.

1.2.4.a Main points of Paper D

1. A total of 52 new OH/IR stars is found; they form the low luminosity part of the distribution and probably have similar metallicity and bolometric magnitudes in comparison to the already known sources

2. The OH luminosity distribution peaks at $10^{43.4}$ photons per second, but we cannot determine a clear cut-off in the OH luminosity distribution in the data

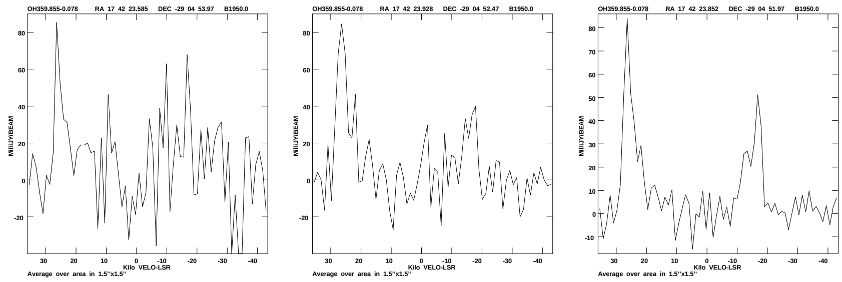

Figure 1.1 These figures concern the OH source 359.855−0.078, a typical low luminosity OH/IR star in the direction of the GC. We use it to demonstrate and justify the concatenation process in Chapter 5 in order to find weak and yet unknown OH/IR stars in the VLA data sets. On the left, one finds a spectrum of an ordinary VLA monitor data set. This source is too weak to be monitored by Van Langevelde et al. (1993) as the signal hardly can be distinguished from the noise. This data set is as sensitive as the original OH/IR star survey of Lindqvist et al. (1992a) and one might only suspect that there is an OH/IR star to be found here. Second, (middle frame) an intermediate result of the concatenation project is shown. This spectrum is taken from the concatenation of six VLA B-array monitor data sets. From this spectrum it becomes clear that this star has a second peak at a velocity of -18 km s^{-1}. The right figure shows a spectrum of this source in the final data set. Apart from an increase in signal to noise, the spectrum looks more like a genuine OH/IR star spectrum than the former ones. This is also caused by averaging the variable flux density of the source over the 17 epochs. The RMS noise is 8 mJy

3. In total we found four high-negative velocity stars (no positive ones), the three previously known ones are confirmed. They do not form the high-end tail of the velocity distribution
4. We introduce a new reduction and search method for large spectral line data cubes
5. For some sources, quadruple peaked OH maser spectra are found; the residual OH emission in the maps is possibly shock excited OH in Sgr A East, and we find severe OH absorption in cores of the molecular cloud G−0.13−0.08

1.2.5 Chapter 6

The distribution of expansion velocities in the deep survey shows a very narrow peak at about 19 km s^{-1}, much narrower than can be expected from luminosity measurements. From this one concludes that the sample of OH/IR stars in the

GC has a higher metallicity than any sample known in other parts of the Galaxy and the Magellanic Clouds. We think further, that the only way to explain the narrow distribution, is by arguing that a large fraction of stars were formed at the same time. We hypothesise that the Galaxy has undergone the starburst phase at least a Giga-year ago, and that some OH/IR stars represent a remnant of this epoch of enhanced star formation.

Thus one can distinguish three different groups of stars in the GC: an old bulge-like population, a group of relatively young stars formed from continously infalling gas and a shrinking population of low-mass stars, formed in an isolated era. Furthermore, by comparing OH/IR stars and a particular cloud of high-velocity gas, we provide proof that gas is currently still falling into the center and will result in enhanced star formation in the GC in the future (supporting the view of both Sevenster et al. 1995 and Serabyn & Morris 1996).

1.2.5.a Main points of Paper E

1. The expansion velocity distribution for the GC OH/IR stars shows an excess of stars at $v_{\rm exp} = 19$ km s^{-1}, which we interpret as evidence for a starburst episode
2. The stars were formed in an already in the GC resident rotating molecular cloud with a mass of at least 10^8 M$_\odot$
3. Clouds are still infalling, leading to periods of enhanced star formation in the GC in the future

1.2.6 Chapter 7

In the final chapter, a preliminary version of a paper on the properties of OH/IR stars at the GC, we analyse the OH maser data and derive mass-loss rates. We find a peculiar cluster of stars in the very center, for which the mass-loss rate is anomalously small. The understanding of the cause of the difference in mass-loss rate, e.g. because of a different physical or chemical structure of the shell or a difference in ambient interstellar matter, should provide clues for a better understanding of the mass-loss mechanism.

1.2.6.a Main points of Paper F

1. We confirm the statistical difference between groups of low and high expansion velocity found by Lindqvist (1992b)

2. The stronger OH masers, in particular the group with low expansion velocities, might be biassed toward sources close, but in front of the GC
3. There is a peculiar cluster within 4′ (10 pc) of Sgr A* that has a low mass loss rate. We suspect that the circumstellar envelope and the OH maser is affected by the GC environment

References

Blitz L., Binney J., Lo K.Y., Bally J., Ho P.T.P. 1993, Nat 361, 417
Blum R.D., Sellgren K., DePoy D.L. 1996, AJ 112, 1988
Genzel R., Hollenbach D., Townes C.H. 1994, Rep. Prog. Phys. 57, 417
Habing H.J. 1996, A&AR 7, 97
Habing H.J. 1993, in "Galactic bulges", Dejonghe H., Habing H.J. (eds.) Kluwer Academic Publishers, Dordrecht, p. 57
Levine D.A., Figer D.F., Morris M., McLean I.S. 1995, ApJ 447, L101
Lindqvist M. 1991, PhD thesis, Chalmers University of Technology
Lindqvist M., Winnberg A., Habing H.J., Matthews H.E. 1992a, A&AS 92, 43
Lindqvist M., Habing H.J., Winnberg A. 1992b, A&A 259, 118
Mezger P.G., Duschl W.J., Zylka R. 1996, A&AR 7, 289
Morris M., Serabyn E. 1996, ARAA 34, 645
Reid M.J. 1993, ARAA 31, 345
Serabyn E., Morris M. 1996, Nature 382, 602
Sevenster M.N., Dejonghe H., Habing H.J. 1995, A&A 299, 689
van Langevelde H.J., Janssens A.M., Goss W.M., Habing H.J., Winnberg A. 1993, A&AS 101, 109

Chapter 2

OH counterparts for H_2O masers in the Galactic center

evolved stars instead of signs of recent star formation

Abstract.
We present the detection of OH maser emission associated with the H_2O masers recently found in the Galactic center by Levine et al. (1995) and by Yusef-Zadeh & Mehringer (1995). The 1612 MHz OH masers were found in high-sensitivity maps created by combining 17 VLA observations taken by Van Langevelde et al. (1993) as well as in new observations with the ATCA. Both Levine et al. (1995) and Yusef-Zadeh & Mehringer (1995) consider the H_2O emission to be clues for recent massive star formation, by associating it with a supergiant and an HII region. The newly found OH masers show the typical double peaked spectra for evolved oxygen-rich stars and do not stand out amongst other OH/IR stars in this region, neither in H_2O nor OH maser characteristics. We conclude that the H_2O maser detections are associated with evolved, low to intermediate mass stars and that these H_2O masers thus cannot be regarded as signposts for massive young stars or star forming regions.

Co-authored by:
H.J. van Langevelde

2.1 Introduction

Claimed signs of recent massive star formation in the inner few parsecs of the Galactic center (GC) have resulted in an ongoing debate. The total mass and luminosity of young stars found until recently has been insufficient to power and drive the phenomena in the central few parsecs of our Galaxy, giving rise to searches for signs of a central engine, an accretion disk around a massive black hole. Recent reports on the detection of young and massive stars, that could provide the energy needed to explain the observations, undermine the necessity for a massive black hole located in the center (cf. Lacy et al, 1980; Krabbe et al., 1995; Zylka et al., 1995; Genzel et al., 1994 for a review).

From the observations presented here we cannot tell whether massive star formation has occurred in the past couple of hundred million years. We merely want to react upon Letters written by Levine et al. (1995, hereafter referred to as LFMM) and by Yusef-Zadeh and Mehringer (1995, Y-ZM), who both used an H_2O maser as evidence for recent or ongoing massive star formation in the central 10 parsecs of the GC.

LFMM associate the H_2O maser with a luminous and massive supergiant that could be physically connected to the circumnuclear disk and hence argue for recent star formation. The link to ongoing high-mass star formation by Y-ZM is based on lacking 1612 MHz OH maser emission and the coincidence of the H_2O maser with a possible shocked or pressurized molecular cloud.

However, in two surveys to find new OH masers for dynamical studies, we have found that both H_2O maser sources coincide with 1612 MHz OH maser sources, both with a double peaked spectrum which is typical for oxygen-rich stars undergoing spherical mass-loss on the asymptotic giant branch (AGB). As the OH and H_2O maser emission characteristics seem to indicate that both objects are AGB stars, OH/IR stars or Mira variables, the two H_2O masers found by LFMM and Y-ZM cannot be used as proper indicators for star formation in the GC in the last couple of hundred million years.

In the following sections we describe the method of detection and present 1612 MHz OH spectra. The characteristics of the observed OH and H_2O maser emission will be discussed and compared to masers of previously known OH/IR stars in the GC. We discuss the near-infrared photometry available for the LFMM source in terms of an evolved AGB star. We argue that both objects are low to intermediate mass, evolved stars and therefore at least several hundred million years old (Iben & Renzini, 1983, for a review on AGB star evolution).

2.2 Observations

In a monitoring program with the VLA[1], Van Langevelde et al. (1993) observed the strongest OH/IR stars found by Lindqvist et al. (1992a) in a survey of the GC in the 1612 MHz maser line of the OH molecule (Van Langevelde et al., 1993, and Lindqvist et al., 1992a, for details on the observations). We have combined 17 epochs of the monitor data into a high-sensitivity visibility data set. OH/IR stars can vary up to a factor of two in integrated 1612 MHz flux densities. The profile of OH/IR stars varies with periods in the range of 400 to 2,000 days (e.g. Van Langevelde et al., 1993). Finding weak OH/IR stars in this combined data set is therefore probably more efficient than searching each epoch separately or than searching new high-sensitivity observations at one epoch. The data reduction techniques and our final results, including a complete list of many weak and previously unknown OH masers in the GC, will be presented in a forthcoming paper.

In addition, we used the ATCA[2] in July 1994 to search for high velocity OH/IR stars (Chapter 5). Both the OH data sets have comparable sensitivities and are about four times more sensitive than the original Lindqvist et al. (1992a) survey.

We give the OH counterpart detections and approximate integrated flux densities in Table 2.1. Allowing for resolution and possible systematic effects in the radio maps, the OH maser positions are consistent with the H_2O masers. Both sources are clearly variable in the OH maser line, but it is difficult to interpret the integrated flux density from the VLA data as the flux density is an average over 17 epochs, taken in a time-span of almost three years. The 1612 MHz spectra from the VLA data can be found in Fig. 2.1a and 2.1b. In Fig. 2.2a and 2.2b the spectra from our ATCA survey are displayed. Note that there are considerable difficulties when reaching such low noise levels in the GC area; residuals of the extended OH absorption, continuum subtraction and very strong maser sources cause the poor baselines in both the VLA and ATCA data. The OH masers have expansion velocities of about 15 and 19.5 $\mathrm{km\,s^{-1}}$ centered on stellar radial velocities (line-of-sight, with respect to the LSR) of about 49 and 105 $\mathrm{km\,s^{-1}}$ respectively, very well in agreement with the observations of LFMM and Y-ZM. We therefore believe the H_2O and OH masers are associated with the same object in both cases.

[1]The Very Large Array (VLA), as part of the National Radio Astronomy Observatory, is operated by Associated Universities, Inc., under cooperative agreement with the National Science Foundation.

[2]The Australia Telescope Compact Array (ATCA) is operated by the Australia Telescope National Facility, CSIRO, as a National Research Facility.

Table 2.1 H_2O and OH detections

survey	Right Ascension & Declination (1950)		($''$)	Radial Velocity[a] ($km\,s^{-1}$) low	mean	high	resolution	Line flux ($mJy\,km\,s^{-1}$)
LFMM source: OH 359.956–0.050								
H_2O LFMM	17 42 32.00	−28 58 47.8	(±0.2)	...	45.3	55.8	(5.0)	...
H_2O Y-ZM	17 42 31.87	−28 58 46.8	...	...	44.7	...	(2.6)	603
OH VLA	17 42 31.95	−28 58 47.9	(±1.9)	34.3	48.5	62.7	(1.2)	610
OH ATCA	17 42 31.96	−28 58 50.0	(±3.3)	34.2	50.2	66.2	(1.5)	190
Y-ZM source: OH 359.980–0.077								
H_2O Y-ZM	17 42 41.65	−28 58 26.78	...	86.1	...	...	(2.6)	112
OH VLA	17 42 41.71	−28 58 25.80	(±0.63)	85.4	104.7	124.0	(1.2)	360
OH ATCA	17 42 41.64	−28 58 27.15	(±0.73)	85.1	104.7	124.3	(1.5)	640

a: With respect to LSR

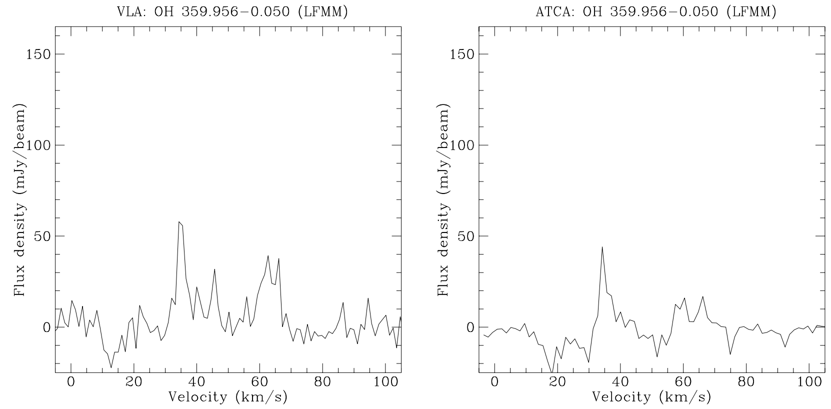

Figure 2.1 1612 MHz OH spectra from the VLA monitor: a) OH 359.956–0.050, the counterpart for the H_2O maser found by LFMM and b) OH 359.980–0.077, the counterpart for the H_2O maser found by Y-ZM. Both spectra are an average over 17 epochs

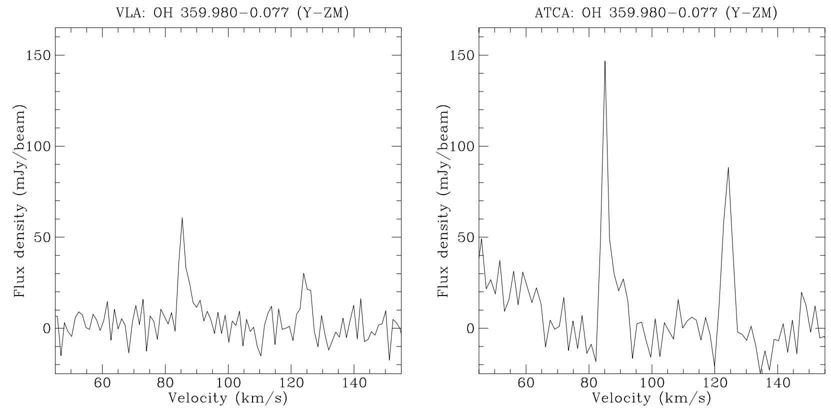

Figure 2.2 1612 MHz OH spectra from the ATCA survey: a) OH 359.956–0.050 (LFMM) and b) OH 359.980–0.077 (Y-ZM)

2.3 Discussion

Most of the previously unknown double peaked OH masers found are seen in both the combined VLA monitor data and our new ATCA observations. So far we have only searched for OH emission exceeding 40 mJy, which is already a factor 2.5 deeper than the Lindqvist et al. (1992a) survey. The weaker intrinsic OH emission explains why LFMM and Y-ZM unsuccessfully searched the survey of Lindqvist et al. (1992a) for a previous OH detection of their H_2O maser sources.

We assume that our new, double peaked OH masers are associated with similar objects as the Lindqvist et al. (1992a) stars, i.e. low to intermediate mass, evolved AGB stars. We reach this conclusion by noting that our newly detected OH masers compare very well with the stronger OH masers detected by Lindqvist et al. (1992a) in all their properties (sky distribution, radial velocity distribution, expansion velocities, OH maser variability). Also, the expansion velocity distribution ranges from about 5 to 30 $\mathrm{km\,s^{-1}}$ and has a mean of 17 $\mathrm{km\,s^{-1}}$ for both the known and newly found OH/IR stars in the GC (cf. e.g. Blommaert et al., 1994). Adopting the same metallicity, the distribution of the expansion velocities indicates a similar bolometric luminosity distribution for the weaker OH maser stars (Habing et al., 1994); they appear not to be different from the previously known OH/IR stars in any other respect than showing a weaker OH maser.

Parallel to the observations of LFMM and Y-ZM, our group has conducted a VLA survey for H_2O maser emission in the 150 OH/IR stars found previously near the GC. The detection rate for H_2O in OH/IR stars is low, partly because the H_2O masers are intrinsically weak. Also, in contrast to the OH masers, the H_2O maser emission varies strongly and irregularly. At the distance of the GC, as a consequence of sensitivity limits, one will find in most cases only one dominant H_2O peak near one of the OH maser peaks, a few $\mathrm{km\,s^{-1}}$ closer to the mean velocity, or H_2O emission at the mean velocity. The H_2O masers in the GC that we and Lindqvist et al. (1990) did detect in OH/IR stars, as well as the detections of LFMM and Y-ZM, all have similar H_2O maser characteristics: a double peaked H_2O profile with the same mean (stellar) velocity as the OH maser or one single peak close to the mean velocity (e.g. Engels et al., 1986). The combination of the LFMM and Y-ZM H_2O masers and our OH detections fit the general OH/IR star maser picture as outlined above. For supergiants and star forming regions one finds in general much stronger H_2O masers with a complex spectral profile (cf. Engels et al., 1988; Reid et al., 1988).

In general the OH maser luminosities for evolved, low to intermediate mass OH/IR stars are 1 – 100 times higher than the H_2O maser luminosities. Depending on the mass-loss rate, occasionally the opposite is also found for the thinner circumstellar shells of Mira and semi-regular variables (e.g. Bowers & Hagen, 1984). Of course, when working with variable sources one has to be careful to make comparisons between luminosities. Nevertheless, we think we can regard the H_2O luminosity for the Y-ZM source to be less than the OH luminosity, suggesting that this object is a regular OH/IR star, whereas the comparison of OH and H_2O for the LFMM maser indicates a thinner circumstellar shell (see Table 2.1).

Lindqvist et al. (1992b) discuss the kinematics of the OH/IR stars found in Lindqvist et al. (1992a). In good agreement with the results of McGinn et al. (1989), Sellgren et al. (1990) and Rieke & Rieke (1988) for K and M giants, the OH/IR stars show Galactic rotational behavior. The stars have a large dispersion in radial velocity (70 $\mathrm{km\,s^{-1}}$ or more) and the agreement of the radial velocity of the LFMM star with the circumnuclear disk is in our view accidental. The agreement is no strong evidence for such an object to be young, i.e. a couple of tens of million years.

The strongest argument by LFMM for a young age of the star associated with the H_2O maser is its very high luminosity (100,000 $L_\odot$). LFMM derive this from H, K and L band photometry by arguing that these observations are consistent with an M5 supergiant, seen at large visual extinction ($A_V \approx 37$) when applying a standard interstellar reddening law. With the knowledge that the star must have a considerable circumstellar shell, because it supports an OH 1612 MHz maser, the red colors of the object can be understood readily with less foreground extinction. Moreover, following the identification with a circumstellar shell, the near-infrared flux is produced mostly by this extended envelope. Hence the bolometric correction is much more moderate, resulting in a lower bolometric luminosity for the star.

The detailed calculation of a total luminosity or an accurate bolometric correction is quite uncertain because only near-infrared colors are available. Most of the luminosity is expected at M band and beyond, where the extinction correction would be less steep as well. Correcting the photometry with a standard extinction law (Rieke & Lebovsky, 1985) and a value of $A_V = 30$, which seems more appropriate for the location of this object (Catchpole et al., 1990), we find colors that are quite blue for OH/IR stars, but still consistent with a circumstellar envelope. We estimate a bolometric correction in L band of 4.9 magnitudes in this case (cf. Jones et al., 1994). With these uncertainties the total bolometric luminosity could be in the range 7,000 – 10,000 $L_\odot$. In fact, the interstellar extinction law is a possible source of uncertainty and we favor a reddening law based on extinction curve no. 15 of Van de Hulst (1949) for the GC, which leads to even a lower bolometric luminosity of 5,500 $L_\odot$ (Blommaert et al., 1997).

The estimated luminosity, based on the identification as an AGB star, is comparable with the luminosity of the known OH/IR stars in the GC (Jones et al., 1994; Blommaert et al., 1992). This indicates a main sequence mass of the star in the order of 2 $M_\odot$and an age largely exceeding several hundred million years (e.g. Van der Veen & Habing, 1990). The near-infrared colors would then imply a $(K\text{-}L)_0$ as low as 0.56, corresponding to a mass-loss rate of about 3.5×10^{-6} $M_\odot$ yr^{-1}(Lepine et al., 1995). This mass-loss rate is sufficient to form an OH masering circumstellar shell (Bowers & Hagen, 1984), but the low value of $(K\text{-}L)_0$ also indicates the circumstellar shell itself is optically thin in the near-infrared, such as in the optically visible Mira variables or proto-planetary nebulae (e.g. Lepine et al., 1995). The latter however, normally have no H_2O masers (Lewis, 1989). A thin circumstellar shell is also justified by the earlier remark that the H_2O luminosity might be higher than the OH luminosity. We therefore base our classification of the LFMM object as an evolved low mass Mira type OH/IR star on the OH maser profile and the OH and H_2O maser characteristics. This is entirely consistent with the near-infrared measurements taken by LFMM.

A final remark about the object found by LFMM concerns an article written by McGinn et al. (1989). They use integrated infrared starlight to determine mean stellar velocity and velocity dispersion in several 20$''$ diameter telescope apertures to probe the stellar kinematics and mass distribution in the GC. One of the telescope beams (45$''$ NE) is pointed towards the LFMM maser source and McGinn et al. (1989) derive an average stellar velocity of 48 ($\pm$8) km s^{-1} for this beam. This is exactly the velocity of the LFMM maser source. It seems likely that the LFMM maser source has dominated the telescope beam. The observation of an increasing velocity dispersion towards the dynamical center seen by McGinn et al. (1989) and also by Sellgren et al. (1990), could differ from the constant velocity dispersion observed by Rieke & Rieke (1988), because of telescope beams being dominated by single stars instead of representing true stellar averages.

In summary, we conclude that the H_2O maser of Y-ZM is associated with an evolved OH/IR star. We think the H_2O maser found by LFMM, instead of a massive supergiant, is more likely to be a Mira type OH/IR star. We cannot rule out recent massive star formation in the GC, but we do conclude the H_2O masers found by LFMM and Y-ZM do not support the presence of a young population of massive stars.

Acknowledgements. We thank Joris Blommaert and Wil van der Veen for their help with the interpretation of the infrared results and Harm Habing, Anders Winnberg and Michael Lindqvist for carefully reading the manuscript. HJvL acknowledges support for this research by the European Union under contract CHGECT920011.

References

Blommaert J.A.D.L., van Langevelde H.J., Habing H.J., van der Veen W.E.C.J., Epchtein N. 1992, in "Variable Stars and Galaxies", B. Warner (ed.), ASP Conf. Ser. Vol. 30, p. 269

Blommaert J.A.D.L., van Langevelde H.J., Michiels W.F.P. 1994, A&A 287, 479

Blommaert J.A.D.L., van der Veen W.E.C.J., van Langevelde H.J., Habing H.J., Epchtein N., Sjouwerman L.O. 1997, accepted for publication in *Astronomy & Astrophysics*; see Blommaert J.A.D.L. 1992, PhD thesis, Leiden University, Chapter 3 or van Langevelde, H.J. 1992, PhD thesis, Leiden University, Chapter 7

Bowers P.F., Hagen W. 1984, ApJ 285, 637

Catchpole R.M., Whitelock P.A., Glass I.S. 1990, MNRAS 247, 479

Engels D., Schmid-Burgk J., Walmsley C.M. 1986, A&A 167, 129

Engels D., Schmid-Burgk J., Walmsley C.M. 1988, A&A 191, 283

Genzel R., Hollenbach H., Townes C.H. 1994, Rep. Prog. Phys. 57, 417

Habing H.J., Tignon J., Tielens A.G.G.M. 1994, A&A 286, 523

Iben I., Renzini A. 1983, ARA&A 21, 271

Jones T.J., McGregor P.J., Gehrz R.D., Lawrence G.F. 1994, AJ 107, 1111

Krabbe A., Genzel R., Eckart A., Najarro F., Lutz D., Cameron M., Kroker H., Tacconi-Garman L.E., Thatte N., Weitzel L., Drapatz S., Geballe T., Sternberg A., Kudritzki R. 1995, ApJ 447, L95

Lacy J.H., Townes C.H., Geballe T.R., Hollenbach D.J. 1980, ApJ 241, 132

Levine D.A., Figer D.F., Morris M., McLean I.S. 1995, ApJ 447, L101 (LFMM)

Lepine J.R.D, Ortiz R, Epchtein N. 1995, A&A 299, 453

Lewis B.M. 1989, ApJ 338, 234

Lindqvist M., Winnberg A., Forster J.R. 1990, A&A 229, 165

Lindqvist M., Winnberg A., Habing H.J., Matthews H.E. 1992a, A&AS 92, 43

Lindqvist M., Habing H.J., Winnberg A. 1992b, A&A 259, 118

McGinn M.T., Sellgren K., Becklin E.E., Hall D.N.B. 1989, ApJ 338, 824

Reid M.J., Schneps M.H., Moran J.M., Gwinn C.R., Genzel R., Downes D., Rönnäng B. 1988, ApJ 330, 809

Rieke G.H., Lebovsky M.J. 1985, ApJ 288, 618

Rieke G.H., Rieke M.J. 1988, ApJ 330, L33

Sellgren K., McGinn M.T., Becklin E.E., Hall D.N.B. 1990, ApJ 359, 112

van de Hulst H.C. 1949, Rech. Astr. Obs. Utrecht, Vol 11, Part 2

van der Veen W.E.C.J., Habing H.J. 1990, A&A 231, 404

van Langevelde H.J., Janssens A.M., Goss W.M., Habing H.J., Winnberg A. 1993, A&AS 101, 109

Yusef-Zadeh, F., Mehringer D.M. 1995, ApJ 452, L37 (Y-ZM)

Zylka, R., Mezger P.G., Ward-Thompson D., Duschl W.J., Lesch H. 1995, A&A 297, 83

Chapter 3

Detection of 22 GHz H_2O and 43 GHz SiO maser emission

in Galactic center OH/IR stars and in the G−0.13−0.08 molecular cloud

Abstract.

We describe targeted surveys for 22 GHz H_2O and 43 GHz SiO maser emission in Galactic center OH/IR stars with the Very Large Array. We will use the detections to investigate the possibility of measuring stellar proper motions in the Galactic center. Because of heavy interstellar scattering and the extent of the circumstellar OH maser, higher frequency masers are a necessity to obtain stellar positions with high accuracy. In contrast to the sample of OH masers, the reported number of H_2O and SiO masers so far is too small for a proper motion study. Here we report on the detection of 36 H_2O and 18 SiO masers in OH/IR stars within 2°, and within $15'$ of Sgr A* respectively, and on an increase of the total number of proper motion candidates from 15 to 46. Serendipitously, we found that the core of the molecular cloud G−0.13−0.08 exhibits numerous variable H_2O maser spots which we relate to present day star formation.

Co-authored by:
M. Lindqvist, H.J. van Langevelde & P.J. Diamond

3.1 Introduction

The dynamics of the central region of the Galaxy still poses some big questions. The mass distribution and whether Sgr A* is a massive black hole are the most intriguing issues. Further out from the center, observations provide evidence for a 'bar', and/or a tri-axial bulge. In the past decade many studies to probe the inner Galactic gravitational potential have been performed, using line-of-sight velocities of gas and stars. However, in this part of the Galaxy interstellar gas is an unreliable probe to sample the local velocity field, because it might be subject to non-gravitational forces such as stellar winds, radiation pressure and magnetic fields. Also, gas may be transported inward on non-circular motions by a barred gravitational potential. Recent reviews about the Galactic center (GC) can be found e.g. in Blitz et al. (1993), Genzel et al. (1994), Morris & Serabyn (1996) and Mezger et al. (1996).

Stellar objects make much better test particles, because they are less susceptive to non-gravitational forces. However, except in a few special cases, the interstellar extinction ($A_V >$ 25 mag) toward the GC prevents us to observe the stellar population in the GC. In the (near-)infrared the interstellar extinction is less, allowing stars that are bright or have particular emission lines at these wavelengths to be studied: for example He I emission line stars, or thermal emission from the more abundant M type (super)giants.

We plan to measure transverse velocities of OH/IR stars found previously in the GC. However, because of severe interstellar scattering toward the GC (Van Langevelde et al. 1992b; Frail et al. 1994), the 1612 MHz OH masers are not useful. The higher frequency 22 GHz H_2O and 43 GHz SiO masers, known to occur frequently in circumstellar shells of evolved stars, are more favorable since scattering scales as λ^2. However, so far hardly any studies on H_2O and SiO masers in the GC have been performed, limiting the number of candidate objects for a proper motion survey. Early single dish observations by Lindqvist et al. (1990, 1991) resulted in 15 stellar proper motion candidates. More recently additional individual stars have become available (Levine et al. 1995; Yusef-Zadeh & Mehringer 1995; Chapter 2; Menten et al. 1997). For further reading about AGB stars and circumstellar shells, we recommend monographs by Habing (1996) and Iben (1991).

We have performed a search for H_2O and SiO maser emission in OH/IR stars in the GC with the Very Large Array (VLA) to obtain a larger sample of proper motion candidates. In addition, all stars are located at the same distance of 8 kpc (Reid 1993). The combination of OH, H_2O and SiO data, and data found in the literature (e.g. bolometric luminosities and periods from Jones et al. 1994), provide valuable information on the physical processes (in particular the mass-loss mechanism) in the star and its envelope.

We describe the observations in Sect. 2, the data reduction in Sec. 3, and the results in Sect. 4. We will attempt to identify the stellar sources from H_2O maser emission associated with star forming regions (SFR's) among our detections and comment on the complex of H_2O masers found in G−0.13−0.08 (also known as the "+20 km s^{-1} molecular cloud", cf. Zylka et al. 1990) in Sect. 5. We conclude with the number of proper motion candidates. A first report on measuring their position can be found in Chapter 4. A discussion of the data in terms of the evolution of circumstellar material and AGB stars is beyond the scope of this paper (Chapter 7).

3.2 Observations

In this section we first comment on the chronology of the observations. The second part of this section contains general comments on the calibration. During the course of this project, our focus shifted from 22 GHz H_2O masers to 43 GHz SiO masers, because it became clear that SiO masers would yield a better prospect for the proper motion study. The actual flux determination has lower priority and also has to do with the fact that we used the new VLA 43 GHz receivers before a proper calibration could be determined. In 1993, we aimed to detect H_2O masers with accurate positions. Due to the moderate quality of the 22 GHz data, we wanted to obtain a list of more (reliable) detections, either in the SiO or the H_2O maser line. Finally, after we decided to use only SiO masers for our proper motion campaign, we also used the opportunity to obtain line intensity ratios for the SiO masers.

3.2.1 Observational history

In July 1993 we used the VLA to search for 22 GHz H_2O masers in the ≈ 150 OH/IR stars that were known in the Galactic center (GC) in 1993[1]. The details of the observations, and of subsequent observations, can be found in Table 3.1. The phases were calibrated every 15 minutes, and with an on-source time of 5 minutes (and a bad calibrator choice), we obtained a very low detection rate ($\approx$ 10%). Apart from bad weather, this is possibly also due to the variable nature of the H_2O masers. We concluded that we did not have enough detections for a proper motion campaign.

[1]For a compilation of the data, see the appendix in Chapter 5 where also more than 50 additional OH/IR stars found in the central $35'$ (80 pc) are listed.

Table 3.1 Observational summary

Set	Date	ν_{rest} GHz	Array	BW MHz	$\Delta\nu$ kHz	Mode
H_2O maser surveys:						
1a	07 Jul 93	22.231	C	6.25	97.7	2AC
1b	10 Jul 93					
1c	13 Jul 93					
2a	21 May 94	22.231	A^1	6.25	97.7	2BD
3a	02 Jun 94		BnA^1			
SiO maser surveys:						
2b	21 May 94	42.820	A^2	12.50	390.6	2AC
3b	02 Jun 94		BnA^2	6.25	97.7	
4a	29 Jan 95	42.820	DnC^3	6.25	195.3	2AC
4b		43.122		6.25	195.3	2BD

1: 17 antennas on the outer stations of the configuration
2: 9 antennas on the inner three stations along each arm
3: 9 antennas with 43 GHz receivers put in a spiral pattern

In the beginning of 1994, a number of VLA antennas were equipped with 43 GHz receivers, enabling us to search for SiO masers in the OH/IR stars. We selected about 50 OH/IR stars from the list of Lindqvist et al. (1992) which were located within 15′ of Sgr A*. In May and June 1994 they were observed at 22 GHz in a search for H_2Omasers, and at 43 GHz for ($J = 1 \rightarrow 0,\ v = 2$) SiO maser emission as well. The VLA was divided up into two sub-arrays: one sub-array with the 43 GHz receivers on the VLA antennas located on the 'inner arms', and another sub-array with all the other ('outer arm') antennas.

With phase calibrating every 30 (or 15) minutes and an on-source time of typically 14 minutes, the H_2O maser detection rate was much higher ($\approx 30\%$). However, we also encountered broad-band interference hindering the bandpass calibration for the June 2 observations; these data were disregarded. As this was also more or less the case for the 43 GHz measurements for this day, we suppose the interference had to do with the sub-array or IF system setup.

For the 43 GHz observations we integrated for 6 minutes on each source and calibrated the phase between source switches. Much of the data was lost, how-

Table 3.2 Image cube summary

Set	Resolutions ″	km s^{-1}	J1733−130 Jy	Sgr A* Jy	RMS [a]	#
H_2O maser surveys:						
1a	0.25	1.3	4.6	0.3[b]	15	153
1b			4.0	0.7		
1c			4.2	0.7		
2a	0.085	1.3	6.1	0.9	10	19
3a			5.1	0.9	x	17
SiO maser surveys:						
2b	0.20	2.8	9[c]	1.4	60	25
3b		0.7	9[c]	1.5	x	23
4a	0.40	1.4	9[c]	1.1	15	19
4b		1.4	9[c]	1.1		

a: Typical RMS noise level in mJy beam^{-1}
b: On July 7, the flux of J1744−312 instead of Sgr A*
c: Adopted 43 GHz flux of 9 Jy for J1733−130

ever, because of poor phase stability over the relatively long integration and large array configuration. Phases were stable in several one to three minute intervals, but changed rapidly in between. Visibility averaging or mapping the source did not allow many direct results. However, with a self-calibration scheme (Sect. 3.1) we found hints that several OH/IR stars indeed had detectable SiO masers. Because of an unreliable bandpass calibration in addition to the rapid atmospheric phase fluctuations, the June 2 measurements did not yield any results from direct imaging with, or without bandpass calibration.

In January 1995 we re-observed 19 OH/IR stars for SiO maser emission, subjectively selected from the tentative detection in May 1994 (Sect. 3.1), simultaneously in the 43 GHz ($J = 1 \rightarrow 0,\ v = 1$) and ($J = 1 \rightarrow 0,\ v = 2$) transitions. In 1994 we chose only the ($v = 2$) transition of SiO, because it is supposed to be the stronger one in OH/IR stars (Nyman et al. 1986, 1993; Lindqvist et al. 1991). With half the calibration cycle of the June 94 observations and 7 minutes on-source, we obtained a relatively high detection rate (well over 70%). During these observations the VLA was in its most compact array configuration, with the 43 GHz receivers arranged in a 'spiral configuration' and not on the 'inner' three antennas on each arm as had been practice before.

3.2.2 Calibrator sources

On July 7 1993 we used J1744−312 as phase calibrator, but we noted that it was too weak at 22 GHz (Table 3.2). Since then we chose Sgr A* as phase calibrator, at 22 and at 43 GHz, despite the extended background radiation of the Sgr A complex since it was mostly resolved by the array configuration; all baselines longer than 25 and 20 kλ are usable for 22 and 43 GHz, respectively.

For all observations we used J1733−130 for bandpass calibration, which for the 43 GHz observations were preceeded by pointing scans on J1733−130 taken every one or two hours. For the 22 GHz observations we included J1331+305 for absolute flux calibration. Due to the new capabilities of observing at 43 GHz with the VLA at that time, an accurate absolute flux calibration at 43 GHz was not possible. With an adopted 43 GHz flux density for J1733-130 (of 9$\pm$3 Jy, VLA Test memo 192), we determined flux densities for Sgr A* as shown in Table 3.2. We expect that the approximate fluxes do not deviate more than 30 percent from the true values. For future reference, with this choice we measured a flux of 0.49$\pm$0.03 Jy for the (point source) flux calibrator J0137+331 in January 1995 (J1331+305 was not observed).

3.3 Data reduction

All data sets were calibrated according to a standard spectral line calibration scheme with the NRAO AIPS package. Because of problems determining a bandpass calibration, we quickly scanned the 2 July 1994 22 and 43 GHz data sets for strong masers in the autocorrelation spectra before we had to regard the data as not usable. For all the other data sets, we made image cubes of about 25$''$ in diameter around the OH maser positions. In cases where we pointed the telescopes such that more than one OH/IR star would fall in the primary beam (and velocity coverage), we chose to image the full primary beam (2$'$ or 1$'$ for 22 and 43 GHz respectively). For these larger image cubes, we searched the OH/IR star positions and detected several masers by accident. Generally, the Jul 93 data are badly calibrated which resulted in a large fraction of tentative detections. A summary on the image cubes can be found in Table 3.2, where we also give a representative value for the noise in the cube and the total number of fields searched for emission. The (non-)detections from the cubes are given in Tables 3.3, 3.4 and 3.5.

3.3.1 Self-calibration

Inspection of the 43 GHz image cubes of the 21 May 1994 observations yielded 6 clear detections out of 25 (Fig. 3.1). From both Lindqvist et al. (1992) and Chapter 5 we have very good OH positions (accurate to $\sim 1''$). However, some SiO maser deviate considerably (up to $10''$) from this position. We think these are due to serious phase calibration problems. Detected were OH359.946−0.047, OH359.974+0.162, OH359.977−0.087, OH 0.007−0.088, OH 0.071−0.205 and OH 0.083+0.064. The OH maser names are taken from Lindqvist et al. (1992). However, in many image cubes we found channels with emission exceeding the noise. We figured this emission was from improperly imaged sources; not from noise. Analysing the proper detections, we could see that the visibility phases were stable, but different in several one minute scans. Using knowledge on the spectral profile of SiO masers, we attempted to image more sources, or at least to obtain a list of suspicious sources to re-observe. For this we make use of the fact that SiO emission is found around the stellar velocity (the mean of the OH maser peaks) and usually has a width of about 5 $\mathrm{km\,s^{-1}}$ (e.g. Nyman et al. 1986; Lindqvist et al. 1991). Furthermore, we assume the noise in individual, uniformly weighted frequency channels to be independent and take the interval of atmospheric phase stability to be one minute.

Assuming that a certain channel covers a part of the broad SiO maser profile, we collected all emission for this channel in one point with self-calibration. Next the self-calibration solution was applied to all channels. Now, if the channel does not contain line emission, noise in this channel will add up into a spurious detection. However, because the noise in each channel is independent, the solution for this channel applied to the next channels will not yield a proper adding of noise there; no significant systematic emission at this location in the next channels.

We found many sources – also in the 'unusable' 43 GHz June observations – for which a solution for one frequency channel aligned flux in several consecutive channels. We regarded such sources as suspicious. Because of the extra contribution of the noise in one channel and a missing bandpass calibration for the June data set, spectral profiles and fluxes are not determined for these sources. Also, a chance alignment of a source in the primary beam other than the source we pointed at, cannot be excluded. However, we re-observed most of the sources successfully in January 1995. For the H_2O masers, the spectral profile is much less regular and many maser spots are spectrally unresolved in our data sets. Hence, the scheme outlined above does not work properly for the H_2O masers.

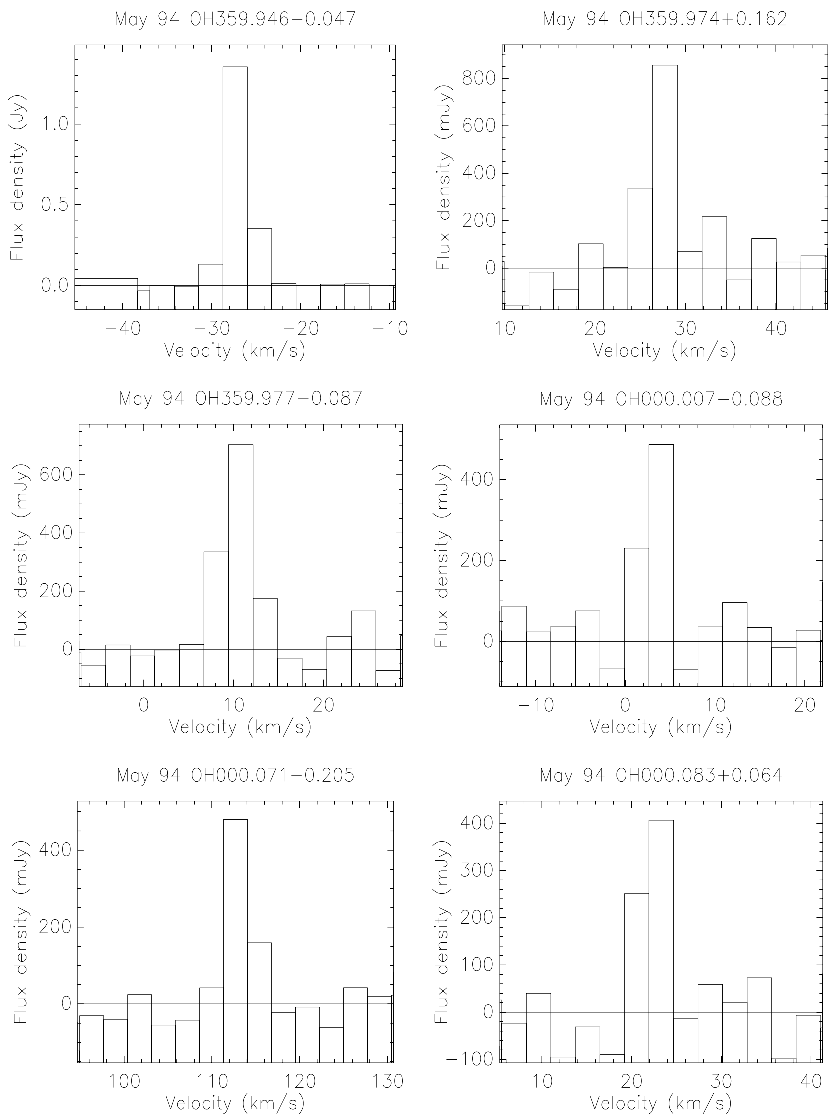

Figure 3.1 SiO $(J = 1 \rightarrow 0,\ v = 2)$ maser detections in May 1994

Table 3.3 Non-detections

May 94 H_2O maser survey:	
359.803−0.021	359.952−0.036
359.810−0.070	359.954−0.041
359.855−0.078 (detected in Jul 93)	
359.880−0.087	359.955−0.031
359.902+0.061	359.996−0.144
359.939−0.052	0.053−0.062
359.946−0.047 (detected in May 94)	
Jan 95 SiO maser survey:	
359.873−0.209	359.970−0.049
359.977−0.087 (detected in May 94)	
0.007−0.088 (detected in May 94)	

OH name from Lindqvist et al. 1992

3.4 Results

Summarising, we have 36 H_2O maser detections in OH/IR stars (19 of which 1 re-detection plus 18 tentative), and 18 SiO masers (6 plus 16 minus 4 re-detections).

In July 1993 we detected 19 H_2O maser sources of which 6 by accident (H_2O maser emission not associated with the OH masers we pointed at). The number of tentative detections, for which the phase calibration is questionable, is 20 of which probably 2 by accident. In May 1994 we detected 12 H_2O maser sources (6 accidental) and 2 tentative (1 accidental) sources. We were able to confirm 3 detections of the H_2Omasers that were found in the July 1993 data and that are not associated with OH/IR stars. Of the 16 SiO maser detections in January 1995 (of which one by accident from an extra OH/IR star in the beam), 4 had been already detected in May 1994. The H_2O maser detections are given in Table 3.4, the SiO maser detections in Table 3.5.

All detections, in both tables have entries for the given name of the source in Galactic coordinates, the code of the data set and the position in J2000 coordinates (for this data set) with the maximum of the formal error in either R.A. or Dec. in arcseconds (Δ). For the H_2O masers we list further the veloc-

Table 3.4 H_2O maser detections in the Galactic center

H_2O Name	Set	Position (J2000) R.A.	Dec.	Δ $''$	V_{blue} (km s^{-1})	$V_{central}$ (km s^{-1})	V_{red} (km s^{-1})	S_{peak} Jy	I_{total} [a]	Notes	
359.431+0.035	1a	17 44 7.372	−29 24 7.65	0.144	−0.6			0.50	0.74	AGB	
359.485+0.082	1a	17 44 4.098	−29 19 54.90	0.053	−74.2	−47.9		0.30	0.59	AGB	
359.511+0.177	1b	17 43 45.624	−29 15 34.86	0.062	−134.5		−98.9	0.25	0.56	AGB	
359.513+0.173	1c	17 43 46.772	−29 15 37.83	0.262	114.2			0.23	0.95	AGB	OK
359.517+0.001	1a	17 44 27.655	−29 20 48.63	0.098	−146.9		−111.4	0.22	0.44	AGB	OK
359.701−0.087	1b	17 45 14.760	−29 14 10.00	0.093		38.0		0.12	0.34	SFR	
359.711−0.263	1c	17 45 57.566	−29 19 9.81	0.079	−17.0	−7.7		0.35	1.08	AGB	OK
359.745−0.404	1b	17 46 35.629	−29 21 49.68	0.150	173.3			0.18	0.56	AGB	OK
359.751−0.371	1b	17 46 28.712	−29 20 29.16	0.053	−25.6		−9.8	1.05	7.95	SFR	OK
359.759+0.071	1c	17 44 45.989	−29 6 13.86	0.234	−73.3			0.14	0.75	AGB	OK
359.764+0.081	1c	17 44 44.517	−29 5 40.17	0.207	93.1	107.6		0.17	1.69	AGB	OK
359.767−0.208	1a	17 45 52.676	−29 14 33.29	0.144	−169.1		−136.2	0.08	0.28	AGB	OK
359.784−0.392	1a	17 46 38.348	−29 19 24.66	0.120		209.0	226.1	0.10	0.12	AGB	
359.837+0.120	1a	17 44 45.842	−29 0 42.59	0.243			−341.8	0.09	0.39	AGB	OK
359.854−0.079	1a	17 45 34.734	−29 6 2.70	0.148	−8.4		21.8	0.16	2.03	AGB	OK
359.859−0.079	2a	17 45 35.461	−29 5 47.86	0.021		12.6		0.28	0.48	SFR	OK
359.860−0.081	1a	17 45 36.297	−29 5 49.63	0.077		8.7		0.25	1.85	SFR	OK
359.861−0.082	2a	17 45 36.377	−29 5 49.16	0.028		10.0		0.31	1.80	SFR	OK

Table 3.4 H_2O maser detections in the Galactic center

H_2O Name	Set	Position (J2000) R.A.	Dec.	Δ ″	V_{blue} $km\,s^{-1}$	$V_{central}$ $km\,s^{-1}$	V_{red} $km\,s^{-1}$	S_{peak} Jy	I_{total} [a]	Notes	
359.864−0.084	1a	17 45 37.458	−29 5 44.28	0.093		8.0	11.3	0.14	0.77	SFR	OK
359.864−0.083	2a	17 45 37.214	−29 5 41.48	0.040		10.0		0.13	0.33	SFR	
359.864−0.084	1a	17 45 37.527	−29 5 42.83	0.124		3.4		0.12	1.48	SFR	OK
359.864−0.085	2a	17 45 37.676	−29 5 43.80	0.015		28.4		0.41	0.87	SFR	OK
359.865−0.085	1a	17 45 37.832	−29 5 42.88	0.062	−17.7	−13.1	−8.4	0.95	6.91	SFR	OK
359.865−0.085	2a	17 45 37.917	−29 5 42.64	0.019	−13.7	−10.4	−7.1	0.29	1.22	SFR	OK
359.874−0.079	1a	17 45 37.754	−29 5 2.99	0.043		−13.7		0.15	0.98	SFR	OK
359.896−0.069	2a	17 45 38.396	−29 3 35.83	0.015		−132.1		0.08	0.15	AGB	OK
359.906−0.042	2a	17 45 33.528	−29 2 16.24	0.003	−156.0		−125.7	0.63	1.96	AGB	OK
359.925+0.032	1c	17 45 18.961	−28 58 56.94	0.105	−92.5			0.17	0.53	AGB	OK
359.935−0.145	1b	17 46 1.966	−29 3 58.78	0.235		−13.2		1.52	9.47	SFR	OK
359.936−0.145	2a	17 46 1.969	−29 3 58.48	0.002		−19.8		1.88	5.76	SFR	OK
359.944+0.261	1a	17 44 28.035	−28 50 49.08	0.344	−202.4			0.10	0.44	AGB	
359.946−0.048	2a	17 45 40.674	−29 0 23.51	0.005	−44.3			0.46	0.93	AGB	OK
359.956−0.051	2a	17 45 42.763	−28 59 57.20	0.015		43.5	56.7	0.16	0.62	AGB	OK
359.956−0.050	1c	17 45 42.749	−28 59 56.83	0.073		44.8		0.35	1.44	AGB	OK
359.970−0.049	2a	17 45 44.356	−28 59 12.99	0.033			92.2	0.07	0.31	AGB	OK
359.971−0.120	2a	17 46 0.990	−29 1 23.04	0.010	−23.0		4.7	0.09	0.35	AGB	OK

Table 3.4 H_2O maser detections in the Galactic center

H_2O Name	Set	Position (J2000) R.A.	Dec.	Δ $''$	V_{blue}	$V_{central}$ km s^{-1}	V_{red}	S_{peak} Jy	I_{total} [a]	Notes	
0.040−0.057	2a	17 45 56.127	−28 55 51.71	0.008	56.9			0.24	0.77	AGB	OK
0.061−0.015	2a	17 45 49.244	−28 53 29.43	0.023		−1.4	15.7	0.06	0.12	AGB	
0.070+0.126	1c	17 45 17.635	−28 48 36.46	0.155	−52.8			0.20	0.36	AGB	OK
0.071−0.207	1a	17 46 35.720	−28 58 58.39	0.195		110.1	128.5	0.10	0.10	AGB	
0.076+0.146	1b	17 45 13.876	−28 47 42.05	0.210	5.8		33.5	0.09	0.63	AGB	
0.132−0.023	1c	17 46 1.417	−28 50 6.57	0.293	−40.2			0.18	0.60	AGB	
0.141+0.022	1b	17 45 52.255	−28 48 14.11	0.184	2.8	25.2	48.9	0.12	0.32	AGB	
0.181−0.055	1a	17 46 15.825	−28 48 35.62	0.168	−48.8		−23.7	0.11	0.46	AGB	
0.186+0.036	1a	17 45 55.315	−28 45 27.21	0.156	143.4			0.11	0.19	AGB	
0.347+0.050	1c	17 46 14.959	−28 36 46.92	0.151		39.7		0.29	0.47	AGB	
0.379+0.159	1a	17 45 54.059	−28 31 45.20	0.186	127.4	139.3	153.8	0.12	0.24	AGB	
0.466+0.026	1b	17 46 37.405	−28 31 26.10	0.105		93.4	105.2	0.09	0.21	AGB	
0.495−0.211	1b	17 47 36.987	−28 37 21.57	0.210		4.4		0.16	0.20	SFR	
0.544−0.045	1b	17 47 4.897	−28 29 39.78	0.315	−16.6			1.20	5.41	AGB	
0.549−0.059	1c	17 47 9.076	−28 29 51.65	0.129			−16.5	0.40	0.63	AGB?	
0.587−0.107	1c	17 47 25.633	−28 29 20.65	0.273		−202.6	−189.5	0.32	0.87	AGB	
0.649−0.060	1c	17 47 23.365	−28 24 42.10	0.073		66.0		1.20	12.05	SFR	

a: Total integrated line flux I in units of Jy km s^{-1}

ity of the most blue-shifted, the central and the most redshifted components (where appropriate), the highest peak flux of the profile, the total (spatially and spectrally) integrated line flux, the most likely origin of the emission and an 'OK' if we find the detection 'reliable' (i.e. good position and spectral profile from properly calibrated data). The SiO maser table is completed by listing the mean velocity, the highest peak flux and the total integrated line flux for the ($v = 2$), and for the ($v = 1$) transition, respectively. The spectra for the detections can be found in Figs. 3.1, 3.2, 3.3 and 3.4.

For the 22 GHz May 94 (and 43 GHz Jan 95) observations, we also give the non-detections in Table 3.3. We do not give the non-detections for the 22 GHz July 93 (over 100 sources) and June 1994, and for the 43 GHz May and June 94 observations, because many might have been detected with a proper phase or bandpass calibration. Positions and spectra measured for many (tentative) detections in these data sets may have very large offsets (on the order of $10''$) or improper channel alignment which made clear (spectral) identification difficult. Looking at the data, we suspect that there is a number of H_2O masers (either in AGB stars or star forming regions) to be found in several of our observed fields, but we lack sufficient signal-to-noise to make a definite statement about this. An exception is the field around G$-$0.13$-$0.08 for which we refer to Sect. 5.3 (see also Menten et al. 1997 for additional H_2Omasers around Sgr A*, and Chapter 5 for newly found OH/IR stars that can be searched for H_2O and SiO masers).

For an impression of the long term variability and the occurrence of multiple maser lines, we list the sources that were detected (denoted with '+') in both our, or previous surveys in Table 3.6. However, the overlap of the (reliable part of the) data sets is generally small and non-detections (denoted with '$-$') might be due to low sensitivity. Some of these sources could provide an opportunity to measure a proper motion of the star from the H_2O and SiO maser lines independently.

3.4.1 Notes on individual H_2O masers

We have compared our detections with the 1612 MHz OH maser detections from our input catalogue. In addition to the given H_2O names according to their measured positions, we give OH names from Lindqvist et al. (1992) when not stated otherwise. In particular, we comment on the possible nature of the objects ("SFR" or "AGB") that are not obviously OH/IR stars. See also Sect. 5.2. Note that some remarks concern tentative detections for which we do not have reliable positions or spectra.

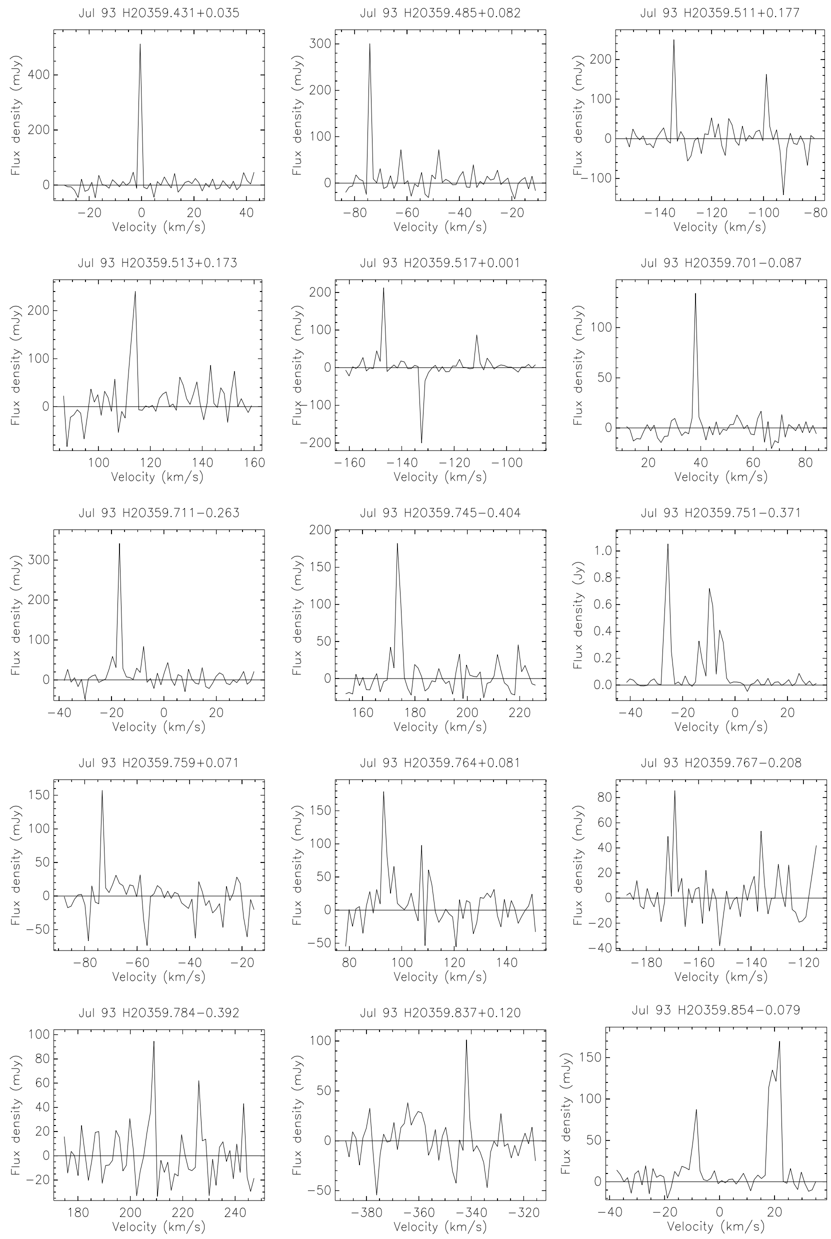

Figure 3.2 22 GHz H_2O maser detections. The velocity resolution is 1.3 km s^{-1}

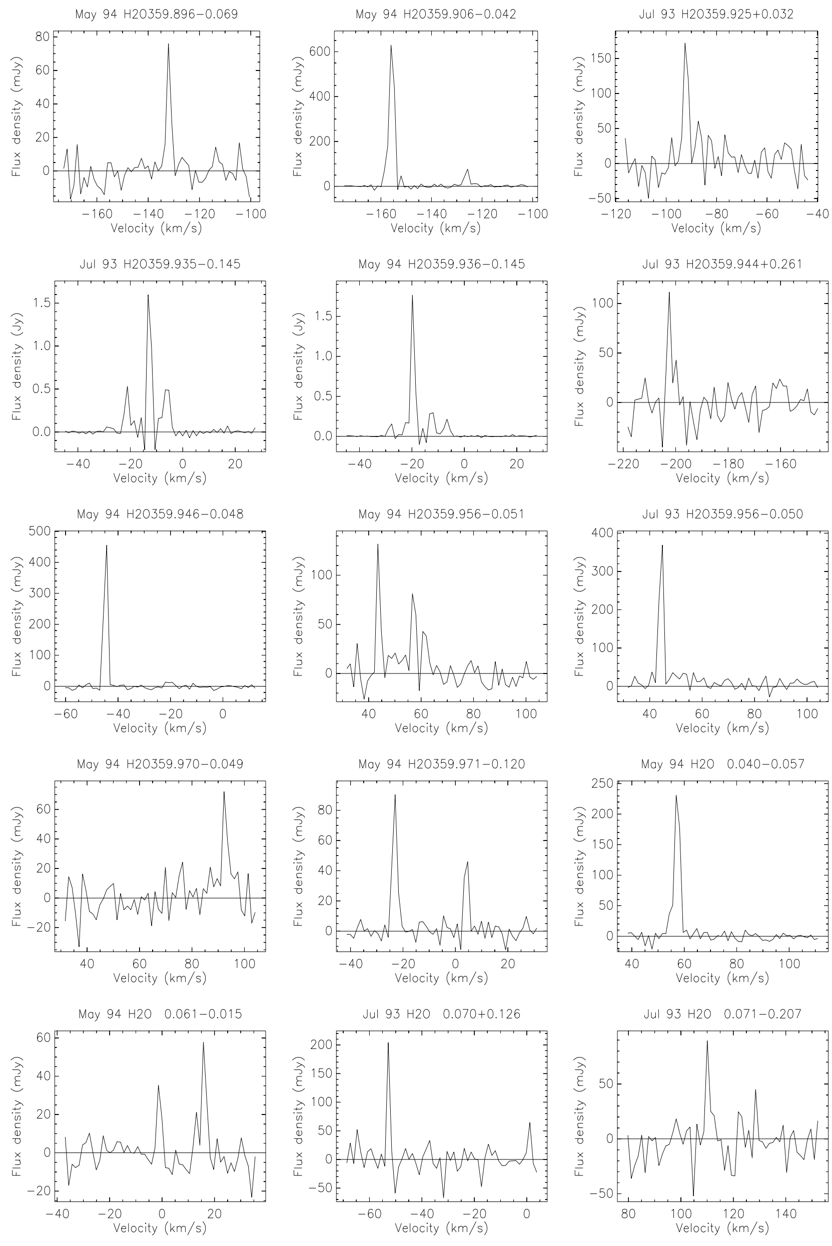

Figure 3.2 22 GHz H_2O maser detections (continued)

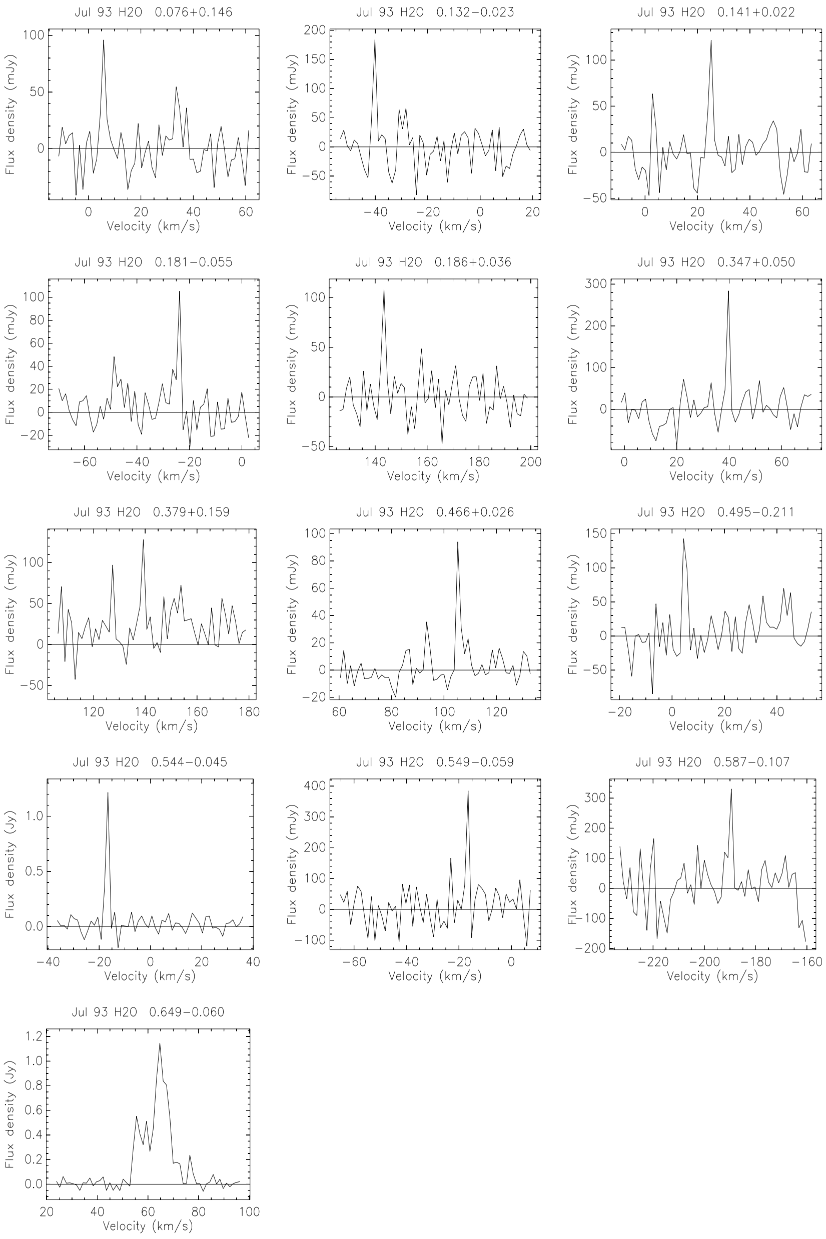

Figure 3.2 22 GHz H_2O maser detections (continued)

H_2O359.431+0.035: In the 1612 MHz OH maser line, this source (OH359.429 +0.035) has a peculiar spectrum from which Lindqvist et al. (1992) could not clearly conclude whether this star is an OH/IR star or connected to a star forming region. With the detection of H_2O maser emission at the (proposed) stellar velocity, we conclude it is most probably a single AGB star.

H_2O359.701−0.087: Unknown source in the ($2'$ large) field; not related to the OH/IR stars we were looking for.

H_2O359.711−0.263: Detected as a single 1612 MHz OH peak (OH359.712 −0.263) at a velocity of −5 km s^{-1}, but shows the expected H_2O maser profile of an AGB star.

H_2O359.751−0.371: Also a single peak 1612 MHz OH detection (OH359.751 −0.371) at −8.5 km s^{-1}. In the H_2O maser line it resembles spectra of young stellar objects with CO outflows in SFR's (e.g. Genzel & Downes 1977; Felli et al. 1992). However, the source does not show up in the search for compact radio continuum sources (HII regions) by Downes et al. (1979), possibly because it is just outside their surveyed area.

H_2O359.837+0.120: A high velocity ($|v_{\rm LSR}| > 250$ km s^{-1}) OH/IR star (OH359.837+0.120, Van Langevelde et al. 1992a), which also has been confirmed in the 1612 MHz OH line in Chapter 5.

All sources around **H_2O359.86−0.08:** In this region one finds the dense molecular cloud core G−0.13−0.08, an ultra compact HII region, and two OH/IR stars. One of these OH/IR stars is detected as an H_2O maser, and with the possible exception of H_2O359.864−0.085, all the other H_2O masers found here are likely to be connected to the formation of stars. Some of the stronger H_2Omasers have been detected previously. For easy comparison, we show these spectra in Fig. 3.4 separate from the spectra in Fig. 3.2. A discussion can be found in Sect. 5.3.

H_2O359.864−0.085: A characteristic double peaked H_2O maser which has not been detected in the 1612 MHz OH line by either Lindqvist et al. (1992) or Chapter 5. Therefore, we hesitate to classify this object to be an OH/IR star. See however the remark on H_2O359.896−0.069 (next). We cannot exclude that the H_2O emission at 13 km s^{-1} is a side-lobe of H_2O359.861−0.082 in which case this detection would be one of the many SFR's in the direction of G−0.13−0.08.

H_2O359.896−0.069: In Chapter 5 we concluded this source (OH359.90−0.07, Habing et al. 1983) is probably not an OH/IR star, because this source has never been confirmed in the 1612 MHz OH line. However, with this H_2O maser detection, we confirm with reservation that there is an object as reported by Habing et al. (1983). If this source is an AGB – or post-AGB – star, it does not

Table 3.5 SiO maser detections in OH/IR stars in the Galactic center

SiO Name	Set	Position (J2000) R.A.	Dec.	Δ $''$	($v=2$), 42.820 GHz $V_{\rm system}$ km s^{-1}	$S_{\rm peak}$ Jy	$I_{\rm total}$ Jy km s^{-1}	($v=1$), 43.122 GHz $V_{\rm system}$ km s^{-1}	$S_{\rm peak}$ Jy	$I_{\rm total}$ Jy km s^{-1}
359.763−0.042	4b	17 45 13.069	−29 9 34.99	0.252	122.7	0.17	0.25	122.7	0.19	0.61
359.765+0.081	4b	17 44 44.460	−29 5 37.33	0.106	111.5	0.62	2.87	111.5	0.97	4.05
359.778+0.009	4a	17 45 3.244	−29 7 12.35	0.102	−28.4	0.50	1.47	−28.4	0.58	1.47
359.802−0.021	4a	17 45 13.928	−29 6 55.17	0.112	−16.3	0.75	3.79	−15.0	0.31	1.84
359.810−0.070	4a	17 45 26.401	−29 8 2.30	0.306	−36.6	0.29	1.58	−33.9	0.22	1.11
359.854−0.079	4b	17 45 34.769	−29 6 3.14	0.178	4.0	0.41	2.62	4.0	0.38	1.76
359.946−0.048	4b	17 45 40.639	−29 0 24.10	0.214	−27.3	0.37	3.47	−27.3	0.44	2.96
359.951−0.036	4a	17 45 38.676	−28 59 45.57	0.296	84.9	0.19	0.27	84.9	0.28	1.21
359.954−0.041	4a	17 45 40.250	−28 59 46.86	0.359	69.9	0.29	1.33	71.3	0.19	1.64
359.970−0.120	4a	17 46 0.967	−29 1 22.77	0.177	−8.5	2.13	9.87	−9.9	0.47	1.72
359.974+0.161	4a	17 44 55.639	−28 52 26.21	0.387	27.7	0.57	2.24	27.7	0.51	3.38
359.977−0.087	2b	17 45 54.368	−29 00 2.66	0.075	10.8	0.70	3.80	not detected in Jan 95		
359.996−0.144	4b	17 46 10.413	−29 0 51.17	0.445	-	-	-	−32.3	0.34	0.79
0.007−0.088	2b	17 45 58.956	−28 58 34.83	0.120	4.0	0.43	1.52	not detected in Jan 95		
0.070−0.206	4a	17 46 35.364	−28 58 56.92	0.081	114.1	0.55	1.20	114.1	0.46	1.00
0.079−0.115	4a	17 46 15.377	−28 55 42.52	0.492	51.4	0.21	2.48	-	-	-
0.083+0.063	4a	17 45 34.270	−28 49 55.93	0.262	23.3	0.27	0.92	23.3	0.28	1.17
0.141+0.025	4a	17 45 51.339	−28 48 6.96	0.225	23.9	0.26	1.21	23.9	0.27	0.77

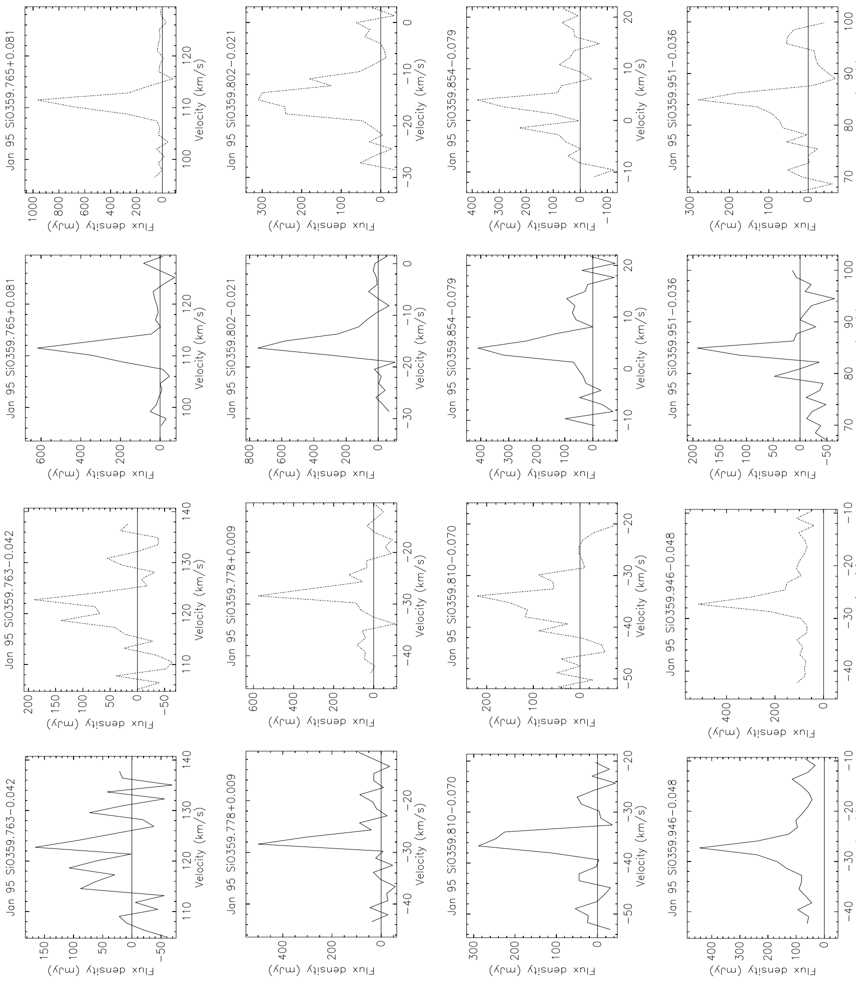

Figure 3.3 43 GHz SiO ($J = 1 \rightarrow 0$) maser detections in January 1995. Solid lines (1st and 3rd column when the page is rotated 90 degrees ccw) are the spectra for ($v = 2$), the corresponding spectra for the ($v = 1$) lines are dotted (2nd and 4th column)

fit the 'maser chronology'; an evolutionary scheme for maser emission around AGB stars proposed by Lewis (1989).

H_2O359.936−0.145: Seen as single 1612 MHz OH peak (OH359.936−0.144), and because it resembles the H_2O maser detection of H_2O359.751−0.371 we

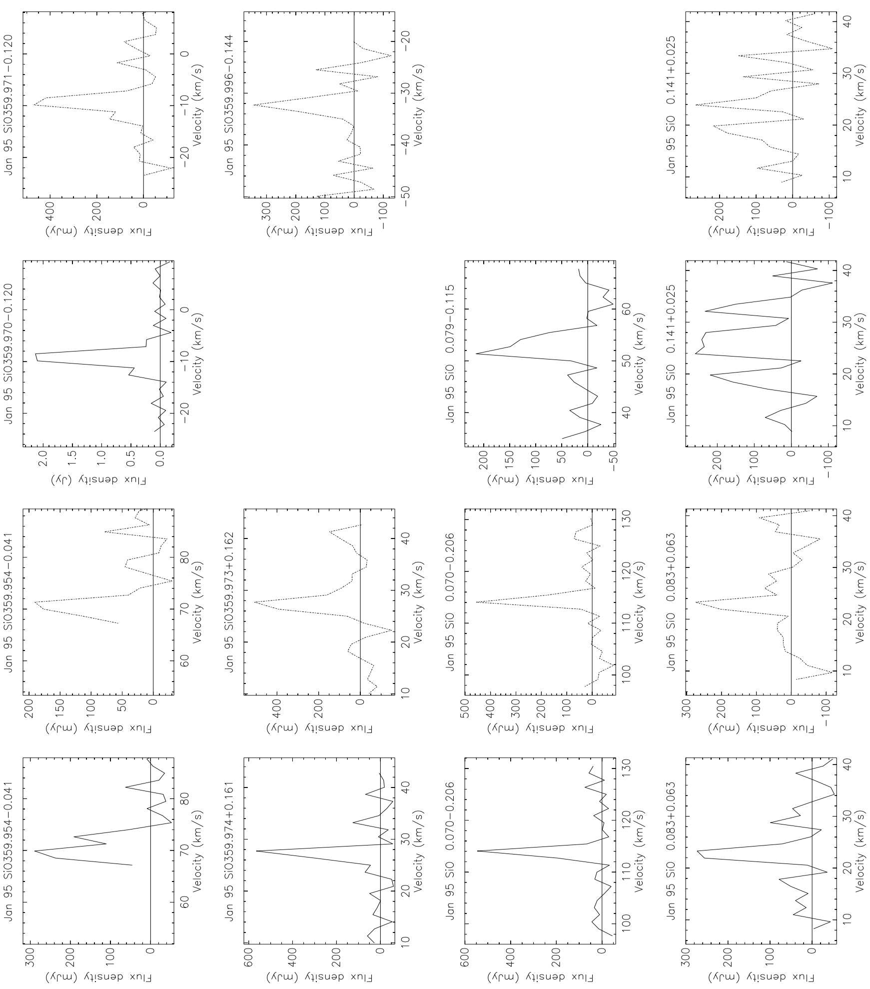

Figure 3.3 SiO maser detections in January 1995 (continued)

believe also this source has a young stellar origin. Similarly, this source has not been found as a compact continuum source because it is located at the edge of the Downes et al. (1979) survey.

H_2O359.956−0.051: Previously found as H_2Omaser (Levine et al. 1995; Yusef-Zadeh & Mehringer 1995). It is one of the newly found OH/IR stars (OH359.956−0.050, Chapter 5) and already extensively discussed in Chapter 2.

H_2O 0.347+0.050: A source in the field toward the 1612 MHz OH source

OH 0.349+0.053 and close to the H_2O and 1665/1667 MHz mainline OH maser H_2O/OH 0.37+0.04 observed with a single dish (Parkes) by Caswell et al. (1983), and Caswell & Haynes (1983) respectively. The latter do not report 1612 MHz OH maser emission for H_2O/OH 0.37+0.04. However, their detection limit might have been too high. If the position difference can be accounted for, all maser line detections are consistent with an AGB star (OH 0.349+0.053) as listed by Lindqvist et al. (1992). We then propose this source to be a Type I OH/IR star characterised by stage 4 (showing SiO (not known for this source), H_2O and strong 1665/1667 MHz OH, as well as 1612 MHz OH maser lines) in the maser chronology (Lewis 1989).

H_2O 0.548−0.059: Observed in the 43 GHz SiO maser lines by Shiki et al. (1997). Because of its strong 43 GHz emission and large OH expansion velocity, they suggest that this is a foreground supergiant. Although the source therefore is probably less useful for the proper motion study, it might be very useful for calibration purposes.

3.4.2 Notes on the SiO masers

In contrast to the H_2O detections, a large fraction of the tentative SiO maser (May 94) detections were confirmed with emission close to the systemic (stellar) velocity derived from the OH maser profile. Striking counter examples are **OH359.977−0.087** and **OH 0.007−0.088**. We are however convinced that they were detected in May 94 (Fig. 3.1) and that the derived SiO positions are reliable ($\lesssim 1''$, confirmed by the OH maser position). We note that the former has been detected at 43 GHz previously (OH359.98−0.09, Lindqvist et al. 1991). As for the H_2O masers, we attribute the non-detections to the SiO maser variability.

Sources **SiO359.996−0.144** and **SiO 0.079−0.115** were only detected in one of the 43 GHz lines. For **SiO359.946−0.048** we subtracted a baseline, due to the extended continuum radiation of the Sgr A mini-spiral, before measuring the peak flux, and the integrated line flux. Source **SiO359.954−0.041** was unintentionally observed in the beam of SiO359.951−0.036. Despite the unusual spectra for **SiO359.763−0.042** and **SiO 0.141+0.205** (see however some SiO maser spectra in Mira-type stars in Jewel et al. 1991), we conclude that all SiO maser detections are from AGB stars.

Table 3.4 Multiple and previous detections in AGB stars

OH name[a]	Previous		This work[d]	
	H_2O[b]	SiO[c]	H_2O	SiO
359.675+0.069	+	+		
359.678−0.024	−	+		
359.762+0.120		+, +[1]		
359.765+0.082			+	+
359.825−0.024	−	+		
359.855−0.078			+, −	+
359.899+0.222	−	+		
359.946−0.047	+	+[2]	−, +	+, +
359.954−0.041	+	+	−	+
359.956−0.050	+[3], +[4]		+, +	
359.971−0.119	−	+	+	+
359.974+0.161				+, +
359.977−0.087	−	+		+, −
359.986−0.061	−	+		
0.007−0.088				+, −
0.040−0.056	−	+	+	
0.071−0.205	−	+	+	+, +
0.076+0.146	+	−	+	
0.083+0.064				+, +
0.113−0.060	−	+		
0.142+0.026	−	−	+	+
0.189+0.052	−	+		
0.548−0.059		+[5]	+	
H_2O(−8.4,+13.5)[e]	+			
H_2O(+1.3, −4.7)[e]	+			
SiO(+0.0, +5.6)[e]		+		
SiO(+1.2,+11.3)[e]		+		

a: Lindqvist et al. (1992)
b: Lindqvist et al. (1990)
c: Lindqvist et al. (1991)
d: See also Tables 3.3, 3.4, and 3.5
e: Menten et al. (1997)

1: Van Paradijs et al. (1995)
2: Menten et al. (1997)
3: Levine et al. (1995)
4: Yusef-Zadeh & Mehringer (1995)
5: Shiki et al. (1997)

3.5 Discussion

3.5.1 43 GHz line ratios

We do not see any significant differences between the intensity of the ($v = 2$) and ($v = 1$) line detections in this sample. However, we do confirm that the average ($v = 2$) line intensity is generally a factor 1.5 larger than for ($v = 1$) (Lindqvist et al. 1991; compared to e.g. 0.7–1.3 for low-mass, Mira-type Galactic bulge sources in Nakada et al. 1993, or $\gtrsim 4.5$ for the high mass-loss rate, thick and cool Galactic disk OH/IR sources in Nyman et al. 1993). Statistical differences between line ratios of different samples of SiO masering objects in the Galaxy can mostly be accounted for by the single entry of source SiO359.970−0.120. With a period of 1400 days (Van Langevelde et al. 1993) and a near-infrared color K−L of about 7 (Blommaert et al. 1997), this source is a prototype 'cool thick envelope' OH/IR star (Nyman et al. 1993).

3.5.2 H_2O maser profiles

Many studies of H_2O masers in different types of objects have been performed in collections of late-type stars with circumstellar environments caused by mass-loss: supergiants, semi-regular variable stars, Mira and OH/IR stars (Olnon et al., 1980, Engels et al., 1986, 1988, Nyman et al., 1986, 1993, and Engels & Lewis 1996; see also the compilation of other objects in Comoretto et al. 1990, Brand et al. 1994). From these studies, a distinction between the several types of stars, and star forming regions, may be made based on the characteristics of the H_2O and OH maser emission. However, the classification scheme is not 100% tight, in particular in the GC where helpful additional optical or infrared information is difficult to obtain.

For OH/IR stars, Engels et al. (1986) divided the H_2O maser detections into two groups, A and B, characterised by their spectral shape. Olnon et al. (1980) have proposed a similar sub-division in combination with several OH maser lines for several species of late-type variable stars. Type A masers show a single H_2O maser peak close to the systemic velocity; type B H_2O masers are double peaked and usually with the same mean velocity, but a smaller velocity separation between the H_2O maser peaks than the 1612 MHz OH maser. Whether a source shows an A or B (or A/B, Engels & Lewis 1996) type H_2O maser is strongly dependent on the IRAS colors of the source; blue Miras predominantly show A, red OH/IR stars mainly type B spectra (Engels & Lewis 1996). The variability of the maser is reflected in the peak flux of the emission at fixed velocities. In our search for detections we were helped by these

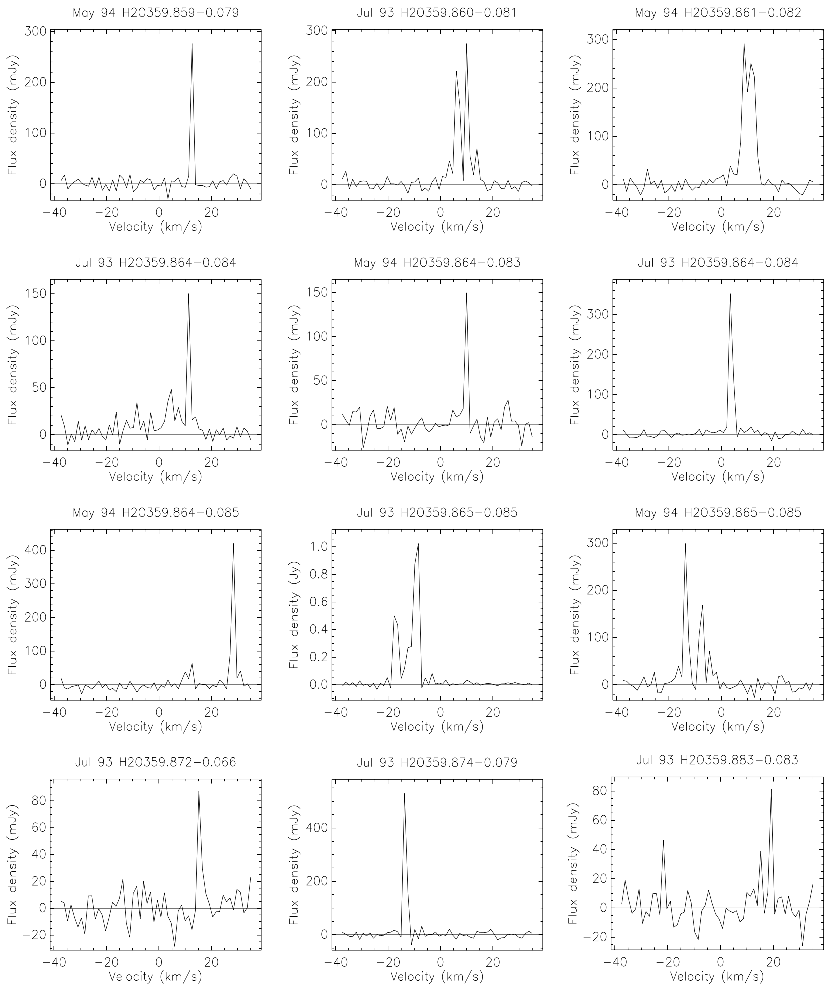

Figure 3.4 Serendipitous H_2O masers in G−0.13−0.08

characterisations and the knowledge of the 1612 MHz OH profiles. Most of our detections toward the 1612 MHz OH maser sources can be characterised as type A or type B H_2O masers. Because of sensitivity limits, at the GC we often find only one (the dominant) peak of the double peaked H_2O maser profile. Supergiants, OB star associations and star forming regions are known to have much more complex, and changing H_2O (and OH) maser spectral profiles (e.g. Engels et al. 1988; Genzel & Downes 1977, 1979; Reid et al. 1988; Engels

& Lewis 1996). For H_2O359.956−0.051 we find a B type H_2O maser, which is typical for an AGB star. We therefore argue again for the AGB nature of H_2O359.956−0.051 (Levine et al. 1995; Chapter 2; Blum et al. 1996).

3.5.3 H_2O masers in G−0.13−0.08

For one of our fields toward two OH/IR stars, we have good calibrated observations of both the Jul 93 and May 94 sessions. In July 1993 we detected one of the OH/IR stars (H_2O359.854−0.079) and, serendipitously, 5 additional H_2O maser sources. We found that we had been pointing at (one of) the compact continuum core(s) of the molecular cloud G−0.13−0.08, 5.3′ or ≈ 12 projected parsec from Sgr A* (source number 6 in Downes et al. 1979 and the most southern of the three 20 cm radio continuum sources south of Sgr A in Fig. 5b of Pedlar et al. 1989; see also e.g. Armstrong & Barrett 1985; Zylka et al. 1990, 1996). At least two of these masers had been found previously by Okumura et al. (1989) and in single beam observations by Güsten & Downes (1983) and Lindqvist et al. (1990; note the resemblance with the spectra of Güsten & Downes, 1983, and our weak source H_2O359.864−0.084 from Jul 93, *not* the strong source H_2O359.865−0.085).

Two among the 5 accidentally found H_2O maser sources in the May 94 data set were re-detections from our Jul 93 observations (filled triangles in Fig. 3.5). From this study, it brings the total amount of confirmed H_2O masers in this part of G−0.13−0.08 from 1 to at least 3 (and an additional 5 unconfirmed, excluding the OH/IR stars). We exclude the possibility of sidelobe detections (maybe except for H_2O359.864−0.083). Güsten & Downes (1983) did not detect our strongest source H_2O359.865−0.085, whereas we were unable to confirm the +35 km s^{-1} component found in Okumura et al. (1989) and Lindqvist et al. (1990) due to limited velocity coverage. One should be careful to associate H_2O masers to star formation regions solely based on the detection of H_2O maser emission (Chapter 2), but because OH maser emission does not show up in this region in our very sensitive 1612 MHz survey (Chapter 2) and because of e.g. the variation in the spectrum, we think here we have a clear case.

The velocity structure for 4 features at negative R.A. offsets in Fig. 3.5 is very narrow around 10 km s^{-1}. Close to the location of the ultra compact HII region (the pentagon in Fig. 3.5; Güsten & Downes 1983) the velocities of the masers seem to diverge. However, in 1612 MHz OH absorption maps we found deep absorption at 11 (and 14) km s^{-1} at this location (for a description see Chapter 5; see also the HNCO observations by Lindqvist et al. 1995), giving credit to the thought that all these features are physically associated. In this respect, the formation of stars close to the HII region may be more advanced

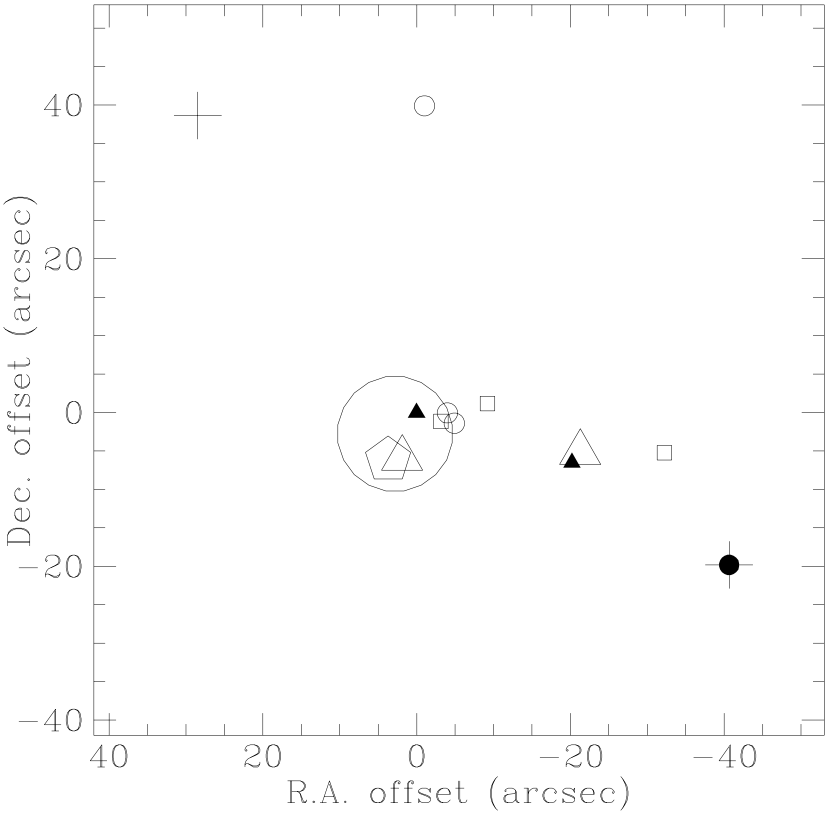

Figure 3.5 Serendipitous H_2O masers in G−0.13−0.08. The offsets are with respect to the position of H_2O359.885−0.085 (in J2000: R.A. $17^h45^m37.^s68$ DEC. $-29°05'43.''8$), the strongest maser we found in this region. Triangles depict confirmed H_2O masers, either in this work (filled, both detected in July 1993 and May 1994) or from the literature (open triangles, with typical errors from 1 to 15 arcseconds). The filled circle is one of the OH/IR stars (crosses) in the field, which was detected in July 1993. Open circles are the other masers from the Jul 93, and open squares from the May 94 observations. The pentagon identifies an ultra compact HII region and the large circle marks the extent of the 1612 MHz OH absorption

resulting in dynamical scattering of the objects. Furthermore, we are struck by the almost linear (and velocity) alignment of the masers. To determine whether this is due to a shock front that triggered the star formation, we are currently searching for shock excited 1720 MHz masers (Yusef-Zadeh et al. 1996; Sandqvist, pers. comm.). Clearly this is a very interesting region to study present day star formation very close to the GC.

It has been suggested that the GC region is devoid of H_2O masers, i.e. deficient of massive star formation ($\gtrsim 15$ $M_\odot$) in the inner 100 pc with respect to the amount of molecular gas present (Güsten & Downes 1983; Odenwald & Fazio 1984). However, with the (confirmed) detection of additional H_2O masers we have evidence for a number of massive OB stars currently being formed in G−0.13−0.08. We suggest that this region should be surveyed with a larger velocity coverage, also to confirm all 8 masers and the +35 km s^{-1} feature (Okumura et al. 1989; Lindqvist et al. 1990).

3.6 Conclusions

In two observing sessions we have detected 53 H_2O masers in the GC; 4 H_2O masers are detected in both sessions, 36 (and 1 re-detection) are associated with individual AGB stars (of which 18 tentative), probably 2 (of which one has been re-detected) with young stellar objects and the rest with SFR's. Serendipitously we have found 8 individual H_2O masers in the molecular cloud G−0.13−0.08 and confirm that the masers found previously by Güsten & Downes (1983) and Okumura et al. (1989) are different masers. Of the 7 previously reported H_2O masers in AGB stars, we observed 4 sources and confirmed 3.

Similarly we have detected 18 SiO masers in AGB stars. From the 17 previously detected SiO masers, we observed 5 masers and confirm all 5. For proper motion measurements, a catalogue of 46 (and 16 tentative) masers, either H_2O or SiO, in individual AGB stars is now available. Considering the variability of the sources, this number may be small for conclusive statistical analysis, but obtaining several proper motions might provide important information on the type of stellar orbits in the GC.

Acknowledgements. In this paper we used observations obtained with the Very Large Array (VLA) of the National Radio Astronomy Observatory (NRAO). NRAO is operated by Associated Universities Inc. under cooperative agreement with the National Science Foundation. For data reduction facilities, LOS acknowledges the hospitality of NRAO's Array Operations Center. HJvL acknowledges support for his research by the European Union under contract CHGECT920011.

References

Armstrong J.T., Barrett A.H. 1985, ApJS 57, 537
Blitz L., Binney J., Lo K.Y., Bally J., Ho P.T.P. 1993, Nat 361, 417
Blommaert J.A.D.L., van der Veen W.E.C.J., van Langevelde H.J., Habing H.J., Sjouwerman L.O. 1997, accepted for publication in *Astronomy & Astrophysics*
Blum R.D., Sellgren K., DePoy D.L. 1996, AJ 112, 1988
Brand J., et al. 1994, A&AS 103, 541
Caswell J.L., Haynes R.F. 1983, Aust. J. Phys. 36, 361
Caswell J.L., Batchelor R.A., Forster J.R., Wellington K.J. 1983, Aust. J. Phys. 36, 401
Comoretto G., et al. 1990, A&AS 84, 179
Downes D., Goss W.M., Schwarz U.J., Wouterloot J.G.A. 1979, A&AS 35, 1
Engels D., Lewis B.M. 1996, A&AS 116, 117
Engels D., Schmid-Burgk J., Walmsley C.M. 1986, A&A 167, 129
Engels D., Schmid-Burgk J., Walmsley C.M. 1988, A&A 191, 283
Felli M., Palagi F., Tofani G. 1992, A&A 255, 293
Frail D.A., Diamond P.J., Cordes J.M., van Langevelde H.J. 1994, ApJ 427, L43
Genzel R., Downes D. 1977, A&A 61, 117
Genzel R., Downes D. 1979, A&A 72, 234
Genzel R., Hollenbach D., Townes C.H. 1994, Rep. Prog. Phys. 57, 417
Güsten R., Downes D. 1983, A&A 117, 343
Habing H.J. 1996, A&AR 7, 97
Habing H.J., Olnon F.M., Winnberg A., Matthews H.E., Baud B. 1983, A&A 128, 230
Iben I. 1991, ApJS 76, 55
Jewell P.R., Snyder L.E., Walmsley C.M., Wilson T.L., Gensheimer P.D. 1991, A&A 242, 211
Jones T.J., McGregor P.J., Gehrz R.D., Lawrence G.F. 1994, AJ 107, 1111
Levine D.A., Figer D.F., Morris M., McLean I.S. 1995, ApJ 447, L101
Lewis, B.M. 1989, ApJ 338, 234
Lindqvist M., Ukita N., Winnberg A., Johansson L.E.B. 1991, A&A 250, 431
Lindqvist M., Winnberg A., Forster J.R. 1990, A&A 229, 165
Lindqvist M., Winnberg A., Habing H.J., Matthews H.E. 1992, A&AS 92, 43
Lindqvist M., Sandqvist Aa., Winnberg A., Johansson L.E.B., Nyman L.-Å 1995, A&AS 113, 257
Menten K.M., Reid, M.J., Eckart A., Genzel R. 1997, ApJ 475, L111
Mezger P.G., Duschl W.J., Zylka R. 1996, A&AR 7, 289
Morris M., Serabyn E. 1996, ARAA 34, 645
Nakada Y., Onaka T., Yamamura I., Deguchi S., Ukita N., Izimiura H. 1993, PASJ 45, 179
Nyman L.-Å, Johansson L.E.B., Booth R.S. 1986, A&A 160, 352
Nyman L.-Å, Hall P.J., Le Bertre T. 1993, A&A 280, 551
Odenwald S.F., Fazio G.G. 1984, ApJ 283, 601
Okumura S.K., Ishiguro M., Fomalont E.B., Chikada Y., Kasuga T., Morita K.,

Kawabe R., Kobayashi H., Kanzawa T., Iwashita H., Hasegawa T. 1989, ApJ 347, 240
Olnon F.M., Winnberg A., Matthews H.E., Schultz G.V. 1980, A&AS 42, 119
Pedlar A., Anantharamaiah K.R., Ekers R.D., Goss W.M., van Gorkom J.H., Schwarz U.J., Zhao J-H. 1989, ApJ 342, 769
Reid M.J. 1993, ARAA 31, 345
Reid, M.J., Schneps, M.H., Moran, J.M., Gwinn, C.R., Genzel, R., Downes, D., Rönnäng B. 1988, ApJ, 330, 809
Shiki S., Ohishi M., Deguchi S. 1997, ApJ 478, 206
van Langevelde H.J., Brown A.G.A., Lindqvist M., Habing H.J., de Zeeuw P.T. 1992a, A&A 261, L17
van Langevelde H.J., Frail D.A., Cordes J.M, Diamond P.J. 1992b, ApJ 396, 686
van Langevelde H.J., Janssens A.M., Goss W.M., Habing H.J., Winnberg A. 1993, A&AS 101, 109
van Paradijs J., Spruit H.C., van Langevelde H.J., Waters L.B.F.M. 1995, A&A 303, L25
Yusef-Zadeh F., Mehringer D.M. 1995, ApJ 452, L37
Yusef-Zadeh F., Roberts D.A., Goss W.M., Frail D.A., Green A.J. 1996, ApJ 466, L25
Zylka R. 1996, in "The Galactic Center", R. Gredel (ed.) ASP Conf. Ser. Vol. 102, p. 77
Zylka R., Mezger P.G., Wink J.E. 1990, A&A 234, 133

Chapter 4

Stellar positions from SiO masers in the Galactic center

Abstract.

We report on the possibility of determining milli-arcsecond accurate positions for 43 GHz SiO masers in OH/IR stars located at the Galactic center. The positions of the OH/IR stars, known to have SiO masers from a previous Very Large Array survey, are measured relative to Sgr A*. We used part of the Very Long Baseline Array and the phased Very Large Array in a special setup, necessary to accomplish a phase-referencing scheme with a cycle time of 40 seconds, and with the $\approx$ 2 Jy continuum source Sgr A* as phase-reference source. Because of the atmospheric phase instability at 43 GHz, the detection rate is low. However, we show that reliable positions can be obtained with calculable errors, which allows one to measure the proper motion of these stars accurate to $\approx$ 15 km s^{-1} in 5 years.

Co-authored by:
H.J. van Langevelde & P.J. Diamond

4.1 Introduction

In order to understand the nature of the central region of the Galaxy, it is crucial to have a good estimate of the mass distribution within the central parsecs of the dynamical center. The most outstanding issue is that of the existence of a central massive black hole, with Sgr A* as the most prospective candidate. On a larger scale, the evidence for a 'bar', or a tri-axial bulge in our Galaxy accumulates. In the past decade many studies to probe the inner Galactic gravitational potential have been performed, using line-of-sight velocities of gas and stars. However, because the exact type of orbits of the objects in study are unknown, the line-of-sight velocity information alone is of limited use. Therefore, the evidence for the existence of a massive black hole or a tri-axial bulge, then becomes a queer function of the assumptions made about the three-dimensional motions and the assumed potential. Genzel et al. (1994) and Mezger et al. (1996) have reviewed the possibility of a black hole in the Galactic center (GC). A review about the 'bar' is written by Blitz et al. (1993), and another one is included e.g. in Morris & Serabyn (1996).

From radial velocity measurements of late-type stars it is known that so-called high-velocity ($|v_{\rm LSR}| > 250$ km s^{-1}) stars exist (Baud et al. 1975; Rieke & Rieke 1988; Van Langevelde et al. 1992a; and more recently from Genzel et al. 1996; Eckart & Genzel 1996). These high-velocity stars are an important constituent of the stars seen in the Galactic nucleus, and hence in the modeling thereof. If the stellar orbits are isotropic, as suggested by Eckart & Genzel (1996) for the inner parsec (measured from Sgr A*, the alleged dynamical center of the Galaxy), the high-velocity stars outline the tail of the stellar velocity distribution and therefore are indicative of the central mass distribution. On the other hand, Lindqvist et al. (1992b; see also Sevenster et al. 1995) have shown that there is a considerable fraction of stars within $\approx$ 100 parsec of Sgr A* that clearly participate in Galactic rotation, which conflicts with isotropic orbits at this scale. Furthermore, if the high-velocity stars are merely bulge stars on highly elongated orbits penetrating the center (argued by Van Langevelde et al. 1992a; Blommaert et al. 1997), the derived line-of-sight velocity dispersions – the velocity profiles – give a distorted picture. Axi-symmetric models must then be replaced by tri-axial bulge models in order to study the dynamics of even the very center.

Transverse motions

High-velocity stars are present in the radial velocity domain. We expect high-velocity stars to be present in the transverse velocity domain as well. With current technology, it is possible to actually measure proper motions in the GC, and to deduce the type of stellar orbits within a few years of observing.

Recently, the former has nicely been demonstrated by Eckart & Genzel (1996) using near-infrared images of late-type stars in the central 0.4 parsec of the GC. However, with infrared cameras, the field of view is limited to less than one arcminute ($\lesssim$ 2.5 parsec).

At the distance of the GC (8 kpc, Reid 1993), a typical stellar velocity of 100 km s^{-1} corresponds to $\approx$ 2.5 milli-arcsecond (mas) per year. We initiated a project to measure transverse velocities of OH/IR stars with VLBI in the GC. The OH/IR stars form a slightly different sample of stars than the objects studied by Eckart & Genzel (1996), because they are located further out ($\lesssim 45'$, or $\lesssim$ 100 parsec) from Sgr A*. The sample of OH/IR stars trace and pinpoint the dynamical center on a larger scale, and provide a possibility to recover the complete velocity information for these individual stars. The sample of SiO masers used in this project is selected from SiO maser surveys in OH maser sources, and we will assume that the objects are oxygen rich AGB stars. For further reading about AGB stars and their circumstellar envelopes we refer to Iben & Renzini (1983) or Habing (1996).

One reason not to use the 1612 MHz OH masers in these OH/IR stars is the strong angular broadening due to interstellar scattering toward the GC (Van Langevelde et al. 1992b; Frail et al. 1994). As scattering scales as λ^2, higher frequency observations are more favorable. Furthermore, it is well known that the circumstellar 22 GHz H_2O and 43 GHz SiO masers are generated closer to the star than the OH masers, increasing the accuracy of the determination of stellar positions. Most notably, SiO masers originate from the parts of the circumstellar shell that are very close to the star (a few stellar radii, typical diameter $\approx$ 10 AU: Diamond et al. 1994; Miyoshi et al. 1995). Although the individual SiO maser spots are variable (but not as variable as H_2O masers) and are located around the star, the "average" position, integrated over the velocity width of the feature, represents the stellar position within 1 mas. Also, the expected spot size due to scattering is less than 1 mas, altogether allowing a proper motion measurement of the underlying star accurate to about 15 km s^{-1} within 5 years.

Outline of this paper

We report on the efforts of observing a first epoch milli-arcsecond accurate position for H_2O and SiO masers in OH/IR stars in the GC with the Very Long Baseline Array (VLBA). Because of the low elevation of the GC, the rapid phase fluctuations at 22 and 43 GHz and the low fluxes of the masers we used the special observing mode, with the phased Very Large Array (VLA) at 43 GHz as described in Sect. 2. The resulting milli-arcsecond positions and accuracies achieved for 2 masers are given in Sect. 3, which includes an estimate of the

Table 4.1 Observational summary

		VLBA UT	VLA UT
a	1995 May 8	05^h-14^h	- -
b	1995 Dec 23	14^h-22^h	18^h00^m-20^h30^m
c	1996 Jan 12	13^h-22^h	14^h45^m-21^h45^m
Rest frequency			42.820 GHz
			for May 1995 also 22.235 GHz
Total bandwidth			16 MHz
Baseband channels			2(a,c), 4(b)
Sampling rate			32 Msamp/sec
			with 2 bit samples
Aggregate bit rate			128(a,c), 256(b) Mbps
Spectral resolution			63(a), 125(b,c) kHz
Integration time			1 sec
Spectral weighting			uniform
Position Sgr A* (J2000):			$17^h45^m40\overset{s}{.}0500$ $-29°00'28\overset{''}{.}120$

coherence time, and position errors. In Sect. 4. we finish with our conclusions and recommendations for future measurements.

4.2 Observations

4.2.1 Setup

For target masers we selected the brightest detections of Chapter 3 and which are closest to Sgr A*. The first VLBA experiment was scheduled for May 8, 1995 (nighttime). We used the full VLBA and attempted to detect a few strong H_2O and SiO masers with cycle times which we varied between 30 and 240 seconds at both frequencies. The cycle time should be a trade-off between the atmospheric phase stability and signal to noise ratio on our extended phase-reference source Sgr A*. Unfortunately the weather in the south-west of the

Table 4.2 Array and station setup

Sub-array	Station names	Polarisation
VLBA	BR FD KP LA OV PT (+ HN MK NL SC in May 95)	Left & Right
VLA-Ref	N16 N8 E4 E12/2* W4/2*	Right
VLA-Mas	N20 N12 N4 E8 E16/6* W16/6* W12/8*	Left

*: Entries like 'E12/2' mean the telescope was shifted from location E12 to location E2 in between Dec 23 and Jan 12

USA was not optimal, and due to unknown reasons the data from the Pie Town (PT) antenna were lost. All of this resulted in low sensitivity observations or no data at all on the, for this project crucial, shortest baselines of the array. Because of considerable scattering at the GC, the longer baselines were of less use for the detection of the scatter broadened masers and Sgr A*. At both 22 and 43 GHz no masers were found except for VX Sgr, the source we used to check our setup at 43 GHz. However, for both 22 and 43 GHz we were able to detect our intended phase-reference source Sgr A* with sufficient signal to noise for fringe-fitting in 15 second scans on the shorter baselines. For longer cycle times ($\gtrsim$ 60 seconds) phase coherence was either lost, or phase referencing would leave phase ambiguities unresolved. Therefore, we concluded a cycle time of 40 seconds was optimal for future experiments. The SiO results looked most promising, although even at 43 GHz interstellar scattering severely affected all baselines other than from the inner 6 VLBA antennas. The SiO masers are also expected to be more persistent compared to the H_2O masers.

The second series of experiments took place in the local early mornings of December 23, 1995 and January 12, 1996 and included the phased VLA (in B-array and in transition from B- to CnB-array, respectively). The VLA proved to be crucial for this experiment for providing short baselines, sensitivity and a contemporary check on the flux of the maser targets. In addition we used a total bit rate of 256 Msamples/s for the second epoch, increasing the sensitivity by oversampling.

As the VLBA antennas are designed for fast source switching, the VLA is not. Actually, it is the VLA correlator software that requires 20 seconds in between

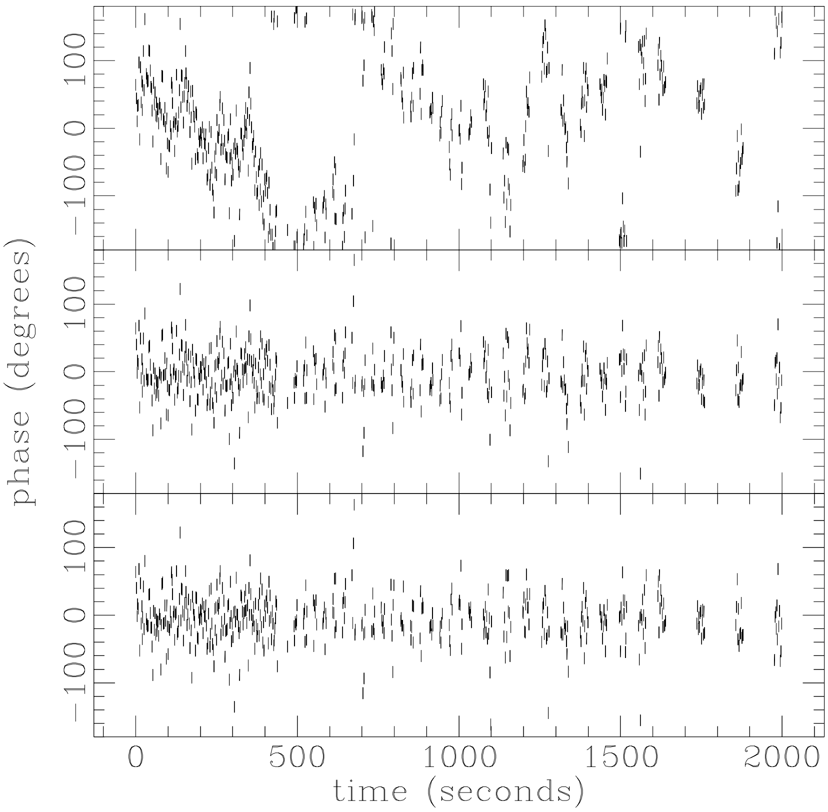

Figure 4.1 Phases on a short baseline (FD-KP) for Sgr A* during a part of the 43 GHz test (May 95). The different cycle times can be seen by the (maser) source gaps: continuously on Sgr A*, 15 seconds on – 15 seconds off Sgr A* and 30 seconds on – 90 seconds off Sgr A*, respectively. On top we display the phases after only a–priori calibration, i.e. corrected for amplitude and a constant delay. In addition to atmospheric effects a large scatter is also caused by the low signal-to-noise ratio on Sgr A*. The middle frame displays the phases for Sgr A*, after fringe-fitting and interpolation. With a third order polynomial fit to the phases (the bottom frame) we have taken out most of the residual phase slopes and ambiguities

source changes[1] and makes phase-referencing with a single VLA antenna, or with the complete VLA as one phased array for our project impossible. To circumvent this problem the VLA was divided up into two sub-arrays. One sub-array was used to observe the phase-reference source (Sgr A*), the other the maser target. The antennas were carefully divided in two interspersed sub-arrays, such that the atmospheric effects, and thus the calibration, would be comparable for each of the sub-arrays. For sensitivity reasons, we chose 5 antennas in the phase-reference array, and 8 in the maser/target one. This implies that only one of the left circular or right circular polarisations could be recorded for the phase-reference source, and the complementary polarisation for the masers. Other specific issues that had to be taken care of are pointing scans (roughly each hour) and phasing up the VLA sub-array (as often as possible), all in pace with the "normal" VLBA observations. A summary of the observations is given in Table 4.1; the array setup can be found in Table 4.2.

Every 70 minutes, all antennas were directed to J1733−130 for pointing scans and calibration. Thereafter, while the VLBA array was independently performing its phase-reference schedule with a (20 + 20) second cycle time, both VLA sub-arrays were observing in simultaneous blocks of 260 seconds: 60 seconds on Sgr A* to phase up the sub-array and 200 seconds *continuously* on either Sgr A* (sub-array VLA-Ref) or a selected maser source (sub-array VLA-Mas).

This complex schedule was implemented by creating a VLBA schedule for the spectral line experiment. The same schedule that controlled all VLBA telescopes was also used to drive the recorder at the VLA. This produced the necessary log file that instructs the VLBA correlator to process the VLA data. For the frequency and pointing setup of both VLA sub-arrays we created schedules by hand. These schedules also included phasing up and pointing scans, all carefully synchronised with the overall VLBA schedule. With one sub-array connected to one polarisation input on the recorder, one can expect the VLA tape to yield meaningful information at certain combinations of time and polarisation.

4.2.2 Data reduction

The VLBI calibration was performed in a standard way. After data editing, bandpass correction and calibration of antenna gains, a constant delay for the entire experiment based on fringe finder observations was taken out. The

[1] Since the fall of 1996, the VLA can be used in a "Fast-Switching" mode. If available at the time of our observations, it would have enabled us to use the "full VLA", i.e. all 13 of the 27 antennas with a 43 GHz receiver, in a phase-reference scheme with cycles of 40 seconds (VLA Scientific memo 169).

resulting phases, shown in the top frame of Fig. 4.1, contain effects of the atmosphere, source structure and possibly the effects of an improper correlator model, including positional errors for the sources and telescopes. However, we expect that the largest effect will be atmospheric, in particular tropospheric. At 43 GHz, the absolute flux calibration is determined with a relatively high uncertainty of about 30%. For calibration of the VLA gains, note that with a 40 second cycle time, it is essential to specifically ask for 5 to 10 second calibration entries in the log files of the VLA sub-arrays (in the "cal" files) as the default of 30 or 60 seconds is too large to calibrate the data. For the Jan 96 experiment we approximated the missing VLA sub-array system temperature by scaling Tant/Tsys with the single antenna value system temperature.

The implementation of phase-referencing with respect to Sgr A* is simply done by fringe-fitting on Sgr A*, and applying the solutions for phase, delay and rate to the maser data. In this way one can attempt to calibrate all aforementioned effects to the extent that they are identical in the direction of Sgr A* and the target. The proper fringe-fit solution interval is found by "trial and error". When applying the solutions to the maser data, a linear phase connection using rates did not remove all phase ambiguities. Therefore a third order polynomial fit to the phases was used. Figure 4.1 shows the slight improvement from the middle frame to the lower frame. We think this latter yields the best estimates for the maser source phases (relative to Sgr A*). Next we may attempt to detect the masers *without* further (self-)calibration.

4.3 Results

4.3.1 Optimal cycle time

To determine the optimal observing conditions we examined the May 95 observations by plotting the temporal phase structure functions. For a particular baseline and time interval τ, the phase difference $\phi(t+\tau)-\phi(t)$ of the visibility phases after antenna calibration (see top of Fig. 4.1) was measured. We estimate the coherence time as the largest time τ for which the average RMS phase error $\sigma(\tau)$ is less than 1 radian.

For calculating $\sigma(\tau)$ we used all short baselines with usable data on our calibrator source J1733-130; Sgr A* is too weak because of its scattered, and therfore extended appearance. We plotted the May 95 structure functions for baselines with antennas FD KP LA and OV in Fig. 4.2. We find a coherence time on the good baselines of approximately 20 seconds for 43 GHz in the May 95 observations. Because of the bad weather, the coherence time is only an indication for possible cycle times.

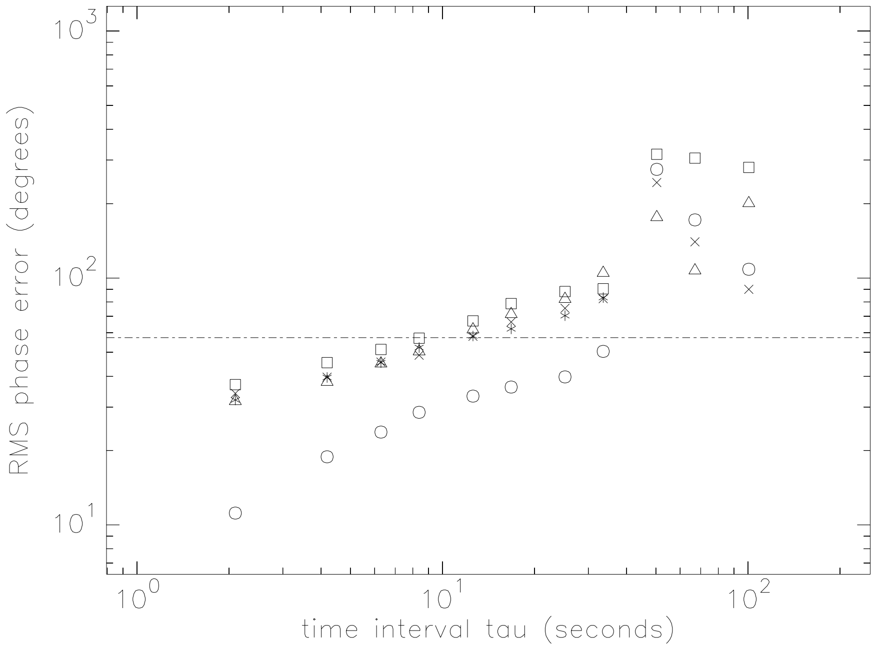

Figure 4.2 43 GHz RMS phase error $\sigma(\tau)$ in May 1995 for different time intervals τ. Different symbols represent different baselines. For $\tau \gtrsim 50$ seconds the proper number of cycles is more difficult to recover, resulting in an unreliable calculation of the structure function. From the plot we read a coherence time τ of about 20 seconds for the 'good' baselines on J1733−130

4.3.2 Detections

With total on-source integration times of 30 to 60 minutes, 2 sources were detected. Source OH359.971−0.119 was detected in the Dec 95 observations at a SNR of 6.5 and a velocity of -10.5 ± 0.9 km s^{-1}. An attempt to re-detect source OH359.971−0.119 in the Jan 96 observations was unsuccessful, although it was observed and detectable in the simultaneous VLA data. We are convinced the detection is real, as the maser can be seen consistently in two phase-referencing blocks that are more than two hours apart. In the Jan 96 experiment we detected source OH359.810−0.070 at a SNR of 7.6 and a velocity of -34.1 ± 0.9 km s^{-1}. We show the images, made from the visibility data on all baselines for the channel with the highest peak flux, in Fig. 4.3 and Fig. 4.4. Positions and velocities were measured from the image with the AIPS task IMFIT and are given in Table 4.3.

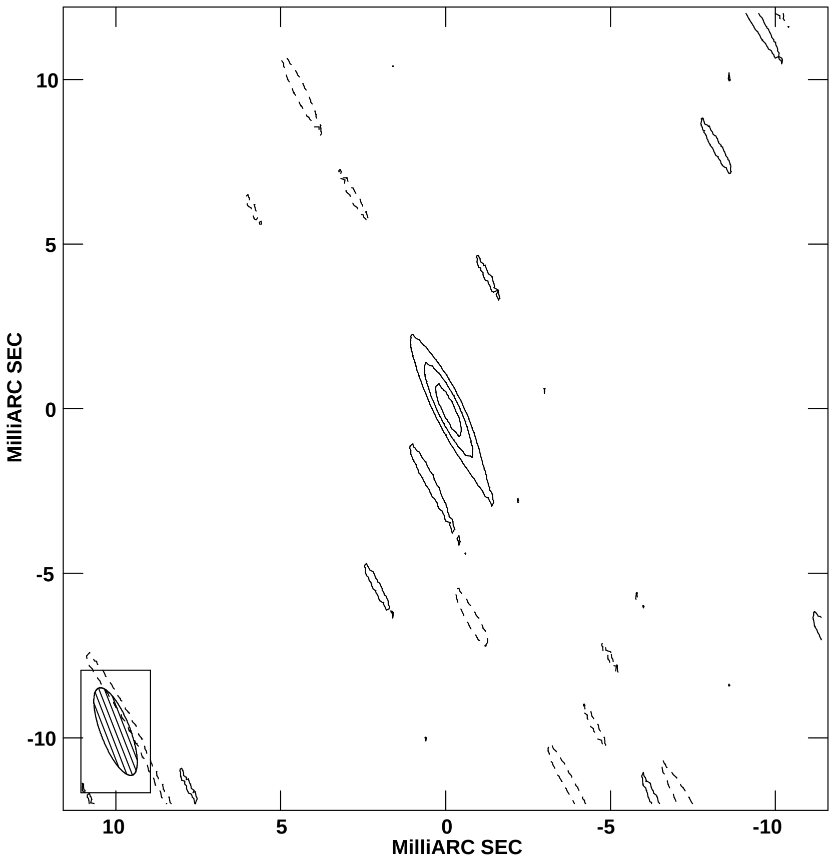

Figure 4.3 Detection of OH359.971−0.119 at −10.5 km s^{-1}. Contour levels are −2, 2, 4 and 6 times the RMS noise level of the map

The detection of OH359.971−0.119 in Fig. 4.3, was obtained with a phase connection to Sgr A* over 4$'\!.$6. For OH359.810−0.070, at a distance of 8$'\!.$2, a phase connection could also be made, but the quality of the resulting image is not as convincing as for OH359.971−0.119. Only from a detection in an adjacent channel we have a consistent position for the peak identified in Fig. 4.4 and quoted in Table 4.3. In May 95, the only maser source detected was the strong SiO maser in VX Sgr at a distance of about 8° from our phase-reference source. But clearly no phase connection could be made and we used self-calibration for VX Sgr. We do not think phase referencing over 8$'\!.$2 should be much more different than over 4$'\!.$6, but better understanding of this distance

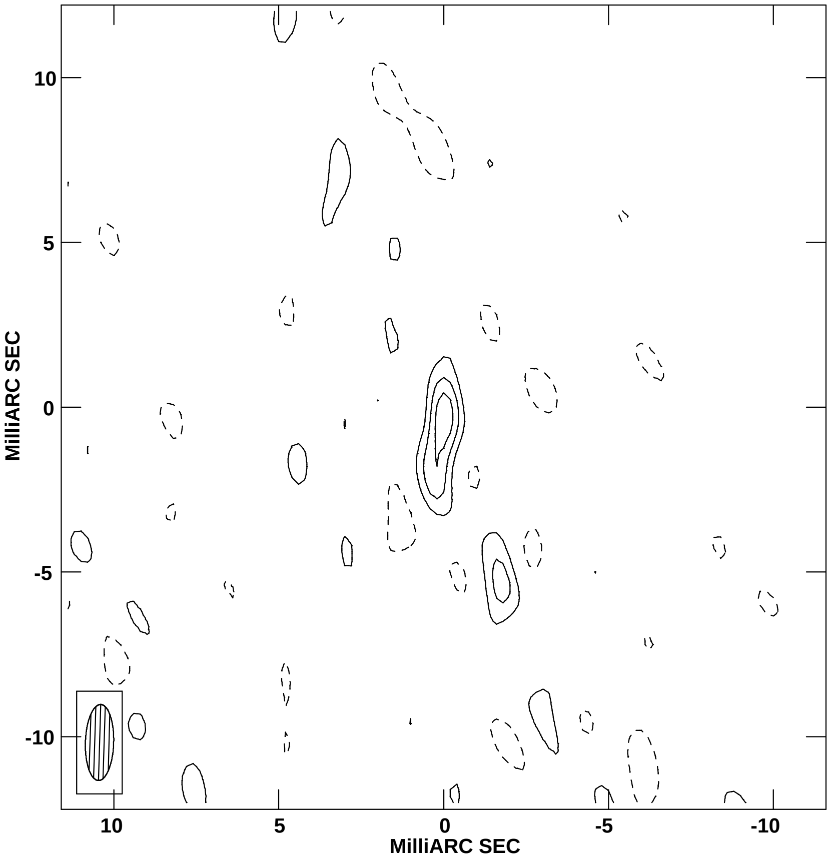

Figure 4.4 Detection of OH359.810−0.070 at −43.1 km s^{-1}. Contour levels are −2, 2, 4 and 6 times the RMS noise level of the map. Note that some of the flux is scattered into two more components The main component is also detected in an adjacent channel

dependence is needed.

4.3.3 Non–Detections

In the first experiment (May 95), without the VLA, no target maser sources were detected. In addition only 2 VLBA detections were obtained from 11 attempts, from which 7 have simultaneous VLA detections (of the remaining 4, 3 had no VLA time scheduled). A possible explanation for not detecting the masers, is that their variability played a role. In the second series of experiments, we were able to independently check the actual presence and approximate flux density of the masers in the VLA data. Importantly, this also provides a first guess where to look for the maser source in the VLBI data. The VLA detections (and VLA correlator setup) can be found in Table 4.4, where we assumed a rather low flux density of 6 Jy for J1733−130 to estimate a lower limit on the maser source flux densities. For the Dec 95 experiment, not all masers in the total VLBI schedule could be observed within the allocated VLA time. A large fraction of maser sources is present in the VLA data during the second series of experiments, with a sufficient flux density to detect them in the VLBI measurements as well. Therefore, we conclude that the variability of the SiO maser does not explain the low VLBI detection rate.

Another reason for not detecting a source is the uncertainty of the maser position. Together with uncertainties in the exact velocity channel and the optimal calibration procedure, a large effort is necessary to search for the maser spots in the phase reference data cubes. Positional errors from the OH maser surveys can be as large as one arcsecond. We mainly used OH maser positions from Lindqvist et al. (1992a) for our input source catalogue, which are consistent at the $1''$ level with our SiO maser positions (Chapter 3). However, Lindqvist et al. (1992a) do not give a position for Sgr A*, leaving the possibility that the positional error with respect to Sgr A* is larger than $2''$. The source would then be located outside the field of view.

However, we believe that the detection rate is mostly limited by difficulties to make a phase connection. This is partly due to atmospheric instabilities. In combination with low signal to noise on Sgr A*, it is likely that not all phase slopes have been removed in our 20 second fringe-fit interval. This partly reflects the fact that we are observing with cycle times that are not much shorter than the coherence time; shorter cycles are currently impossible because Sgr A* is difficult to detect already. We conclude that it is important to observe at the best available conditions, when the atmospheric water vapour contribution is low, and possibly with larger continuum bandwidth.

4.3.4 Positional accuracy

It is important to make estimates of the accuracy of the measured positions. The first component in the positional uncertainty is simply the noise in the observations of the target sources. Although this determination is also affected by residual effects in the phase connection, we simply take the formal error of the fit in the map for this. This will yield a conservative estimate.

The next thing we have to account for is the uncertainty in the phase-reference

Table 4.3 VLBA maser positions *referenced to Sgr A**

OH/IR star	Right Ascension (J2000)	Declination (J2000)
December 1995		
OH359.971−0.119	$17^{h}46^{m}00\overset{s}{.}95601$	$-29°01'23\overset{''}{.}5096$
formal fit error	$0\overset{s}{.}00002$	$0\overset{''}{.}0005$
reference phase ϵ	$0\overset{s}{.}00003$	$0\overset{''}{.}0004$
VLA phase cal. δ	$0\overset{s}{.}00004$	$0\overset{''}{.}0006$
correlator model	$0\overset{s}{.}00002$	$0\overset{''}{.}0003$
total error:	$0\overset{s}{.}00006$	$0\overset{''}{.}0009$
January 1996		
OH359.810−0.070	$17^{h}45^{m}26\overset{s}{.}35937$	$-29°08'04\overset{''}{.}1804$
formal fit error	$0\overset{s}{.}00001$	$0\overset{''}{.}0003$
reference phase ϵ	$0\overset{s}{.}00003$	$0\overset{''}{.}0004$
VLA phase cal. δ	$0\overset{s}{.}00004$	$0\overset{''}{.}0006$
correlator model	$0\overset{s}{.}00002$	$0\overset{''}{.}0003$
total error:	$0\overset{s}{.}00005$	$0\overset{''}{.}0008$

calibration scheme. Ideally the residual visibility phase ϕ of the calibrator source on all baselines should be zero and without any phase slopes. Phase deviation from zero will result in a distortion of the image of the target, possibly scattering the flux of the target over multiple images. However, Fig. 4.1 (bottom frame) shows that the average on Sgr A* is indeed zero, albeit with a large scatter. It suffices to estimate the RMS phase error ϵ, due to noise on the reference and estimate the uncertainty on the derived position. The estimates for these errors in position can be found in Table 4.3.

An additional problem can originate from the VLA data. The VLA may well be a dominant factor in our results, because of its sensitivity and the short baselines it provides. Therefore it is important to check our assumption that the atmosphere over the VLA sub-arrays is identical. The maximum magnitude of the phase error δ due to phase instabilities on a VLA baseline can be estimated from the VLA data.

At the start of the phased VLA observations, we observed J1733−130 for 8 minutes in "auto-phasing" mode and more than 5 minutes in "extended-phasing" mode (Fig. 4.5). In "auto-phasing" mode, the antenna phases are

Table 4.4 Phased VLA maser observations and detections

Rest frequency			42.820 GHz
Correlator mode			1D
Integration time			5 sec
IF Bandwidth			25 MHz
Number of channels			32
Spectral resolution			5.5 $\mathrm{km\,s^{-1}}$
OH/IR star	Peak flux Jy	SNR	Velocity $\mathrm{km\,s^{-1}}$
December 1995			
OH359.803−0.021	(not observed)		
OH359.855−0.078	not detected		
OH359.873−0.209	(not observed)		
OH359.946−0.047	(not observed)		
OH359.971−0.119	0.17	8.0	−11
OH359.974+0.162	0.19	6.2	−27
January 1996			
OH359.762+0.120	0.28	9.0	−6
OH359.778+0.010	0.36	24.6	−27
OH359.810−0.070	0.24	16.4	−33
OH359.971−0.119	0.26	17.0	−11
OH000.142+0.026	0.11	5.2	+27

continously monitored for deviations from the source model and the derived corrections are fed back into the system to form the optimal phased–array response. This method can only be applied if the source is strong and compact enough with a well determined position. For the maser sources we had to rely on extrapolating the corrections from a calibrator ("extended-phasing" mode). Figure 4.5 shows the phases are generally zero for the "auto-phasing" mode data on J1733−130. However, during the "extended-phasing" mode (after $t = 24$ minutes in Fig. 4.5), the phase starts to drift due to uncorrected changes in the atmosphere. Nevertheless, the deviations stay well within a range of 50 degrees, sufficient to coherently average the VLA antennas.

Figure 4.6 shows the determined $\delta(T)$ for the J1733−130 Dec 95 observations. The maximum length T before the effect will be calibrated was 200 seconds.

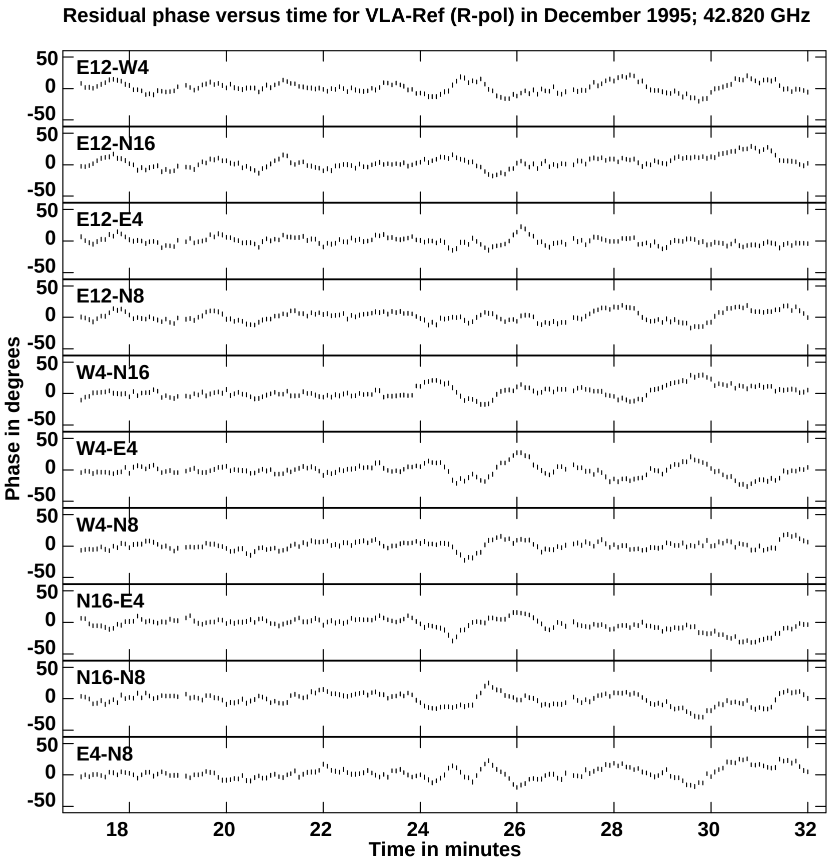

Figure 4.5 Residual 43 GHz phase for all baselines in VLA-Ref in December 1995: first the auto-phasing mode, then from $t = 24$ minutes the extended-phasing mode. Note that the offsets are not entirely random for short time intervals ($\sim$ 1 minute)

We see that the "auto-phasing" scans have a phase error of about 10°. Next, the average phase error in sub-array VLA-Mas is about 50% larger than for VLA-Ref in the "extended-phasing" mode. The larger extent of the VLA-Mas sub-array allows larger phase errors, because the phases and necessary corrections for the outer antennas change fastest. We take this RMS phase error as an estimate of the *maximal*, total VLA phase error and estimate the positional error for the case that the position would only be derived from VLA baselines in Table 4.3.

The positions given in Table 4.3 are positions of the source *relative* to the

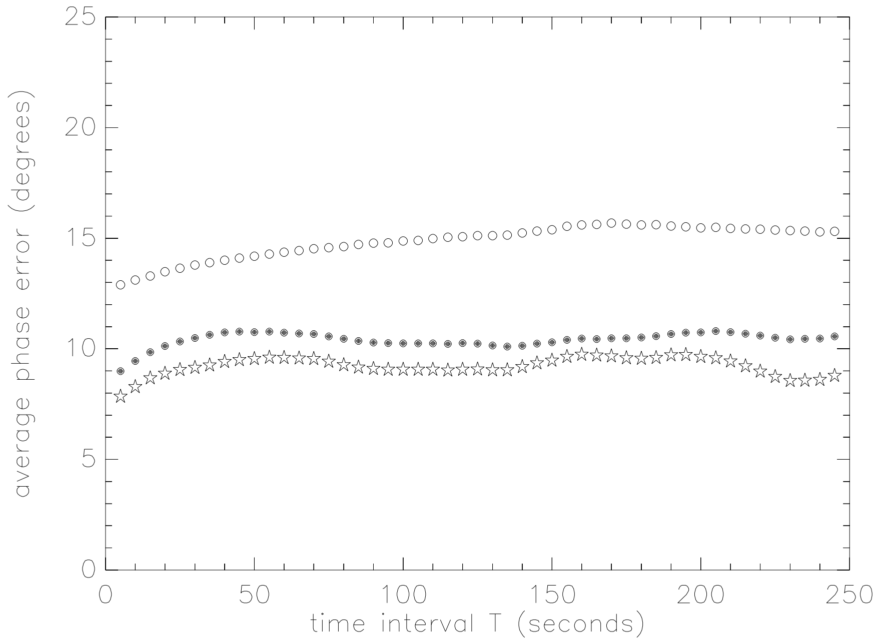

Figure 4.6 Average 43 GHz phase error $\delta(T)$ over the VLA baselines in December 1995 over different time intervals T on the calibrator source J1733−130. The star symbols (lower line) are averages over all the "auto-phasing" scans in VLA-Ref. The filled circles are determined from the "extended-phasing" scans for VLA-Ref; the open circles are determined from the 'extended-phasing' scans in the larger sub-array VLA-Mas. VLA-Mas, which contains the maser source observations, is the relevant sub-array. The averages for the 'auto-phasing' scans for VLA-Mas lie just below the 'extended-phasing' VLA-Ref scans (filled circles) and are therefore omitted for clarity

adopted position of Sgr A* (Table 4.1). Any error in the absolute position for Sgr A*, will affect the positions for the masers in Table 4.3. For example proper motion of Sgr A* has been inferred and is consistent with the motion of the Sun in the Galaxy (Backer & Sramek, 1982). However, for measuring proper motions with respect to Sgr A*, our primary goal, precise absolute positions are not important.

Another source of systematic errors can be the processing model. We have relied on the accuracy of the VLBA correlator model to register positional information. The experiment described here offers no independent means to check this, but Reid & Menten (pers. comm.) find in a similar project a systematic effect of 0.3 mas introduced by an improper troposphere model.

We have added this positional uncertainty to our list of errors.

Finally an intrinsic error in the *stellar position* remains because the SiO maser surrounds the stellar atmosphere. This effect can be estimated to be on the order of 1 mas or less for 43 GHz, still much larger than the errors calculated so far. This is the best accuracy nature permits.

4.4 Conclusions

We have successfully determined positions, relative to Sgr A*, for 2 SiO masers that are associated with AGB stars. The actual measurement is difficult because of the very rapid phase fluctuations at 43 GHz, and to a lesser extent to the variability and low quality a-priori positions of the masers. However, we have demonstrated that it is actually possible to obtain the positions, and thus proper motions, accurately with VLBI observations. The positional errors remain within the intrinsic positional uncertainty of the location of the SiO maser in the circumstellar shell: 1 mas.

For future measurements, the Fast-Switching VLA mode will improve the sensitivity as well as reducing the phase errors compared to our experiments. However, observations need to be done under very good conditions for observing at these high frequencies and the phased VLA is essential to obtain sufficient sensitivity and short interferometer spacings. It would be advantageous to use higher bandwidth recording in the future.

Acknowledgements. We thank Bob Treuhaft and Rene Vermeulen for discussing proper cycle times. In this paper we used observations obtained with the Very Large Baseline Array (VLBA) and the Very Large Array (VLA) of the National Radio Astronomy Observatory (NRAO). NRAO is operated by Associated Universities Inc. under cooperative agreement with the National Science Foundation. For data reduction facilities LOS acknowledges the hospitality of NRAO's Array Operations Center. HJvL acknowledges support for his research by the European Union under contract CHGECT920011.

References

Backer D.C., Sramek R.A. 1982, ApJ 260, 512

Baud B., Habing H.J., Matthews H.E., O'Sullivan J.D., Winnberg A. 1975, Nat 258, 406

Blitz L., Binney J., Lo K.Y., Bally J., Ho P.T.P. 1993, Nat 361, 417

Blommaert J.A.D.L., van der Veen W.E.C.J., van Langevelde H.J., Habing H.J., Sjouwerman L.O. 1997, accepted for publication in *Astronomy & Astrophysics*

Diamond P.J., Kemball A.J., Junor W., Zensus A., Benson J., Dhawan V. 1994, ApJ 430, L61

Eckart A., Genzel R. 1996, Nat 383, 415

Frail D.A., Diamond P.J., Cordes J.M., van Langevelde H.J. 1994, ApJ 427, L43

Genzel R., Hollenbach D., Townes C.H. 1994, Rep. Prog. Phys. 57, 417

Genzel R., Thatte N., Krabbe A., Tacconi-Garman L.E. 1996, ApJ 472, 153

Habing H.J. 1996, A&AR 7, 97

Iben I., Renzini A. 1983, ARA&A 21, 271

Lindqvist M., Winnberg A., Habing H.J., Matthews H.E. 1992a, A&AS 92, 43

Lindqvist M., Habing H.J., Winnberg A. 1992b, A&A 259, 118

Mezger P.G., Duschl W.J., Zylka R. 1996, A&AR 7, 289

Miyoshi M., Matsumoto K., Kameno S., Takaba T., Iwata T. 1995, Nat 371, 395

Morris M., Serabyn E. 1996, ARAA 34, 645

Reid M.J. 1993, ARAA 31, 345

Rieke G.H., Rieke M.J. 1988, ApJ 330, L33

Sevenster M.N., Dejonghe H., Habing H.J. 1995, A&A 299, 689

van Langevelde H.J., Brown A.G.A., Lindqvist M., Habing H.J., de Zeeuw P.T. 1992a, A&A 261, L17

van Langevelde H.J., Frail D.A., Cordes J.M, Diamond P.J. 1992b, ApJ 396, 686

Chapter 5

A new sample of OH/IR stars in the Galactic center

Abstract.

Two independent, largely overlapping 1612 MHz data sets were searched for OH/IR stars in the Galactic center. One set, taken with the Very Large Array in the period 1988 to 1991, consists of 17 epochs monitoring data of Van Langevelde et al. (1993). The other set was observed in 1994, using the Australia Telescope Compact Array. This article describes the data reduction procedures as well as a different way of searching image cubes for narrow line sources, and lists a total of 155 double peak OH maser detections within 18′ or 40 projected parsecs of Sagittarius A*, the compact radio continuum source in the Galactic nucleus. Presented are 65 formerly unseen double peaked 1612 MHz emitters, of which 52 are OH/IR stars. Also given are 3 single peak sources, which we believe to be masers of OH/IR stars. Apart from being less bright in their 1612 MHz OH maser line, the previously unknown OH/IR stars do not seem to be different from the previously known population of OH/IR stars in the Galactic center. We find that the OH/IR star OH maser luminosity distribution peaks at $L_{\rm OH} \approx 10^{43.4}$ photons per second. Further physical and kinematical analysis of the new sample will be presented in additional papers.

Co-authored by:
H.J. van Langevelde, A. Winnberg & H.J. Habing

5.1 Introduction

When a star of low to intermediate main sequence mass (1-7 $M_{\odot}$) has reached the stage where its central part is built up of a degenerate nucleus of carbon and oxygen, it starts ascending the asymptotic giant branch (AGB) of the Hertzsprung-Russell diagram. While burning hydrogen and helium in a shell around the nucleus it will expand its envelope. The star pulsates and starts losing mass at a high rate (10^{-7} to 10^{-4} $M_{\odot}$ yr^{-1}). The star will be obscured in the visible wavelengths by its dense shell of circumstellar matter. In this slowly expanding and cooling shell molecules form and with regularity conditions are met, such that the molecules in the circumstellar shell support a maser.

Since the discovery of the double peaked profile of the hydroxyl maser satellite line at 1612 MHz in late-type infrared stars, the so-called OH/IR stars have been studied to investigate stellar evolution and Galactic dynamics. The characteristic double spectral feature originates from hydroxyl (OH) masers in the expanding circumstellar shells of oxygen rich AGB stars. It is easy to recognise the object as an OH/IR star; one obtains the position and line-of-sight velocity of the star as well as the shell expansion velocity directly from the double peaked spectrum.

As the variable stellar radiation at visible and near-infrared wavelengths is absorbed, the only means of investigating the properties of the underlying star is by observing radiation that is re-emitted by the shell: infrared and sub-mm emission of the dust and gas, in which the molecules can show maser emission (OH, H_2O and SiO). Reviews on the star and its envelope can be found in Iben & Renzini (1983) and in Habing (1996).

Apart from studying the underlying star, one can also make use of OH/IR stars to probe the Galaxy for its structure, evolution and dynamics. For example, Whitelock et al. (1991) derived a period-luminosity relationship similar to the Mira variables and Blommaert et al. (1994) compared the OH/IR stars in the center, bulge and outer part of our Galaxy. Good reviews about using OH/IR stars as tools, are from Habing (1993) and Dejonghe (1993).

The Galactic center

Lindqvist et al. (1992a; hereafter LWHM) surveyed the Galactic Center (GC) region for OH/IR stars with the Very Large Array (VLA) in 1984 and 1985. The OH/IR stars in the GC are one of the few stellar samples in the GC that can be directly observed despite the enormous visual extinction ($A_V > 25$ mag) in front of the GC. The total of 150 OH/IR stars found (see appendix) are all at about the same distance and thus can be studied as a sample without assumptions on their individual distances (e.g. Baud et al. 1981; Jones et al.

1994; Blum et al. 1996). In Lindqvist et al. (1992b) the stars are investigated for their spatial and kinematic properties and used as tracers of the central potential and mass distribution. It is shown that the distribution of the GC sample generally depends on the shell expansion velocity at 1612 MHz and that the surface density increases strongly towards Sagittarius A* (Sgr A*). Sevenster et al. (1995) have shown that the OH/IR stars in the GC consist of a global Galactic component and a separate, strongly rotating disk of 'younger' OH/IR stars, possibly formed at a distinct event. Unfortunately the number of OH/IR stars known is too low to do a conclusive dynamical study, especially within about 10-20 pc of Sgr A*. Lindqvist et al. (1997) show that there should be many more OH/IR stars in the GC with apparent weak OH masers. The reason why they have not been found in the LWHM survey is mainly a matter of sensitivity. Also the OH masers vary in luminosity, as they are indirectly pumped by the variable stellar radiation. To find all stars one should preferably observe and search the same region for more than one epoch.

By monitoring the variability of some of the LWHM OH sources with the VLA, Van Langevelde et al. (1993; hereafter vLJGHW, or the 'monitor') have tried to measure phase-lag distances to these OH/IR stars in order to get a direct estimate of the distance to the GC. However, a highly scattering interstellar medium was discovered in the direction of the GC, making it impossible to achieve their primary goal (Van Langevelde & Diamond 1991). Nevertheless, 20 observations of the GC region had been done, each in sensitivity comparable to the original LWHM survey observations. A 'cheap' way of finding faint OH/IR stars is by analysing the concatenated data set. In that way the search can be done in a high-sensitivity data cube, and one is able to detect OH/IR stars which were in a minimum of their OH maser luminosity at the time of the LWHM survey. By averaging many different epochs taken over a time longer than the typical periods of the stars, the detection becomes effectively a function of the time averaged flux density in the spectral peaks. With 20 epochs, the most sensitive way to find stars is by using the concatenated data rather than to search all epochs separately (under the assumption that the OH/IR stars vary typically a factor of two during the monitor).

We intend to use the new, extended sample of OH/IR stars for testing the location of, and probing the potential in the very center of our Galaxy, and, secondly, to study the sample of OH/IR stars in the GC compared to all other known samples of OH/IR stars. To overcome asymmetry problems, introduced by the particular pointing of the VLA data (optimised for the monitoring program; see below), we used the Australia Telescope Compact Array (ATCA). The bandwidth for the ATCA observations has been chosen to include an equal

Table 5.1 1612 MHz Survey image cubes

Survey		Image cube center	(epoch)	Size	Resolution	Channel width		RMS	Velocity range
				$'$	$''$	$\mathrm{km\,s^{-1}}$	kHz	mJy	$\mathrm{km\,s^{-1}}$
a	VLA	$17^{h}42^{m}12\overset{s}{.}6$ $-28°56'18\overset{''}{.}0$	(B1950)	37	2.2	1.14	6.1	7.2	$-93 \rightarrow +176$
b	VLA	$17^{h}42^{m}29\overset{s}{.}3$ $-28°59'18\overset{''}{.}0$	(B1950)	17	0.5	2.27	12.2	3.7	$-92 \rightarrow +176$
c	ATCA	$17^{h}45^{m}40\overset{s}{.}0$ $-29°00'28\overset{''}{.}0$	(J2000)	37	2.2	1.45	7.8	4.5	$-600 \rightarrow +700$

sensitive search for high-velocity[1] OH/IR stars (velocity up to 600 $\mathrm{km\,s^{-1}}$), which might add important clues for future dynamical modelling.

Outline of this paper
In this paper we describe the data reduction procedure of the VLA monitor data set and of the ATCA observations in Sect. 2. Section 3 presents a list of both known and suspected OH/IR stars in the GC. Here, when we refer to an OH/IR star, we actually refer to *circumstellar OH maser emission*. The large interstellar visual extinction prevents us to make a clear distinction between optically thick circumstellar shells, as for genuine OH/IR stars, and optically thin circumstellar shells as for the evolutionary closely related Mira variables. We may even have picked up an individual supergiant; however, see Blum et al. (1996) for recent evidence that the number of supergiants in the GC is low. Section 3 also includes an error budget for our measurements. In Sect. 4, we comment on some of the detections. We discuss the survey sensitivity and anomalous features in some OH/IR star spectra. Briefly, we compare the previously unknown OH/IR stars with the known OH/IR stars and derive the OH luminosity distribution. From this we conclude in Sect. 5, that the central stars of the new detections are not different from the AGB stars that constitute the known population in the GC.

We do not attempt to measure the periods of the individual detections as the objects are too faint to be detected in each epoch separately. Also, detailed discussion of the spatial, kinematic and physical properties of the new, extended sample of OH/IR stars in the GC, as well as the issue whether Sgr A* is the dynamical center of the OH/IR star sample, is deferred to additional papers. A preliminary result on the survey can be found in Chapter 2.

5.2 Data handling and image analysis

Table 5.1 summarises the characteristics of the three different image cubes made; Figure 5.1 depicts an overview of the sky area surveyed, together with the sensitivity contours thereof.

5.2.1 The VLA data catena

The monitor data was in 1992 the most extended, uniform 1612 MHz spectral line data set of the GC known by the authors. We did not consider extending

[1] Stellar velocities in this paper refer to line-of-sight velocities as measured with respect to the local standard of rest reference frame (LSR).

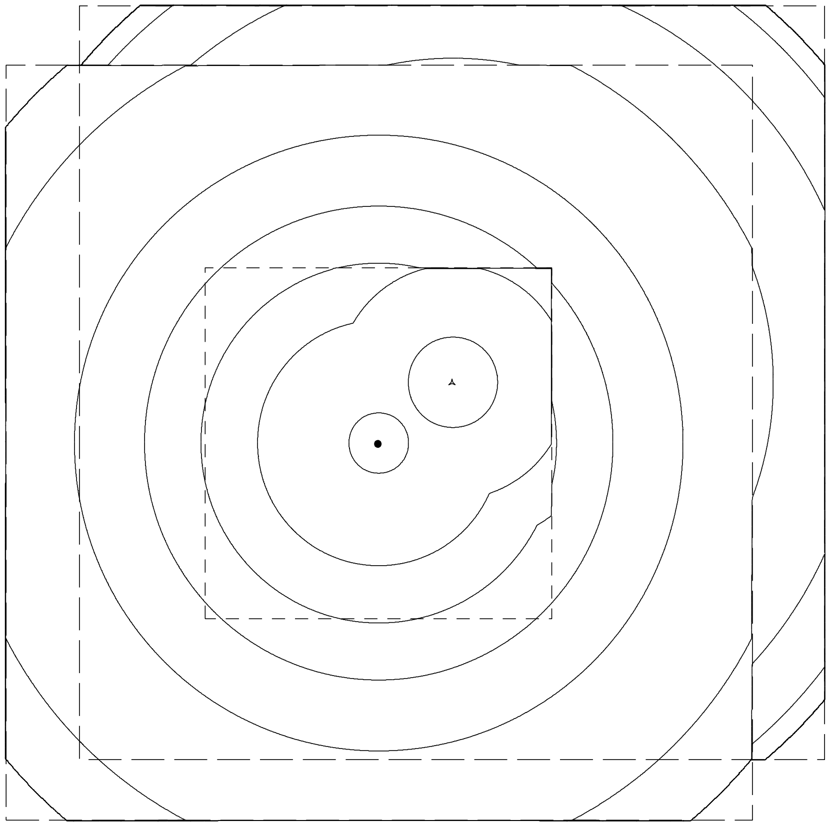

Figure 5.1 Composite survey area. The filled circle represents the position of Sgr A*, as well as the center for both the high resolution VLA and the ATCA image cubes. The triangle represents the image cube center for the concatenated VLA monitor data. Long-dashed squares are the 37′ VLA and ATCA surveys; we filtered out the corners for which the distance to the field (pointing) center was larger than 24′. The short-dashed square encloses the high resolution, 17′ VLA image. Drawn in solid lines are contours of equal detection probability; lines connecting points with equal sensitivity, according to the most sensitive image cube, after correcting for the primary beam attenuation (thus acting as a 'primary beam response' for this combined survey). Contours drawn are, from inside out, 1.005, 1.1, 1.25, 1.5, 2, 4, 8 and 16 times 25 mJy. Note that the VLA beam degrades faster because of a larger dish size; the VLA has 25 meter, the ATCA has 22 meter dishes. Approximate J2000 corner coordinates are: upper right $17^h44^m05^s$ $-28°40'31''$ to lower left $17^h47^m06^s$ $-29°19'02''$

the concatenation with observations by others (Habing et al. 1983; LWHM), because those observations were taken in a period when the VLA was limited in its spectral line capabilities. The observations and data reduction of the monitor data used are described in detail in vLJGHW. We chose to start from their calibrated data sets, mainly because bad visibilities and interference from the Russian GLONASS satellite positioning system had already been removed.

In summary, the $\approx$ 4 GByte of calibrated visibility data sets consist of 20 epochs of two-hour VLA observations, taken in different array configurations in the period from January 1988 to January 1991. Unfortunately for the current project, the sky position is not exactly centered on Sgr A*, and the velocity coverage is limited to only -110 to $+190$ km s^{-1}. The data have been reduced, calibrated and analysed using the NRAO AIPS reduction package (versions from 15JAN88, up to 15JUL94), which we continued to use on the concatenated data set. Being forced to use different AIPS versions over the years introduced some problems with the data tables during the concatenation process. We will comment on that below. We are confident that the final results are not different from what could have been obtained if we had started with the raw visibility data and performed the concatenation in one AIPS version only.

5.2.1.a Initial VLA data set selection

The following steps were taken for each individual data set to ensure the homogeneity of the sets, before concatenating them to one visibility file for final processing.

Each of the calibrated monitor data sets was checked for consistency by fully imaging a couple of known strong OH sources. Because of different problems, three epochs had to be regarded lost for our project. We did not process the raw data, as a few missing epochs would not make a significant difference in the noise statistics or detection probabilities. Also, due to inconsistent removal of interference in several epochs, we did not use any of the visibility data which could have been affected. Therefore, all data for which the baselines were shorter than 3 kλ was disregarded. If necessary, the u,v,w vectors were recalculated to have the coordinates (B1950) RA $17^{\mathrm{h}}42^{\mathrm{m}}12\overset{\mathrm{s}}{.}600$ and DEC $-28°58'18\overset{''}{.}00$ as phase center.

The largest effect of using different AIPS versions could be seen in some tables containing additional information to the data. We mainly had to deal with the flagging tables as the table format had changed. It was impossible to restore the original flagging, so for each combination of baseline and time in a flagging table, all visibility information was marked as bad data. Whenever applying the task SPLIT, the sky frequency (different for each epoch) and velocity information in each header and antenna file got reset and had to be repaired by hand. As we will not use frequencies (but velocities instead) and the velocity consistency had already been checked with spectra and maps, we took an arbitrary file header and used it to set all the relevant values to match. The same was done for the frequency information in the antenna file. By doing this, one introduces an error less than 0.05%, in appearance comparable to radial bandwidth smearing, but in net effect negligible. At this time the data sets were also converted from circular polarisations to Stokes 'I' to reduce the file sizes with a factor of two immediately.

As the absolute flux calibration of each data set had been done carefully by vLJGHW for the flux monitoring program, we have not performed any further bandpass or amplitude correction, visibility phase recalculation or flagging operation on the individual monitor data sets.

5.2.1.b Concatenated VLA data set processing

All data sets were added in a similar manner to create one concatenated visibility data set of about 35 observing hours. Each epoch was put in a different sub-array without rescaling the visibility weights. Due to different calibration paths, the individual weights of the visibility points differed per monitor data set. To get each epoch contribute equally, we treated all visibility weights to be unity. Although formally one has to account for the epochs that are taken in one polarisation only (two data sets before August 1988), we have not looked into this matter after converting each data set to Stokes 'I'.

To subtract confusing continuum emission, a baseline was fitted to each visibility spectrum, using three regions in the total spectral band which seemed to be void of line sources (Van Langevelde & Cotton 1990; Cornwell et al. 1992). Several channels of each region were averaged, and interpolated to represent the continuum emission. This visibility model for the continuum emission was subtracted from all channels of the concatenated VLA data set. On the fly, all visibility points exceeding twice the expected flux in the channel with the strongest source, were clipped. For epoch alignment we used a single self-cal iteration on the visibility phases. It corrects for *relative* systematic (atmospheric) effects in the different monitor data sets. We selected the red shifted peak of OH359.938−0.077; a single channel with only one strong, 6 Jy peak, and close to the field center.

From this calibrated visibility data set we made two naturally weighted image cubes and a number of 'clean boxes'; strong sources outside the main image cube were mapped in small fields to limit their side-lobe interference. The first image cube is a full primary beam, low spatial, but full frequency resolution image cube (survey 'a' in Table 5.1). The next is a small field, high spatial resolution image cube ('b') of the same VLA data set, for which we averaged two channels. The latter was centered on Sgr A* and the – not fully removed – extended continuum emission of the Sgr A complex. The low resolution image was chosen to match the spatial resolution of the ATCA. The large pixel size resulted in having only the shorter baselines (about one half of the 550,000 visibilities) contribute to the image, whereas for the high resolution image cube, about 90% of the visibilities could be used. Using an even higher resolution, to allow all visibilities to be used, would result in huge maps or alternatively too many 'clean boxes' (more than 15). It would thus require an extra pass of subtraction of sources, without a substantial decrease in noise level. The numbers used were a trade-off between resolution, noise level, sky coverage, execution time and disk usage. For reference, to map the entire region at full spatial and spectral resolution would require at least 34 Gb of disk space (with our choices less than 4), and because the execution time is strongly dependent on the disk I/O speed, even with modern workstations it would take months to execute (compared to a handful of days). Effectively, only the baselines between 4 and 32.2 kλ and 4 and 143.8 kλ were used for the low and high spatial resolution images, respectively. Fitted RMS noise levels per channel were measured to be 7.2 and 3.7 mJy on average, respectively.

5.2.2 ATCA observations and data reduction

The ATCA was used on 8, 10, 11 and 13 July 1994. To reduce broadband interference by GLONASS and to filter out as much as possible of the extended continuum emission in the GC region, the longest baseline configuration was selected for all the observations. The GC was observed at a central frequency of 1612.0 MHz, covering 8 MHz bandwidth over 1024 frequency channels. The integration time was about 12 hours for each of the observing days. To circumvent GLONASS interference in the bandpass calibration, the primary flux calibrator B1934−638 was observed three times per observing run; typically every 6 hours. The phase calibrator B1748−253 was observed roughly every 40 minutes. Once per observing run we also observed the VLA primary flux calibrator B1328+307 to check the consistency of the flux density measurements between the ATCA and VLA. Actually, for July 10th, we used B1328+307 for bandpass calibration, because interference affected all B1934−638 observations of that day.

After removing bad visibility data points and applying the bandpass calibration, the sky-frequencies were converted to LSR velocities. Following the standard phase calibration, the extended continuum emission from compact HII regions and the Sgr A complex was subtracted with a simple two region baseline interpolation in the visibility domain. Excessive amplitude visibilities were clipped before applying one self-calibration iteration solution of the visibility phases, on the same peak and in a similar manner as to the concatenated VLA data set. Again we used 'clean boxes' for removing side-lobes of strong sources outside the main image cube. To avoid remaining effects of interference by GLONASS and the subtracted continuum emission of the Sgr A complex in the image cube, we only used baselines exceeding 4 kλ. Because of the large amount of disk space required (5 MB per channel), full resolution images were made by the hundred for channels 69 to 964 (−600 to 700 km s^{-1}). The RMS noise level is about 4.5 mJy on average.

Because we used self-cal to align different observing days after we had removed all continuum emission from the data, all positions of the OH/IR stars changed with respect to Sgr A*. Therefore, the channel with the maser line we used for self-cal, was mapped from the unsubtracted calibrated ATCA data set. In this map, the positions of Sgr A* and the line were measured, after which the maser positions with respect to Sgr A* could be determined. The same was done for one of the A-array VLA monitor data sets. The positional offsets with respect to Sgr A* in Table 5.2 link both VLA and ATCA observations together.

5.2.3 Image cube analysis

In order to search for discrete line sources, each of the three dimensional image cubes was projected into one two dimensional image in the following way: for each pixel in the sky plane, the maximum intensity over the whole frequency/velocity axis was stored in a new, two dimensional sky image. We shall refer to this image as the "maxmap". In that way one gets an overall view of the sky location of intensity maxima, although without directly knowing the velocity corresponding to the peaks. The "maxmap" resembles a continuum image (but recall that we already have filtered out the continuum emission), but with a much higher signal to noise ratio than if we would have averaged the pixel intensities over all channels. Alternatively, one can make a total intensity map (or "zeroth order map"); an image for which the flux densities that are higher than the threshold are integrated over the feature. However, as the total intensity map takes into account every pixel above a certain threshold – and thus indeed would be very useful when looking for double peaked features – it is also very sensitive to broad line sources anywhere in the spectrum. Because we have to deal with the remains of the extended continuum emission of the Sgr A complex, we observe a vast amount of broad line sources (see also Fig. 5.8). These sources cause severe problems in searching the GC area; from non-linear spectral slopes to different noise and detection statistics. With this in mind, we prefer to use the "maxmap" instead of the total intensity map concept. The final results in both methods do not differ much, but the search is much more straightforward in the "maxmap".

Resulting were three "maxmaps" that all have the same noise level for the detection of sources as the original image cubes, but now consisting of pixels containing sources and the high-end part of the noise distribution of the original map (i.e. only positive values around and above the RMS noise level; comparable to a Rayleigh noise distribution with a constant offset). Now, instead of searching the original image cubes in each channel separately, and finding each source in several channels, one obtains the same detections by searching the (one channel) "maxmap" only. The "maxmaps" were searched for pixels with intensities over 40 mJy (5.5σ), 25 mJy (6.7σ) and 25 mJy (5.5σ) for the VLA $37'$, VLA $17'$ and the ATCA $37'$ image cubes, respectively. Pixels were then grouped in "islands" and for each "island", the spectrum in the original image cube was taken at the position with the highest pixel value.

The major advantage is that one would only get one spectrum for each "island" (e.g. 7,000 pixels make 200 islands, thus only 200 spectra), risking that one could miss a second object that is spatially adjacent to the object whose spectrum is drawn. Chances of missing a star are higher close to stronger sources (having larger "islands", beam area) and close to the remnants of improperly removed continuum features of the Sgr A complex (non-linear spectral slopes). Therefore we checked individual pixels of the local maxima in the confused area of the central $5'$ by hand. We think we might have missed only a couple of objects in our total analysis. The expectation value for two sources to be positionally coincident is less than 1% over the data set, but on the other hand we cannot correct for sources submerged in areas of absorption, or the bowl of negative emission caused by the extended background. The spectra were inspected for a second peak, which we required to be at least 4.5σ (respectively 32.4, 16.6 and 20.2 mJy observed flux density) and within the interval of 5-80 $\mathrm{km\,s^{-1}}$ of the first peak.

5.3 Results

Figures 5.2 and 5.3 summarise our results, where it should be noted that the stronger (previously known) sources can be detected further out from the pointing center because of the drop in sensitivity. Tables 5.2 and 5,3 (also available electronically through CDS) list all detections within the surveyed area, also when it concerns a previously known source. Figures 5.4 and 5.5 (*only* available electronically through CDS) display the 1612 MHz OH maser spectra of all sources. Single peak or suspected double peak detections with a peak flux exceeding 8σ (36 mJy before correction in the ATCA data), are also listed.

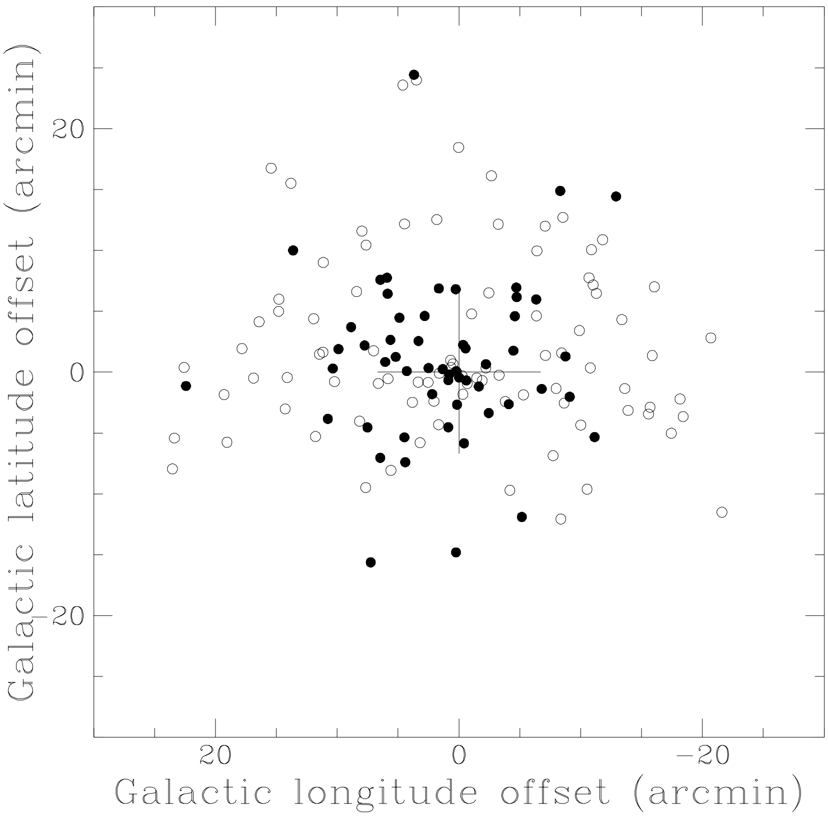

Figure 5.2 Sky distribution. Closed symbols are new detections, open symbols the previously known OH/IR stars re-detected in this survey. The offsets refer to Sgr A* (Δl, Δb in Table 5.2). Note that the overall concentration of the new detections toward the center is partly due to the 'survey beam response' (Fig. 5.1); the concentration in the very center is however real

However, we do not list any of the obvious single peaks in the region where confusion with the extended continuum emission occurs. These detections are probably not of stellar origin. This means we have excluded all single peak detections within the box defined by $l \,\epsilon$ [359.92, 359.99], $b \,\epsilon$ [-0.08, -0.03], even when the peak flux exceeds 36 mJy. Actually, some of the double peak detections in this region might be debatable for being stellar sources. Such cases are indicated in Table 5.3. In case of a failure detecting the second peak, we usually took the velocity of the second peak from our VLA/ATCA data, or else from LWHM.

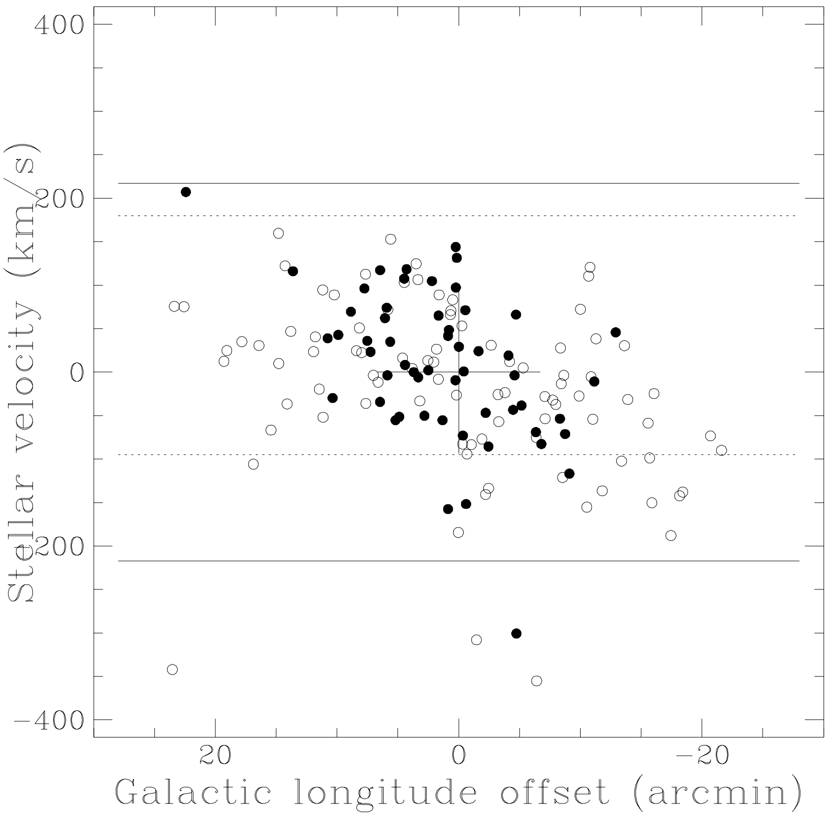

Figure 5.3 Velocity distribution. Symbols as in Fig. 5.2. The dotted lines outline the limited coverage of the monitor; the solid lines the velocity interval covered by LWHM

For each detection, at the red and blue shifted peaks, fluxes and velocities were determined. The position, together with the formal errors were measured with the AIPS fitting program IMFIT, in the channel with the highest peak flux. For the VLA data, J2000 positions and Galactic coordinates (l, b) were calculated from the B1950 positions and then truncated according to the IAU convention. The Galactic coordinates from the ATCA data were calculated after the inverse transformation from J2000 to B1950. All positional and kinematic data of the detections are given in Table 5.2. Table 5.3 lists corresponding physical data to each entry in Table 5.2. Where appropriate, we first list the VLA ('a', or 'b') and secondly the ATCA ('c') data. If seen in both the low and high resolution VLA image cubes, we used the high resolution ('b') result for the position (Table 5.2) and the low resolution ('a') result for the velocity and flux information (Tables 5.2 and 5.3 and Fig. 5.4); the other result was used as consistency check in such cases.

As the fluxes measured for the VLA data are averages over 17 observations and depend on the resolution, we show VLA and ATCA spectra separately in Fig. 5.4 and in Fig. 5.5. There are considerable difficulties when reaching such low noise levels in the GC area; residuals of the extended OH absorption, continuum subtraction, and very strong maser sources cause poor baselines in both the VLA and ATCA data. Therefore, at the position of the star in the image cube and avoiding the region of the stellar maser emission, a linear baseline was fitted to, and subtracted from the spectrum.

In Table 5.2 for each entry we list in order: the survey code, the given name according to its Galactic coordinates, the measured R.A. and Declination in J2000 with the maximum error in either R.A. or Declination, the blue and red shifted velocities, the derived stellar velocity and the Galactic coordinate offsets with respect to Sgr A*. The stellar velocity is taken as the mean of the velocities of both intensity maxima, whereas the Galactic coordinate offsets (i.e. for a 'flat sky', or cos $b \equiv 1$) is defined with respect to Sgr A*: $\Delta l = l_{\mathrm{OH}} - l_{\mathrm{Sgr\ A*}}$, $\Delta b = b_{\mathrm{OH}} - b_{\mathrm{Sgr\ A*}}$.

In Table 5.3 we repeat the survey code and source name, give the primary beam attenuation factor, the peak flux density and (spatially and spectrally) integrated flux together with the estimated relative integrated flux error for the blue shifted side, as well as for the red shifted side of the stellar velocity. We also list the the shell expansion velocity, and the OH maser luminosity (for an assumed isotropic radiation field and a distance of 8 kpc to the GC; Reid 1993). If the source appears to be extended, we determined an approximate deconvolved elliptical Gaussian for the source (the major axis, minor axis and position angle). The angular broadening of sources is probably caused by instrumental effects, time averaging of the visibilities or the extended background, but we cannot exclude that an extreme case of interstellar scattering of individual sources also plays a role (Van Langevelde & Diamond 1991; Van Langevelde et al. 1992b; Frail et al. 1994). The primary beam attenuation factor was calculated for both the VLA and ATCA with a polynomial, given internally in AIPS. The expansion velocity is half of the velocity separation between the maxima at both sides; however, it is not always the full extent of the feature. The blue and red shifted integrated fluxes are calculated by integrating flux densities over the channels from the stellar velocity to the first negative flux density outside the maximum.

5.3.1 The errors

Both VLA and ATCA data sets show positional offsets when compared with the positions measured by LWHM and vLJGHW. The small difference between the LWHM and vLJGHW data is due to using phase calibrators with different positional accuracies (B1730−130 and B1748−253, respectively); the LWHM and vLJGHW positions however are consistent with each other. The internal alignment of the VLA data introduced a systematic positional shift, as did the self-cal iteration of the ATCA data. Hence, there is a significant offset of a few arc-seconds between the positions measured in our VLA and ATCA image cubes. Our ATCA positions however are roughly consistent with the LWHM and vLJGHW data. We therefore attribute the systematic difference between our VLA and ATCA positions to the self-cal iteration performed to align the monitor data. Furthermore, small errors are introduced by transforming the coordinates to (and from) epoch J2000. We stress that our *absolute* positions are not expected to be accurate at the one arc-second level. By measuring the offsets with respect to Sgr A* (assuming no measurable relative proper motion of the OH/IR stars with respect to Sgr A* during the monitor), however we have taken out the relative differences between our VLA and ATCA observations, and from there they can be linked to other data sets.

The positional error quoted, for a given source in a data set, is the larger of the formal errors in R.A. and Declination as derived by IMFIT in the channel with the highest peak flux density of the source. The measured positions in individual channels are consistent with the position of the source. Flux density errors are also taken from IMFIT. This relative error can be used to derive the error in the OH maser luminosity. Because the spectral features are unresolved, we can only quote the velocity resolution as estimate of the error in velocity: 1.14 (or 2.27) $\mathrm{km\,s^{-1}}$ for the VLA and 1.45 $\mathrm{km\,s^{-1}}$ for the ATCA observations.

Similarly, the flux densities from the VLA data set depend on the spectral resolution used and on the effect of averaging flux densities over several epochs. OH/IR star OH flux densities and luminosities are variable, up to a factor two (e.g. Harvey et al. 1974; Herman & Habing 1985; Van Langevelde et al. 1990). The measured ATCA fluxes are therefore snapshots of the flux variability; the VLA fluxes approximate the average fluxes better, because of averaging out the amplitude variations over the monitor period. Estimating the variability effect would require detailed knowledge of the OH period and amplitude distributions and is therefore not attempted.

Table 5.2 OH/IR stars in the Galactic center: positional and kinematic data

	OH Name	R. A. and Declination J2000.0	$\delta^{\rm max}$ $''$	$V_{\rm blue}$ km s^{-1}	$V_{\rm red}$ km s^{-1}	$V_{\rm star}$ km s^{-1}	Δl $'$	Δb $'$	Ref.
c	359.583−0.239	17 45 33.497 −29 24 57.82	0.096	−103.8	−76.2	−90.0	−21.607	−11.505	1 (13)
c	359.598−0.000	17 44 39.612 −29 16 46.27	0.167	−92.1	−54.4	−73.3	−20.698	2.814	1 (14)
c	359.636−0.108	17 45 10.357 −29 18 11.81	0.233	−160.4	−115.4	−137.9	−18.420	−3.650	1 (17)
c	359.640−0.084	17 45 5.324 −29 17 13.50	0.648	−157.5	−127.0	−142.3	−18.163	−2.206	1 (18)
c	359.652−0.131	17 45 18.051 −29 18 4.75	0.381	−208.4	−167.7	−188.0	−17.450	−5.021	1 (19)
a	359.675+0.070	17 44 34.321 −29 10 31.77	0.336	−42.9	−6.5	−24.7	−16.057	7.005	1 (21)
c	359.676+0.069	17 44 34.492 −29 10 37.34	0.094	−42.8	−6.4	−24.6	−16.040	6.981	1 (21)
c	359.678−0.025	17 44 56.832 −29 13 25.39	0.141	−172.1	−128.5	−150.3	−15.885	1.359	1 (22)
a	359.681−0.095	17 45 13.695 −29 15 21.73	0.389	−118.3	−79.2	−98.7	−15.688	−2.844	1 (23)
c	359.681−0.095	17 45 13.854 −29 15 28.49	0.140	−118.3	−79.1	−98.7	−15.703	−2.881	1 (23)
c	359.683−0.105	17 45 16.352 −29 15 39.41	0.423	−76.2	−41.3	−58.7	−15.575	−3.441	1 (24)
a	359.711−0.100	17 45 19.159 −29 13 59.82	0.466	−50.8	−12.2	−31.5	−13.901	−3.148	1 (25)
c	359.711−0.100	17 45 19.329 −29 14 6.06	0.093	−51.5	−12.2	−31.9	−13.912	−3.184	1 (25)
a	359.716−0.070	17 45 12.792 −29 12 49.26	0.345	8.2	52.5	30.4	−13.624	−1.351	1 (26)
c	359.716−0.070	17 45 12.931 −29 12 54.88	0.129	8.1	51.7	29.9	−13.623	−1.373	1 (26)

Table 5.2 OH/IR stars in the Galactic center: positional and kinematic data (cont.)

	OH Name	R. A. and Declination J2000.0	$\delta^{\max}$ $''$	V_{blue} km s^{-1}	V_{red} km s^{-1}	V_{star} km s^{-1}	Δl $'$	Δb $'$	Ref.
c	359.720+0.025	17 44 51.266 −29 9 44.94	0.275	−124.1	−80.5	−102.3	−13.385	4.314	1 (27)
a	359.728+0.193	17 44 12.900 −29 3 57.50	0.530	30.9	60.4	45.7	−12.907	14.430	
c	359.746+0.134	17 44 29.422 −29 4 58.57	0.216	−144.4	−128.5	−136.5	−11.805	10.879	1 (29)
a	359.755+0.061	17 44 47.819 −29 6 44.73	0.645	19.6	57.0	38.3	−11.290	6.471	1 (31)
c	359.755+0.061	17 44 47.953 −29 6 48.03	0.354	19.7	57.5	38.6	−11.249	6.472	1 (31)
c	359.757−0.136	17 45 34.368 −29 12 52.95	1.015	−31.1	9.5	−10.8	−11.143	−5.343	
a	359.759+0.072	17 44 45.759 −29 6 9.83	0.515	−74.6	−33.8	−54.2	−11.029	7.159	1 (32)
c	359.760+0.072	17 44 45.967 −29 6 13.32	0.475	−74.7	−34.0	−54.4	−10.982	7.144	1 (32)
a	359.761+0.120	17 44 34.797 −29 4 31.67	0.138	−20.2	9.4	−5.4	−10.887	10.055	1 (33)
c	359.762+0.120	17 44 34.949 −29 4 35.39	0.042	−19.5	9.5	−5.0	−10.846	10.051	1 (33)
a	359.763−0.041	17 45 12.917 −29 9 31.55	0.345	107.0	134.2	120.6	−10.798	0.346	1 (34)
c	359.763−0.042	17 45 13.032 −29 9 35.95	0.327	106.9	134.5	120.7	−10.782	0.338	1 (34)
a	359.765+0.082	17 44 44.283 −29 5 33.63	0.738	91.1	129.7	110.4	−10.684	7.748	1 (35)
c	359.765+0.082	17 44 44.386 −29 5 38.81	0.765	95.3	128.7	112.0	−10.670	7.740	1 (35)
c	359.767−0.208	17 45 52.594 −29 14 32.55	0.639	−174.9	−135.7	−155.3	−10.530	−9.619	1 (36)

Table 5.2 OH/IR stars in the Galactic center: positional and kinematic data (cont.)

	OH Name	R. A. and Declination J2000.0	$\delta^{\max}$ $''$	$V_{\rm blue}$ km s^{-1}	$V_{\rm red}$ km s^{-1}	$V_{\rm star}$ km s^{-1}	Δl $'$	Δb $'$	Ref.
a	359.776−0.120	17 45 33.162 −29 11 18.03	0.282	59.3	85.4	72.3	−10.004	−4.349	1 (37)
c	359.776−0.120	17 45 33.283 −29 11 23.43	0.117	58.9	85.1	72.0	−10.017	−4.371	1 (37)
b	359.778+0.010	17 45 3.065 −29 7 10.38	0.235	−48.5	−6.5	−27.5	−9.901	3.416	1 (38)
c	359.779+0.010	17 45 3.214 −29 7 12.63	0.163	−48.6	−6.4	−27.5	−9.860	3.414	1 (38)
c	359.791−0.081	17 45 26.297 −29 9 24.63	0.487	−116.8	−116.8	−116.8	−9.097	−2.029	6
b	359.797−0.025	17 45 14.132 −29 7 18.20	0.300	−90.5	−51.9	−71.2	−8.750	1.286	*
a	359.799−0.090	17 45 29.347 −29 9 11.97	0.157	−22.4	15.0	−3.7	−8.646	−2.543	1 (40)
c	359.799−0.090	17 45 29.477 −29 9 16.56	0.110	−22.4	13.9	−4.3	−8.643	−2.560	1 (40)
c	359.801+0.165	17 44 30.082 −29 1 14.09	0.208	−135.7	−106.7	−121.2	−8.541	12.712	1 (41)
b	359.802−0.021	17 45 13.769 −29 6 52.93	0.178	−36.0	9.4	−13.3	−8.432	1.574	1 (42)
c	359.803−0.021	17 45 13.911 −29 6 55.80	0.407	−35.5	9.5	−13.0	−8.407	1.566	1 (42)
c	359.803−0.248	17 46 7.306 −29 13 58.00	0.279	9.5	45.9	27.7	−8.373	−12.064	1 (43)
a	359.804+0.201	17 44 22.112 −28 59 48.62	0.555	−72.4	−34.9	−53.6	−8.318	14.886	1a (5)
c	359.805+0.200	17 44 22.320 −28 59 54.71	0.633	−71.8	−34.0	−52.9	−8.300	14.852	1a (5)
b	359.810−0.069	17 45 26.219 −29 8 1.35	0.069	−58.7	−15.6	−37.2	−7.986	−1.340	1 (44)
c	359.810−0.070	17 45 26.350 −29 8 4.16	0.147	−58.7	−15.2	−36.9	−7.968	−1.347	1 (44)

Table 5.2 OH/IR stars in the Galactic center: positional and kinematic data (cont.)

	OH Name	R. A. and Declination J2000.0	$\delta^{\max}$ $''$	V_{blue} km s^{-1}	V_{red} km s^{-1}	V_{star} km s^{-1}	Δl $'$	Δb $'$	Ref.
a	359.814−0.162	17 45 48.428 −29 10 40.52	0.651	−51.9	−12.2	−32.1	−7.731	−6.866	1 (45)
c	359.814−0.162	17 45 48.489 −29 10 45.81	0.168	−51.5	−10.8	−31.1	−7.766	−6.884	1 (45)
b	359.825−0.024	17 45 17.705 −29 5 51.37	0.082	−74.6	−32.6	−53.6	−7.108	1.376	1 (47)
c	359.825−0.024	17 45 17.822 −29 5 53.53	0.072	−74.7	−32.6	−53.6	−7.078	1.378	1 (47)
a	359.825+0.153	17 44 36.341 −29 0 16.41	0.262	−45.1	−11.1	−28.1	−7.084	11.992	1 (46)
c	359.826+0.153	17 44 36.466 −29 0 19.13	0.178	−44.2	−10.8	−27.5	−7.032	12.001	1 (46)
b	359.829−0.070	17 45 29.129 −29 7 1.72	0.195	−100.9	−64.4	−82.7	−6.806	−1.365	
c	359.830−0.070	17 45 29.255 −29 7 5.17	0.451	−100.9	−64.5	−82.7	−6.799	−1.377	
c	359.836+0.119	17 44 45.898 −29 0 51.03	0.218	−374.0	−336.2	−355.1	−6.409	9.964	3
b	359.837+0.030	17 45 6.803 −29 3 31.75	0.117	−82.6	−67.8	−75.2	−6.366	4.621	1 (48)
c	359.838+0.030	17 45 6.909 −29 3 33.46	0.099	−83.4	−67.4	−75.4	−6.325	4.632	1 (48)
b	359.837+0.052	17 45 1.580 −29 2 48.21	0.177	−81.4	−56.5	−69.0	−6.344	5.973	1a (6), 6
c	359.838+0.053	17 45 1.674 −29 2 49.67	0.273	−80.5	−55.8	−68.2	−6.297	5.990	1a (6), 6
b	359.855−0.078	17 45 34.680 −29 6 0.25	0.067	−16.8	26.4	4.8	−5.299	−1.865	1 (50)
c	359.855−0.078	17 45 34.784 −29 6 2.88	0.204	−16.6	27.0	5.2	−5.288	−1.868	1 (50)
c	359.857−0.245	17 46 14.286 −29 11 8.26	0.381	−57.3	−19.5	−38.4	−5.167	−11.896	
c	359.864+0.056	17 45 4.706 −29 1 24.57	0.279	−313.0	−288.3	−300.6	−4.743	6.165	6

Table 5.2 OH/IR stars in the Galactic center: positional and kinematic data (cont.)

	OH Name	R. A. and Declination J2000.0		δ^{max} $''$	V_{blue} km s^{-1}	V_{red} km s^{-1}	V_{star} km s^{-1}	Δl $'$	Δb $'$	Ref.
b	359.864+0.068	17 45 1.705	−29 0 54.29	0.377	46.8	85.4	66.1	−4.710	6.941	6
b	359.867+0.030	17 45 11.149	−29 2 1.98	0.313	−20.2	12.8	−3.7	−4.594	4.592	
c	359.867+0.029	17 45 11.272	−29 2 3.30	0.522	−19.5	13.9	−2.8	−4.547	4.603	
b	359.868−0.018	17 45 22.495	−29 3 24.32	0.207	−62.2	−24.7	−43.4	−4.471	1.761	
c	359.869−0.018	17 45 22.584	−29 3 26.26	0.282	−61.6	−25.3	−43.5	−4.443	1.770	
a	359.873−0.209	17 46 7.999	−29 9 7.92	0.726	−8.8	33.2	12.2	−4.187	−9.709	1 (51)
c	359.872−0.210	17 46 8.083	−29 9 15.21	0.203	−7.9	32.8	12.4	−4.260	−9.758	1 (51)
b	359.875−0.091	17 45 40.589	−29 5 22.66	0.356	5.4	32.6	19.0	−4.091	−2.639	
b	359.880−0.087	17 45 40.379	−29 5 0.95	0.012	−33.8	−13.3	−23.6	−3.806	−2.412	1 (52)
c	359.880−0.087	17 45 40.478	−29 5 3.34	0.047	−34.0	−13.7	−23.9	−3.797	−2.414	1 (52)
b	359.888−0.051	17 45 33.145	−29 3 27.05	0.199	−76.9	−37.2	−57.0	−3.295	−0.248	1 (53)
c	359.888−0.051	17 45 33.212	−29 3 28.85	0.289	−77.6	−36.9	−57.3	−3.274	−0.236	1 (53)
a	359.889+0.155	17 44 44.926	−28 56 54.45	0.227	−40.6	−11.1	−25.8	−3.233	12.151	1 (55)
c	359.890+0.155	17 44 45.032	−28 56 57.95	0.178	−39.8	−12.2	−26.0	−3.196	12.156	1 (55)
a	359.898+0.222	17 44 30.776	−28 54 21.03	0.167	13.9	47.9	30.9	−2.673	16.127	1 (56)
c	359.899+0.222	17 44 30.863	−28 54 24.81	0.079	13.9	48.8	31.3	−2.638	16.134	1 (56)

Table 5.2 OH/IR stars in the Galactic center: positional and kinematic data (cont.)

	OH Name	R. A. and Declination J2000.0	$\delta^{\max}$ $''$	V_{blue} km s^{-1}	V_{red} km s^{-1}	V_{star} km s^{-1}	Δl $'$	Δb $'$	Ref.
b	359.902−0.103	17 45 47.321 −29 4 21.50	0.188	−105.2	−65.6	−85.4	−2.453	−3.362	
c	359.902−0.103	17 45 47.408 −29 4 23.43	0.239	−105.2	−66.0	−85.6	−2.448	−3.364	
c	359.902+0.061	17 45 8.830 −28 59 16.62	0.315	−153.2	−113.9	−133.6	−2.455	6.508	1 (57)
c	359.906−0.041	17 45 33.477 −29 2 16.45	0.060	−160.4	−121.2	−140.8	−2.215	0.343	1 (58)
b	359.906−0.036	17 45 32.215 −29 2 3.68	0.137	−67.8	−25.8	−46.8	−2.215	0.650	6, *
c	359.906−0.036	17 45 32.293 −29 2 5.55	0.117	−68.9	−25.3	−47.1	−2.193	0.659	6, *
b	359.911−0.059	17 45 38.199 −29 2 31.71	0.090	−99.4	−55.3	−77.4	−1.932	−0.709	1 (59)
c	359.911−0.059	17 45 38.284 −29 2 33.34	0.423	−99.4	−54.4	−76.9	−1.911	−0.701	1 (59)
c	359.916−0.067	17 45 40.821 −29 2 34.13	1.283	16.8	31.3	24.1	−1.636	−1.183	
c	359.918−0.055	17 45 38.467 −29 2 3.56	0.057	−326.0	−289.7	−307.9	−1.466	−0.477	3
b	359.925+0.032	17 45 18.845 −28 58 56.34	0.201	−95.1	−71.2	−83.2	−1.076	4.771	1 (60)
c	359.926+0.033	17 45 18.925 −28 58 58.03	0.206	−95.1	−71.8	−83.4	−1.045	4.784	1 (60)
c	359.929−0.110	17 45 52.897 −29 3 12.55	0.896	22.6	47.3	35.0	−0.819	−3.776	
c	359.931−0.050	17 45 39.105 −29 1 17.14	1.692	3.7	31.3	17.5	−0.734	−0.193	
b	359.931−0.063	17 45 42.059 −29 1 35.73	0.042	−113.9	−73.5	−93.7	−0.694	−0.943	1 (61)
c	359.932−0.063	17 45 42.135 −29 1 37.56	0.081	−113.9	−74.7	−94.3	−0.683	−0.938	1 (61)

Table 5.2 OH/IR stars in the Galactic center: positional and kinematic data (cont.)

	OH Name	R. A. and Declination J2000.0		$\delta^{\max}$ $''$	V_{blue} km s^{-1}	V_{red} km s^{-1}	V_{star} km s^{-1}	Δl $'$	Δb $'$	Ref.
c	359.932−0.059	17 45 41.324	−29 1 25.61	0.363	−159.0	−144.4	−151.7	−0.605	−0.682	6
b	359.934−0.059	17 45 41.505	−29 1 23.34	0.672	9.4	30.9	20.1	−0.581	−0.732	
b	359.934−0.015	17 45 31.098	−28 59 57.59	0.398	50.8	91.6	71.2	−0.549	1.953	
a	359.936−0.145	17 46 1.874	−29 3 54.31	0.472	−11.1	12.8	0.8	−0.419	−5.848	1a (7)
b	359.937−0.010	17 45 30.462	−28 59 37.99	0.246	−95.1	−50.8	−73.0	−0.343	2.242	6
c	359.938−0.010	17 45 30.544	−28 59 39.26	0.555	−95.1	−51.5	−73.3	−0.311	2.257	6
b	359.938−0.077	17 45 46.363	−29 1 44.26	0.018	−95.1	−71.2	−83.2	−0.325	−1.819	1 (62)
c	359.938−0.078	17 45 46.440	−29 1 46.32	0.016	−95.1	−70.4	−82.7	−0.321	−1.819	1 (62)
b	359.938−0.052	17 45 40.572	−29 0 53.96	0.062	34.3	71.8	53.1	−0.270	−0.303	1 (63)
c	359.939−0.052	17 45 40.651	−29 0 55.80	0.065	34.2	70.6	52.4	−0.256	−0.297	1 (63)
c	359.939−0.034	17 45 36.536	−29 0 21.34	0.777	29.9	53.1	41.5	−0.230	0.772	*
c	359.943−0.055	17 45 41.842	−29 0 48.17	1.939	22.6	35.7	29.2	−0.013	−0.454	*
c	359.943+0.260	17 44 28.171	−28 50 55.81	0.172	−201.1	−167.7	−184.4	0.024	18.459	1 (64)
b	359.944−0.068	17 45 45.309	−29 1 10.12	0.998	26.4	42.3	34.3	0.041	−1.326	
c	359.944−0.068	17 45 45.074	−29 1 8.34	1.146	24.1	43.0	33.5	0.065	−1.234	

Table 5.2 OH/IR stars in the Galactic center: positional and kinematic data (cont.)

	OH Name	R. A. and Declination J2000.0	δ^{max} $''$	V_{blue} km s^{-1}	V_{red} km s^{-1}	V_{star} km s^{-1}	Δl $'$	Δb $'$	Ref.
a	359.946−0.092	17 45 50.856 −29 1 45.48	0.876	114.9	147.8	131.4	0.159	−2.675	6
c	359.946−0.092	17 45 50.994 −29 1 49.10	0.367	115.6	149.0	132.3	0.154	−2.695	6
b	359.946−0.075	17 45 46.987 −29 1 12.49	0.412	53.1	87.1	70.1	0.199	−1.660	
b	359.946−0.048	17 45 40.552 −29 0 22.03	0.082	−46.3	−6.5	−26.4	0.182	−0.022	1 (65)
c	359.946−0.047	17 45 40.628 −29 0 23.47	0.216	−45.7	−6.4	−26.0	0.201	−0.012	1 (65)
c	359.947−0.294	17 46 38.540 −29 8 1.36	0.431	122.9	165.0	143.9	0.241	−14.807	
b	359.947−0.046	17 45 40.281 −29 0 16.34	0.534	89.4	105.3	97.3	0.232	0.078	*
b	359.947+0.066	17 45 14.104 −28 56 44.12	0.282	−28.1	9.4	−9.4	0.263	6.805	6
b	359.951−0.036	17 45 38.535 −28 59 43.88	0.047	69.5	96.8	83.1	0.494	0.685	1 (66)
c	359.951−0.036	17 45 38.599 −28 59 45.53	0.054	69.1	96.7	82.9	0.512	0.697	1 (66)
c	359.952−0.058	17 45 43.881 −29 0 26.72	0.579	27.0	45.9	36.4	0.522	−0.649	
b	359.954−0.041	17 45 40.097 −28 59 46.03	0.056	50.2	91.1	70.6	0.642	0.375	1 (67)
c	359.954−0.041	17 45 40.169 −28 59 47.73	0.023	50.2	90.9	70.6	0.658	0.384	1 (67)
b	359.954−0.031	17 45 37.873 −28 59 25.16	0.213	46.8	85.4	66.1	0.685	0.971	1 (68)
c	359.955−0.031	17 45 37.989 −28 59 27.25	1.053	45.9	83.6	64.7	0.704	0.970	1 (68)

Table 5.2 OH/IR stars in the Galactic center: positional and kinematic data (cont.)

	OH Name	R. A. and Declination J2000.0	$\delta^{\max}$ $''$	V_{blue} km s^{-1}	V_{red} km s^{-1}	V_{star} km s^{-1}	Δl $'$	Δb $'$	Ref.
b	359.956−0.050	17 45 42.654 −28 59 55.65	0.100	35.5	61.6	48.5	0.797	−0.185	4
c	359.956−0.050	17 45 42.713 −28 59 58.85	0.836	34.2	60.4	47.3	0.787	−0.189	4
c	359.957−0.123	17 45 59.866 −29 2 12.16	0.695	−157.5	−157.5	−157.5	0.876	−4.535	6
c	359.957−0.069	17 45 47.276 −29 0 30.18	1.029	51.7	66.2	58.9	0.857	−1.315	
b	359.958−0.058	17 45 44.690 −29 0 6.49	0.519	32.6	50.8	41.7	0.875	−0.659	
b	359.959−0.078	17 45 49.498 −29 0 39.90	0.711	55.9	75.2	65.5	0.949	−1.845	
c	359.959−0.078	17 45 49.601 −29 0 40.79	1.122	51.7	70.6	61.1	0.968	−1.842	
c	359.959−0.067	17 45 47.140 −29 0 20.63	1.222	29.9	56.0	43.0	0.978	−1.206	
b	359.965−0.043	17 45 42.258 −28 59 15.24	0.306	−73.5	−37.2	−55.3	1.327	0.240	*
b	359.970−0.049	17 45 44.250 −28 59 11.39	0.245	83.1	94.5	88.8	1.609	−0.098	1 (69), *
b	359.970−0.047	17 45 43.741 −28 59 7.77	0.624	34.9	53.1	44.0	1.603	0.028	
c	359.970−0.047	17 45 43.915 −28 59 8.92	1.370	37.1	57.5	47.3	1.633	0.020	
b	359.971−0.119	17 46 0.869 −29 1 20.58	0.067	−28.1	11.6	−8.2	1.665	−4.319	1 (70)
c	359.970−0.119	17 46 0.936 −29 1 23.24	0.110	−28.2	11.0	−8.6	1.648	−4.331	1 (70)
b	359.970+0.067	17 45 17.163 −28 55 30.90	0.214	47.9	82.0	65.0	1.653	6.871	1a (8)
c	359.971+0.068	17 45 17.208 −28 55 32.04	0.280	47.3	82.2	64.7	1.690	6.896	1a (8)

Table 5.2 OH/IR stars in the Galactic center: positional and kinematic data (cont.)

	OH Name	R. A. and Declination J2000.0	$\delta^{\max}$ $''$	V_{blue} km s^{-1}	V_{red} km s^{-1}	V_{star} km s^{-1}	Δl $'$	Δb $'$	Ref.
a	359.972−0.046	17 45 43.904 −28 59 0.29	1.217	40.0	53.6	46.8	1.716	0.055	
a	359.973+0.162	17 44 55.513 −28 52 24.03	0.306	2.5	50.2	26.4	1.821	12.530	1 (71)
c	359.974+0.162	17 44 55.600 −28 52 27.98	0.630	2.3	50.2	26.3	1.847	12.534	1 (71)
a	359.974−0.058	17 45 47.056 −28 59 14.84	1.264	30.9	62.7	46.8	1.869	−0.659	
c	359.974−0.058	17 45 47.012 −28 59 15.80	0.583	24.1	61.8	43.0	1.886	−0.619	
b	359.977−0.087	17 45 54.260 −29 0 0.58	0.030	−5.4	28.6	11.6	2.051	−2.392	1 (72)
c	359.977−0.087	17 45 54.328 −29 0 2.85	0.066	−5.0	28.4	11.7	2.043	−2.398	1 (72)
b	359.980−0.077	17 45 52.322 −28 59 34.58	0.118	85.4	124.0	104.7	2.200	−1.805	5
c	359.980−0.077	17 45 52.395 −28 59 36.47	0.157	85.1	124.3	104.7	2.199	−1.807	5
b	359.985−0.061	17 45 49.358 −28 58 47.40	0.042	−6.5	33.2	13.3	2.533	−0.843	1 (73)
c	359.985−0.061	17 45 49.420 −28 58 49.44	0.039	−6.4	32.8	13.2	2.533	−0.842	1 (73)
b	359.985−0.042	17 45 44.678 −28 58 12.65	0.182	−9.9	13.9	2.0	2.494	0.332	*
c	359.985−0.041	17 45 44.710 −28 58 13.56	0.374	−13.7	13.9	0.1	2.510	0.351	*
b	359.990+0.030	17 45 28.729 −28 55 42.18	0.087	−69.0	−31.5	−50.2	2.813	4.614	*
c	359.990+0.030	17 45 28.801 −28 55 43.81	0.167	−68.9	−32.6	−50.7	2.841	4.628	*
b	359.996−0.144	17 46 10.260 −29 0 48.33	0.199	−50.8	−15.6	−33.2	3.192	−5.793	1 (74)
c	359.996−0.144	17 46 10.328 −29 0 51.11	0.248	−50.0	−18.1	−34.0	3.171	−5.808	1 (74)

Table 5.2 OH/IR stars in the Galactic center: positional and kinematic data (cont.)

	OH Name	R. A. and Declination J2000.0	$\delta^{\max}$ $''$	V_{blue} km s^{-1}	V_{red} km s^{-1}	V_{star} km s^{-1}	Δl $'$	Δb $'$	Ref.
b	359.998−0.005	17 45 37.985 −28 56 20.48	0.081	−25.8	13.9	−6.0	3.325	2.554	6
c	359.999−0.004	17 45 38.008 −28 56 22.10	0.336	−25.3	13.9	−5.7	3.340	2.574	6
b	359.999−0.061	17 45 51.216 −28 58 5.03	0.129	88.8	124.0	106.4	3.348	−0.821	1 (75)
c	359.999−0.061	17 45 51.279 −28 58 7.17	0.293	88.0	124.3	106.2	3.344	−0.823	1 (75)
a	0.001+0.353	17 44 14.903 −28 44 58.84	0.402	114.9	134.2	124.6	3.493	23.992	1 (76)
a	0.005+0.360	17 44 13.690 −28 44 34.89	0.791	.0	−71.2	.0	3.694	24.427	
b	0.007−0.089	17 45 58.832 −28 58 32.48	0.131	−19.0	27.5	4.2	3.826	−2.481	1 (77)
c	0.007−0.089	17 45 58.922 −28 58 34.84	0.174	−19.5	27.0	3.7	3.817	−2.494	1 (77)
b	0.014−0.046	17 45 49.900 −28 56 48.52	0.219	100.2	136.5	118.3	4.287	0.088	*
c	0.014−0.046	17 45 49.968 −28 56 49.98	0.458	99.6	135.9	117.8	4.294	0.092	*
a	0.016−0.171	17 46 19.426 −29 0 35.36	0.597	−11.1	27.5	8.2	4.410	−7.400	
c	0.015−0.171	17 46 19.521 −29 0 41.81	0.340	−12.2	28.4	8.1	4.346	−7.447	
b	0.018−0.137	17 46 11.614 −28 59 28.87	0.188	88.8	126.3	107.5	4.478	−5.357	6
c	0.017−0.137	17 46 11.679 −28 59 32.15	0.237	89.4	127.2	108.3	4.449	−5.377	6
a	0.017+0.156	17 45 3.220 −28 50 19.51	0.280	95.6	110.4	103.0	4.474	12.175	1 (78)
c	0.018+0.156	17 45 3.332 −28 50 23.27	0.354	96.7	109.8	103.2	4.502	12.175	1 (78)

Table 5.2 OH/IR stars in the Galactic center: positional and kinematic data (cont.)

	OH Name	R. A. and Declination J2000.0	δ^{max} $''$	V_{blue} km s^{-1}	V_{red} km s^{-1}	V_{star} km s^{-1}	Δl $'$	Δb $'$	Ref.
a	0.020+0.346	17 44 19.169 −28 44 14.53	0.561	−8.8	41.1	16.2	4.612	23.582	1 (79)
c	0.020+0.346	17 44 19.231 −28 44 21.84	0.801	−7.9	40.1	16.1	4.596	23.565	1 (79)
b	0.024+0.027	17 45 34.236 −28 54 0.74	0.275	−69.0	−33.8	−51.4	4.886	4.467	
c	0.024+0.027	17 45 34.313 −28 54 1.68	0.830	−68.9	−32.6	−50.7	4.918	4.484	
b	0.029−0.026	17 45 47.528 −28 55 25.84	0.069	−74.6	−36.0	−55.3	5.193	1.248	6?
c	0.030−0.026	17 45 47.587 −28 55 27.72	0.129	−74.7	−35.5	−55.1	5.196	1.252	6?
a	0.036−0.182	17 46 24.849 −28 59 55.90	0.688	135.3	170.5	152.9	5.589	−8.071	1 (80)
c	0.035−0.182	17 46 24.875 −29 0 1.16	0.222	134.5	170.8	152.6	5.532	−8.096	1 (80)
b	0.037−0.003	17 45 43.104 −28 54 19.81	0.255	29.8	40.0	34.9	5.627	2.647	6
c	0.037−0.003	17 45 43.162 −28 54 19.94	0.426	29.9	40.1	35.0	5.660	2.669	6
b	0.040−0.056	17 45 56.036 −28 55 49.46	0.041	50.2	93.3	71.8	5.828	−0.545	1 (81)
c	0.040−0.056	17 45 56.094 −28 55 51.85	0.067	50.2	92.3	71.3	5.816	−0.551	1 (81)
b	0.041+0.060	17 45 28.887 −28 52 9.29	0.524	−21.9	14.5	−3.7	5.860	6.434	
a	0.042+0.082	17 45 23.886 −28 51 24.20	0.759	54.8	93.3	74.1	5.917	7.753	
c	0.042+0.082	17 45 23.932 −28 51 26.85	0.721	54.6	93.8	74.2	5.942	7.771	
b	0.044−0.033	17 45 51.196 −28 54 54.50	0.484	41.7	82.6	62.1	6.058	0.835	

Table 5.2 OH/IR stars in the Galactic center: positional and kinematic data (cont.)

	OH Name	R. A. and Declination J2000.0	δ^{max} $''$	V_{blue} km s^{-1}	V_{red} km s^{-1}	V_{star} km s^{-1}	Δl $'$	Δb $'$	Ref.
a	0.051−0.165	17 46 22.917 −28 58 38.80	0.831	−54.2	−14.5	−34.3	6.467	−7.042	6
c	0.050−0.165	17 46 22.979 −28 58 44.80	0.144	−54.4	−15.2	−34.8	6.404	−7.080	6
a	0.051+0.079	17 45 25.829 −28 51 2.04	0.674	97.9	136.5	117.2	6.455	7.583	
c	0.051+0.079	17 45 25.910 −28 51 5.34	0.299	98.2	135.9	117.0	6.473	7.588	
b	0.053−0.063	17 45 59.430 −28 55 20.66	0.150	−29.2	5.9	−11.6	6.624	−0.929	1 (82)
c	0.053−0.063	17 45 59.468 −28 55 23.34	0.126	−29.7	6.6	−11.5	6.604	−0.935	1 (82)
b	0.060−0.018	17 45 49.871 −28 53 37.01	0.047	−23.6	16.2	−3.7	7.009	1.755	1 (83)
c	0.060−0.018	17 45 49.912 −28 53 39.45	0.084	−23.9	15.4	−4.3	7.000	1.756	1 (83)
c	0.064−0.308	17 46 58.391 −29 2 27.44	0.566	6.6	40.1	23.3	7.247	−15.628	*
b	0.068−0.123	17 46 15.651 −28 56 27.83	0.347	19.0	53.1	36.0	7.515	−4.542	6
c	0.067−0.123	17 46 15.690 −28 56 31.81	0.385	18.3	53.1	35.7	7.470	−4.565	6
a	0.070+0.127	17 45 17.526 −28 48 32.36	0.212	−54.2	−17.9	−36.0	7.634	10.435	1 (84)
c	0.070+0.127	17 45 17.565 −28 48 35.93	0.159	−52.9	−18.1	−35.5	7.648	10.447	1 (84)
a	0.071−0.205	17 46 35.279 −28 58 53.87	0.197	99.0	126.3	112.6	7.657	−9.482	1 (85)
c	0.070−0.205	17 46 35.321 −28 58 57.14	0.082	99.6	125.8	112.7	7.629	−9.495	1 (85)
b	0.072−0.011	17 45 49.944 −28 52 45.25	0.324	79.7	112.6	96.2	7.754	2.191	
a	0.076+0.146	17 45 13.848 −28 47 39.09	0.108	1.4	43.4	22.4	7.971	11.585	1 (86)
c	0.076+0.146	17 45 13.894 −28 47 42.70	0.060	0.8	43.0	21.9	7.988	11.597	1 (86)

Table 5.2 OH/IR stars in the Galactic center: positional and kinematic data (cont.)

	OH Name	R. A. and Declination J2000.0	$\delta^{\max}$ $''$	V_{blue} km s^{-1}	V_{red} km s^{-1}	V_{star} km s^{-1}	Δl $'$	Δb $'$	Ref.
b	0.079−0.114	17 46 15.186 −28 55 38.69	0.156	36.6	65.0	50.8	8.161	−4.030	1 (87)
c	0.078−0.115	17 46 15.258 −28 55 42.50	0.069	37.1	64.7	50.9	8.124	−4.056	1 (87)
a	0.083+0.063	17 45 34.222 −28 49 52.45	0.279	4.8	44.5	24.7	8.404	6.619	1 (88)
c	0.083+0.063	17 45 34.234 −28 49 54.94	0.177	5.2	44.4	24.8	8.420	6.642	1 (88)
a	0.091+0.014	17 45 46.678 −28 51 0.81	0.569	61.6	77.5	69.5	8.856	3.699	
a	0.108−0.016	17 45 56.219 −28 51 4.16	0.619	21.8	63.8	42.8	9.898	1.888	6
c	0.107−0.016	17 45 56.267 −28 51 8.42	1.058	21.2	60.4	40.8	9.868	1.875	6
b	0.113−0.060	17 46 7.405 −28 52 11.75	0.138	71.8	105.8	88.8	10.221	−0.782	1 (90)
c	0.113−0.061	17 46 7.470 −28 52 15.43	0.163	70.6	105.4	88.0	10.188	−0.804	1 (90)
a	0.116−0.042	17 46 3.523 −28 51 30.06	0.739	−48.5	−11.1	−29.8	10.363	0.298	6
c	0.115−0.043	17 46 3.560 −28 51 34.80	0.774	−47.1	−12.2	−29.7	10.321	0.280	6
a	0.122−0.111	17 46 20.626 −28 53 18.35	0.615	21.8	55.9	38.9	10.769	−3.838	
c	0.121−0.112	17 46 20.736 −28 53 24.98	0.375	21.2	56.0	38.6	10.704	−3.890	
a	0.129−0.020	17 46 0.238 −28 50 6.90	0.340	76.3	112.6	94.5	11.171	1.633	1 (92)
c	0.128−0.020	17 46 0.305 −28 50 12.00	0.248	76.4	112.7	94.5	11.131	1.608	1 (92)
a	0.129+0.103	17 45 31.422 −28 46 17.14	0.120	−63.3	−40.6	−51.9	11.146	9.013	1 (91)
c	0.129+0.103	17 45 31.450 −28 46 21.78	0.082	−63.1	−41.3	−52.2	11.136	9.015	1 (91)

Table 5.2 OH/IR stars in the Galactic center: positional and kinematic data (cont.)

	OH Name	R. A. and Declination J2000.0	$\delta^{\max}$ $''$	$V_{\rm blue}$ km s^{-1}	$V_{\rm red}$ km s^{-1}	$V_{\rm star}$ km s^{-1}	Δl $'$	Δb $'$	Ref.
a	0.134−0.023	17 46 1.540 −28 49 57.39	0.771	−39.5	0.3	−19.6	11.455	1.472	1 (93)
c	0.134−0.023	17 46 1.658 −28 49 59.92	0.369	−39.8	−0.6	−20.2	11.456	1.459	1 (93)
a	0.139−0.135	17 46 28.707 −28 53 11.89	0.847	19.6	61.6	40.6	11.781	−5.293	1 (94)
c	0.138−0.136	17 46 28.732 −28 53 19.90	0.377	18.3	61.8	40.1	11.684	−5.343	1 (94)
a	0.142+0.026	17 45 51.293 −28 48 2.09	0.102	0.3	46.8	23.5	11.927	4.388	1 (95)
c	0.141+0.026	17 45 51.329 −28 48 6.82	0.041	0.8	47.3	24.1	11.893	4.376	1 (95)
a	0.170+0.119	17 45 33.470 −28 43 39.36	0.789	93.3	138.8	116.0	13.625	10.000	
a	0.173+0.211	17 45 12.423 −28 40 37.70	0.807	29.8	63.8	46.8	13.798	15.516	1 (96)
a	0.178−0.055	17 46 15.309 −28 48 41.36	0.266	−53.1	−20.2	−36.6	14.107	−0.444	1 (97)
c	0.177−0.055	17 46 15.347 −28 48 47.86	0.078	−52.9	−19.5	−36.2	14.037	−0.480	1 (97)
a	0.181−0.098	17 46 25.752 −28 49 53.32	0.546	103.6	141.0	122.3	14.272	−3.021	1 (98)
c	0.180−0.098	17 46 25.839 −28 49 59.97	0.437	101.1	140.3	120.7	14.202	−3.071	1 (98)
a	0.189+0.053	17 45 51.857 −28 44 45.50	0.735	−9.9	29.8	9.9	14.789	5.988	1 (99)
c	0.189+0.052	17 45 51.914 −28 44 51.19	0.079	−9.3	29.9	10.3	14.743	5.964	1 (99)
a	0.190+0.036	17 45 55.806 −28 45 15.66	0.177	145.6	173.9	159.7	14.814	4.990	1 (100)
c	0.190+0.036	17 45 55.826 −28 45 18.32	0.066	144.6	173.7	159.2	14.801	4.995	1 (100)
a	0.200+0.232	17 45 11.488 −28 38 36.27	0.448	−82.6	−50.8	−66.7	15.430	16.753	1 (101)

Table 5.2 OH/IR stars in the Galactic center: positional and kinematic data (cont.)

	OH Name	R. A. and Declination J2000.0	δ^{max} ″	V_{blue} km s^{-1}	V_{red} km s^{-1}	V_{star} km s^{-1}	Δl ′	Δb ′	Ref.
c	0.216+0.022	17 46 3.000 −28 44 22.16	0.831	12.4	48.8	30.6	16.416	4.137	1 (103)
a	0.226−0.055	17 46 22.117 −28 46 15.52	0.475	−122.7	−89.4	−106.0	16.960	−0.455	1 (105)
c	0.224−0.055	17 46 22.118 −28 46 22.40	0.112	−122.7	−89.2	−105.9	16.878	−0.489	1 (105)
c	0.240−0.015	17 46 14.952 −28 44 18.67	0.558	16.8	53.1	35.0	17.825	1.927	1 (106)
c	0.260−0.143	17 46 47.832 −28 47 14.91	0.234	18.3	31.3	24.8	19.053	−5.761	1 (107)
c	0.264−0.078	17 46 33.125 −28 45 0.79	0.394	−5.0	29.9	12.4	19.292	−1.845	1 (108)
c	0.317−0.066	17 46 37.780 −28 41 58.06	0.359	194.0	220.2	207.1	22.424	−1.136	
a	0.319−0.041	17 46 32.163 −28 41 1.33	0.117	57.0	93.3	75.2	22.579	0.385	1 (111)
c	0.321−0.040	17 46 32.132 −28 40 56.17	0.067	57.5	92.3	74.9	22.661	0.457	1 (111)
c	0.333−0.138	17 46 56.730 −28 43 22.13	1.273	58.9	92.3	75.6	23.380	−5.417	1 (112)
c	0.335−0.180	17 47 6.964 −28 44 33.03	0.073	−356.5	−327.5	−342.0	23.533	−7.948	2

1	Lindqvist et al. 1992a (number) and references therein	4	Levine et al. 1995
1a	Lindqvist et al. 1992a, single peak (number)	5	Yusef-Zadeh & Mehringer 1995
2	Baud et al. 1979	6	I.S. Glass, pers. comm. (Glass et al. 1996)
3	Van Langevelde et al. 1992a	*	See remarks in main text

Table 5.3 OH/IR stars in the Galactic center: physical data

	OH Name	PBF	S_{blue}	I_{blue}	ϵ	S_{red}	I_{red}	ϵ	V_{exp}	L_{OH}	Deconvolved			Note
			mJy	^{a}	%	mJy	^{a}	%	$\mathrm{km\,s^{-1}}$	^{b}	″	″	°	
c	359.583−0.239	8.48	3773.7	19.68	0.2	1460.2	11.22	1.3	13.80	45.1	0.0	0.0	0	
c	359.598−0.000	4.17	383.8	1.31	0.8	517.8	1.31	2.3	18.89	44.0	0.0	0.0	0	
c	359.636−0.108	3.05	541.1	2.36	0.6	229.1	1.70	2.6	22.51	44.2	0.0	0.0	0	
c	359.640−0.084	2.87	35.6	0.10	14.0	175.4	0.33	13.2	15.26	43.2	0.0	0.0	0	LWHM
c	359.652−0.131	2.82	86.1	0.39	3.3	257.5	0.79	4.9	20.33	43.7	0.0	0.0	0	
a	359.675+0.070	2.87	443.0	2.82	0.8	564.3	2.61	2.7	18.16	44.3	4.5	1.8	165	
c	359.676+0.069	2.59	487.8	2.47	0.3	682.0	2.58	0.9	18.16	44.3	0.0	0.0	0	
c	359.678−0.025	2.20	312.0	1.11	0.5	348.0	1.05	1.8	21.79	43.9	0.0	0.0	0	
a	359.681−0.095	3.38	.0	.00	99.0	288.2	0.96	5.8	19.56	43.6	0.0	0.0	0	ATCA
c	359.681−0.095	2.21	255.6	1.67	0.6	595.4	2.17	1.5	19.61	44.2	0.0	0.0	0	
c	359.683−0.105	2.21	120.7	0.41	1.6	43.8	0.14	14.1	17.43	43.3	0.0	0.0	0	
a	359.711−0.100	2.75	200.4	1.00	1.7	288.1	0.95	5.6	19.29	43.9	0.0	0.0	0	
c	359.711−0.100	1.89	402.6	1.46	0.4	576.5	1.89	1.0	19.61	44.1	0.0	0.0	0	
a	359.716−0.070	2.42	229.8	1.55	0.9	318.3	1.74	2.5	22.13	44.1	3.3	2.4	9	
c	359.716−0.070	1.79	390.2	1.71	0.5	525.1	1.99	1.3	21.79	44.2	0.0	0.0	0	

Table 5.3 OH/IR stars in the Galactic center: physical data (cont.)

	OH Name	PBF	S_{blue} mJy	I_{blue} ^{a}	ϵ %	S_{red} mJy	I_{red} ^{a}	ϵ %	V_{exp} km s^{-1}	L_{OH} ^{b}	Deconvolved ″	″	°	Note
c	359.720+0.025	1.85	164.1	0.55	1.0	12.3	.00	99.0	21.79	43.3	0.0	0.0	0	LWHM
a	359.728+0.193	2.79	118.9	0.06	19.3	54.1	0.05	66.5	14.76	42.6	0.0	0.0	0	
c	359.746+0.134	2.21	168.1	0.37	2.1	287.1	0.62	3.9	7.99	43.6	0.0	0.0	0	
a	359.755+0.061	1.71	130.8	0.66	1.4	78.6	0.61	4.9	18.73	43.7	8.5	1.1	179	
c	359.755+0.061	1.68	123.1	0.33	1.6	86.0	0.38	4.2	18.89	43.4	0.0	0.0	0	
c	359.757−0.136	1.61	39.1	0.10	8.0	52.4	0.11	22.0	20.34	42.9	0.0	0.0	0	
a	359.759+0.072	1.69	96.9	0.92	0.9	123.1	0.76	3.2	20.43	43.8	3.4	2.0	12	
c	359.760+0.072	1.70	149.2	0.67	1.3	137.2	0.59	4.6	20.34	43.7	0.0	0.0	0	
a	359.761+0.120	1.82	1372.4	3.66	1.9	3250.3	9.58	2.3	14.76	44.7	0.0	0.0	0	
c	359.762+0.120	1.96	2305.5	7.50	0.5	7013.8	20.98	0.6	14.53	45.0	0.0	0.0	0	
a	359.763−0.041	1.74	117.5	0.26	3.0	170.1	0.40	5.8	13.62	43.4	0.0	0.0	0	
c	359.763−0.042	1.43	125.6	0.45	1.3	150.5	0.49	3.7	13.80	43.6	0.0	0.0	0	
a	359.765+0.082	1.66	71.8	0.46	1.6	100.0	0.93	2.6	19.30	43.7	0.0	0.0	0	
c	359.765+0.082	1.71	28.1	0.21	3.8	92.6	0.58	4.1	16.71	43.5	0.0	0.0	0	
c	359.767−0.208	1.88	74.0	0.33	2.5	104.4	0.27	9.2	19.61	43.4	0.0	0.0	0	

Table 5.3 OH/IR stars in the Galactic center: physical data (cont.)

	OH Name	PBF	S_{blue} mJy	I_{blue} ^{a}	ϵ %	S_{red} mJy	I_{red} ^{a}	ϵ %	V_{exp} km s^{-1}	L_{OH} ^{b}	Deconvolved ″	″	°	Note
a	359.776−0.120	2.06	453.2	1.07	1.6	193.3	0.51	10.1	13.05	43.8	1.9	1.2	67	
c	359.776−0.120	1.44	615.3	1.19	0.7	231.1	0.48	5.7	13.07	43.8	0.0	0.0	0	
a	359.778+0.010	1.51	116.0	0.44	1.4	128.4	0.59	3.0	21.00	43.6	0.0	0.0	0	
c	359.779+0.010	1.39	195.1	0.46	0.9	181.2	0.61	1.9	21.06	43.6	0.0	0.0	0	
c	359.791−0.081	1.30	84.5	0.23	2.0	84.5	0.23	2.0	.00	43.0	0.0	0.0	0	
a	359.797−0.025	1.44	55.1	0.16	5.5	70.0	0.24	12.1	19.30	43.2	0.0	0.0	0	
a	359.799−0.090	1.67	302.6	1.81	1.2	1013.0	2.71	2.5	18.73	44.2	0.0	0.0	0	
c	359.799−0.090	1.27	416.2	2.65	0.5	1041.7	3.87	1.1	18.16	44.4	0.0	0.0	0	
c	359.801+0.165	2.06	169.4	0.33	1.6	223.8	0.70	2.4	14.53	43.6	0.0	0.0	0	
a	359.802−0.021	1.39	109.5	0.51	1.0	61.5	0.22	6.8	22.70	43.5	0.0	0.0	0	
c	359.803−0.021	1.24	76.3	0.38	1.1	47.4	0.08	15.0	22.52	43.3	0.0	0.0	0	
c	359.803−0.248	1.95	132.2	2.59	0.8	9.2	.00	99.0	18.16	44.0	0.0	0.0	0	LWHM
a	359.804+0.201	1.97	119.1	0.60	1.2	97.6	0.63	3.4	18.73	43.7	10.8	3.2	2	
c	359.805+0.200	2.44	77.3	0.12	7.2	108.4	0.28	9.3	18.89	43.2	0.0	0.0	0	
a	359.810−0.069	1.50	250.2	0.98	0.8	134.1	0.70	3.6	21.56	43.8	0.0	0.0	0	
c	359.810−0.070	1.21	394.2	1.09	0.7	243.1	0.78	2.9	21.79	43.9	0.0	0.0	0	

Table 5.3 OH/IR stars in the Galactic center: physical data (cont.)

	OH Name	PBF	S_{blue} mJy	I_{blue} ^{a}	ϵ %	S_{red} mJy	I_{red} ^{a}	ϵ %	V_{exp} km s^{-1}	L_{OH} ^{b}	Deconvolved ″	″	°	Note
a	359.814−0.162	2.12	151.8	0.82	1.1	69.3	0.84	3.3	19.86	43.8	9.0	3.9	1	
c	359.814−0.162	1.39	181.9	0.64	0.6	82.2	0.39	2.8	20.34	43.6	0.0	0.0	0	
a	359.825−0.024	1.28	536.2	2.07	0.6	525.6	2.42	1.6	21.00	44.2	0.0	0.0	0	
c	359.825−0.024	1.16	349.6	1.58	0.2	442.2	2.00	0.6	21.06	44.1	0.0	0.0	0	
a	359.825+0.153	1.51	220.9	1.07	0.6	136.8	0.70	2.8	17.02	43.8	5.7	2.1	0	
c	359.826+0.153	1.81	264.2	0.96	0.6	120.6	0.49	3.4	16.71	43.7	1.7	1.2	35	
a	359.829−0.070	1.39	.0	.00	99.0	80.4	0.47	4.5	18.24	43.3	4.0	2.9	45	ATCA
c	359.830−0.070	1.15	57.2	0.30	1.1	42.9	0.17	5.9	18.16	43.3	0.0	0.0	0	
c	359.836+0.119	1.53	153.2	0.46	1.0	166.4	0.37	4.0	18.89	43.5	0.0	0.0	0	
a	359.837+0.030	1.17	503.8	1.49	0.6	234.2	0.73	3.4	7.38	43.9	0.0	0.0	0	
c	359.838+0.030	1.19	520.2	1.80	0.3	228.4	0.70	2.8	7.99	44.0	0.0	0.0	0	
a	359.837+0.052	1.18	68.6	0.17	6.7	276.1	0.51	6.8	12.49	43.4	0.0	0.0	0	
c	359.838+0.053	1.25	24.9	0.09	4.6	130.8	0.38	3.3	12.35	43.3	0.0	0.0	0	
a	359.855−0.078	1.32	119.0	0.57	1.3	198.0	1.21	2.0	21.57	43.8	3.9	0.2	143	
c	359.855−0.078	1.09	84.1	0.43	1.1	196.9	0.90	1.5	21.79	43.7	0.0	0.0	0	
c	359.857−0.245	1.68	99.8	0.54	1.1	136.0	0.64	2.8	18.89	43.7	0.0	0.0	0	
c	359.864+0.056	1.19	89.4	0.26	1.2	25.8	0.15	6.7	12.35	43.2	0.0	0.0	0	

Table 5.3 OH/IR stars in the Galactic center: physical data (cont.)

	OH Name	PBF	$S_{\rm blue}$ mJy	$I_{\rm blue}$ ^{a}	ϵ %	$S_{\rm red}$ mJy	$I_{\rm red}$ ^{a}	ϵ %	$V_{\rm exp}$ km s^{-1}	$L_{\rm OH}$ ^{b}	Deconvolved ″	″	°	Note
a	359.864+0.068	1.11	37.5	0.17	3.5	48.6	0.19	11.0	19.30	43.1	0.0	0.0	0	
a	359.867+0.030	1.08	74.0	0.25	2.8	45.0	0.27	7.9	16.46	43.3	4.8	0.5	5	
c	359.867+0.029	1.12	75.7	0.22	2.2	24.2	0.13	11.4	16.71	43.1	0.0	0.0	0	
a	359.868−0.018	1.11	57.8	0.24	2.4	107.4	0.44	3.8	18.73	43.4	0.0	0.0	0	
c	359.869−0.018	1.06	85.8	0.29	1.3	109.9	0.47	2.4	18.16	43.5	0.0	0.0	0	
a	359.873−0.209	2.34	59.7	0.13	6.8	119.6	0.27	9.6	21.00	43.2	6.5	3.8	38	
c	359.872−0.210	1.41	17.6	0.10	4.0	165.0	0.38	3.3	20.34	43.3	0.0	0.0	0	
b	359.875−0.091	1.31	47.5	0.11	3.6	21.3	0.08	15.5	13.62	42.9	0.0	0.0	0	
a	359.880−0.087	1.28	7608.0	20.20	0.2	2379.7	7.11	1.4	10.22	45.0	0.0	0.0	0	
c	359.880−0.087	1.06	6140.3	20.20	0.2	2161.7	6.41	1.7	10.17	45.0	0.0	0.0	0	
a	359.888−0.051	1.13	100.7	0.66	0.8	111.6	0.59	2.6	19.86	43.7	0.0	0.0	0	
c	359.888−0.051	1.03	55.7	0.48	0.8	104.1	0.50	2.3	20.34	43.6	0.0	0.0	0	
a	359.889+0.155	1.27	109.5	0.60	0.8	169.8	0.61	2.4	14.75	43.7	4.8	2.7	179	
c	359.890+0.155	1.62	185.2	0.76	0.8	295.4	0.93	2.0	13.80	43.8	0.0	0.0	0	
a	359.898+0.222	1.68	326.1	1.73	0.6	446.9	1.94	1.6	17.02	44.2	4.7	1.9	180	
c	359.899+0.222	2.26	495.2	2.31	0.3	806.0	2.62	0.9	17.43	44.3	0.0	0.0	0	

Table 5.3 OH/IR stars in the Galactic center: physical data (cont.)

	OH Name	PBF	S_{blue} mJy	I_{blue} [a]	ϵ %	S_{red} mJy	I_{red} [a]	ϵ %	V_{exp} $km\,s^{-1}$	L_{OH} [b]	Deconvolved ″	″	°	Note
a	359.902−0.103	1.30	.0	.00	99.0	81.3	0.48	4.4	19.82	43.3	0.0	0.0	0	ATCA
c	359.902−0.103	1.05	127.1	0.37	0.9	76.0	0.26	3.9	19.61	43.4	0.0	0.0	0	
c	359.902+0.061	1.14	118.7	0.27	1.5	16.9	0.12	10.5	19.61	43.2	0.0	0.0	0	
c	359.906−0.041	1.01	736.0	2.77	0.3	1200.7	3.52	0.8	19.61	44.4	0.0	0.0	0	
a	359.906−0.036	1.07	52.8	0.10	3.4	210.9	0.64	1.6	21.00	43.5	0.0	0.0	0	
c	359.906−0.036	1.01	77.0	0.20	2.0	287.5	0.70	1.8	21.79	43.5	0.0	0.0	0	
a	359.911−0.059	1.12	.0	.00	99.0	111.4	0.51	3.8	22.03	43.3	0.0	0.0	0	ATCA
c	359.911−0.059	1.01	87.8	0.38	1.2	73.5	0.48	2.8	22.52	43.5	0.0	0.0	0	
c	359.916−0.067	1.01	18.8	0.11	4.8	36.7	0.10	15.0	7.26	42.9	0.0	0.0	0	
c	359.918−0.055	1.01	45.0	0.24	1.4	531.5	2.38	0.4	18.16	44.0	0.0	0.0	0	
a	359.925+0.032	1.00	.0	.00	99.0	162.8	0.56	3.9	11.93	43.3	0.0	0.0	0	ATCA
c	359.926+0.033	1.06	163.8	0.52	1.0	197.5	0.60	2.6	11.62	43.6	0.0	0.0	0	
c	359.929−0.110	1.04	17.9	0.22	1.6	41.6	0.51	2.0	12.35	43.4	7.5	1.6	42	MC?
c	359.931−0.050	1.00	23.0	0.69	0.6	46.4	0.61	2.7	13.80	43.7	15.5	10.6	9	MC
a	359.931−0.063	1.11	.0	.00	99.0	751.9	3.30	0.8	20.20	44.1	2.0	0.5	154	ATCA
c	359.932−0.063	1.00	545.4	2.41	0.3	748.1	3.18	0.7	19.61	44.3	0.0	0.0	0	

Table 5.3 OH/IR stars in the Galactic center: physical data (cont.)

	OH Name	PBF	S_{blue} mJy	I_{blue} ^{a}	ϵ %	S_{red} mJy	I_{red} ^{a}	ϵ %	V_{exp} km s^{-1}	L_{OH} ^{b}	Deconvolved $''$	$''$	$^{\circ}$	Note
c	359.932−0.059	1.00	50.9	0.24	0.9	21.3	0.11	6.3	7.26	43.1	0.0	0.0	0	
a	359.934−0.059	1.10	37.2	1.48	0.3	66.3	1.93	1.2	10.78	44.1	18.4	11.2	26	MC
b	359.934−0.015	1.02	26.0	0.07	5.3	15.6	0.09	14.1	20.43	42.8	0.0	0.0	0	
a	359.936−0.145	1.51	76.2	0.13	4.5	20.4	0.07	25.3	11.92	42.9	0.0	0.0	0	
a	359.937−0.010	1.01	23.1	0.10	99.0	60.4	0.13	13.1	18.73	44.0	0.0	0.0	0	ATCA
c	359.938−0.010	1.01	59.4	0.19	2.1	57.2	0.19	6.5	21.79	43.2	0.0	0.0	0	
a	359.938−0.077	1.15	.0	.00	99.0	6683.5	38.27	0.2	11.93	45.2	0.0	0.0	0	ATCA
c	359.938−0.078	1.01	5783.3	27.93	0.1	6784.0	35.20	0.1	12.35	45.4	0.0	0.0	0	
a	359.938−0.052	1.08	592.5	1.82	0.7	1030.3	2.88	1.3	18.73	44.3	0.0	0.0	0	
c	359.939−0.052	1.00	466.8	1.52	0.5	896.8	2.76	0.8	18.16	44.2	0.0	0.0	0	
c	359.939−0.034	1.00	41.9	0.99	0.3	17.3	0.32	2.7	11.62	43.7	13.5	6.4	174	MC?
c	359.943−0.055	1.00	36.2	0.84	0.7	63.1	0.80	2.9	6.54	43.8	34.6	3.1	157	MC?
c	359.943+0.260	2.87	542.7	1.47	0.8	228.1	0.82	4.0	16.71	43.9	0.0	0.0	0	
a	359.944−0.068	1.11	46.0	4.13	0.1	87.6	4.00	0.3	7.95	44.5	17.1	11.7	12	MC
c	359.944−0.068	1.00	25.9	0.58	1.6	133.6	3.06	1.0	9.44	44.1	17.1	8.9	170	MC

Table 5.3 OH/IR stars in the Galactic center: physical data (cont.)

	OH Name	PBF	S_{blue} mJy	I_{blue} ^{a}	ϵ %	S_{red} mJy	I_{red} ^{a}	ϵ %	V_{exp} km s^{-1}	L_{OH} ^{b}	Deconvolved ″	″	°	Note
a	359.946−0.092	1.20	31.2	0.19	3.5	46.7	0.20	9.8	16.46	43.2	0.0	0.0	0	
c	359.946−0.092	1.02	21.8	0.06	4.4	52.3	0.14	5.6	16.71	42.9	0.0	0.0	0	
b	359.946−0.075	1.13	37.6	2.06	0.1	15.7	0.92	1.2	17.02	44.1	10.5	3.3	164	MC
a	359.946−0.048	1.06	289.5	2.16	0.6	359.8	1.65	2.6	19.86	44.2	0.0	0.0	0	
c	359.946−0.047	1.00	381.6	3.13	0.4	503.8	2.52	1.7	19.61	44.3	0.0	0.0	0	
c	359.947−0.294	1.97	88.8	0.20	3.2	95.6	0.19	10.0	21.07	43.2	0.0	0.0	0	
b	359.947−0.046	1.06	34.8	0.17	3.3	24.5	0.10	18.0	7.94	43.0	0.0	0.0	0	
a	359.947+0.066	1.00	41.9	0.31	1.9	19.5	0.16	10.7	18.73	43.3	7.0	2.4	36	
a	359.951−0.036	1.04	133.7	0.53	2.9	1012.2	3.67	1.3	13.62	44.2	0.0	0.0	0	
c	359.951−0.036	1.00	102.1	0.48	1.5	1059.3	4.41	0.5	13.80	44.3	0.0	0.0	0	
c	359.952−0.058	1.00	79.3	0.82	0.5	28.0	0.20	6.9	9.44	43.6	9.0	3.1	156	MC?
a	359.954−0.041	1.05	2138.1	9.12	0.2	2641.7	12.04	0.5	20.43	44.9	0.0	0.0	0	
c	359.954−0.041	1.00	2227.4	9.54	0.1	3051.3	13.59	0.2	20.34	45.0	0.0	0.0	0	
a	359.954−0.031	1.03	79.0	0.61	1.0	61.4	0.47	4.0	19.30	43.6	7.2	2.9	5	
c	359.955−0.031	1.00	51.6	0.15	4.4	28.0	0.15	13.0	18.89	43.1	0.0	0.0	0	

Table 5.3 OH/IR stars in the Galactic center: physical data (cont.)

	OH Name	PBF	S_{blue} mJy	I_{blue} [a]	ϵ %	S_{red} mJy	I_{red} [a]	ϵ %	V_{exp} km s^{-1}	L_{OH} [b]	Deconvolved ″	″	°	Note
a	359.956−0.050	1.07	84.6	0.17	4.3	45.2	0.20	10.9	13.05	43.2	0.0	0.0	0	
c	359.956−0.050	1.00	55.8	0.17	3.4	20.9	0.05	37.7	13.07	42.9	0.0	0.0	0	
c	359.957−0.123	1.06	46.2	0.13	9.7	46.2	0.13	9.7	.00	43.0	0.0	0.0	0	
c	359.957−0.069	1.01	97.1	2.17	0.3	26.8	1.20	1.9	7.26	44.1	20.9	5.3	24	MC
b	359.958−0.058	1.09	27.1	0.23	1.5	31.3	0.25	9.0	9.08	43.3	0.0	0.0	0	
a	359.959−0.078	1.15	54.5	3.33	0.1	47.6	3.23	0.4	9.65	44.4	21.0	12.4	177	MC
c	359.959−0.078	1.01	55.3	0.57	0.9	19.5	0.24	7.0	9.44	43.5	10.9	0.8	154	MC
c	359.959−0.067	1.01	19.3	0.36	1.2	47.7	0.91	1.6	13.08	43.7	23.1	7.2	170	MC
a	359.965−0.043	1.06	57.5	0.18	3.8	42.0	0.20	11.0	18.16	43.2	0.0	0.0	0	
a	359.970−0.049	1.07	36.6	0.65	0.9	51.5	0.62	2.7	5.68	43.7	10.5	4.4	36	
b	359.970−0.047	1.06	30.0	0.74	0.3	16.7	0.41	3.8	9.08	43.6	10.4	1.5	28	MC
c	359.970−0.047	1.01	61.0	0.62	1.3	27.4	0.32	7.4	10.17	43.6	10.1	4.5	176	MC
a	359.971−0.119	1.34	500.1	2.49	0.3	242.8	1.78	1.3	19.86	44.2	0.0	0.0	0	
c	359.970−0.119	1.06	684.1	3.74	0.2	359.6	2.48	1.1	19.61	44.4	0.0	0.0	0	
a	359.970+0.067	1.01	103.5	0.31	2.1	36.2	0.11	18.2	17.03	43.2	0.0	0.0	0	
c	359.971+0.068	1.15	153.0	0.42	1.3	52.0	0.21	8.1	17.43	43.4	0.0	0.0	0	

Table 5.3 OH/IR stars in the Galactic center: physical data (cont.)

	OH Name	PBF	S_{blue}	I_{blue}	ϵ	S_{red}	I_{red}	ϵ	V_{exp}	L_{OH}	Deconvolved			Note
			mJy	[a]	%	mJy	[a]	%	km s^{-1}	[b]	″	″	°	
a	359.972−0.046	1.06	40.9	0.32	2.0	26.5	0.23	8.3	6.81	43.3	9.4	3.6	148	MC
a	359.973+0.162	1.23	79.1	0.32	1.8	142.0	0.41	4.1	23.84	43.4	2.4	2.2	42	
c	359.974+0.162	1.62	65.4	0.25	2.8	107.6	0.28	7.8	23.97	43.3	0.0	0.0	0	
a	359.974−0.058	1.09	24.9	0.77	0.5	46.8	1.19	1.3	15.89	43.9	13.4	7.6	14	MC
c	359.974−0.058	1.01	23.6	0.27	1.1	75.6	1.76	0.6	18.88	43.9	14.5	7.6	167	MC
a	359.977−0.087	1.19	690.8	2.88	0.3	399.5	1.95	1.5	17.03	44.3	0.0	0.0	0	
c	359.977−0.087	1.02	845.3	4.11	0.2	583.8	2.60	0.8	16.71	44.4	0.0	0.0	0	
a	359.980−0.077	1.15	98.8	0.53	1.0	66.3	0.25	6.5	19.29	43.5	3.4	2.2	30	
c	359.980−0.077	1.02	148.9	0.39	0.7	89.7	0.24	3.5	19.61	43.4	0.0	0.0	0	
a	359.985−0.061	1.11	1133.6	5.21	0.4	817.2	3.55	1.8	19.86	44.5	0.0	0.0	0	
c	359.985−0.061	1.02	980.5	5.26	0.1	976.3	4.93	0.3	19.61	44.6	0.0	0.0	0	
a	359.985−0.042	1.06	51.3	0.41	1.0	52.5	0.43	2.8	11.92	43.5	0.0	0.0	0	
c	359.985−0.041	1.01	62.9	0.51	0.7	78.0	0.53	2.0	13.80	43.6	0.0	0.0	0	
a	359.990+0.030	1.00	190.7	0.72	1.4	82.1	0.33	9.1	18.73	43.6	0.0	0.0	0	
c	359.990+0.030	1.08	157.5	0.83	0.4	60.0	0.27	3.5	18.16	43.6	0.0	0.0	0	
a	359.996−0.144	1.53	272.3	0.80	0.9	63.4	0.36	5.9	17.59	43.7	3.4	0.9	149	
c	359.996−0.144	1.13	175.4	0.59	0.8	44.5	0.27	5.4	15.98	43.5	0.0	0.0	0	

Table 5.3 OH/IR stars in the Galactic center: physical data (cont.)

	OH Name	PBF	S_{blue} mJy	I_{blue} ^{a}	ϵ %	S_{red} mJy	I_{red} ^{a}	ϵ %	V_{exp} km s^{-1}	L_{OH} ^{b}	Deconvolved ″	″	°	Note
a	359.998−0.005	1.03	18.1	0.02	19.0	97.5	0.63	1.9	19.86	43.4	0.0	0.0	0	
c	359.999−0.004	1.04	21.8	0.17	1.8	70.7	0.31	3.2	19.61	43.3	0.0	0.0	0	
a	359.999−0.061	1.12	102.6	0.87	0.8	90.9	0.47	4.2	17.59	43.7	0.0	0.0	0	
c	359.999−0.061	1.03	81.3	0.30	1.1	71.3	0.26	3.9	18.16	43.3	0.0	0.0	0	
a	0.001+0.353	4.36	244.6	0.80	2.8	483.4	1.20	5.9	9.65	43.9	5.8	2.6	169	
a	0.005+0.360	4.77	.0	.00	99.0	367.3	1.65	6.5	.00	43.8	0.0	0.0	0	
a	0.007−0.089	1.23	60.5	0.73	0.8	130.3	0.65	2.7	23.27	43.7	0.0	0.0	0	
c	0.007−0.089	1.05	87.6	0.62	0.7	189.6	0.74	1.7	23.24	43.7	0.0	0.0	0	
a	0.014−0.046	1.11	23.3	0.16	3.8	103.5	0.49	3.8	18.16	43.4	0.0	0.0	0	
c	0.014−0.046	1.05	9.4	.00	99.0	60.9	0.31	5.0	18.16	44.0	0.0	0.0	0	VLA
a	0.016−0.171	1.81	163.2	0.61	2.2	87.3	0.57	7.0	19.30	43.7	0.0	0.0	0	
c	0.015−0.171	1.24	112.7	0.64	0.7	58.4	0.46	3.1	20.34	43.6	6.7	0.4	174	
a	0.018−0.136	1.53	107.5	0.40	2.5	39.3	0.17	18.7	18.73	43.3	0.0	0.0	0	
c	0.017−0.137	1.14	145.2	0.47	0.9	60.5	0.20	6.2	18.89	43.4	0.0	0.0	0	
a	0.017+0.156	1.27	127.0	0.40	1.2	140.7	0.33	4.5	7.38	43.5	5.4	3.1	167	
c	0.018+0.156	1.66	136.2	0.32	1.9	130.7	0.23	8.3	6.54	43.3	0.0	0.0	0	

Table 5.3 OH/IR stars in the Galactic center: physical data (cont.)

	OH Name	PBF	S_{blue} mJy	I_{blue} ^{a}	ϵ %	S_{red} mJy	I_{red} ^{a}	ϵ %	V_{exp} km s^{-1}	L_{OH} ^{b}	Deconvolved ″	″	°	Note
a	0.020+0.346	4.19	270.5	2.27	0.8	123.4	0.66	8.7	24.97	44.1	0.0	0.0	0	
c	0.020+0.346	7.38	481.2	1.30	4.0	262.4	1.31	11.5	23.97	44.0	0.0	0.0	0	
a	0.024+0.027	1.05	67.4	0.20	2.4	21.6	0.10	99.0	17.59	42.9	0.0	0.0	0	ATCA
c	0.024+0.027	1.12	45.8	0.13	3.5	9.6	0.07	20.1	18.16	42.9	0.0	0.0	0	VLA
a	0.030−0.026	1.10	110.3	0.57	1.3	169.8	0.65	3.6	19.30	43.7	3.7	0.7	161	
c	0.030−0.026	1.08	160.3	0.62	0.5	188.3	0.77	1.1	19.61	43.7	0.0	0.0	0	
a	0.036−0.182	1.99	144.0	0.60	1.8	73.4	0.41	8.0	17.60	43.6	0.0	0.0	0	
c	0.035−0.182	1.33	164.2	0.62	0.7	56.8	0.28	4.6	18.16	43.5	3.7	1.4	170	
a	0.037−0.003	1.09	49.9	0.11	4.7	81.8	0.19	8.6	5.11	43.1	0.0	0.0	0	
c	0.037−0.003	1.11	51.3	0.18	3.0	115.6	0.36	4.6	5.08	43.3	0.0	0.0	0	
a	0.040−0.056	1.19	376.5	1.27	0.8	454.6	1.49	2.0	21.57	44.0	0.0	0.0	0	
c	0.040−0.056	1.09	386.0	1.17	0.3	486.2	1.67	0.7	21.06	44.0	0.0	0.0	0	
b	0.041+0.060	1.09	33.7	0.19	6.9	55.0	0.15	25.7	18.16	43.1	0.0	0.0	0	
a	0.042+0.082	1.12	47.0	0.30	2.0	82.1	0.47	4.2	19.30	43.5	6.2	3.6	31	
c	0.042+0.082	1.32	64.4	0.19	3.9	80.4	0.22	10.0	19.61	43.2	0.0	0.0	0	
b	0.044−0.033	1.15	17.9	0.24	1.5	35.2	0.21	6.3	20.43	43.2	2.7	1.2	6	

Table 5.3 OH/IR stars in the Galactic center: physical data (cont.)

	OH Name	PBF	S_{blue} mJy	I_{blue} [a]	ϵ %	S_{red} mJy	I_{red} [a]	ϵ %	V_{exp} km s^{-1}	L_{OH} [b]	Deconvolved ″	″	°	Note
a	0.051−0.165	1.88	103.9	0.93	0.7	62.4	0.50	4.2	19.86	43.7	8.2	3.9	129	
c	0.050−0.165	1.31	167.5	0.50	0.6	93.5	0.40	2.2	19.61	43.5	0.0	0.0	0	
a	0.051+0.079	1.14	39.3	0.23	2.8	81.4	0.41	4.7	19.30	43.4	3.1	2.1	172	
c	0.051+0.079	1.34	83.9	0.24	1.9	129.0	0.40	3.3	18.88	43.4	0.0	0.0	0	
a	0.053−0.063	1.26	63.8	0.37	1.7	128.8	0.66	2.8	17.59	43.6	2.2	1.8	142	
c	0.053−0.063	1.13	76.7	0.32	1.1	238.5	1.01	1.1	18.16	43.7	0.0	0.0	0	
a	0.060−0.018	1.17	193.0	1.12	1.4	684.9	1.94	2.6	19.86	44.1	0.0	0.0	0	
c	0.060−0.018	1.15	156.3	1.51	0.5	692.8	2.69	0.8	19.61	44.2	0.0	0.0	0	
c	0.064−0.308	2.51	107.2	0.43	1.8	103.4	0.30	7.4	16.71	43.4	0.0	0.0	0	
b	0.068−0.123	1.63	57.5	0.33	1.4	43.9	0.17	8.4	17.03	43.3	0.0	0.0	0	
c	0.067−0.123	1.25	82.3	0.24	1.4	53.9	0.21	5.3	17.43	43.2	0.0	0.0	0	
a	0.070+0.127	1.33	81.7	0.40	2.1	246.9	1.00	2.5	18.16	43.7	0.0	0.0	0	
c	0.070+0.127	1.66	77.6	0.34	1.6	263.7	1.09	1.4	17.43	43.7	0.0	0.0	0	
a	0.071−0.205	2.50	1013.2	3.57	1.2	1377.4	6.27	2.0	13.62	44.6	0.0	0.0	0	
c	0.070−0.205	1.57	1743.0	8.39	0.3	2788.4	13.81	0.6	13.07	44.9	0.0	0.0	0	
a	0.072−0.011	1.21	56.4	0.28	1.8	24.2	0.14	10.8	16.46	43.2	0.0	0.0	0	
a	0.076+0.146	1.44	227.5	0.86	1.2	642.1	1.48	2.1	21.00	44.0	0.0	0.0	0	
c	0.076+0.146	1.82	316.7	1.28	0.5	948.2	2.16	0.9	21.06	44.1	0.0	0.0	0	

Table 5.3 OH/IR stars in the Galactic center: physical data (cont.)

	OH Name	PBF	S_{blue} mJy	I_{blue} [a]	ϵ %	S_{red} mJy	I_{red} [a]	ϵ %	V_{exp} km s^{-1}	L_{OH} [b]	Deconvolved ″	″	°	Note
a	0.079−0.114	1.63	551.3	1.50	0.8	287.2	1.26	2.7	14.19	44.0	0.0	0.0	0	
c	0.078−0.115	1.27	525.9	2.13	0.2	355.5	1.59	0.8	13.80	44.2	0.0	0.0	0	
a	0.083+0.063	1.24	153.9	0.79	0.7	66.5	0.56	3.0	19.86	43.7	0.0	0.0	0	
c	0.083+0.063	1.40	139.6	0.58	0.5	57.4	0.28	3.2	19.61	43.5	4.7	1.5	176	
a	0.091+0.014	1.26	31.3	0.16	3.5	59.1	0.14	11.6	7.95	43.1	0.0	0.0	0	
a	0.108−0.016	1.39	87.9	0.45	1.4	60.6	0.59	3.2	21.00	43.6	4.3	1.7	3	
c	0.107−0.016	1.35	60.4	0.29	3.0	45.5	0.33	7.9	19.61	43.4	0.0	0.0	0	
a	0.113−0.060	1.56	455.7	2.39	0.5	400.9	2.66	1.3	17.03	44.3	2.8	2.3	142	
c	0.113−0.061	1.36	452.0	2.05	0.4	446.8	2.39	1.2	17.43	44.2	0.0	0.0	0	
a	0.116−0.042	1.51	31.5	0.20	3.3	72.9	0.19	10.1	18.73	43.2	0.0	0.0	0	
c	0.115−0.043	1.37	27.0	0.09	5.5	54.1	0.21	8.0	17.43	43.1	0.0	0.0	0	
a	0.122−0.111	1.90	101.9	0.82	0.9	80.7	0.54	4.0	17.02	43.7	8.7	2.4	161	
c	0.121−0.112	1.48	126.4	0.54	1.0	110.0	0.39	4.3	17.43	43.6	0.0	0.0	0	
a	0.129−0.020	1.55	177.9	0.73	1.0	40.4	0.29	7.4	18.16	43.6	7.0	1.6	164	
c	0.128−0.020	1.46	256.1	0.79	1.0	70.2	0.35	6.9	18.16	43.6	0.0	0.0	0	
a	0.129+0.103	1.60	601.9	2.21	1.0	1287.1	3.10	2.1	11.35	44.3	0.0	0.0	0	
c	0.129+0.103	1.86	561.5	2.74	0.5	1304.6	3.65	1.1	10.90	44.4	0.0	0.0	0	

Table 5.3 OH/IR stars in the Galactic center: physical data (cont.)

	OH Name	PBF	S_{blue} mJy	I_{blue} ^{a}	ϵ %	S_{red} mJy	I_{red} ^{a}	ϵ %	V_{exp} km s^{-1}	L_{OH} ^{b}	Deconvolved ″	″	°	Note
a	0.134−0.023	1.59	49.0	0.46	1.5	82.3	0.52	4.1	19.86	43.6	9.6	2.3	21	
c	0.134−0.023	1.49	47.8	0.34	1.0	74.6	0.23	4.5	19.61	43.3	0.0	0.0	0	
a	0.139−0.135	2.27	61.3	0.86	1.0	110.0	1.21	2.3	21.00	43.9	7.8	2.4	42	
c	0.138−0.136	1.66	91.3	0.50	1.5	164.1	0.74	3.3	21.79	43.7	0.0	0.0	0	
a	0.142+0.026	1.59	418.6	2.15	0.5	878.9	5.80	0.6	23.27	44.5	0.0	0.0	0	
c	0.141+0.026	1.63	613.3	2.93	0.2	1369.2	7.65	0.3	23.24	44.6	2.4	1.2	167	
a	0.170+0.119	2.05	113.5	0.53	2.1	74.0	0.48	6.7	22.70	43.6	4.3	2.5	174	
a	0.173+0.211	2.91	146.4	0.82	1.3	76.4	0.29	11.8	17.02	43.6	8.5	4.0	163	
a	0.178−0.055	2.14	167.6	0.74	3.1	659.2	1.67	4.2	16.46	44.0	0.0	0.0	0	
c	0.177−0.055	1.83	365.2	1.16	0.7	902.1	2.69	0.9	16.71	44.2	0.0	0.0	0	
a	0.181−0.098	2.45	71.2	0.47	1.8	161.3	1.18	2.4	18.73	43.8	5.2	3.8	152	
c	0.180−0.098	1.91	103.0	0.63	1.4	173.4	0.76	3.6	19.61	43.7	0.0	0.0	0	
a	0.189+0.053	2.09	135.3	1.27	0.7	74.0	0.76	3.4	19.86	43.9	0.0	0.0	0	
c	0.189+0.052	2.16	714.1	2.78	0.2	238.2	0.75	2.7	19.61	44.1	0.0	0.0	0	
a	0.190+0.036	2.08	1848.2	8.05	0.7	1720.4	7.03	2.4	14.18	44.8	0.0	0.0	0	
c	0.190+0.036	2.10	3109.5	16.84	0.2	3629.4	16.96	0.6	14.53	45.1	0.0	0.0	0	
a	0.200+0.232	4.01	183.4	0.70	2.2	271.6	0.90	5.2	15.89	43.8	0.0	0.0	0	

Table 5.3 OH/IR stars in the Galactic center: physical data (cont.)

	OH Name	PBF	S_{blue} mJy	I_{blue} ^{a}	ϵ %	S_{red} mJy	I_{red} ^{a}	ϵ %	V_{exp} km s^{-1}	L_{OH} ^{b}	Deconvolved ″	″	°	Note
c	0.216+0.022	2.41	40.4	0.01	47.1	78.7	0.69	2.7	18.16	43.4	8.1	4.1	151	
a	0.226−0.055	2.94	.0	.00	99.0	441.9	2.05	2.9	16.65	43.9	9.6	4.9	27	ATCA
c	0.224−0.055	2.40	537.4	1.41	0.6	596.9	1.80	1.3	16.70	44.1	0.0	0.0	0	
c	0.240−0.015	2.69	135.6	0.72	1.3	121.9	0.80	3.8	18.16	43.8	0.0	0.0	0	
c	0.260−0.143	3.51	219.4	1.30	0.9	453.7	1.50	2.5	6.54	44.0	5.2	1.8	175	
c	0.264−0.078	3.25	312.1	1.70	0.8	72.3	0.48	8.7	17.43	43.9	0.0	0.0	0	
c	0.317−0.066	5.41	450.4	1.08	2.0	290.2	0.68	9.9	13.08	43.8	0.0	0.0	0	
a	0.319−0.041	8.35	1716.4	9.49	0.8	4282.4	15.30	1.4	18.16	45.0	0.0	0.0	0	
c	0.321−0.040	5.64	2557.4	13.91	0.3	5589.0	21.94	0.7	17.43	45.1	0.0	0.0	0	
c	0.333−0.138	7.47	275.7	1.16	3.9	299.1	1.44	8.7	16.71	44.0	0.0	0.0	0	
c	0.335−0.180	9.04	4597.0	17.63	0.2	3942.0	19.50	0.7	14.53	45.2	0.0	0.0	0	

a)	Units in Jy km s^{-1}	LWHM	Peak velocity secondary in Table 2 from Lindqvist et al. 1992a
b)	Units in LOG (photons per second)	VLA	Peak velocity secondary in Table 2 from our VLA data
MC	Molecular cloud complex(es)	ATCA	Peak velocity secondary in Table 2 from our ATCA data

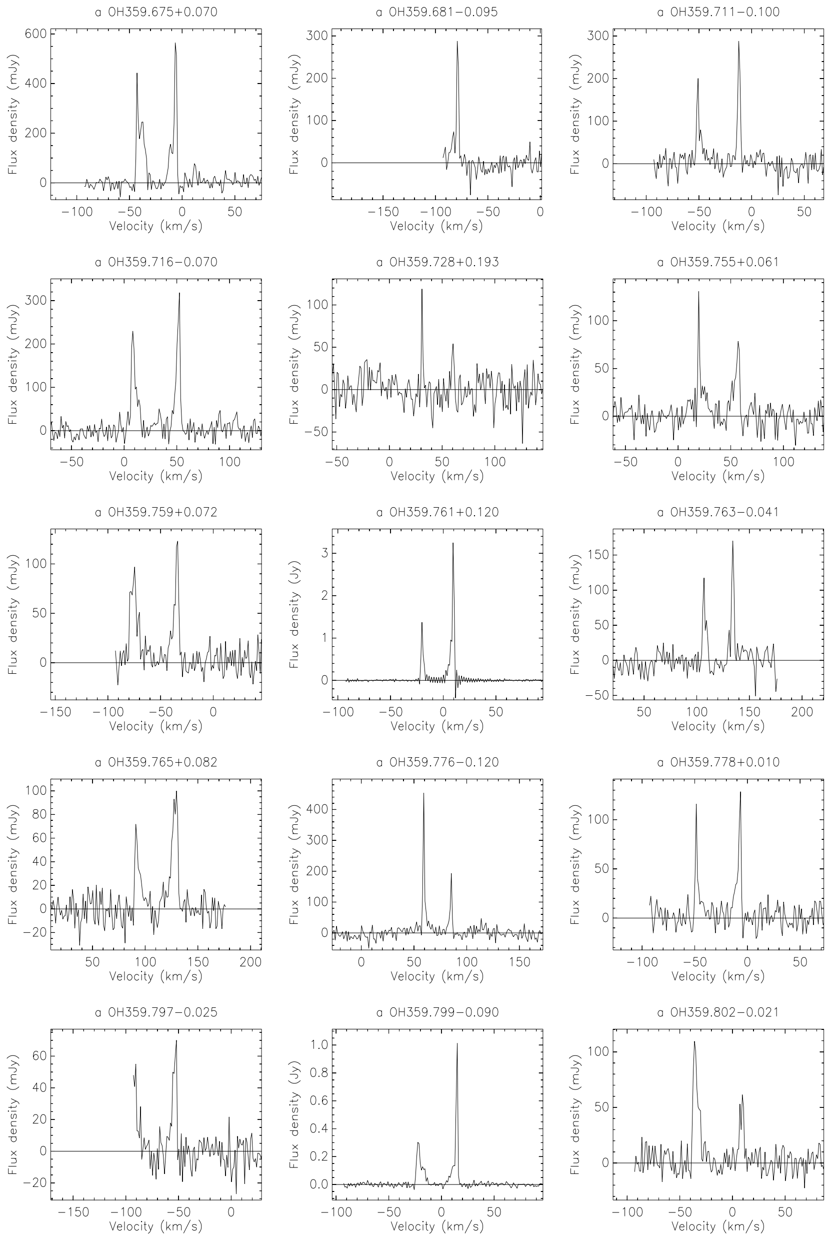

Figure 5.4 Multi-epoch averaged spectra from the VLA survey

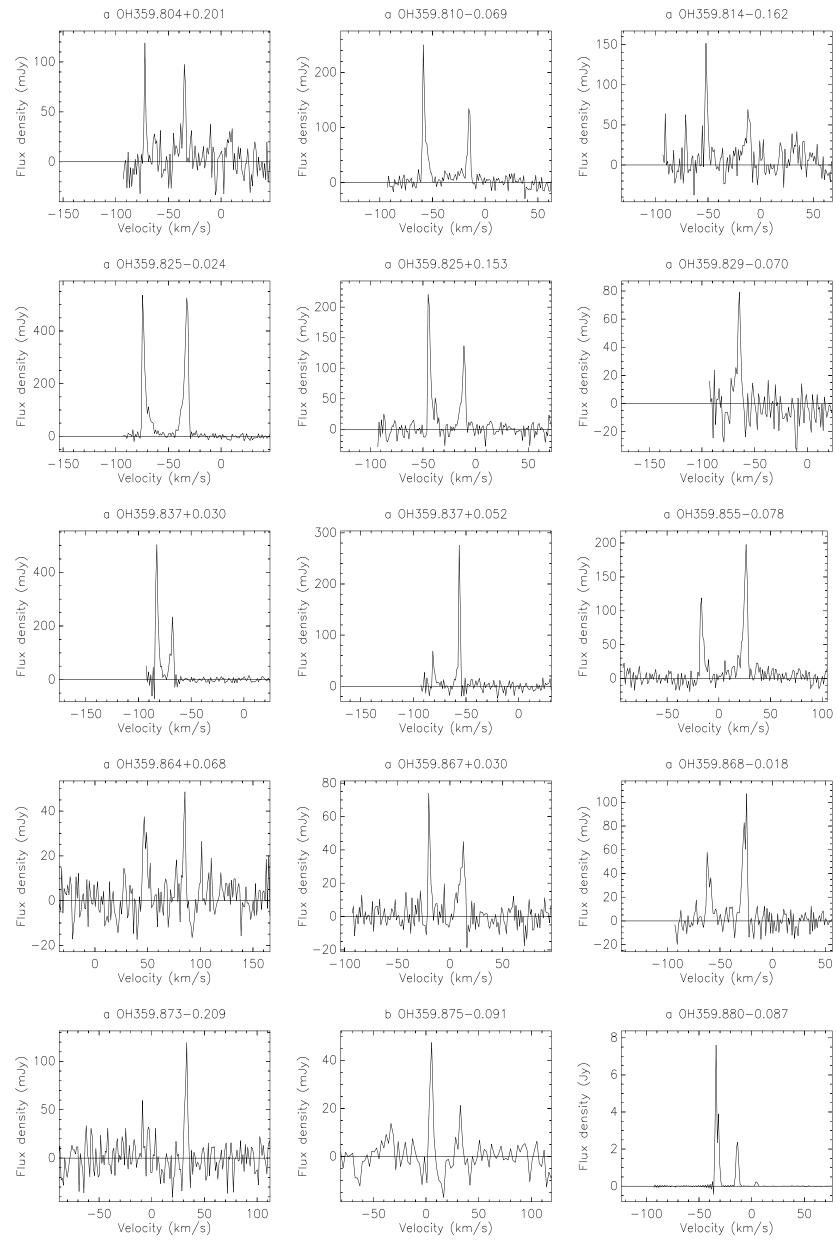

Figure 5.4 (continued)

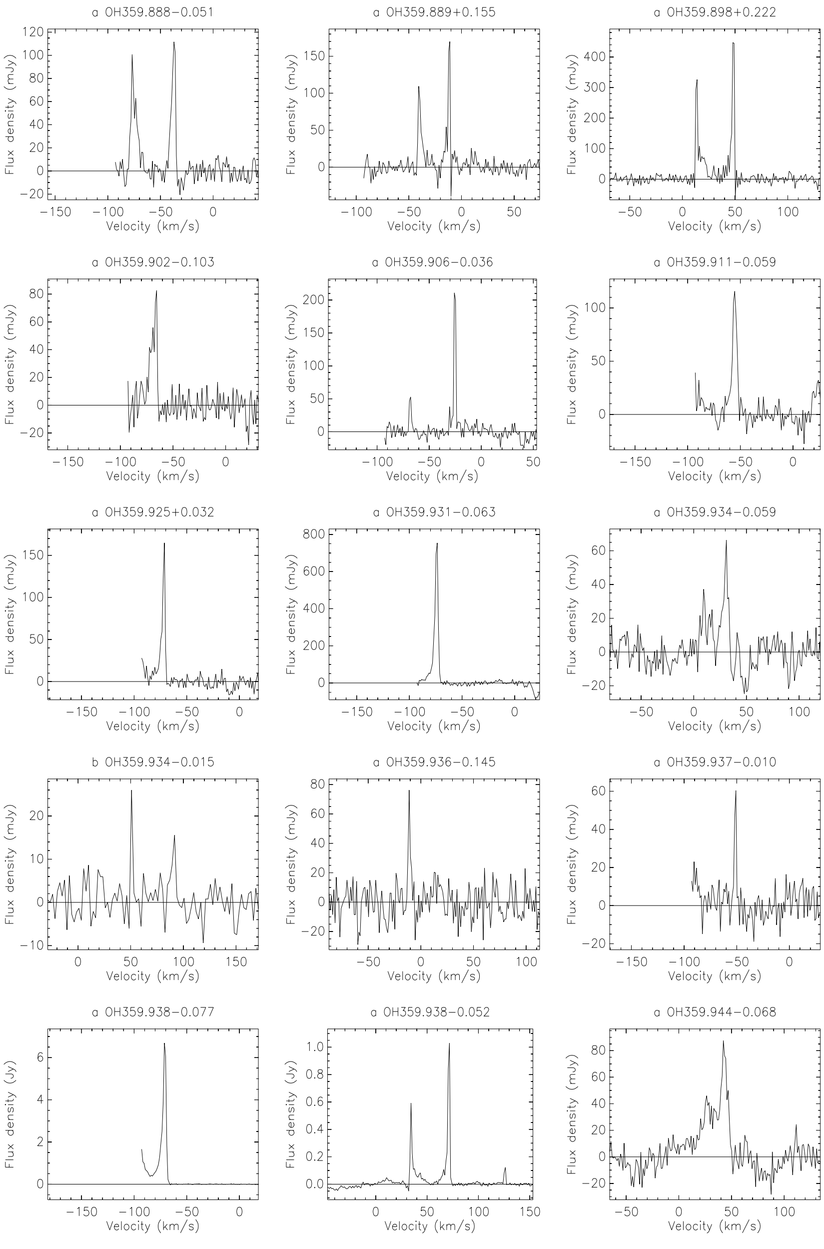

Figure 5.4 (continued)

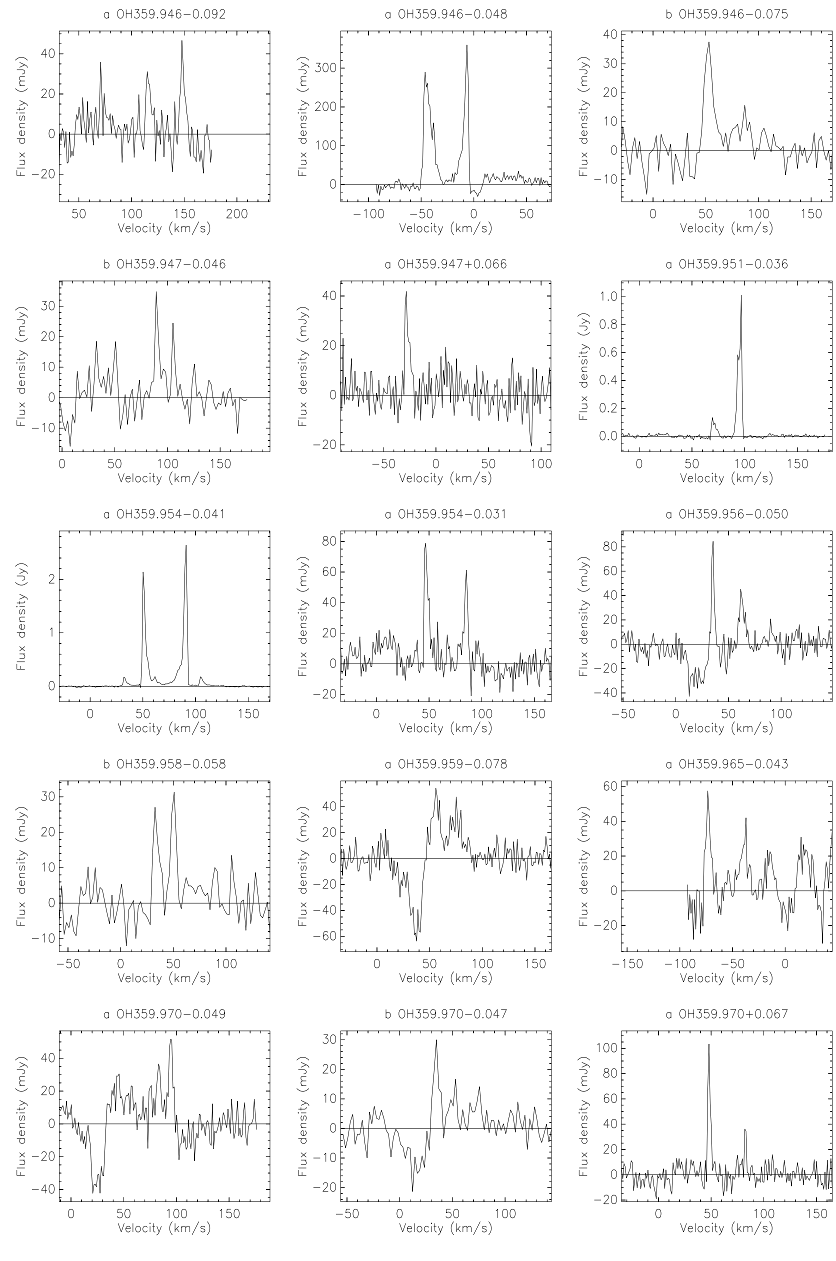

Figure 5.4 (continued)

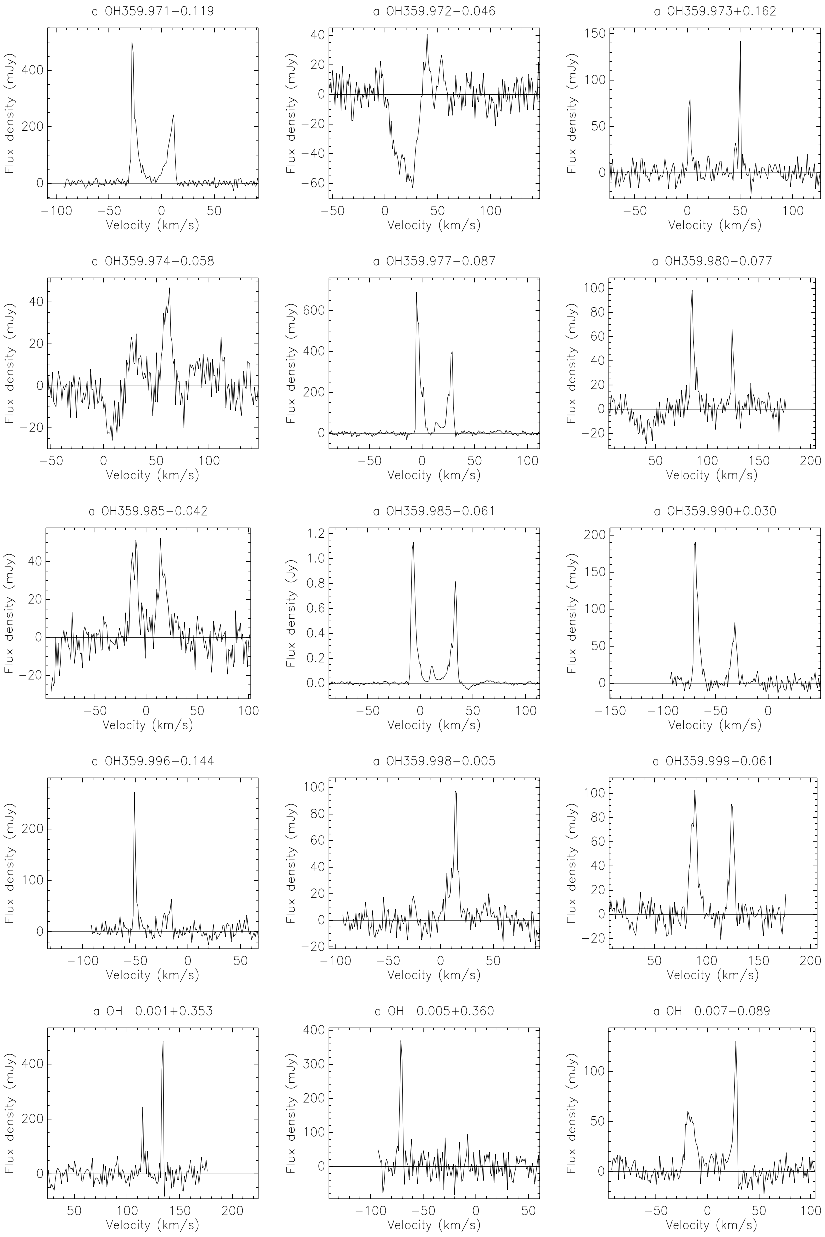

Figure 5.4 (continued)

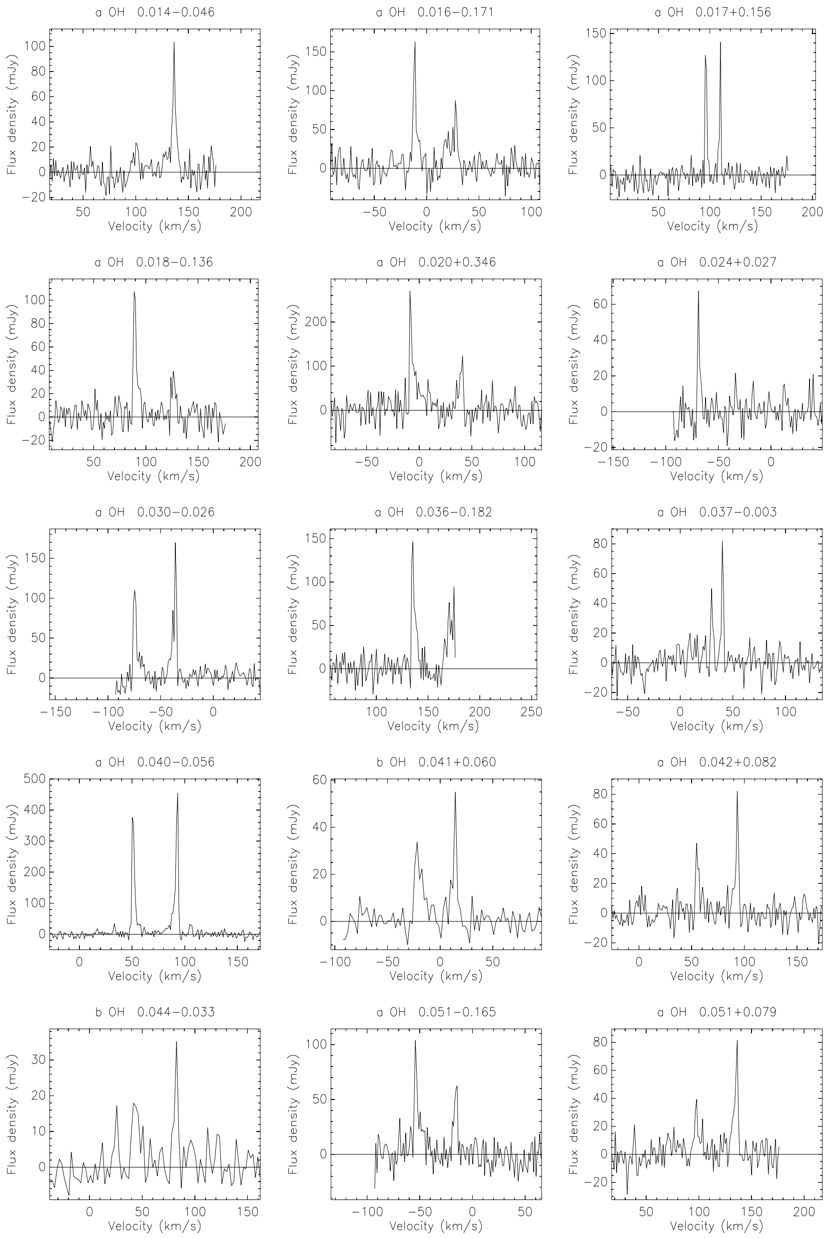

Figure 5.4 (continued)

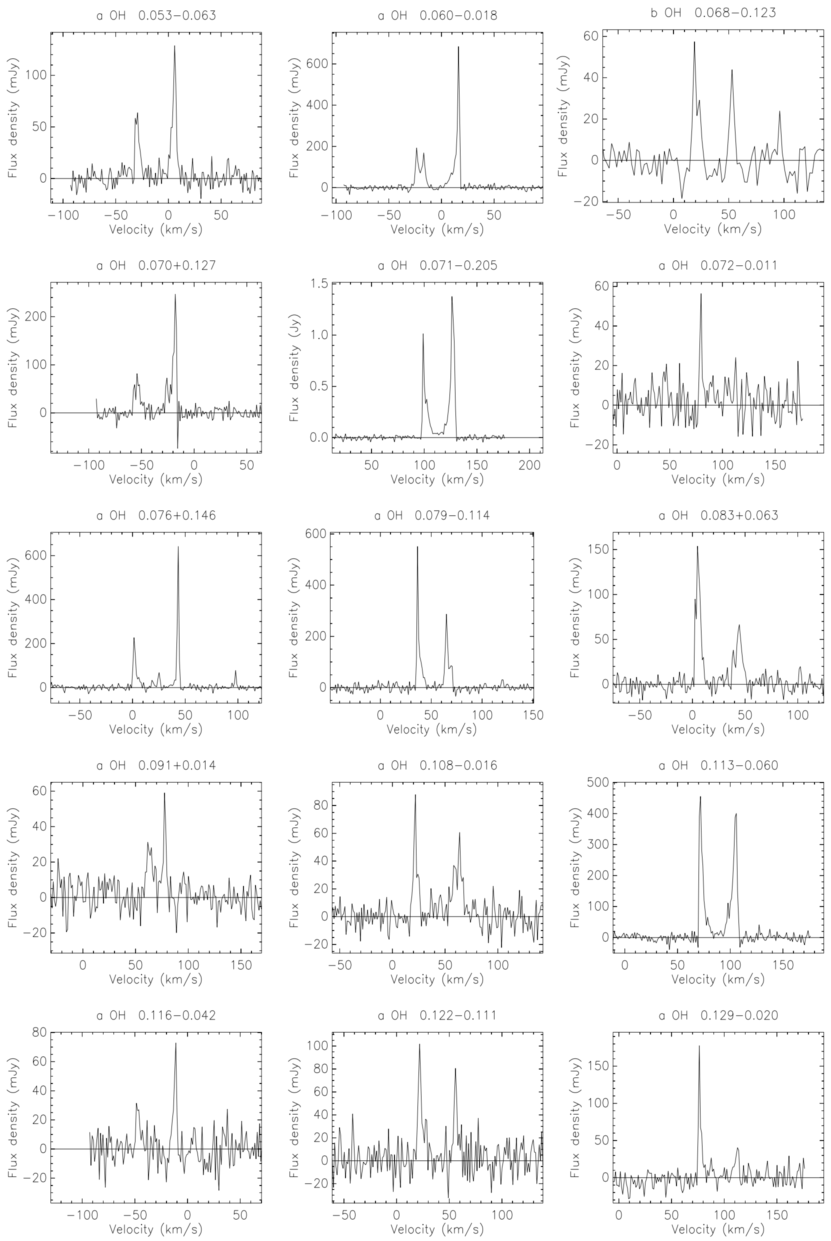

Figure 5.4 (continued)

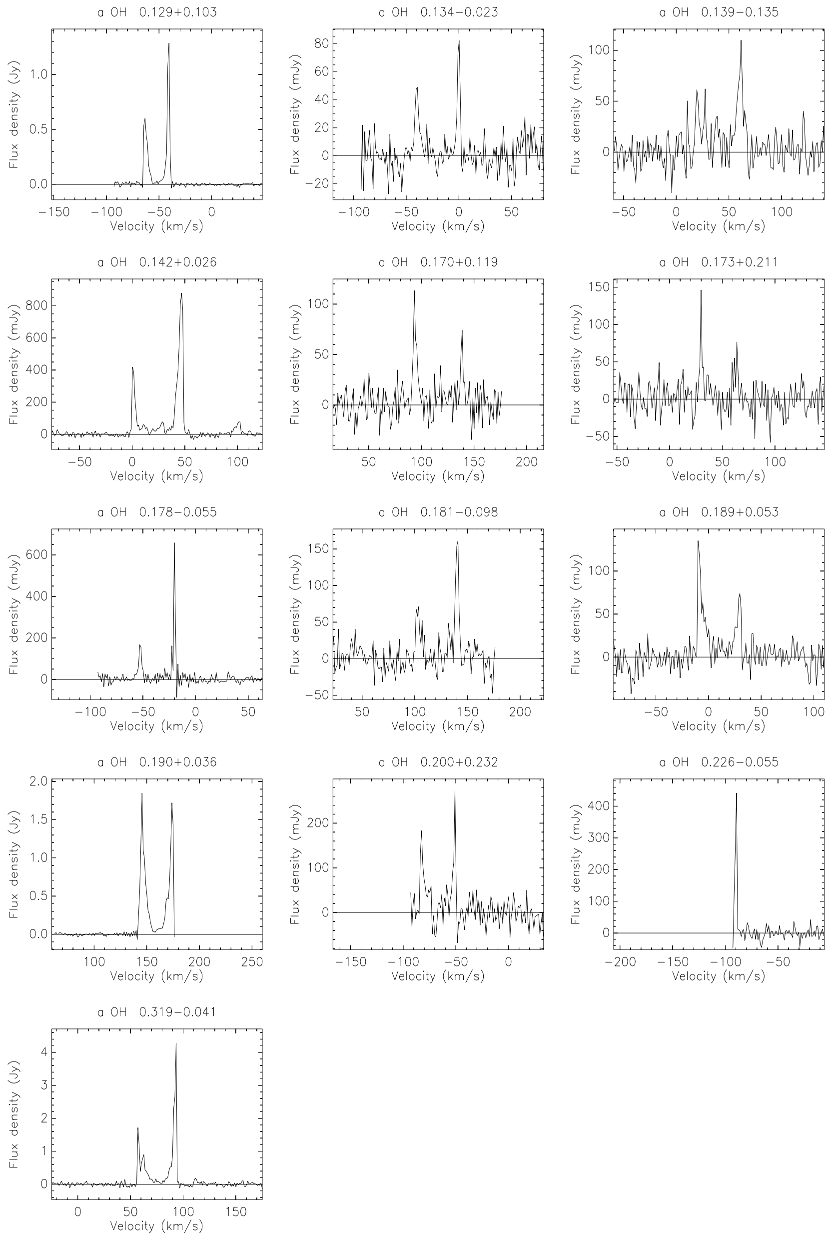

Figure 5.4 (continued)

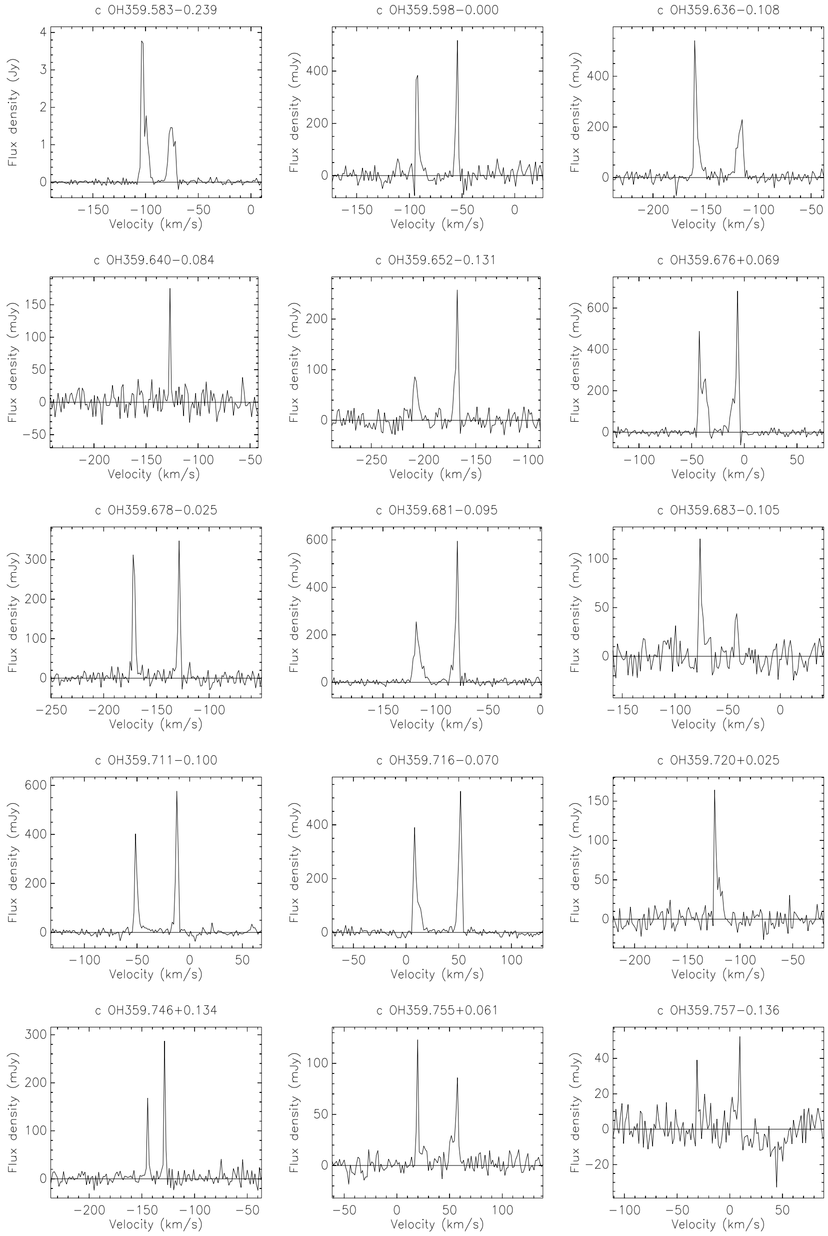

Figure 5.5 Spectra from the ATCA survey

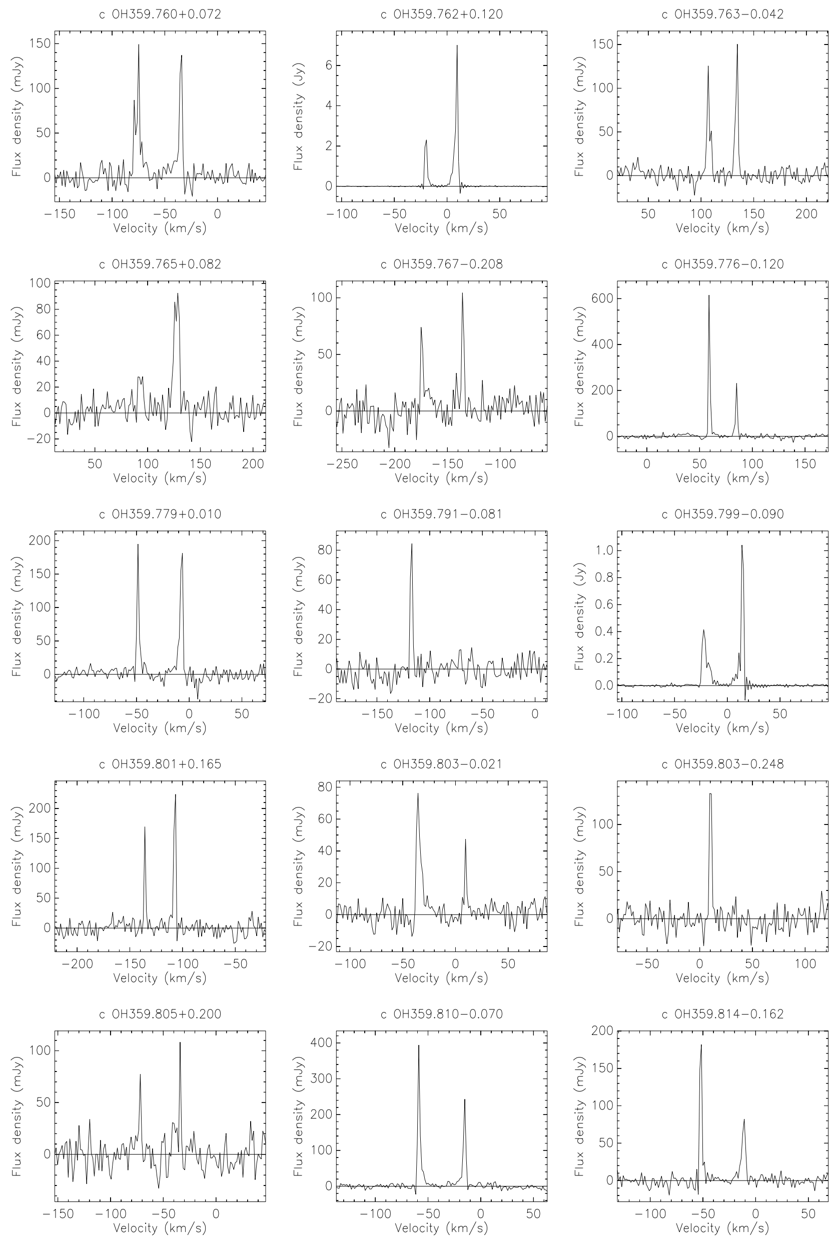

Figure 5.5 (continued)

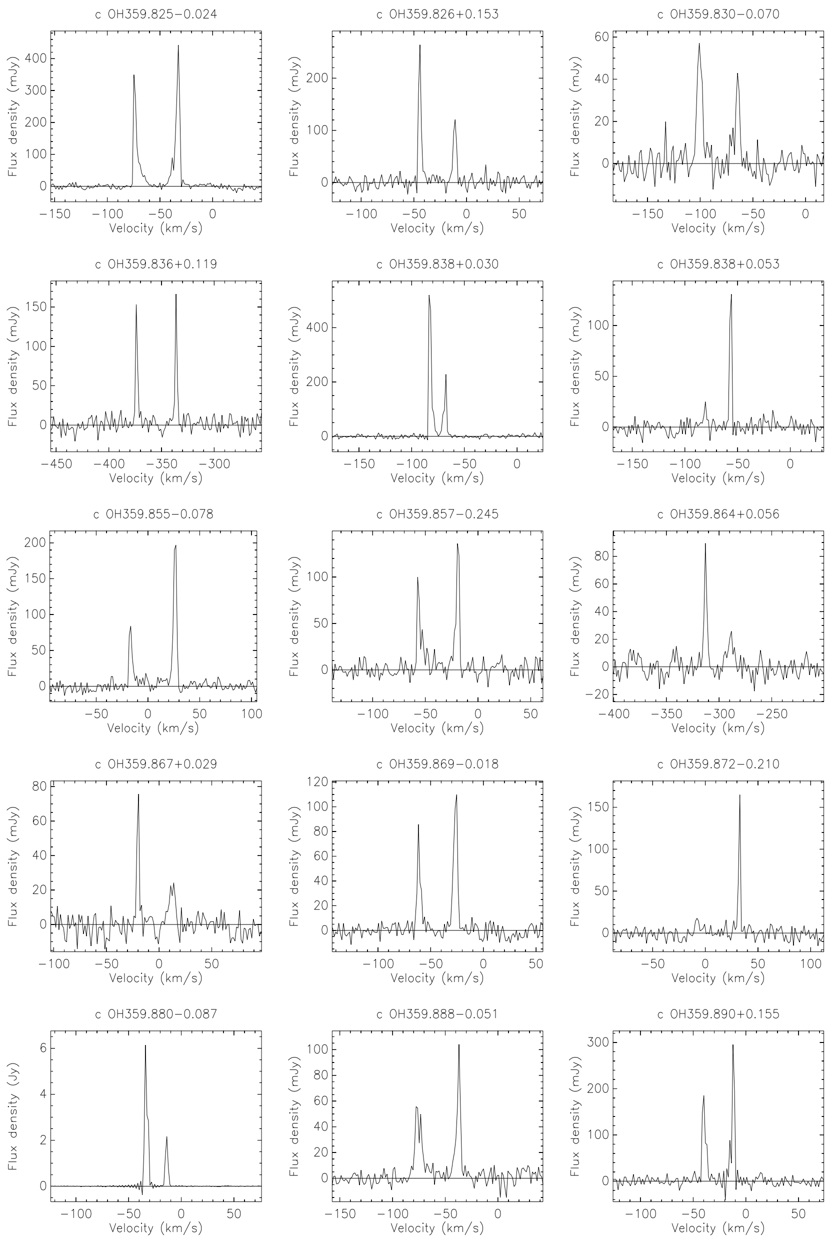

Figure 5.5 (continued)

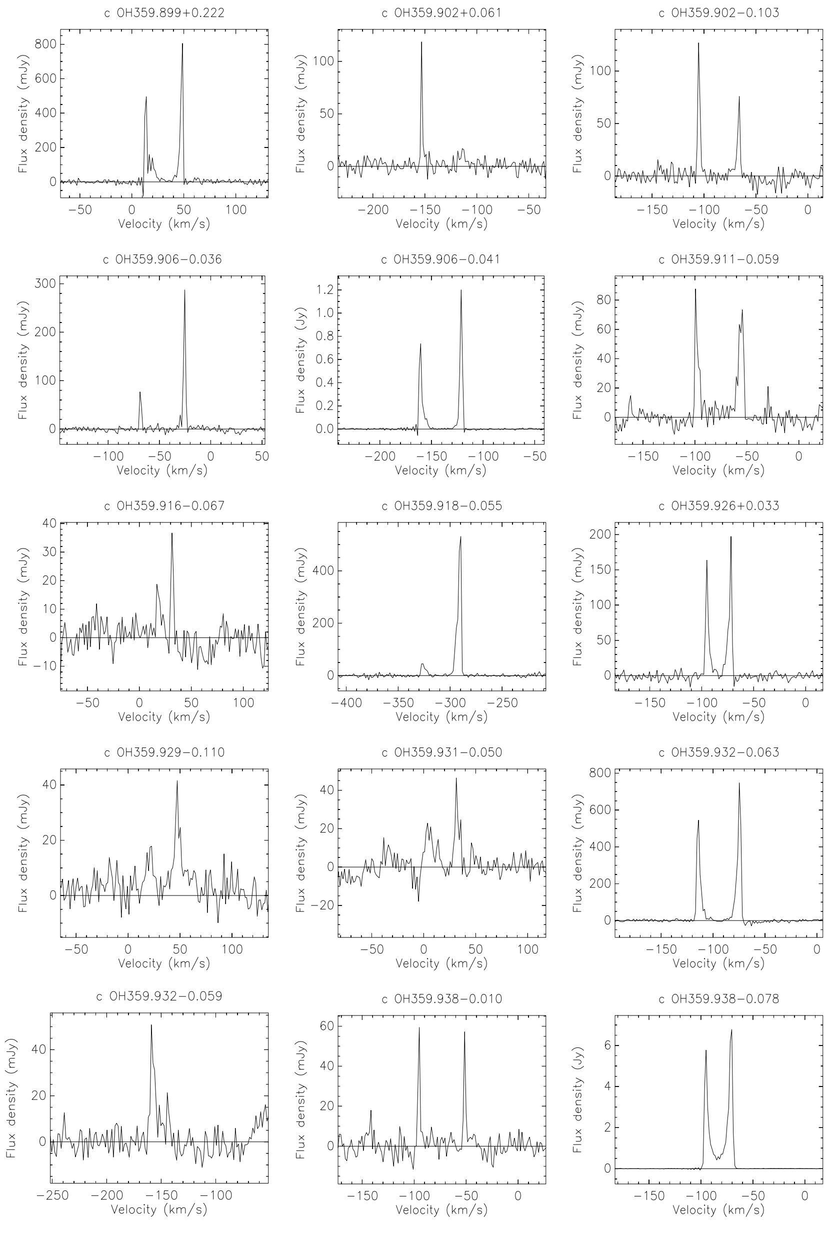

Figure 5.5 (continued)

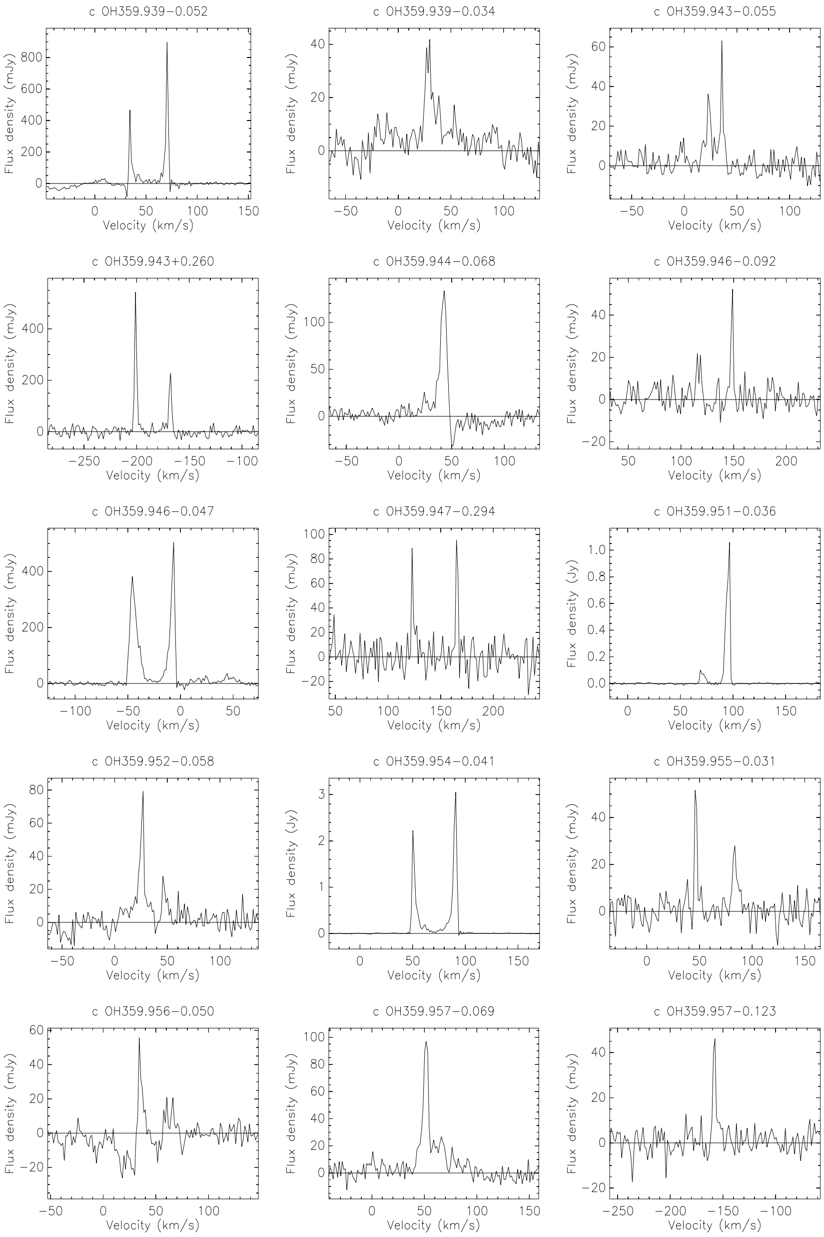

Figure 5.5 (continued)

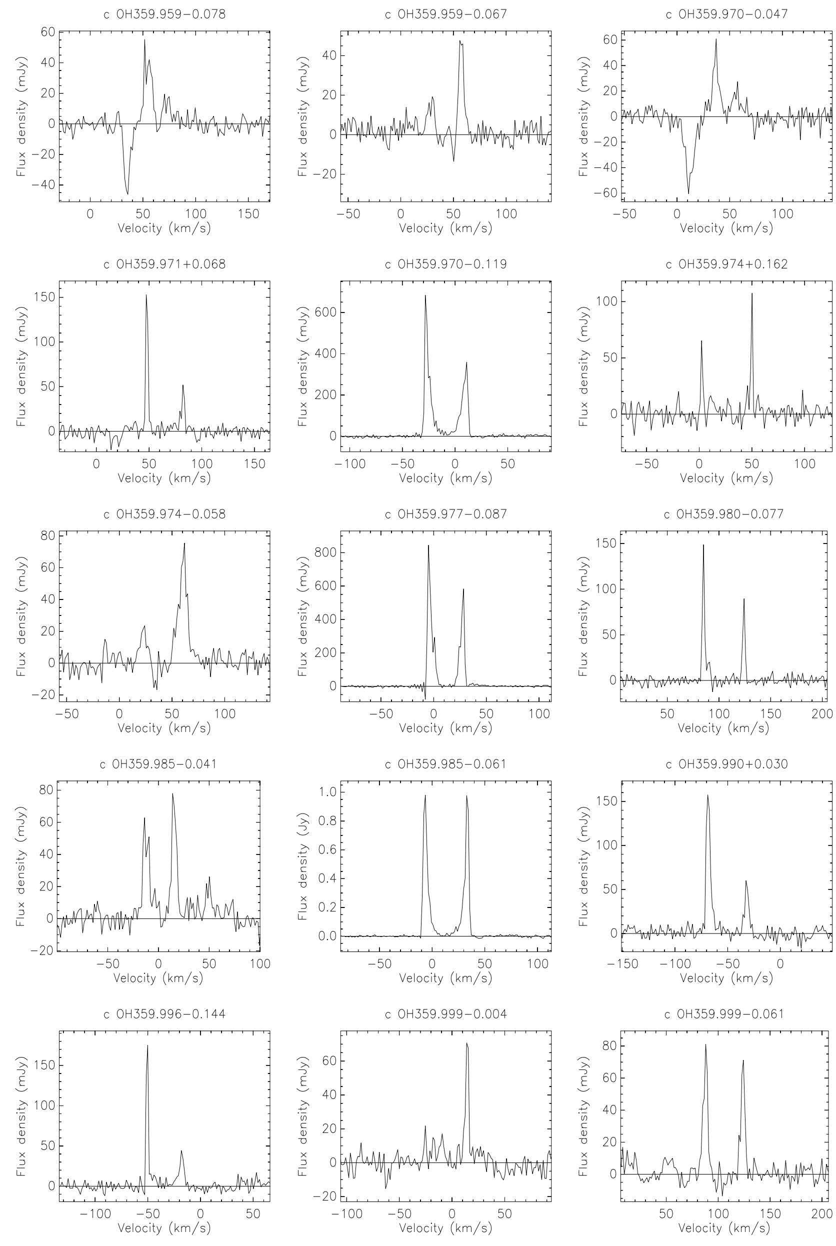

Figure 5.5 (continued)

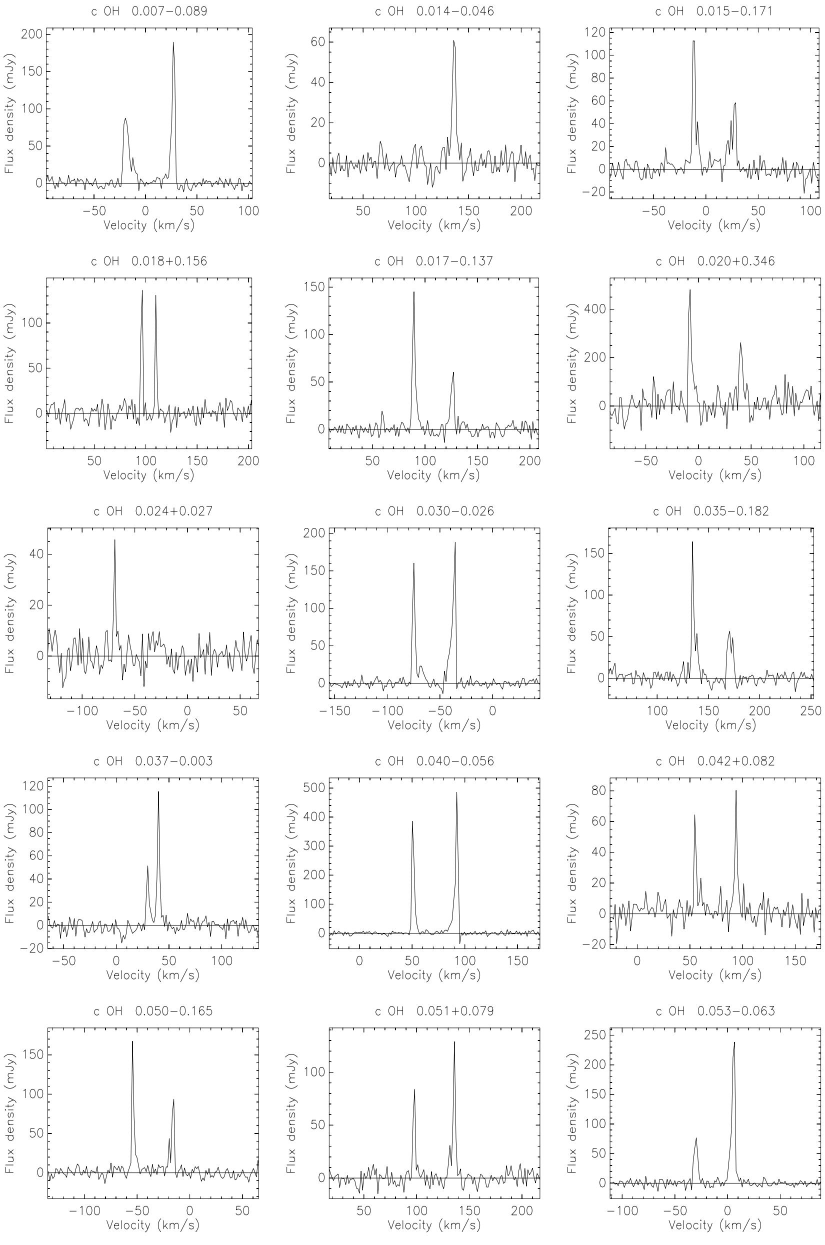

Figure 5.5 (continued)

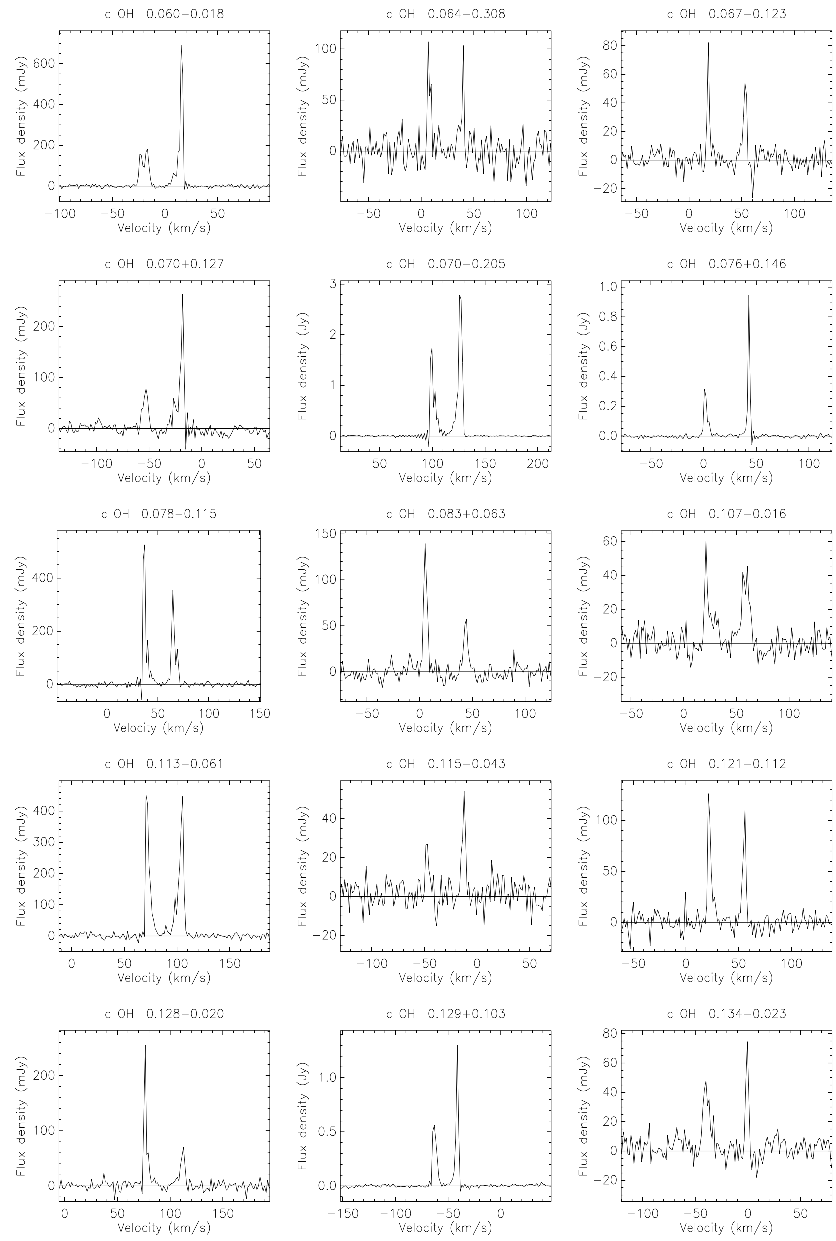

Figure 5.5 (continued)

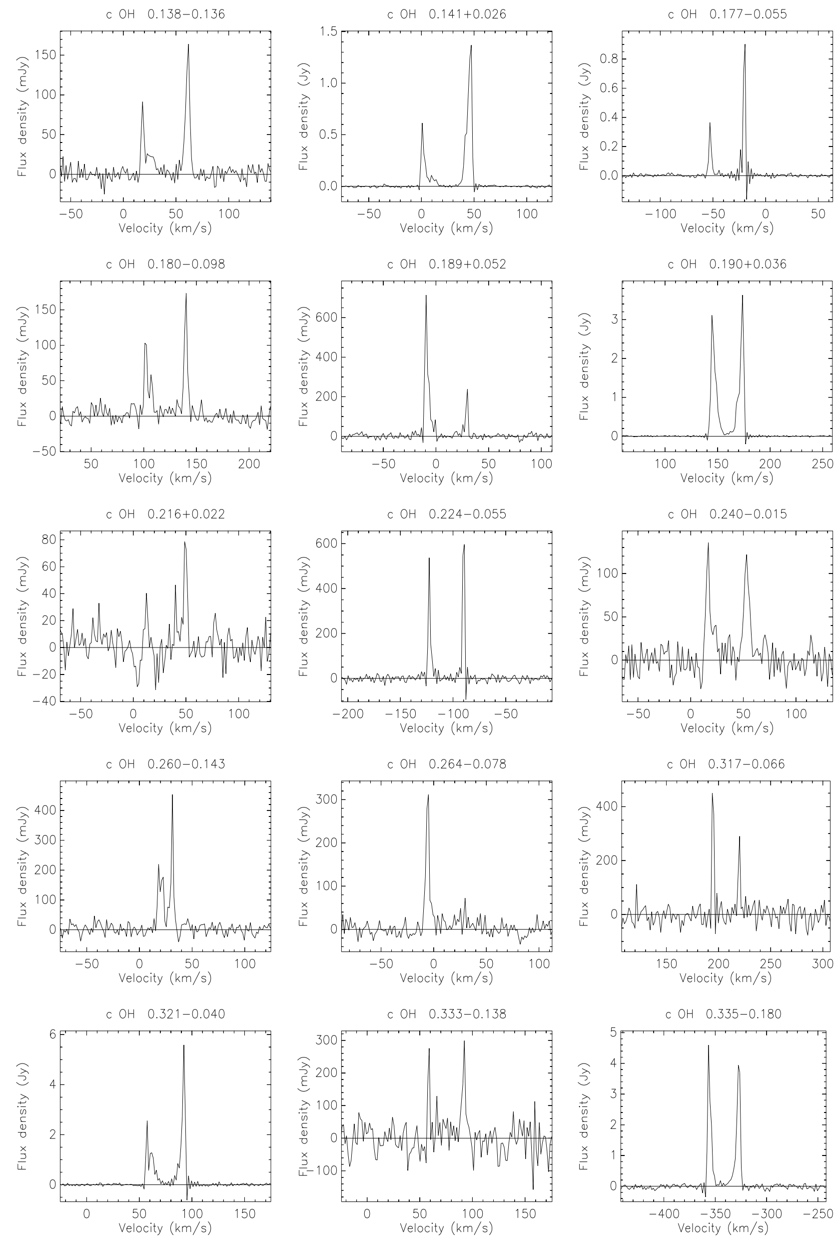

Figure 5.5 (continued)

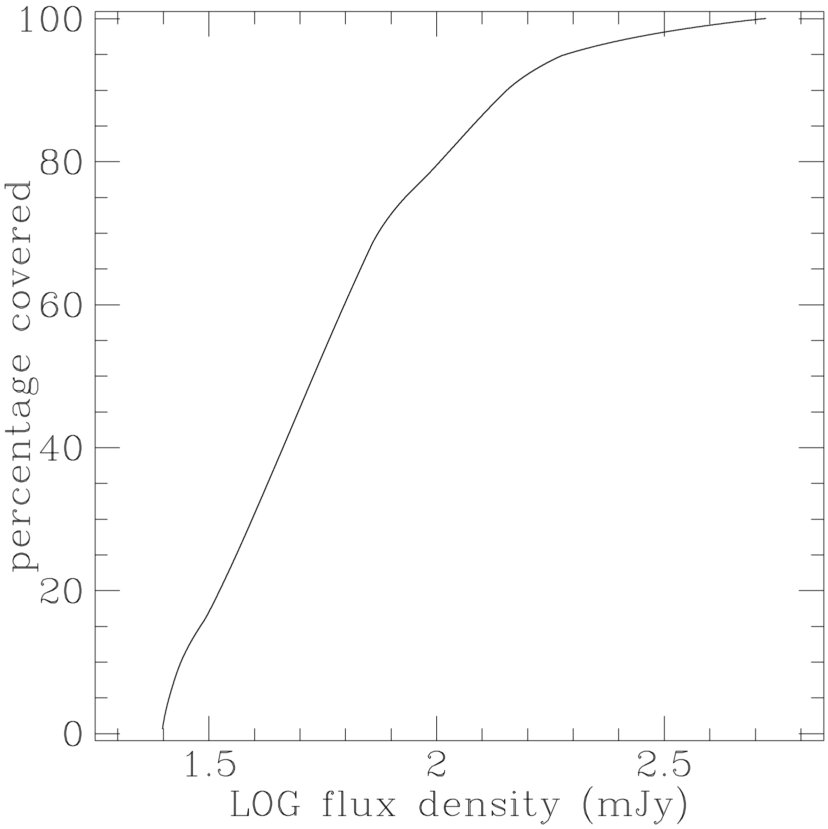

Figure 5.6 Sky sensitivity coverage. Shown is the fraction of the surveyed sky area for which we could have detected a source of given flux density. All sources with a peak flux density over 530 mJy must have been detected; for a homogeneous distribution one reads a detection rate of 80% of the 100 mJy sources and only about 20% of the sources around 30 mJy

5.4 Discussion

5.4.1 Completeness and sensitivity

Figure 5.1 shows approximate contours of the best sensitivity achieved in the survey. We use it to make an empirical estimate of the (in)completeness of the survey. The number of sources detected, as function of highest peak flux density, is corrected by dividing each source by the fraction of the surveyed sky

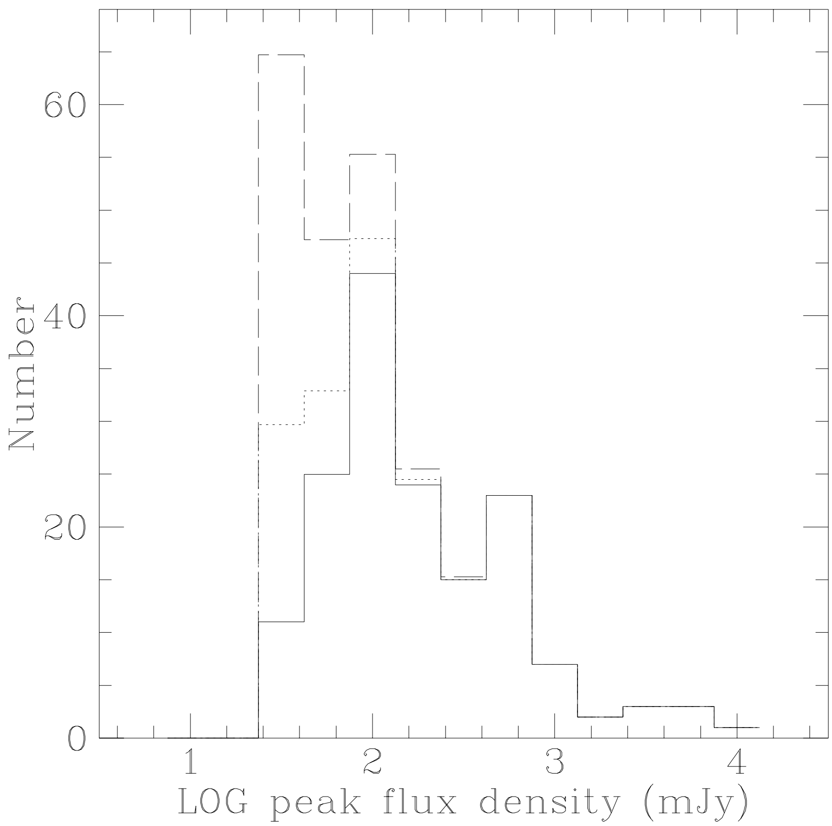

Figure 5.7 Number distribution of peak flux densities. The dashed line gives the distribution empirically corrected for incompleteness; it is however an overestimate (see text). For example, the dotted line shows the effect on the completeness correction, when the stars are spatially distributed according to an arbitrarily scaled surface distribution $\Sigma(R) \sim (R + R_c)^{-1}$

area in which it could have been found. Because the VLA and ATCA data sets have comparable spectral resolutions, we neglect the influence of channel width on the detection probability. The fraction as function of flux density can be found graphically in Fig. 5.6. It also shows that all sources with a peak flux density brighter than 530 mJy must have been detected (fraction = 100%, the empirical completeness limit of the survey; or more formally 390 mJy for 99%). If one would confine the area surveyed to the size of the fields used in Lindqvist et al. (1992a, 1997), i.e. 32′ squared, the completeness limit would be approximately 65 mJy. In Fig. 5.7 we display the number of sources with respect to the highest peak flux density, where we have given preference to the multi-epoch VLA over the one-epoch ATCA data. Because of the variable nature of the OH/IR stars, the distribution is somewhat broadened. By averaging the flux densities in the concatenated monitor data set, the effect should be smaller than in a single epoch observation. However, the exact amount of the broadening is very difficult to calculate, in particular with the mixed observations in this survey.

Strictly, this completeness correction is for a homogeneous number density distribution. As the OH/IR star distribution is concentrated toward Sgr A*, and thus toward the survey center, we expect (and find) the largest number of *faint* stars in the part of the survey that is most sensitive. Correcting parts of the survey that are less sensitive for these faint stars, just by a linear function based on the sensitivity or geometry of the area, would then assume that pointing the telescopes far away from Sgr A*, the detection probability of an OH/IR star is equal to the detection probability when pointing at Sgr A*. This would imply an overestimation of the completeness correction. We have tried to show this effect in Fig. 5.7, by also calculating a completeness correction for an assumed number density proportional to r^{-2}, corresponding to a surface distribution $\Sigma(R) \sim R^{-1}$ (Lindqvist et al. 1992b). It is evident that the magnitude of the effect depends on the actual concentration of stars; it cannot be extracted directly from our data.

5.4.2 Extended emission and absorption complex

Because of confusion at the location of the Sgr A complex, the survey is in practice less sensitive for detections than the actual instrumental response. As an example of the residual line emission, we show the central part of the "maxmap" of the ATCA survey in Fig. 5.8. Note the way the known OH/IR stars stand out with respect to the residuals. Recall that in this region a large continuum emission complex has already been subtracted. Most of the remaining line emission is located as separate spots in a ring-like shape at the inside of the supernova remnant that forms the eastern part of the Sgr A complex (e.g. Ekers et al. 1983; Pedlar et al. 1989). The few absorption measurements done in our data set, have not been explicit about the line-of-sight location of the spots with respect to the absorption and emission lines of the supernova remnant. The ring-like shape cannot be seen in individual or several consecutive frequency channels. The majority of the emission features have a velocity between 25 and 70 $\mathrm{km\,s^{-1}}$, placing them at, or close to either the '+50 $\mathrm{km\,s^{-1}}$' molecular cloud complex behind, or the 'streamer' molecular cloud complex G−0.02−0.07 in front of Sgr A* (Zylka et al. 1990). This

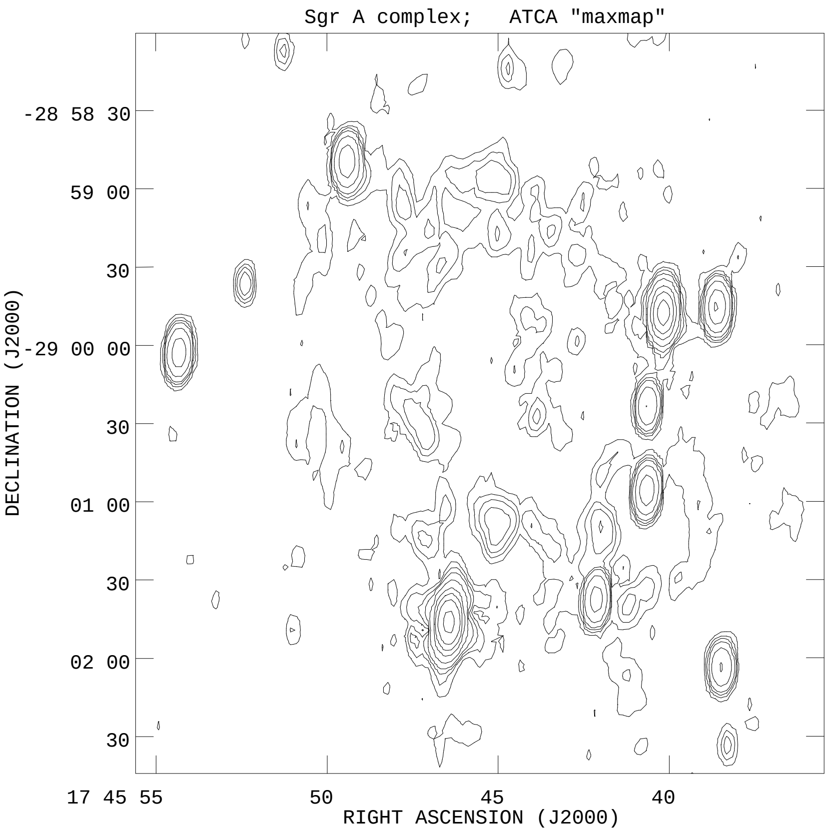

Figure 5.8 ATCA "maxmap" of the Sgr A complex. Contours are at 0.030, 0.050, 0.070, 0.100, 0.200, 0.500, 1, 2 and 5 Jy. Sgr A* is located in the middle of the right side of the image. The ring-like shape is due to Sgr A East and is not to be confused with the circumnuclear disk

emission may be indicative for shock fronts, where, on the near and far side of the expanding supernova shell, the shell and the molecular cloud complexes collide. This interpretation would support the recent results of the observation of shock-excited 1720 MHz OH masers by Yusef-Zadeh et al. (1996). In this region, the baselines against which we try to find double peaked OH sources are mostly irregular and make searching difficult. However, because the velocity characteristic is obvious, it is relatively easy to recognise these sources; listing all of them as single – sometimes double – peak detections, on the other hand, has not been the purpose of this survey.

Besides OH emission, the presence of OH molecules also give rise to areas of 1612 MHz absorption, which are not visible in Fig. 5.8 because of the "maxmap" procedure followed. We have similar "minmaps" with the detection of 1612 MHz OH absorption. Apart from the supernova remnant and other distinct regions, it is seen most pronounced in the core of the G−0.13−0.08 molecular cloud. The absorption at +24 km s^{-1} coincides with the densest NH_3 concentration in the GC, that is known to host an ultra-compact HII region, and is very close to two H_2O masers (e.g. Güsten & Downes 1983; Okumura et al. 1989). With a projected distance of only 10 parsec from Sgr A*, it is a perfect candidate cloud to investigate present-day star formation in the GC.

5.4.3 Remarks on individual sources

Current catalogs on OH/IR stars in the GC can be found in the appendix. When reference data is taken from LWHM, Te Lintel Hekkert et al. (1989; hereafter TLH) and Van Langevelde et al. (1992a), we (re)confirm 87 of the 89 sources that should have been visible in the ATCA data set. In the VLA data set, 67 of the 71 sources are found. An additional 3 sources, that are not (but should have been) seen in the VLA data, are confirmed in our ATCA image cube. We also confirm 4 out of 5 single peak detections of LWHM; 3 of which turn out to have a definite double peaked nature. Unconfirmed from previous surveys in the OH 1612 MHz maser line remain 4 sources: OH359.669−0.019, OH 0.204+0.056 plus the single peak OH 0.147+0.062 from LWHM, and the double peaked source OH359.897−0.065 from TLH (see the appendix for two more non-confirmed TLH sources outside this survey).

Summarising the new detections, we find 65 previously unknown double peaked and 3 single peaked OH 1612 MHz masering sources in the VLA and ATCA surveys. We count a total of 52 previously unknown OH/IR stars. Based on a more careful examination of spatial extension and the spectral shapes, we suspect 13 detections to be molecular clouds resembling OH/IR star spectra. We confirm that all three previously known high-velocity OH/IR stars, as well as one newly found high-velocity source, are blue shifted with an absolute line-of-sight velocity exceeding 250 km s^{-1}. Because of being detectable in only one survey, we were not able to confirm 15 VLA and 11 ATCA suspected OH/IR stars ourselves. Some of these sources have, however, been detected in the infrared.

Non-detections

We did not confirm OH359.897−0.065 (TLH number 175); neither did LWHM. We should have seen it in the ATCA data, even when the radiation would have been in its minimum. Considering the flux density and spectrum given by Habing et al. (1983), we conclude that OH359.897−0.065 is not a real OH/IR star. Yet, one or a couple of false detections do not alter the dynamical conclusions discussed in the Habing et al. (1983) paper, or in any following article using this data point.

OH359.669−0.019: LWHM report a highest flux density of 0.09 Jy, which is, adjusted for the primary beam attenuation, just above our detection limit. We may have been unlucky to observe with the ATCA close to the minimum of its radiation. The source lies outside our VLA survey.

OH 0.147+0.062: As opposed to the other single peaks found by LWHM, for which we found a secondary peak in both surveys, this single peak has not been detected here. No counterparts were found in the literature in any other maser line or in the infrared.

OH 0.204+0.056: This source lies close to the edge of the survey. LWHM report a highest peak flux density of 0.11 Jy, which makes it only half of our detection threshold. The source is not covered by our ATCA survey.

Detections

Generally, the 'overlapping' sources – i.e. sources that are in the spatial and velocity domain of both the VLA and ATCA data sets – are detected in each data set. The main cause of 'overlapping' sources being detected in only the VLA data is overall sensitivity (i.e. mean flux density over several epochs); the ATCA observations were apparently done when the star was close to its minimum, and the OH maser flux density therefore below the detection limit. Backwards, sources detected only in the ATCA data are either outside the VLA cube, or the ATCA observations were apparently done when the star was close to its maximum, and the OH maser flux density therefore was larger, and above the detection limit, in contrast to the mean flux density. Following we make individual remarks on a small selection of the sources, where we use the abbreviation RR for sources in, or the paper by Rieke & Rieke (1988).

OH359.791−0.081: Single peak, but most likely of stellar origin because it coincides with a long period K-band variable (I.S. Glass, pers. comm.).

OH359.797−0.025: Either a low expansion velocity source, or the red shifted peak of a double peaked source. Not seen in the ATCA data, but the flux and shape justify its entry. Note that although we give a value for the blue shifted velocity, we cannot distinguish between a second peak and a possible effect of the end of the frequency band.

OH359.804+0.201: Listed as single peak in LWHM.

OH359.837+0.052: Listed as single peak in LWHM.

OH359.864+0.056: The only new source for which the absolute stellar velocity exceeds 250 km s^{-1}.

OH359.906−0.036: Coincides with, and matches the velocity of source #49 in RR. As for all other cases where we find an infrared counterpart for our OH maser sources, we claim the OH and infrared emission to originate from one (stellar) source.

OH359.936−0.145: Found as single peak by LWHM. Most probably double with the second peak at +13 km s^{-1}, but we cannot confirm this; the source is not detected in our ATCA data.

OH359.939−0.034: RR report a source (#32) with a velocity of −14 km s^{-1}. Our velocity measurement of +42 km s^{-1} is within three times their RMS of 20 km s^{-1}. Taking into account the spatial extension of the emission, we are however tempted to attribute the OH emission to molecular clouds on the line-of-sight. If one supposes the velocity of RR is very accurate, one can argue that source #32 can be seen in the OH spectrum with two peaks of $\approx$ 15 mJy, separated by about 10 km s^{-1}.

OH359.943−0.055: Matches the velocity of the nearby source GCIRS 19 (Sellgren et al. 1987; source #22 in RR), but we doubt the identification as such. Besides, GCIRS 19 is classified as probably being a supergiant (most recently by Blum et al. 1996), for which one would expect a shell expansion velocity larger than the 6.5 km s^{-1} found here.

OH359.947−0.046: Although our absolute positions are not expected to be very accurate (see Sect. 3.1), our VLA position for this source agrees within one arcsecond of the position of GCIRS 5. The velocity measured matches the one given in Krabbe et al. (1991) and Haller et al. (1996). We propose this source to be the OH counterpart for GCIRS 5. Note that the OH maser reveals a low shell expansion velocity, hinting toward a low metallicity, and low mass AGB star.

OH359.954−0.041: The clearest example of interesting spectral structure seen in some (of the stronger) OH/IR stars in the GC. We discuss these peculiar spectra further in Sect. 4.5.

OH359.956−0.050: Found as an H_2O maser by Levine et al. (1995) and Yusef-Zadeh & Mehringer (1995). Its nature – a young, massive supergiant or an evolved, intermediate mass AGB star – has been extensively discussed in Chapter 2. The AGB nature of this object, identified with GCIRS 24 as its infrared counterpart, has been supported recently by Blum et al. (1996), and was initially motivated by Sellgren et al. (1987).

OH359.957−0.123: A single peak detection, but probably stellar: it has been identified with a long period K-band variable (I.S. Glass, pers. comm.).

OH359.965−0.043: The SIMBAD data base reports this position to be close to the position of IRC−30321. However, the error in the position of IRC−30321 is large ($\sim 1'$) and we therefore find it more likely that IRC−30321 coincides with one of the other nearby luminous (previously known) OH/IR stars instead.

OH359.970−0.049: On top of the extended emission we find a double peaked point source. It has most probably been detected by LWHM as their source #69. LWHM apparently mistook a peak of (the molecular cloud) OH359.970 −0.047 as their secondary peak velocity, resulting in a relatively high value for the shell expansion velocity. More likely than OH359.970−0.047, this source seems to be related to source #38 in RR. They give a velocity of 109 $\mathrm{km\,s^{-1}}$ with an RMS of 20 $\mathrm{km\,s^{-1}}$ where we measured 89 $\mathrm{km\,s^{-1}}$.

OH359.971+0.068: Listed as single peak in LWHM.

OH359.980−0.077: Found as an H_2O maser by Yusef-Zadeh & Mehringer (1995), but in fact an OH/IR star; see discussion in Chapter 2.

OH359.985−0.042: RR found a source (#51) at −55 $\mathrm{km\,s^{-1}}$, three times their RMS away from our velocity. However, we are confident that the identification of the OH source with source #51 in RR fits.

OH359.990+0.030: This source lies close to IRAS 17423−2855. Te Lintel Hekkert & Chapman (1996) searched IRAS 17423−2855 for OH emission, but did not find it because of a noise level of 440 mJy. The position of OH359.990+0.030 is however more than $20''$ off from the positions given for several possible near-infrared counterparts for IRAS 17423−2855 in Monetti et al. (1992). Although IRAS 17423−2855 can also be interpreted as an ultra-compact HII region, the association with double peaked OH emission is more convincing for a (post-)AGB object (e.g. Volk & Cohen 1989; Monetti et al. 1994; Te Lintel Hekkert & Chapman 1996).

OH 0.001+0.353: A source named OH359.984+0.349 in TLH (#155), observed by Habing et al. (1983) with the 100m single dish telescope in Effelsberg (Bonn). We confirm the position measured by LWHM; it differs about one arcminute from the position quoted in TLH.

OH 0.005+0.360: Because of its spectral shape and because it is not spatially resolved, we suspect this source to be the red shifted peak of a double peaked OH/IR source.

OH 0.014−0.046: Close to, and maybe related to the infrared source GCS 6 in Kobayashi et al. (1983).

OH 0.053−0.063 and OH 0.060−0.018: The former was marked by LWHM as detected by Winnberg et al. (1985); it should have been the latter.

OH 0.064−0.308: Located near a compact HII region (#16 in Downes et al. 1979).

5.4.4 Comparison with known OH/IR stars

The OH/IR stars found for the first time in this survey have less luminous OH masers in their circumstellar shells compared to the previously known OH/IR stars in the GC. In this section we argue that the newly found stars are of similar nature to the ones previously known. This result was used in Chapter 2.

5.4.4.a Spatial and kinematic distribution

Figures 5.2 and 5.3 show the spatial and kinematic distribution of the known and previously unknown OH/IR stars detected in this survey. It is clear in Fig. 5.2, that the more luminous OH masers, generally the known OH/IR stars, can also be detected further out from the survey center. The fact that there are more stars at positive latitude offsets is an effect of the asymmetry in the survey pointing. Where the survey is sensitive enough, one sees that there is no preferred, and no distinct location for each of the samples. However, we make the observation that the alleged void of known OH/IR stars at small positive longitudes and small positive latitudes, does not comply with the combined sample. Furthermore, a comparison of the location of stars in Fig. 5.2 and Fig. 5.3 between both samples also suggests a similar distribution in phase-space.

5.4.4.b Expansion velocity distribution

To argue further that the samples consist of the same type of stars, we show the distributions of the shell expansion velocity in Fig. 5.9. Both samples[2] have shell expansion velocities sharply peaked around 19 $\mathrm{km\,s^{-1}}$. Expansion velocity distributions for many other samples of OH/IR stars can be found in the literature, e.g. Eder et al. (1988), Te Lintel Hekkert et al. (1991) and Wood et al. (1992). We want to restrict ourselves by comparing the expansion velocities of the OH/IR star in the GC with samples of the Galactic plane (Blommaert et al. 1993, 1994) and the Galactic bulge (Sevenster et al. 1997).

The distribution of the OH/IR stars found in the Galactic plane is also shown in Fig. 5.9. The distribution for the Galactic bulge has its peak around 15

[2]Note that we do not include all stars found in the whole GC region in our analysis; only the stars detected in this survey.

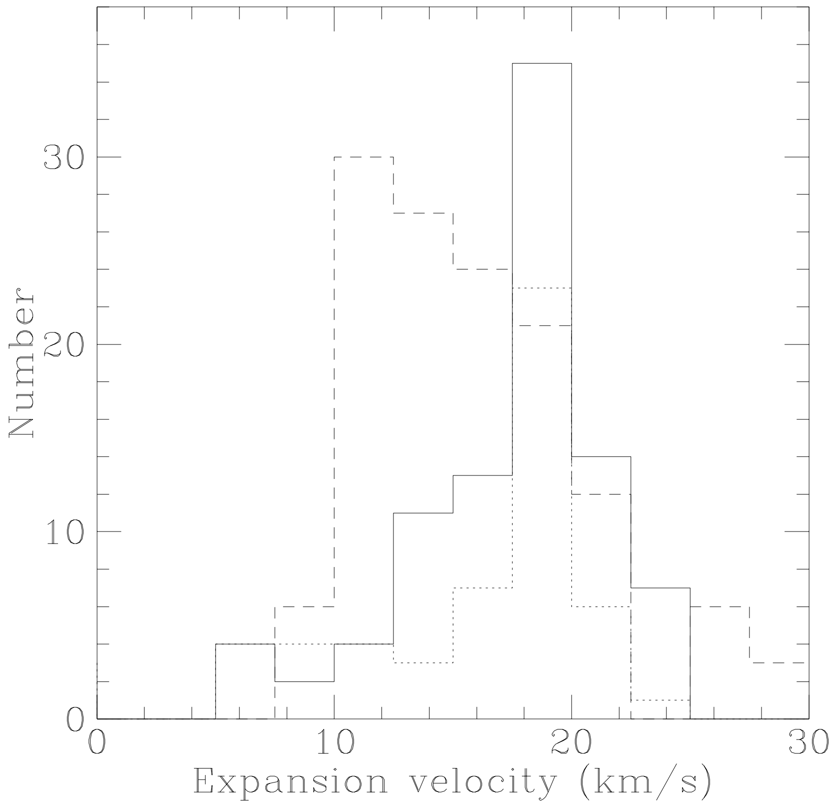

Figure 5.9 Expansion velocity distribution. The solid line is the distribution of previously known OH/IR stars in our survey, new detections are distributed according to the dotted line. The striking resemblance of both distributions is in large contrast to the expansion velocity distributions of OH/IR stars with a different metallicity, for example in the outer Galaxy and Galactic plane (dashed: Blommaert et al. 1993 plus Blommaert et al. 1994, multiplied by three for display purposes)

$\mathrm{km\,s^{-1}}$, and is broader than for the GC (see Sevenster et al. 1997). When comparing the expansion velocities of the OH/IR stars in the GC with the ones in the Galactic plane and bulge, we reach two conclusions. First, the expansion velocity distribution in the GC is different from the expansion velocity distribution of any other sample known, which we attribute to generally higher metallicities in the GC (see the discussions in e.g. Wood et al. 1992, Blommaert et al. 1994 and Habing 1996). Second, we note the striking resemblance of the expansion velocity distribution of the known and the previously unknown OH/IR stars in this survey, and argue for generally *identical* metallicities for both of our samples. Hence, as the shell expansion velocity is a function of metallicity and stellar luminosity, we conclude that the stellar luminosity distribution for both of our samples is identical; as far as we can tell, the central stars are the same.

5.4.4.c OH maser luminosity function

Because both the known and previously unknown OH/IR stars are intrinsically identical, we can investigate the combined OH luminosity distribution. Figure 5.10 shows the result when we assume that all stars are located at a distance of 8 kpc. That the new detections are mainly the low OH luminosity sources can be seen readily from the difference in the total distribution and the known OH/IR star distribution. Also shown is the *maximum* extent of the distribution when it is corrected for (in)completeness. We calculated this correction by weighing each source by the inverse of its detection probability and assuming a homogeneous number distribution.

Again, this correction is an overestimate. Unfortunately the number of sources with respect to the corrections at the left-hand side of the luminosity distribution is small. In general these are the sources with a low peak flux density for which the survey is not complete. It prevents us to derive a firm conclusion about a possible low luminosity cut-off in the OH maser distribution. We can however state, that the distribution peaks at $L_{\mathrm{OH}} \approx 10^{43.4}$ photons per second within the statistical errors.

5.4.5 Triple and quadruple maser lines

In Sect. 4.3 we mentioned non-standard spectral structure seen in OH359.954 −0.041 (a category 1 OH variable in vLJGHW). Less clear examples, both variable (category 1, 2) and non-, or irregularly variable[3] (category 3) sources, are OH359.675+0.070 (cat. 2), OH359.879−0.087 (cat. 1), OH359.938−0.052 (cat. 2), OH 0.040−0.056 (cat. 3), OH 0.076+0.146 (cat. 1), OH 0.083+0.063 (not monitored), OH 0.142+0.026 (cat. 1) and OH 0.319−0.041 (cat. 3). The masers in OH359.954−0.041 and OH 0.040−0.056 are quadruple peaked, the rest are triple peaked. In addition to the 'a' spectra in Fig. 5.5, Fig. 5.11 shows the lower frequency resolution spectra measured in image cube 'b' for four of these stars. We have only seen this type of spectra in the concatenated data; spectra with *regular* additional emission features at roughly either 15 or

[3] However, OH 0.040−0.056 and OH 0.079−0.114 were found to be regularly variable in the infrared by Jones et al. (1994). OH 0.319−0.041 was not in their sample.

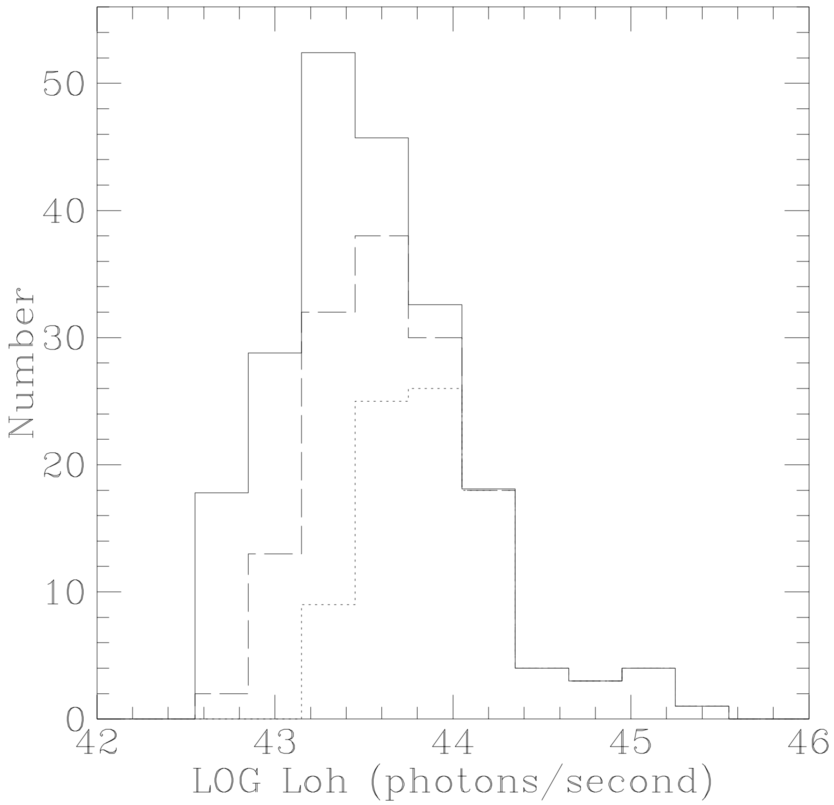

Figure 5.10 OH luminosity distribution. The dashed curve combines the previously known OH/IR stars in our survey and the new detections. The known OH/IR star luminosity distribution is depicted by the dotted line. The solid line outlines the maximum extent of the distribution, i.e. corrected for incompleteness according to a homogeneous spatial distribution

50 $\mathrm{km\,s^{-1}}$ on the redshifted side of the redshifted peak, or about 15 $\mathrm{km\,s^{-1}}$ 'outside' both main peaks. Instrumental effects (e.g. the Gibbs phenomenon) and side-lobe features of nearby sources can be excluded.

In the case of OH359.954−0.041 we measured a consistent positional offset of 1.34 arcsecond ($\sim$ 10,000 AU, or 10 times the shell radius that was measured from the phase-lag of the main peaks by vLJGHW) to the southwest, from the main peaks to both outer peaks. The 61 $\mathrm{km\,s^{-1}}$ feature 'inside' the main peaks is positionally coincident with the main peaks. The outer peaks of OH 0.040−0.056 are displaced about 0.6$''$ northeast from the main peaks, again

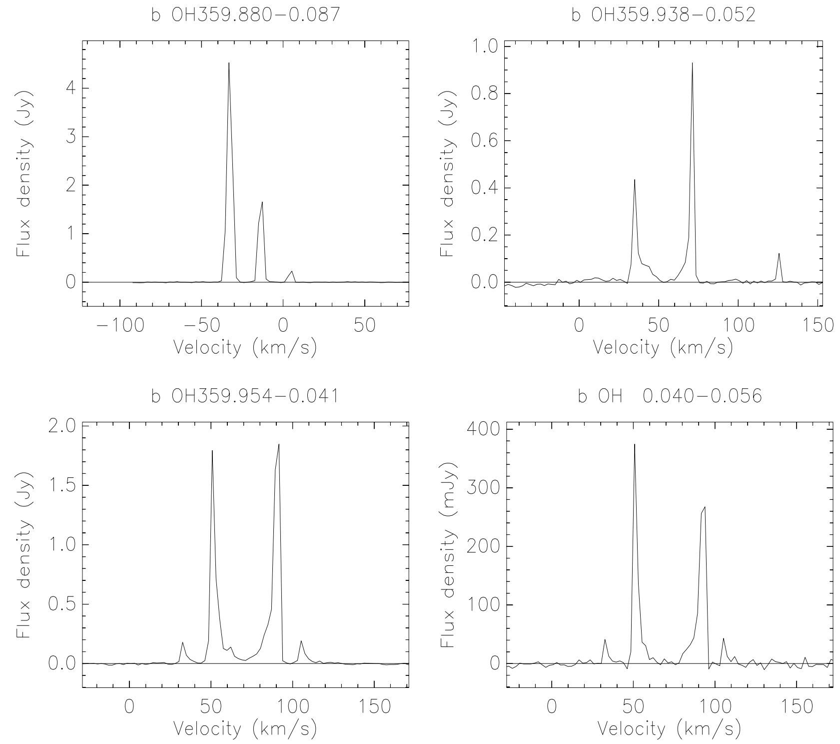

Figure 5.11 Spectra from image cube 'b' for selected sources. See Sect. 4.5

within the errors at mutual excluding positions. Because of the symmetry seen in OH359.954−0.041, and in OH 0.040−0.056, and the rather remarkable velocity interval structure in all examples, we tend to conclude that the emission is from (the shell of) the OH/IR star itself; not from another source (an OH/IR binary, or more exoticly, an OH/IR star captured by an OH masering supergiant) seen at the same projected coordinates. Suggestions then range from a double shell, indicating different epochs of interrupted mass-loss as seen for carbon rich AGB stars (Olofsson et al. 1996), creation of other molecules besides CO already early in the mass-loss history, an effect related or similar to the mode switching seen in the H_2O maser lines of OH 39.7+1.5 (Engels et al. 1997), to bipolar outflow. These stars clearly make excellent test-cases for our understanding of the mass-loss mechanism of evolved stars.

Although the both uniformly sampled VLA and ATCA data sets have a comparable sensitivity, the spectral features are only clearly seen in the concatenated

VLA data set. Therefore the features result from either weak emission from many epochs, or strong emission at a limited amount of individual epochs. Making a case for the latter, other examples of similar, one epoch spectra in the literature can be found, however undiscussed, in Te Lintel Hekkert et al. (1991; IRAS 15452-5459 and IRAS 17253-2824), and in Sevenster et al. (1997; e.g. OH353.421−0.894, OH 2.186−1.660 and OH 5.991+0.252). Furthermore, Eder et al. (1988) mention an identical phenomenon in IRAS 18520+0533 (OH 38.3+1.9), and suggest it to be mapped. However, OH 38.3+1.9 was found unresolved at 1612 MHz with the VLA in CD-array by Lewis et al. (1990), and observations with the European VLBI Network have not been published yet (M. Lindqvist, pers. comm.). Note however, that this OH emission of OH359.954−0.041 and OH 0.040−0.056 cannot be detected with VLBI observations, because of severe scattering of the source at decimeter wavelengths ($0.6''$ at 1612 MHz for OH359.954−0.041; Van Langevelde et al. 1992b).

5.5 Conclusions

We detected 155 double peaked 1612 MHz sources within $18'$ of Sgr A*. Of the 155 detections, 52 are previously unknown OH/IR stars. In addition, 3 single peak detections are given, which are most probably masers of OH/IR stars as well. We have also listed 13 double peaked sources that exceed the RMS noise levels by a factor of 8, and that most probably originate in the molecular cloud complex located at the GC. The sky and velocity distribution, as well as the expansion velocity distribution of the low OH luminosity stars compare very well with the previously known OH/IR stars in the GC. We therefore conclude that this survey revealed the low OH luminosity part of the GC OH/IR star population; the additional sources in the new sample are intrinsically identical to the AGB stars of the known sample, except for a less efficient OH maser. The OH/IR star OH maser luminosity distribution peaks at $L_{\rm OH} \approx 10^{43.4}$ photons per second. From this survey however, we can not conclude with certainty that there is a low luminosity cut-off of the OH maser luminosity distribution.

Acknowledgements. LOS hereby thanks all who made it possible to have this unusually large data set concatenated and analysed; in particular everyone at Sterrewacht Leiden for avoiding the local area network during nighttime, and the AIPS users in Onsala for flexible disk space usage. Thanks to Ian Glass for providing data before publication and to Michael Lindqvist for his continuous interest. For this project LOS received financial support from Sterrewacht Leiden, Svenska Institutet and Onsala Rymdobservatorium. HJvL acknowledges support for his research by the European Union under contract CHGECT920011 and AW acknowledges support by the Swedish Natural Science Research Council. In this article we use observations obtained with the Australia Telescope, which is funded by the Commonwealth of Australia for operation as a National Facility managed by CSIRO, and data collected with the Very Large Array, operated as part of the National Radio Astronomy Observatory by Associated Universities Inc. under cooperative agreement with the National Science Foundation. This research has made use of the SIMBAD database, operated at CDS, Strasbourg, France.

5.6 Appendix: Catalogs

For the identification of OH/IR stars in the Galactic center (GC), the catalog of Lindqvist et al. (1992a; LWHM) is the most complete. The pre-IRAS *catalogue of stellar 1612 MHz maser sources*, compiled from the literature by Te Lintel Hekkert et al. (1989; TLH), lists additional GC stellar OH maser sources that lie outside the area or velocity coverage surveyed by LWHM. However, LWHM did not confirm two sources in the TLH catalog: OH359.897−0.065 and OH 0.482−0.164 (TLH numbers 175 and 207). Source OH359.897−0.065 has been discussed in Sect. 4.3. For OH 0.482−0.164 (TLH#207) TLH give three references: Baud et al. (1979), Baud et al. (1981) and Olnon et al. (1981). The latter however, use the data of Baud et al. (1979).

We noticed that in Baud et al. (1979), comparing with Baud et al. (1981), the velocity and flux data corresponding to OH 0.482−0.164 (OH 0.48−0.13 or OH 0.5−0.1) has been entered for OH 0.503−0.758 (OH 0.5−0.8) and vice versa[4]. Source OH 0.482−0.164 has been confirmed by Habing et al. (1983) and LWHM at the 'proper' (i.e. Baud et al. 1981) velocities; source OH 0.503 −0.758 has probably been detected as an H_2O maser (with a velocity of −58 km s^{-1}; Batchelor et al. 1980 – who, however, did not recognise it as a stellar source), as a signal accidently picked up in a single dish beam pointed towards the HII region G 0.55−0.85 (e.g. Downes et al. 1979). There are no confirmations the other way around. Therefore, the data listed in Baud et al. (1979) should be read as in Baud et al. (1981). This means therefore also, that the velocity and flux data for TLH#207 and TLH#214 should be exchanged. Hence, it appears that TLH#206 and TLH#207, respectively TLH#213 and TLH#214, are entries for the same sources.

Most surveys for OH/IR stars after 1983 are based on the IRAS Point Source Catalog data base, exploiting the highly successful predictive property of the IRAS two-colour diagram for detecting OH/IR stars (Olnon et al. 1984; Van der Veen & Habing 1988). Because of confusion in the GC, these surveys omit

[4] In the first chapter of Baud's thesis, a preliminary version of the 1979 paper, this exchange had not yet occurred.

the GC area (however, see Taylor et al. 1993 for a description of an 'IRAS Galactic Center Catalog').

Additionally to the data listed in TLH and LWHM, two other 1612 MHz surveys covering the GC have been done. Van Langevelde et al. (1992a) found two high-velocity OH/IR stars in the GC, and Sevenster et al. (1997) filled the gap of the GC and bulge, where the IRAS survey had suffered from confusion. Because the latter survey has a low sensitivity compared to LWHM, in particular in the GC region, no new matches were found.

We also extended our search for possible stellar counterparts for our new detections in other wavelength regions. Many matches were found in a preliminary list of long period K-band variables, kindly provided by Ian Glass (for a description see Glass et al. 1996). New detections were cross-correlated with the SIMBAD data base ($\lesssim 20''$ radius), and with data sets found in the main journals between 1979 and 1996. However, in general the overlap is minimal.

References

Batchelor R.A., Caswell J.L., Goss W.M., Haynes R.F., Knowles S.H., Wellington K.J. 1980, Aust. J. Phys. 33, 139
Baud B., Habing H.J., Matthews H.E., Winnberg A. 1979, A&AS 35, 179
Baud B., Habing H.J., Matthews H.E., Winnberg A. 1981, A&A 95, 171
Blommaert J.A.D.L., van der Veen W.E.C.J., Habing H.J. 1993, A&A 267, 39
Blommaert J.A.D.L., van Langevelde H.J., Michiels W.F.P. 1994, A&A 287, 479
Blum R.D., Sellgren K., DePoy D.L. 1996, AJ 112, 1988
Cornwell T.J., Uson J.M., Haddad N. 1992, A&A 258, 583
Dejonghe H. 1993, in "Galactic bulges", Dejonghe H., Habing H.J. (eds.) Kluwer Academic Publishers, Dordrecht, p. 73
Downes D., Goss W.M., Schwarz U.J., Wouterloot J.G.A. 1979, A&AS 35, 1
Eder J., Lewis B.M., Terzian Y. 1988, ApJS 66, 183
Ekers R.D., van Gorkom J.H., Schwarz U.J., Goss W.M. 1983, A&A 122, 143
Engels D., Winnberg A., Walmsley C.M., Brand J. 1997, A&A 322, 291
Frail D.A., Diamond P.J., Cordes J.M., van Langevelde H.J. 1994, ApJ 427, L43
Glass I.S., Matsumoto S., Ono T., Sekiguchi K. 1996, in "The Galactic center", R. Gredel (ed.), ASP Conf. Ser. Vol. 102, p. 312
Güsten R., Downes D. 1983, A&A 117, 343
Habing H.J. 1993, in "Galactic bulges", Dejonghe H., Habing H.J. (eds.) Kluwer Academic Publishers, Dordrecht, p. 57
Habing H.J. 1996, A&AR 7, 97
Habing H.J., Olnon F.M., Winnberg A., Matthews H.E., Baud B. 1983, A&A 128, 230
Haller J.W., Rieke M.J., Rieke G.H., Tamblyn P., Close L., Melia F. 1996, ApJ 456, 194
Harvey P.M., Bechis K.P., Wilson W.J., Ball J.A. 1974, ApJS 27, 331
Herman J., Habing H.J. 1985, A&AS 59, 523
Iben I., Renzini A. 1983, ARA&A 21, 271
Jones T.J., McGregor P.J., Gehrz R.D., Lawrence G.F. 1994, AJ 107, 1111
Kobayashi Y., Okuda H., Sato S., Jugaka J., Dyck H.M. 1983, PASJ 35, 101
Krabbe A., Genzel R., Drapatz S., Rotaciuc V. 1991, ApJ 382, L19
Levine D.A., Figer D.F., Morris M., McLean I.S. 1995, ApJ 447, L101
Lewis B.M., Chengalur J.N., Schmelz J., Terzian Y. 1990, MNRAS 246, 523
Lindqvist M., Winnberg A., Habing H.J., Matthews H.E. 1992a, A&AS 92, 43 (LWHM)
Lindqvist M., Habing H.J., Winnberg A. 1992b, A&A 259, 118
Lindqvist M., Winnberg A., Habing H.J. 1997, *in preparation*
Monetti A., Glass I.S., Moorwood A.F.M. 1992, MNRAS 258, 705
Monetti A., Glass I.S., Moorwood A.F.M. 1994, MNRAS 268, 194
Okumura S.K., Ishiguro M., Fomalont E.B., Chikada Y., Kasuga T., Morita K., Kawabe R., Kobayashi H., Kanzawa T., Iwashita H., Hasegawa T. 1989, ApJ 347, 240
Olnon F.M., Walterbos R.A.M., Habing H.J., Matthews H.E., Winnberg A., Brzezin-

ska H., Baud B. 1981, ApJ 245, L103
Olnon F.M., Baud B., Habing H.J., de Jong T., Harris S., Pottasch S.R. 1984, ApJ 278, L41
Olofsson H., Bergman P., Eriksson K., Gustafsson B. 1996, A&A 311, 587
Pedlar A., Anantharamaiah K.R., Ekers R.D., Goss W.M., van Gorkom J.H., Schwarz U.J., Zhao J-H. 1989, ApJ 342, 769
Reid M.J. 1993, ARAA 31, 345
Rieke G.H., Rieke M.J. 1988, ApJ 330, L33 (RR)
Sellgren K., Hall D.N.B., Kleinmann S.G., Scoville N.Z. 1987, ApJ 317, 881
Sevenster M.N., Dejonghe H., Habing H.J. 1995, A&A 299, 689
Sevenster M.N., Chapman J.M., Habing H.J., Killeen N.E.B., Lindqvist M. 1997, A&AS 122, 79
Taylor G.B., Morris M., Schulman E. 1993, AJ 106, 1978
te Lintel Hekkert P., Versteege-Hensel H.A., Habing H.J., Wiertz M. 1989, A&AS 78, 399 (TLH)
te Lintel Hekkert P., Chapman J.M. 1996, A&AS 119, 459
te Lintel Hekkert P., Caswell J.L., Habing H.J., Haynes R.F., Norris R.P. 1991, A&AS 90, 327
van der Veen W.E.C.J., Habing H.J. 1988, A&A 194, 125
van Langevelde H.J., van der Heiden R., van Schooneveld C. 1990, A&A 239, 193
van Langevelde H.J., Cotton W.D. 1990, A&A 239, L5
van Langevelde H.J., Diamond P.J. 1991, MNRAS 249, 7P
van Langevelde H.J., Brown A.G.A., Lindqvist M., Habing H.J., de Zeeuw P.T. 1992a, A&A 261, L17
van Langevelde H.J., Frail D.A., Cordes J.M, Diamond P.J. 1992b, ApJ 396, 686
van Langevelde H.J., Janssens A.M., Goss W.M., Habing H.J., Winnberg A. 1993, A&AS 101, 109 (vLJGHW or the 'monitor')
Volk K., Cohen M. 1989, AJ 98, 931
Whitelock P., Feast M., Catchpole R. 1991, MNRAS 248, 276
Winnberg A., Baud B., Matthews H.E., Habing H.J., Olnon F.M. 1985, ApJ 291, L45
Wood P.R., Whiteoak J.B., Hughes S.M.G., Bessell M.S., Gardner F.P., Hyland A.R. 1992, ApJ 397, 552
Yusef-Zadeh F., Roberts D.A., Goss W.M., Frail D.A., Green A.J. 1996, ApJ 466, L25
Yusef-Zadeh F., Mehringer D.M. 1995, ApJ 452, L37
Zylka R., Mezger P.G., Wink J.E. 1990, A&A 234, 133

Chapter 6

OH/IR stars as signposts

for ancient and future starburst activity in the Galactic center

Abstract.

We address two different, but related issues about the nucleus of our Galaxy. We base our views primarily on a sample of about 200 OH/IR stars within 100 pc from the center. The first issue is that the distribution of expansion velocities of the circumstellar envelopes is very narrow and differs significantly from those of samples in the bulge and disk of our Galaxy. We conclude that many stars were formed in a short time, one or two Gyr ago. At that time the Galaxy probably would have been classified as a starburst galaxy. Second, we notice that the distribution of high-negative velocity OH/IR stars on the sky resembles that of a cloud of CO gas with high-negative velocity. We suggest that this gas cloud is currently falling into the center along a very elongated orbit, outlined by the orbits of the high-negative velocity OH/IR stars, and will trigger star formation in the future. We support the existence of three different groups of stars in the Galactic center; an old bulge-like population, a collection of young stars formed from continuously infalling clouds, and a shrinking population of stars created in a short time out of a rapidly rotating cloud.

Co-authored by:
H.J. Habing, M. Lindqvist, H.J. van Langevelde & A. Winnberg

6.1 Introduction

Compared to AGN and starburst galaxies, the Galaxy is in a quiescent state. However, a large amount of energy originating in the Galactic center (GC) has been unaccounted for. This lack has led to searches for an accreting central black hole or for luminous massive stars. Recently, much progress has been made by discoveries of very luminous early-type stars in the central star cluster around GCIRS 16, providing sufficient energetic ionising photons to account for the bulk of radiation observed. Nevertheless, these massive stars trace only the most recent history of the GC as their lifetime is short: a few to a few tens of million years. Unfortunately, no conclusive information can be obtained from the general sample of 'older', less massive late-type stars (supergiants and asymptotic giant branch (AGB) stars). This late-type sample is very mixed and their formation history cannot be traced back mainly because of the impossibility to determine their main-sequence masses (0.8 to $\sim$ 20 $M_{\odot}$, with 'ages' of 20×10^9 down to 8×10^6 yr). The GC is reviewed by e.g. Genzel et al. (1994), Morris & Serabyn (1996) and Mezger et al. (1996).

However, one can resolve part of the late-type star history puzzle using OH/IR stars found within 50 pc of the GC. The OH/IR stars are evolved late-type (AGB) stars of different masses – and thus ages – in a shortlived stage of high mass-loss (Iben 1991; Habing 1996). An easily and accurately measured property of the OH/IR stars is $v_{\rm exp}$, the value of the expansion velocity of the circumstellar envelope at large distance from the star. In the disk of the Galaxy OH/IR stars with different expansion velocities originate from stars with different mass (Baud et al. 1981; Baud & Habing 1983). Lindqvist et al. (1992b) showed that there is a statistical difference in spatial and kinematic properties between groups of OH/IR stars with high and low expansion velocities. They conclude that, on average, OH/IR stars with high $v_{\rm exp}$ are 'younger' than stars with low $v_{\rm exp}$ (an old, bulge-like population), because of a smaller velocity dispersion and a stronger concentration toward the Galactic plane. Sevenster et al. (1995) confirm the strong Galactic rotation for the younger group on dynamical grounds and suggest that this group may have formed at a distinct event after the infall of gas to the center. However, Serabyn & Morris (1996) argue that this younger group emerged slowly and steadily via sustained star formation by continuous inflow of mass.

Using several properties of samples of GC OH/IR stars, we argue that the GC has undergone a distinct epoch of rigorous star formation at least a Gyr ago. We estimate the total number of massive stars, and conclude that during this phase, the Galaxy would have been classified as a starburst galaxy. In the second part we suggest that the high-velocity (HV) OH/IR stars outline highly elongated orbits in the line-of-sight, where currently gas is still transported inward e.g. by a barred potential (Binney 1994). We thus support both the views of Serabyn & Morris (1996) and Sevenster et al. (1995) for the high $v_{\rm exp}$ group, i.e. both continuous low-rate star formation and short-term high-rate star formation (did) occur in the GC.

We use the OH/IR stars from our recent 1612 MHz OH maser survey (Chapter 5). We note however, that we could have done this analysis (less convincingly) with the OH/IR stars found by Lindqvist et al. (1992a) and Van Langevelde et al. (1992).

6.2 Shell expansion velocity

Figure 6.1 shows expansion velocity histograms for OH/IR stars in different parts of the Galaxy: for the OH/IR stars in the GC (Chapter 5), in the Galactic bulge (GB, Sevenster et al. 1997a) and in the Galactic disk (GD, Sevenster et al. 1997b). A clear introduction in the topic of circumstellar expansion velocities is given in Habing et al. (1994). The shell expansion velocity $v_{\rm exp}$ is related to the stellar luminosity L, and to the dust opacity or dust-to-gas ratio δ (reflecting 'metallicity') of the circumstellar material: $v_{\rm exp}^2 \sim \delta \cdot \sqrt{L}$. Typically one measures $v_{\rm exp} = 15$ km s^{-1}.

The significantly higher $v_{\rm exp}$ in the distribution of the GC sample with respect to the GB sample cannot be attributed to differences in luminosity. A few bolometric luminosities are available from infrared studies by Jones et al. (1994), and Blommaert et al. (1997). Both groups have studied almost the same sample of GC OH/IR stars (selected on their high OH maser luminosity). There is agreement between the ranges in stellar main-sequence masses (1 to 3 $M_\odot$) and the bolometric magnitudes ($-6 \lesssim M_{\rm bol} \lesssim -4$). This justifies the conclusion by Blommaert et al. (1997), that the luminosities of OH/IR stars in the GC and in the GB are comparable. Hence, as was concluded by e.g. Blommaert (1992) and Habing et al. (1994), on average the stars in the GC must have a significantly higher (but unknown) metallicity than the stars in the GB.

Second, the GC $v_{\rm exp}$ distribution peaks very sharply around 19 km s^{-1}. We call the "extra" stars that form the peak at $v_{\rm exp} \approx 19$ km s^{-1} the starburst ("SB") sample. Because of the significant influence of δ on the $v_{\rm exp}$ distribution (Fig. 6.1), we do not expect large metallicity differences in these SB OH/IR stars. By varying the stellar luminosities (5×10^3 to 2×10^4 $L_\odot$, Jones et al. 1994; Blommaert et al. 1997), one expects a spread in $v_{\rm exp} \sim 7$ km s^{-1} as seen in the GB. But with 40% of all GC stars having $17 < v_{\rm exp} < 20$ km s^{-1}, we observe only half that value. Although the models of e.g. Vassiliadis & Wood (1993, hereafter VW93) show that metallicity is anti-correlated with luminosity

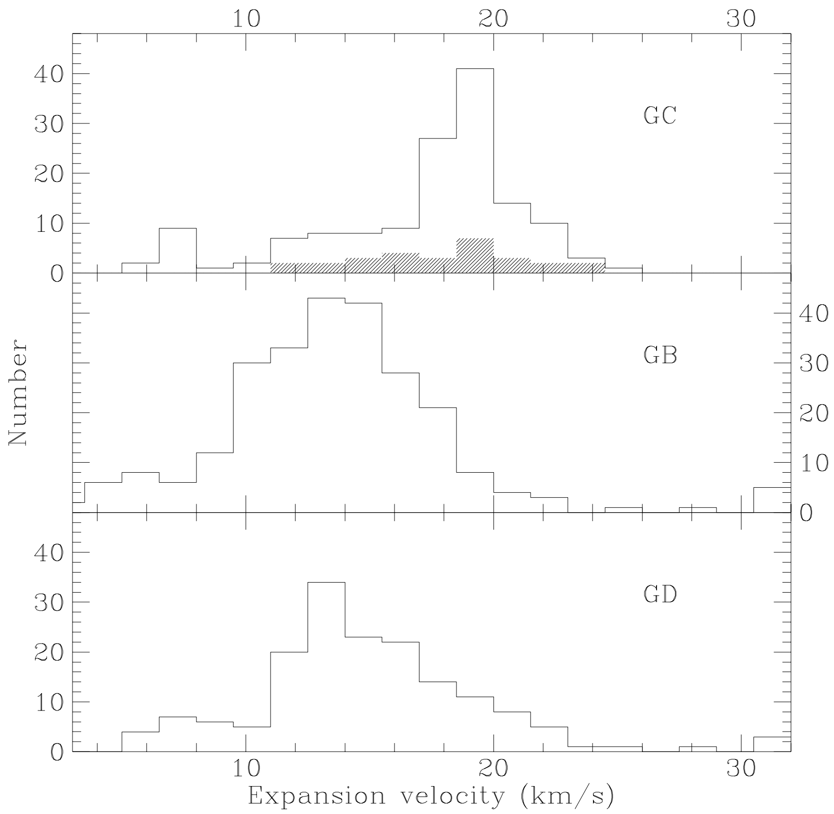

Figure 6.1 Expansion velocity distribution for different samples of OH/IR stars. On top the distribution of OH/IR stars in our Galactic center (GC) survey, next $v_{\rm exp}$ for Galactic bulge (GB) and Galactic disk (GD) OH/IR stars (from Sevenster et al. 1997a,b). Sevenster (pers. comm) will further discuss the differences in the distributions. We shaded the distribution for GC OH/IR stars for which a bolometric luminosity is determined (Blommaert et al. 1997)

for an OH/IR star of a given mass, it is unlikely that differences in metallicity and luminosity cancel so perfectly. We therefore claim that a large fraction of OH/IR stars in the GC have identical metallicities and comparable luminosities. A hint for the latter ($M_{\rm bol} \approx -4.5$ to -5, depending on extinction correction) can be found in the distributions for $M_{\rm bol}$ in Blommaert (1992), and suggests that the spread in luminosity is an effect due to the selection of strong OH masers (partly reflected in the shaded distribution in Fig. 6.1, i.e. not representative for the whole $v_{\rm exp}$ distribution of stars). We are looking forward to check this with bolometric luminosity determinations for the less strong OH maser OH/IR stars. Our claim also explains why the efforts of Blommaert to find a difference between stars of high and low expansion velocities were inconclusive. Because the OH/IR stage is a very short lived phase in stellar evolution, these SB OH/IR stars all have the same main-sequence mass and age, i.e. both in a very narrow range. We conclude that this is evidence for an epoch of enhanced star formation in the GC.

From the models of VW93, we derive that for a star with $M_{\rm bol} \approx -5$, the main-sequence mass is 2 $M_{\odot}$ (or less), the metallicity of the originating molecular cloud within $0.004 < Z < 0.008$, and the age 1.1 Gyr. A much higher overall metallicity ($Z \gtrsim 0.03$), and thus a higher main-sequence mass for the SB OH/IR stars, is then inconsistent with the OH/IR star pulsation periods (P $\lesssim 1000^{\rm d}$, Van Langevelde et al. 1993; Jones et al. 1994). Within the VW93 models, the GC OH/IR stars are therefore not necessarily super metal rich as suggested by Habing et al. (1994). However, these models were constructed for luminous OH/IR stars in the Magellanic Clouds ($L \approx$ 20-40$\times10^3$ $L_{\odot}$, $v_{\rm exp} \approx$ 10 km s^{-1}; Wood et al. 1992) and application of the VW93 models might be in error, possibly because of differing details of dust formation and dust properties between both samples, or e.g. a mistreatment of the stellar pulsation period in the VW93 models.

6.3 Implications for a star formation epoch

The very narrow $v_{\rm exp}$ distribution, and also our claim of similar $M_{\rm bol}$, indicate that the SB OH/IR stars have the same age. The strongest argument that they were formed in a short period (say 10 Myr) is based on dynamical grounds. The difference in velocity dispersion for low (large dispersion) and high (small dispersion) $v_{\rm exp}$ stars is evidence that the high $v_{\rm exp}$ stars have a shorter dynamical evolution; they were formed later (Lindqvist et al. 1992b). Sevenster et al. (1995) drew the same conclusion without explicitly dividing the stars according to $v_{\rm exp}$. The high age (> 1 Gyr), the strong rotation, the identical metallicities and the fact that the SB OH/IR stars have a velocity dispersion similar to the even younger, highest $v_{\rm exp}$ (> 20 km s^{-1}) stars, both half the velocity dispersion for low $v_{\rm exp}$ (< 17 km s^{-1}) stars, indicate that the SB OH/IR stars were formed out of a single cloud circling the center.

Regardless of a precise knowledge of the metallicities, we can make a very simplified calculation of the total number of massive (OB) stars and total luminosity during the epoch of star formation outlined above. Surely, many factors are not well known, or might be different in a high metallicity environment as the GC. For example, we use the $Z = 0.008$ models of VW93 (see also e.g. Fagotto et al. 1994). We assume that an AGB star is observable as an OH/IR star only during the so-called 'superwind' phase on the AGB (9×10^4 yr for M = 2 $M_\odot$) and read in Table 2 of VW93, that the total AGB phase lasts 1.5×10^7 yr. By comparing lifetimes of stars with small mass differences with the lifetime of the 'superwind' phase, we estimate an upper limit of the mass range for the OH/IR stars of 9×10^{-5} $M_\odot$ and infer that each OH/IR star represents 1.8×10^6 AGB stars in that mass range. Hence, because all OH/IR stars have the same mass and age, each OH/IR star observed can be converted to 1.8×10^6 stars with a main-sequence mass of 2 $M_\odot$ during the formation of the stars. From our $v_{\rm exp}$ distribution, we estimate the minimum number N of OH/IR stars that is clearly in excess of what can be expected from the general mix of stars formed at other times, i.e. $N \gtrsim 20$. Without performing a detailed starburst calculation (see e.g. Rieke et al. 1993), we estimate the total number of OB stars ($10 < M < 60$ $M_\odot$) to be roughly 10^6 (or a few 10^7 over all masses) during this event. The luminosity produced in the nucleus during this event ($\sim 10^{10}$ $L_\odot$) is comparable to the luminosity of the Galaxy as a whole. Accordingly, the Galaxy would have been classified as a starburst galaxy during this epoch of enhanced star formation.

Apart from selecting the lowest estimates for the excess of OH/IR stars and the conversion into AGB stars (the zero point of the initial main-sequence mass function (IMF) during the star formation period), there are good reasons to believe that this calculation gives a lower limit for the number of OB stars. It is expected that in a strong gravitational potential like the GC, the formation of low-mass stars is suppressed (e.g. Morris 1993). The low-mass cut-off in the IMF is probably a few $M_\odot$. If this cut-off for the GC is higher than the mass of the observed OH/IR stars, there is a relative deficit of observable OH/IR stars (thus underestimating N). Moreover, we have used a relatively steep power of −3 in the IMF, close to the value for the high-mass end of the IMF (e.g. Rieke et al. 1993). The intermediate-mass part of the IMF is likely to be less steep, resulting in a severe underestimate of the number of OB stars when starting the calculations from M = 2 $M_\odot$. However, the estimate is very sensitive to the AGB star mass, mass range, as well as the adopted stellar models.

Estimating the mass of the molecular material from which our starburst resulted, we come to a cloud of a few times 10^8 $M_\odot$ (with a star formation efficiency of $\sim$ 20%; Genzel et al. 1995). We find our rough estimates consistent with the observations for starburst galaxies, for example the nearby starburst galaxies NGC 3504 and M 82 (Kenney et al. 1993; McLeod et al. 1993).

6.4 High-velocity OH/IR stars

A next question is then, whether the star formation has been a single event from unprocessed nuclear gas (Sevenster et al. 1995, for which we have given support in the previous section), or that gas is continuously transported inward and results in recurrent star formation epochs (Serabyn & Morris 1996). The early-type stars formed recently in the GC, and accumulating evidence for a bar in the Galaxy both point toward the latter (e.g. Krabbe et al. 1995; Stark et al. 1991; Binney et al. 1991; Binney 1994; Carr et al. 1996; Morris & Serabyn 1996). In addition to the single event formation suggestion of Sevenster et al. (1995), we can also support this view of recurrent star formation episodes (Serabyn & Morris 1996) with our high-velocity OH/IR star observations.

Our survey (Chapter 5) was partly designed to detect high-velocity (HV) OH/IR stars; stars with $|v_{\rm LSR}| > 250$ km s^{-1}. The character of the detections of HV OH/IR stars rules out the possibility that the HV OH/IR stars are drawn from an isotropic velocity distribution (as has been shown by Van Langevelde et al. 1992). Moreover, all the stars with high-negative velocities ($v_{\rm LSR} < -130$ km s^{-1}) within 10$'$ of Sgr A* (the GC) occupy a preferred region of the sky. In Fig. 6.2, we compare the sky distribution of our HV OH/IR stars with a cloud of ^{12}CO gas at high-negative velocity in the GC (HVCO, Liszt & Burton 1993). The HVCO gas and HV OH/IR stars are located in the same elongated area on the sky, and have similar high-negative line-of-sight velocities.

Following the conclusion from Van Langevelde et al. (1992) that the HV OH/IR stars move along very elongated orbits in the line-of-sight and thereby outlining the long axis of the Galactic bar or tri-axial bulge, we suggest that the HVCO gas moves along a similar orbit (cf. x_1-orbits in Fig. 5 of Morris & Serabyn 1996). The sense of rotation is consistent with other relatively high-velocity OH/IR stars ($|v_{\rm LSR}| \gtrsim 100$ km s^{-1}). Because we cannot determine a true space distribution, we do not claim an actual physical association between the HVCO cloud and stars. Absorption measurements do seem to contradict each other about the line-of-sight location of high-negative velocity gas clouds (Güsten & Downes 1981; Liszt & Burton 1993; Yusef-Zadeh et al. 1993). We note the different angular scales and interpret the ^{12}CO gas observations on large scale as an infalling cloud on an orbit as outlined above and behind Sgr A*, and on small scale around Sgr A* either the closer part of the cloud, or a separate cloud interacting with the environment. In short, we have indications that gas is currently transported inward to the GC, possibly supplying the matter for future star formation.

It is interesting to hypothesise that this picture may help to explain the small scale, enigmatic GC features and their velocity field, such as the 'mini-cavity'

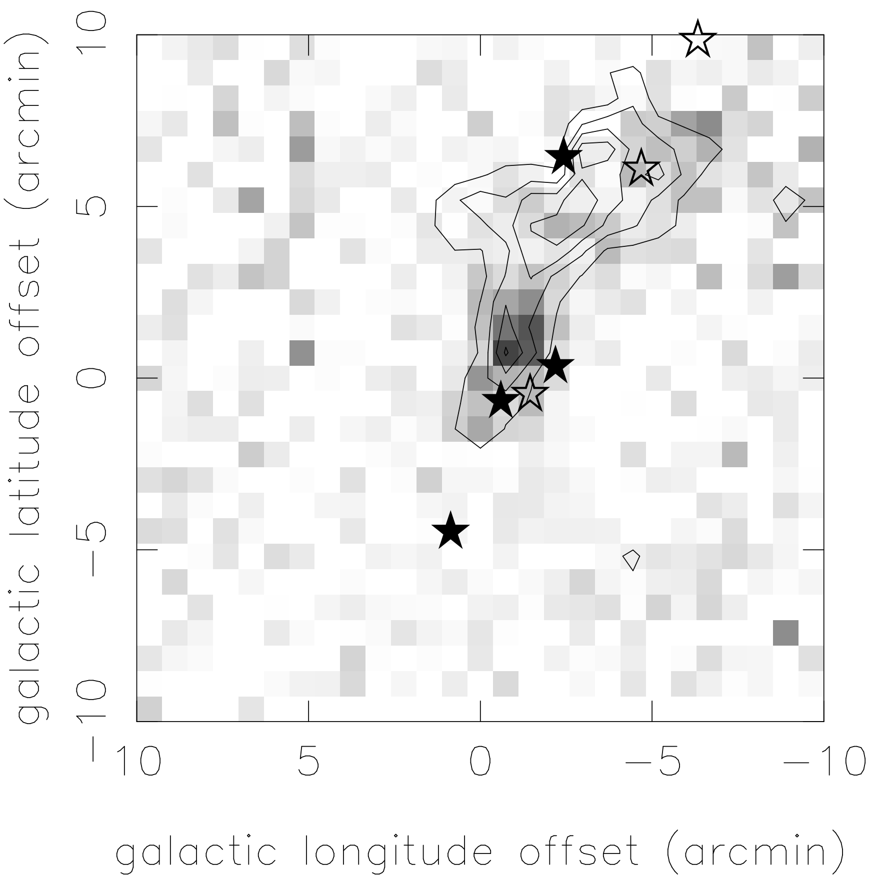

Figure 6.2 Sky distribution of HV OH/IR stars and HV ^{12}CO gas (Liszt & Burton 1993). Offsets are with respect to Sgr A*. The arbitrary contours (gray-scales) outline ^{12}CO gas with $v_{\rm LSR} = -190$ (-213) km s^{-1}. The HV OH/IR stars at $v_{\rm LSR} \sim -320$ (-150) km s^{-1} are the open (closed) symbols

in the ionised 'mini-spiral' streamers in th GC (supporting Zhao et al. 1996 as being a neutral clump of gas which impacts the GC medium from the outside) and the 'mini-spiral' (e.g. Roberts et al. 1996; Serabyn et al. 1988, interpreted as an infalling, approaching gas streamer in the line-of-sight after it has been deflected by the central mass concentration into the arms of the 'mini-spiral' pattern).

Acknowledgements. We thank Maartje Sevenster and Harvey Liszt for supplying data for the figures, and Susanne Aalto-Bergman and Cathy Horellou for a careful reading of the manuscript. HJvL acknowledges support for his research by the European Union under contract CHGECT920011 and AW acknowledges support by the Swedish Natural Science Research Council.

References

Baud B., Habing H.J., Matthews H.E., Winnberg A. 1981, A&A 95, 156
Baud B., Habing H.J. 1983, A&A 127, 73
Binney J. 1994, in The nuclei of normal galaxies, eds. R. Genzel & A.I. Harris p. 75
Binney J., Gerhard O.E., Stark A.A., Bally J., Uchida K.I. 1991, MNRAS 252, 210
Blommaert J.A.D.L. 1992, PhD thesis, Leiden University, Ch 3
Blommaert J.A.D.L., van der Veen W.E.C.J., van Langevelde H.J., Habing H.J., Sjouwerman L.O. 1997, accepted for publication in *Astronomy & Astrophysics*
Carr J.S., Sellgren K., Balachandran S.C. 1996, in "The Galactic center", R. Gredel (ed.), ASP Conf. Ser. Vol. 102, p. 212
Fagotto F., Bressan A., Bertelli G., Chiosi C. 1994, A&AS 105, 29
Genzel R., Hollenbach D., Townes C.H. 1994, Rep. Prog. Phys. 57, 417
Genzel R., Weitzel L., Tacconi-Garman L.E., Blietz M., Cameron M., Krabbe A., Lutz D. 1995, ApJ 444, 129
Güsten R., Downes D. 1981, A&A 99, 27
Habing H.J. 1996, A&AR 7, 97
Habing H.J., Tignon J., Tielens A.G.G.M. 1994, A&A 286, 523
Iben I. 1991, ApJS 76, 55
Jones T.J., McGregor P.J., Gehrz R.D., Lawrence G.F. 1994, AJ 107, 1111
Kenney J.D.P., Carlstrom J.E., Young J.S. 1993, ApJ 418, 687
Krabbe A., Genzel R., Eckart A., Najarro F., Lutz D., Cameron M., Kroker H., Tacconi-Garman L.E., Thatte N., Weitzel L., Drapatz S., Geballe T., Sternberg A., Kudritzki R. 1995, ApJ 447, L95
Lindqvist M., Winnberg A., Habing H.J., Matthews H.E. 1992a, A&AS 92, 43
Lindqvist M., Habing H.J., Winnberg A. 1992b, A&A 259, 118
Liszt H.S., Burton W.B. 1993, ApJ 407, L25
McLeod, K.K.,Rieke G.H., Rieke M.J., Kelly D.M. 1993, ApJ 412, 111
Mezger P.G., Duschl W.J., Zylka R. 1996, A&AR 7, 289
Morris M. 1993, ApJ 408, 496
Morris M., Serabyn E. 1996, ARAA 34, 645
Rieke G.H., Loken K., Rieke M.J., Tamblyn P. 1993, ApJ 412, 99
Roberts D.A., Yusef-Zadeh F., Goss W.M. 1996, in "The Galactic center", R. Gredel (ed.), ASP Conf. Ser. Vol. 102, p. 137
Serabyn E., Morris M. 1996, Nat 382, 602
Serabyn E., Lacy J.H., Townes C.H., Bharat R. 1988, ApJ 326, 171
Sevenster M.N., Dejonghe H., Habing H.J. 1995, A&A 299, 689
Sevenster M.N., Chapman J.M., Habing H.J., Killeen N.E.B., Lindqvist M. 1997a, A&AS 122, 79
Sevenster M.N., Chapman J.M., Habing H.J., Killeen N.E.B., Lindqvist M. 1997b, A&AS 124, 509
Stark A.A., Gerhard O.E., Binney J., Bally J. 1991, MNRAS 248, 14p
van Langevelde H.J., Brown A.G.A., Lindqvist M., Habing H.J., de Zeeuw P.T. 1992, A&A 261, L17
van Langevelde H.J., Janssens A.M., Goss W.M., Habing H.J., Winnberg A. 1993,

A&AS 101, 109
Vassiliadis E., Wood P.R. 1993, ApJ 413, 641 (VW93)
Wood P.R., Whiteoak J.B., Hughes S.M.G., Bessel M.S., Gardner F.F., Hyland R. 1992, ApJ 397, 552
Yusef-Zadeh F., Lasenby A., Marshall J. 1993, ApJ 410, L27
Zhao J-H., Goss W.M., Ho P.T.P. 1996, in "The Galactic center", R. Gredel (ed.), ASP Conf. Ser. Vol. 102, p. 146

Chapter 7

OH maser properties of OH/IR stars in the Galactic center

Abstract.

We report on OH maser properties of a new sample of OH/IR stars in the Galactic center. Mass-loss rates are derived and, when combined with the spatial characteristics, reveal a peculiar cluster of OH/IR stars in the very center (10 pc). The circumstellar envelopes for these OH/IR stars are likely to be influenced by the surrounding medium. We confirm the results of earlier surveys that statistically, the high expansion velocity OH/IR stars form a different kinematical sample than the low expansion velocity OH/IR stars, and give support to the hypothesis that a fraction of the stars share a common origin.

Co-authored by:
(amongst others) M. Lindqvist, A. Winnberg & H.J. van Langevelde

7.1 Introduction

The final stages of the evolution of stars of low to intermediate mass are characterised by a relatively short period of high mass-loss. After the main-sequence evolution, but before the star sheds its envelope to become a planetary nebula and a white dwarf, the star is a so-called asymptotic giant branch (AGB) star; a pulsating variable star with hydrogen (and helium) shell burning around a degenerate C/O core, surrounded by an extended expanding dusty envelope. The thickness (density) of the envelope determines whether we can see the central star as a typical M-type Mira variable, or whether all optical radiation is absorbed and re-radiated at far-infrared wavelengths as for a typical OH/IR star (Iben 1991; Habing 1996).

These AGB stars can be studied by their circumstellar infrared and maser emission (OH, H_2O, SiO). A vast number of optically invisible OH/IR stars has been discovered through the IRAS survey, because the circumstellar envelopes of OH/IR stars (and Mira variables) have very specific "IRAS colors" (e.g. Olnon et al. 1984). Mass-loss rates can be derived (Van der Veen & Olofsson 1990) and supply information about the transformation of AGB stars into planetary nebulae (e.g. Van der Veen 1989). However, the detailed mass-loss process is not well understood. Masers originating from molecules found in the circumstellar envelope may also contain such information, in particular the OH maser located in the outer envelope (e.g. Baud & Habing 1983, hereafter BH83).

In this paper we investigate the properties of the OH masers in a new sample of OH/IR stars in the Galactic center (GC) reported in Chapter 5 (hereafter Paper I). A comparison of OH shell expansion velocities ($v_{\rm exp}$) is discussed in Chapter 6, hereafter Ch 6). Lindqvist et al. (1997, hereafter L97) have analysed physical properties of the stronger OH luminous masering OH/IR stars found in a larger scale, but less sensitive survey (Lindqvist et al. 1992a, hereafter LWHM). Because we show in Paper I that the weaker OH/IR stars are an extension of the more OH luminous masing OH/IR stars, we only comment on the findings of L97 and Lindqvist et al. (1992b, hereafter L92) concerning differences in physical, spatial and kinematical properties between $v_{\rm exp}$ groups where appropriate.

We start with the selection of the data and the relation between different flux definitions in Sect. 2. Shortly, in Sect. 3 we discuss the sky, velocity and $v_{\rm exp}$ distribution of the OH masers. Section 4 contains properties derived from the OH masers, including the derived mass-loss rates. In Sect. 5, we summarise our findings.

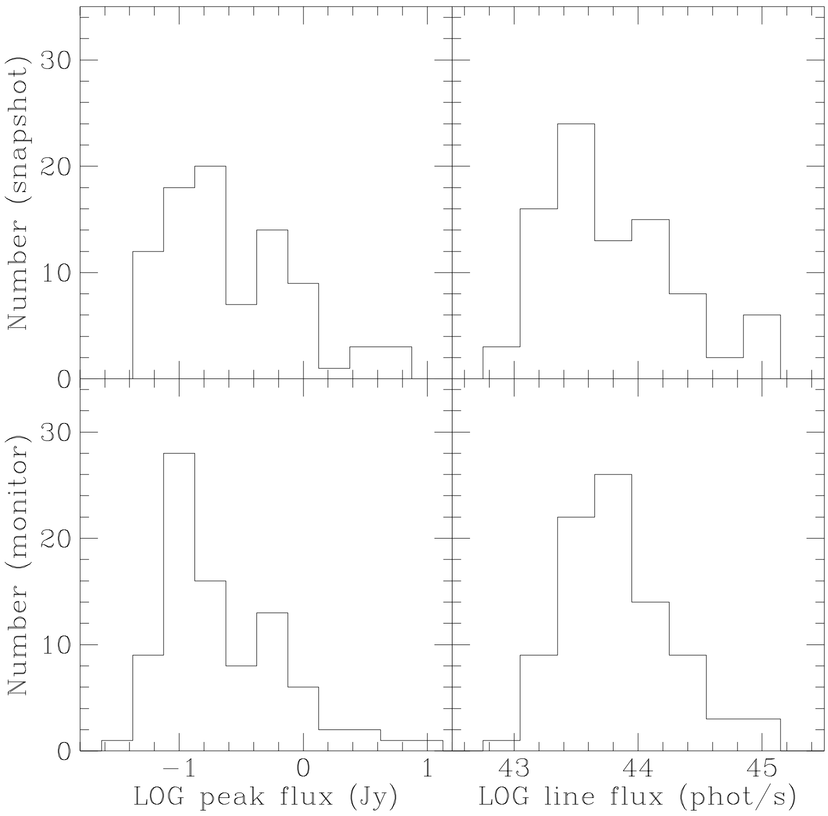

Figure 7.1 OH maser peak and integrated flux distributions based on the 87 OH/IR stars found with good flux determinations in both the 'snapshot' and 'monitor' data sets (Paper I). The top panel shows the distribution if we use the 'snapshot' data, the bottom panel displays the distribution from the 'monitor' data (left the peak flux distribution, on the right hand side the OH luminosity distribution)

7.2 Data selection

Most OH/IR stars found in the direction of GC are listed in LWHM and Paper I (see the appendix of Paper I). To limit confusion of the GC stars with bulge or disk OH/IR stars, we restrict ourselves in this paper to the 145 stars found within 30′ of Sgr A* in Paper I; an analysis of the 134 OH/IR stars found in the larger survey (one degree) of LWHM (extended with an additional 15 stars within one degree of the GC found by Habing et al. 1983) can be found in L92

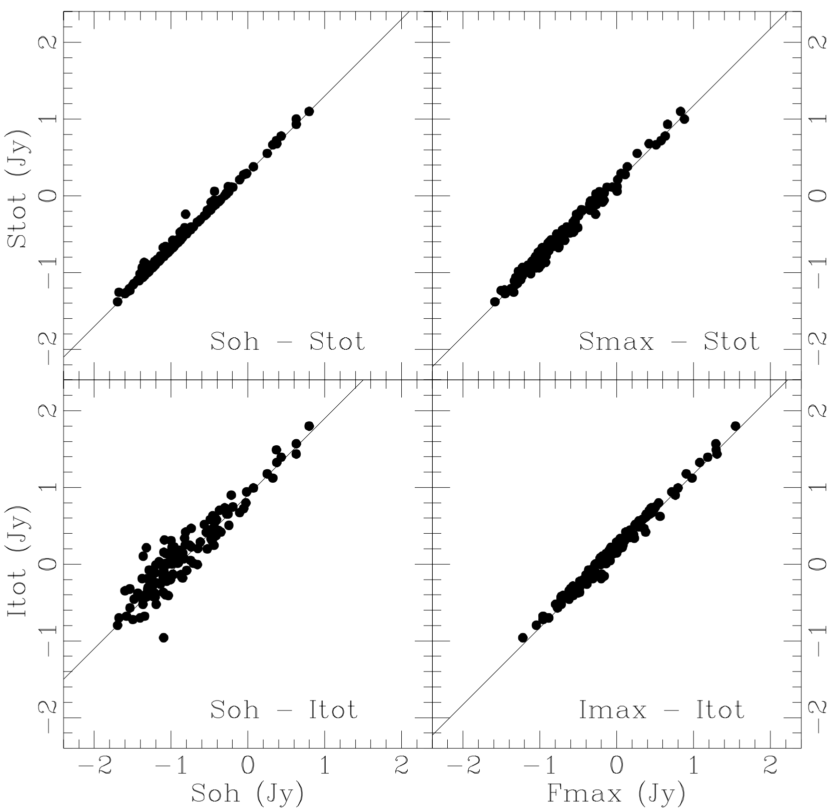

Figure 7.2 Qualitative comparison of different quantities found in the literature. All relations are linear (see text)

and L97.

In Paper I, the OH/IR stars were found in two independent ways: from a one epoch 'snapshot' survey with the Australia Telescope Compact Array, and from a Very Large Array 'monitor' survey, i.e. a concatenation of data from a monitoring campaign (Van Langevelde et al. 1993). Both data sets have a comparable sensitivity limit (RMS $\approx$ 5 mJy) and survey the central $\sim 20'$ around Sgr A*. We generally chose the 'monitor' data. The 'monitor' data has a slightly higher spectral resolution and the measured fluxes are an average over 17 epochs spread over 3 years time. Figure 7.1 shows the measurements for the same sample of stars in the snapshot and monitor data. Although the high-end side of the peak flux density distribution (and thus detection probability) does

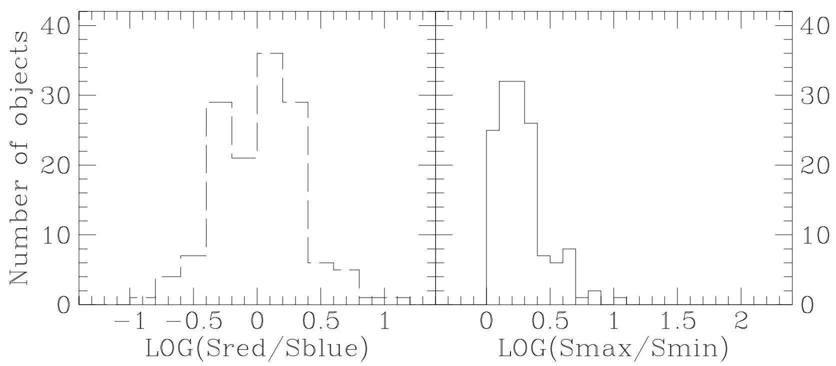

Figure 7.3 Peak flux density ratio's; dashed the distribution of the red-shifted peak flux density over the blue-shifted one (bin size 0.2), solid the distribution of the maximum peak flux density over the secondary one (with bin size 0.1)

not differ very much, the integrated line flux (the OH luminosity) determined from the 'monitor' is much less noisy and therefore approximates the mean OH luminosity better. However, where the source information from the 'monitor' was incomplete (because the second peak was outside the velocity coverage), we selected the 'snapshot' entry. We further included the information available for sources only seen in either the 'snapshot' or the 'monitor' data. We disregarded single peaked sources and alleged double peaked molecular cloud emission. The total 1612 MHz double peaked OH maser emission data set thus consists of 140 stellar sources (100 monitor and 40 snapshot), of which 89 were already found by LWHM.

7.2.1 Flux definitions

Previous investigations of OH maser properties of samples of OH/IR stars use different measurable flux quantities. Since our sample of OH/IR stars is located in the GC, at 8 kpc, we can investigate the approximate relation between the quantities through Fig. 7.2. We use the following notations:

The total peak flux density, and integrated line flux (in Jy, and in Jy km s^{-1} respectively):

$$S_{tot} = S_{blue} + S_{red}, \text{ and } I_{tot} = I_{blue} + I_{red}$$

which is twice the arithmetic mean (e.g. $<S> = S_{tot}/2$).

The geometric mean of the peak flux densities:

$$S_{OH} = \sqrt{S_{blue} \cdot S_{red}}.$$

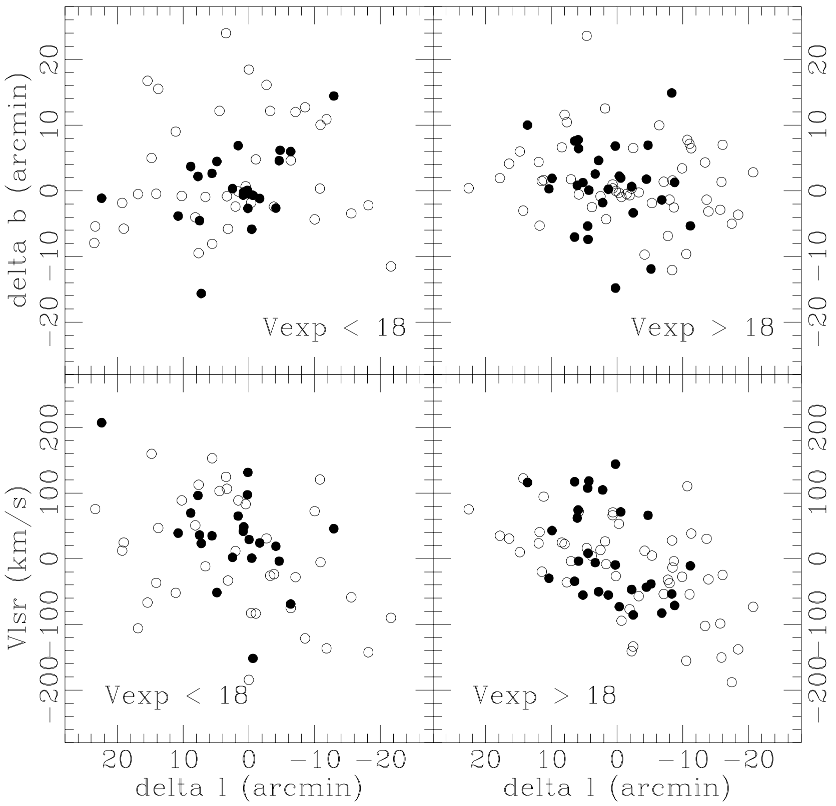

Figure 7.4 Sky (top) and velocity distribution (bottom) of OH/IR stars in the GC when divided up in two groups separated by $v_{exp} = 18$ km s^{-1}. Open symbols depict previous detections (LWHM) found in our survey, filled symbols are new detections (Paper I) and offsets are with respect to Sgr A*. Within our limited sky coverage, we confirm that the stars with high v_{exp} are more concentrated toward the plane and have a smaller velocity dispersion (cf. L92)

The maximum of the peak flux densities, either S_{blue} or S_{red}:

$$S_{max} \text{ or } S_{peak}, \text{ and similarly } I_{max}.$$

In Fig. 7.2 we plotted the quantity log S_{tot} as function of log S_{OH} and log S_{max}. The relations are independent of distance, spectral shape and spectral resolution. We have also drawn the lines log $(2 \times S_{OH})$ and log $(1.5 \times S_{max})$; numbers that result from $S_{tot} = 2 \times \langle S \rangle \approx 2 \times S_{OH}$, and from the peak at $\approx$ 1.6 of the distribution of the ratio of maximum over secondary peak flux density

(Fig. 7.3). We conclude from this that the arithmetic and geometric means are mutually exchangeable, and that for substituting S_{tot} or S_{max} it generally suffices to correct with a factor 2 or ≈ 1.5 respectively (and notice an error within a factor 1.25 for both substitutions).

Converting the peak flux density into an integrated line flux is less straightforward, because the spectral resolution, the spectral shape and noise also play a role. For simplicity, we neglect the difference in spectral resolution between the monitor data (100 sources with 6.1 kHz), the snapshot data (40 sources with 7.8 kHz), and the definition used in BH83, where peak flux densities are defined over 6.5 kHz. We find (with the line 8 S_{OH}; see also Sect. 4) that the spread from a constant conversion factor from peak flux density to integrated line flux, is generally within a factor 2. Notably, all forms of S and I are related linearly (see also e.g. David et al. 1993). Finally we remark that the factor relating I_{max} and I_{tot} is almost the same as 1.5 (drawn in the figure) for S_{max} and S_{tot}, all indicating that the spectral shape for the sample of stars does not vary much.

7.3 Sky, velocity and v_{exp} distribution

We now compare the spatial and kinematic distributions of the new sample of OH/IR stars (Paper I) with the LWHM sample. Because we do not have the spatial coverage of LWHM, we can only confirm the trend found in L92 for the LWHM stars. Following L92, the OH/IR stars are split up into two groups (Fig. 7.4), separated by an expansion velocity of 18 $km\,s^{-1}$ (60 and 80 stars). We confirm that the spatial and velocity distribution is different between the groups; the high expansion velocity group is more confined to the Galactic plane and follows Galactic rotation more tightly. We note however one important difference, which could not be seen in L92 because of a lower sensitivity. Within $4'$ (10 pc) of Sgr A*, we find a concentration of 6 stars with low flux and low expansion velocities; they have a relatively low mass-loss rate (Sect. 4.2).

The division at $v_{exp} = 18$ $km\,s^{-1}$ was chosen by L92 for statistical reasons; to divide the groups into roughly equal numbers. In L97 and Ch 6 it is found that $\approx$ 40% of the stars in the GC have $17 \lesssim v_{exp} \lesssim 20$ $km\,s^{-1}$. A division in groups for any of these velocities will complicate the description of quantitative statistical differences between both groups. Including the range $17 < v_{exp} < 20$ $km\,s^{-1}$, and with a choice of a separation velocity within that range, differences become less clear because one adds a number of stars with the same characteristics to both groups (e.g. M_{bol} in Blommaert et al. 1997). However, statistically there remains a distinction between low and high v_{exp} for a large range of choices

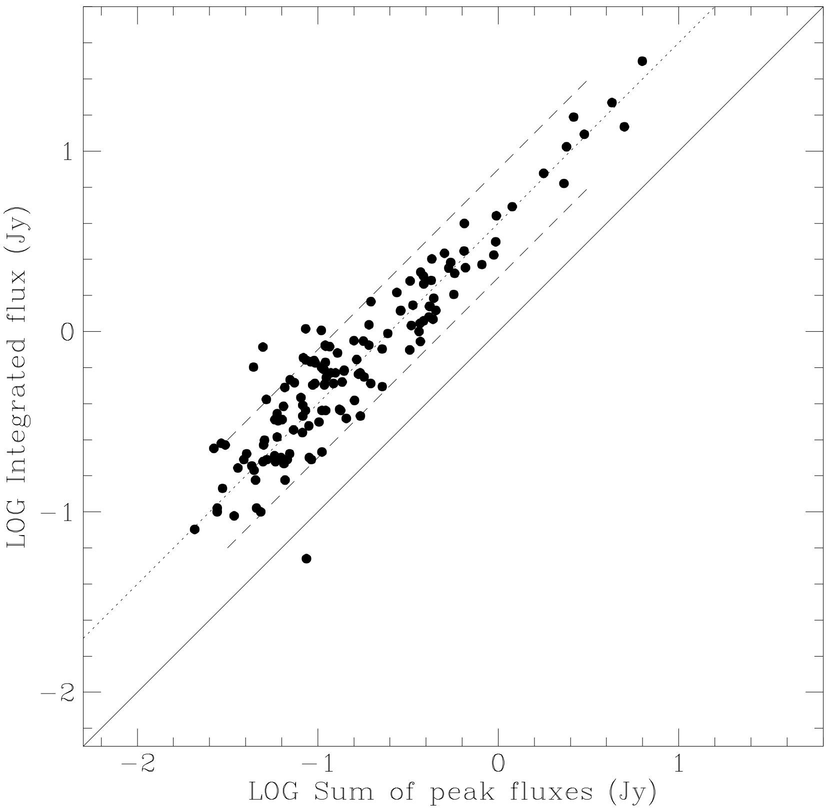

Figure 7.5 Measured sum of the peak flux densities versus measured total integrated line flux. For frequency channels of 6.1-7.8 kHz, the integrated line flux is roughly 4 times the sum of the peak fluxes (dotted line). Deviations of a factor 2, i.e. 2 S_{tot} and 8 S_{tot} are drawn as dashed lines

for the separation v_{exp}. In Ch 6 we explain this by an epoch of enhanced star formation (or a starburst), reflected in the very peaked distribution of v_{exp} for OH/IR stars in the GC compared to the v_{exp} distribution for the Galactic bulge and Galactic disk OH/IR stars. In Ch 6 we hypothesise that a significant fraction of the stars in the GC have the same metallicities, luminosities, masses and ages. Below we investigate whether some of this is also reflected in the derived mass-loss rates.

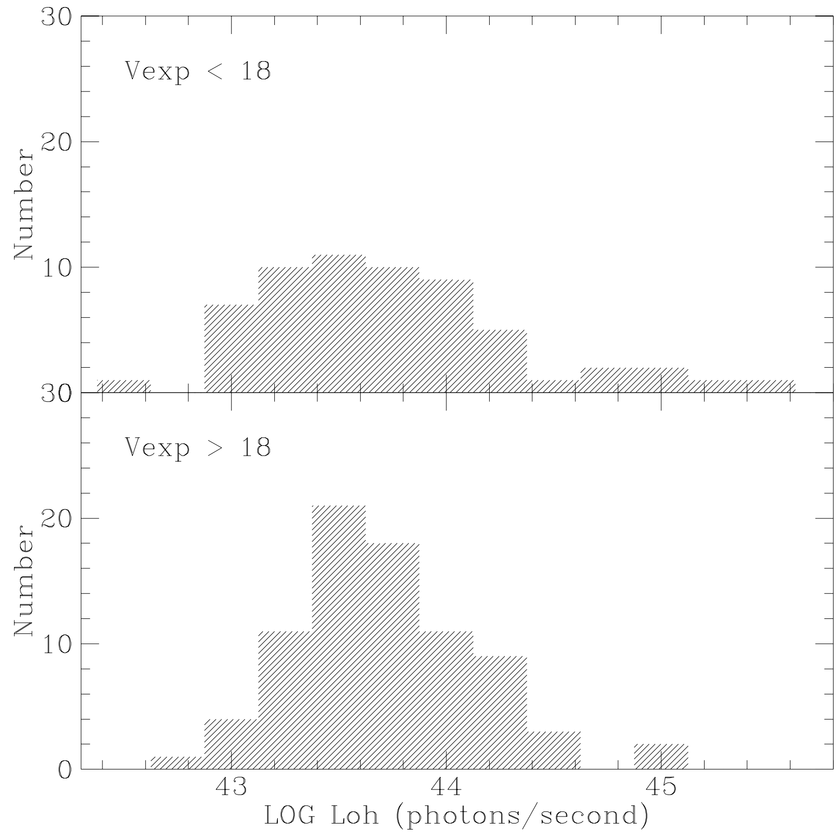

Figure 7.6 Histograms of the logarithm of the OH maser luminosity L_{OH} for the stars found in Paper I, divided up into the groups defined in L92. The flatter distribution for the low v_{exp} group might be due to a larger spread in the assumed distance of 8 kpc to the stars

7.4 Maser properties

In the past several authors have used peak flux densities to derive OH maser properties for OH/IR stars in different parts if the Galaxy. Because we have a sample that is at a known distance, we can compare peak flux densities and OH maser luminosities directly with other samples of OH/IR stars with well known distances.

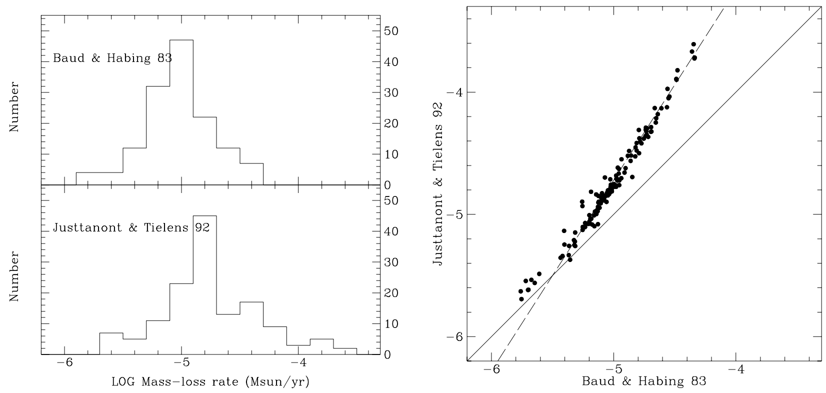

Figure 7.7 Comparison between the OH maser mass-loss rates derived from the method of Baud & Habing (1983) and that of Justtanont & Tielens (1992). Left (a), the distribution of mass-loss rates and right (b) the individual comparisons. Note the small cluster of relatively low mass-loss rates (see text). Except for this cluster, the dashed line with slope 1.56 and offset 3.08 (for $v_{\rm exp} \approx 18$ km s^{-1}) approximates the relative conversion between the two papers

7.4.1 OH maser luminosity function and strong OH masers

First, in Fig. 7.5, we show the logarithm of the integrated line flux ($I_{\rm tot}$) as function of log $S_{\rm tot}$ (cf. Fig. 7.2). Within a factor 2, $I_{\rm tot} = 4 \times S_{\rm tot}$ regardless of low or high $v_{\rm exp}$ group. We indicated the different factors (1, 4, and 2 and 8) with the solid, dotted, and two dashed lines respectively.

Assuming an isotropic radiation field and a location at the GC, $I_{\rm tot}$ can be directly converted into an OH maser luminosity: $L_{\rm OH} = 6.0\times10^{41} \cdot I_{\rm tot}$ (Jy) $\cdot\, D^2$ (kpc^2) photons per second. The corresponding OH maser luminosity distribution can be found in Paper I (their Fig. 10), where is derived that within the statistical errors, the distribution peaks at 2.5×10^{43} photons per second. However, the limited sensitivity of the data set, the spatial distribution of the OH/IR stars and the reordering of $S_{\rm max}$ into $I_{\rm tot}$ – even within a factor of 2 – does not allow a quantitative description of the low-luminosity side (or cut-off) of the OH maser luminosity distribution.

Figure 7.6 displays the OH maser luminosity functions for the groups as defined by L92. The low expansion velocity distribution contains a few more luminous OH masers and has a broader and flatter distribution. There is a similar distribution in $S_{\rm peak}$ (e.g. L97). Because the spatial distribution for this group is more extended (L92 and Sect. 3), we interpret this as a warning. Previous studies selecting OH/IR stars with the stronger OH masers might have a bias toward (bulge) sources that are close to, but in front of the GC, overestimating their distances, bolometric luminosities and mass-loss rates. For example, it has already been indicated in Ch 6, that the expansion velocities of stars for which an $M_{\rm bol}$ was derived by Blommaert et al. (1997), do not represent the distribution of expansion velocities for all OH/IR stars found in the GC. Therefore, caution has to be taken in interpreting the following analyses. Despite our interpretation of more overestimated distances in the low $v_{\rm exp}$ group, it remains an interesting question whether one can explain this difference in OH maser luminosity function with an intrinsic physical property (e.g. a lower OH maser pumping efficiency for increasing metallicity).

7.4.2 OH maser mass-loss rates

One of the methods to investigate the mass-loss during the final stages of stellar evolution is to make use of molecular emission, measuring the (gas) mass-loss rate $\dot{\rm M}$ (as opposed to the dust mass-loss rate $\dot{\rm M}_{\rm d}$ in the infrared; for a review see Van der Veen & Olofsson 1990). Normally one derives the mass-loss rate from infrared (IRAS measurements and dust shell modelling) or molecular line CO (or OH maser) measurements. Neither IRAS nor CO data are available or easily measured for our sample and we therefore must use OH maser relations. Generally, the (empirical) OH maser mass-loss relations have the form:

$$\dot{\rm M} = C \cdot v_{\rm exp} \cdot \hat{L}_{\rm OH}^{\alpha} \cdot f_{\rm OH}^{-1}$$

$$\text{with } \hat{L}_{\rm OH} = D^2 \cdot {\rm S}_{\rm OH}$$

Note the definition of $\hat{L}_{\rm OH}$ as a function of peak flux density S (and not the total integrated line flux $\rm I_{tot}$). The quantity $f_{\rm OH}$ is the OH-abundance, and usually assumed to be fixed and successively taken out of the equation. We quote the constants C and α from two papers; $C = 1.83{\times}10^{-7}$, $\alpha = 0.5$ for the widely used empirical relation found by BH83[1], and $C = 1.86{\times}10^{-7}$, $\alpha = 0.78$ by extrapolating infrared dust shell modelling toward OH maser luminosity (Justtanont & Tielens 1992, hereafter JT92).

We have calculated the mass-loss rates for the OH masers according to both the BH83 and JT92 formulae. We give the histograms and comparison in Fig. 7.7a,b. The mass-loss rate calculated from JT92 extends to higher values because of a stronger dependence on the peak flux density. Although a mass-loss rate of 10^{-4} is not uncommon in the Galactic plane, we find that the

[1] Chengalur et al. 1993 use a constant C that is exactly a factor 10 smaller, but we think that is an unfortunate error.

values for the mass-loss rate on the high-end of the distribution of JT92 is relatively high compared to other samples of pulsating AGB stars (e.g. BH83; JT92; Whitelock et al. 1994; Olofsson et al 1993; Netzer & Knapp 1987). Although both relations might be equally valid, we prefer to use the relation found by BH83 for our sample of OH/IR stars and refer to Fig. 7.7b to convert the BH83 mass-loss rates into the JT92 values (log $\dot{M}_{JT}$ = 3.78 − 0.56 log v_{exp} + 1.56 log $\dot{M}_{BH}$). The general characteristics of the analysis remain valid for each method.

To investigate the dependency of <S> (or S_{OH}) and v_{exp} on the mass-loss rate, we have plotted both quantities as function of the BH83 mass-loss rate in Fig. 7.8. Clearly, the flux is dominant over v_{exp} in determining the mass-loss rate. As also is apparent from Fig. 7.7b, there is a group of stars – of which one is GCIRS 5 – with relatively low mass-loss rates that is standing out in the figures because of a combination of low flux and a low v_{exp}. This is also the case when we calculate the JT92 mass-loss rates. Remarkably, this is the small cluster of stars that causes the spatial distribution of the low v_{exp} OH/IR stars in L92 and Paper I to be different. It would be very interesting to determine bolometric magnitudes, and e.g. metallicities for these stars to determine their nature. For example, for recently formed massive supergiants one would expect a higher v_{exp} (in Paper I we reject a possible identification with the supergiant GCIRS 19 on these grounds); for old, low mass Mira variables one would expect the stars to be much more dispersed (in Paper I two of these stars are identified from a preliminary list of near-infrared long period variable stars).

For comparison, the low metallicity OH/IR stars from the Large Magellanic Cloud (LMC, triangles, Wood et al. 1992) and a sample of Miras and OH/IR stars, mostly in the Galactic plane, with relatively well known distances (filled circles, Van Langevelde et al. 1990, with v_{exp} from Herman & Habing 1985) are also plotted as function of their BH83 OH maser mass-loss rates in the diagrams (recalculated for 8 kpc). For the GC OH/IR stars, for the moment excluding the peculiar low mass-loss rate cluster, we derive a maximum mass-loss rate of 5×10^{-5} $M_\odot$ yr^{-1} which is independent of v_{exp} (top frame). There is also a minimum mass-loss rate apparent, also independent of v_{exp}, but this is most likely caused by the limited sensitivity. For each value of v_{exp} we find a large range of mass-loss rates and vice versa. The maximum mass-loss rate for the GC stars compares well with the maximum mass-loss rate found for the LMC objects, but is definitely lower than for OH/IR stars in the Galactic plane. Plotted in the bottom frame are two lines of constant v_{exp}, showing the dependence of mass-loss rate on OH maser luminosity. By assuming a direct relation between infrared maser pump luminosity and OH maser luminosity (e.g. JT92), and because the v_{exp} is of secondary importance in determining the mass-loss rate, these lines can be expected to correlate roughly with the

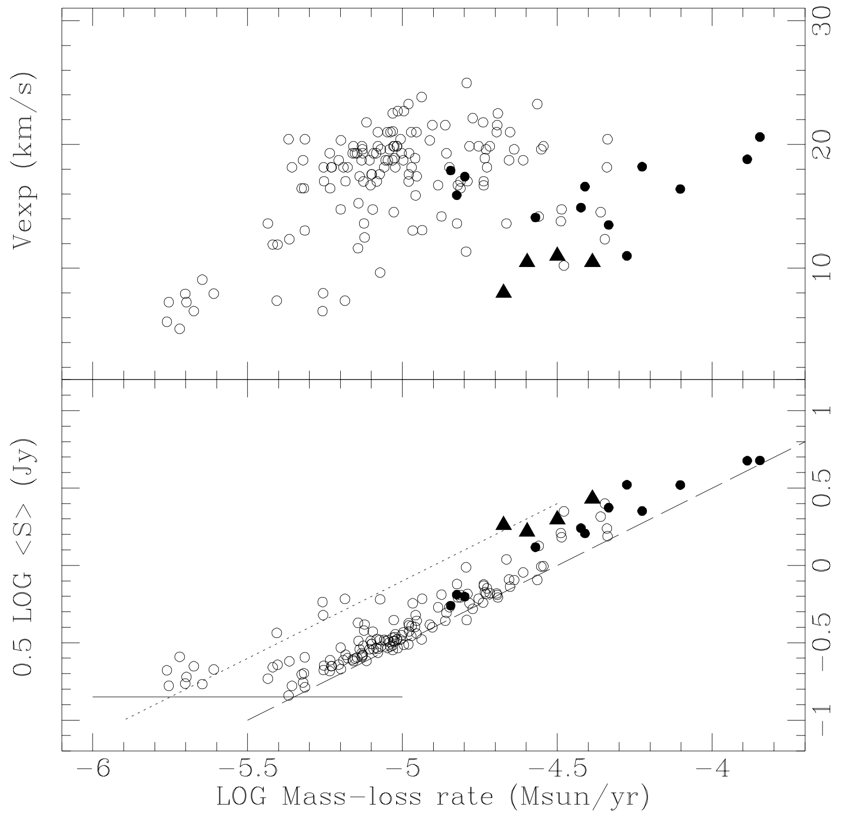

Figure 7.8 BH83 OH maser mass-loss rate as function of $v_{\rm exp}$ and arithmetic mean of the peak flux densities <S>. On top the $v_{\rm exp}$, and below the <S> leading to the mass-loss rate. Open circles are the GC OH/IR stars from Paper I, filled circles form the mixed sample of stars from Van Langevelde et al. (1990) and the triangles are the LMC OH/IR stars from Wood et al. (1992). Note the small cluster of stars with relatively low ($\approx 2\times10^{-6}$) mass-loss rates and the crowding of roughly equal $v_{\rm exp}$ and <S>. The horizontal line at <S> $= 0.020$ Jy depicts the sensitivity limit in Paper I, the dashed and dotted lines show the relation between mass-loss rate and OH maser flux density for a constant expansion velocity of 22 and 9 km s^{-1}, respectively. Further interpretation can be found in the text

bolometric luminosity and stellar mass. The highest mass-loss rates found in the plane are just for the heaviest, most recently formed OH/IR stars.

Larger deviations from the dashed line ($v_{\rm exp} = 22$ km s^{-1}) are caused by lower expansion velocities and/or lower efficiency of converting infrared photons into

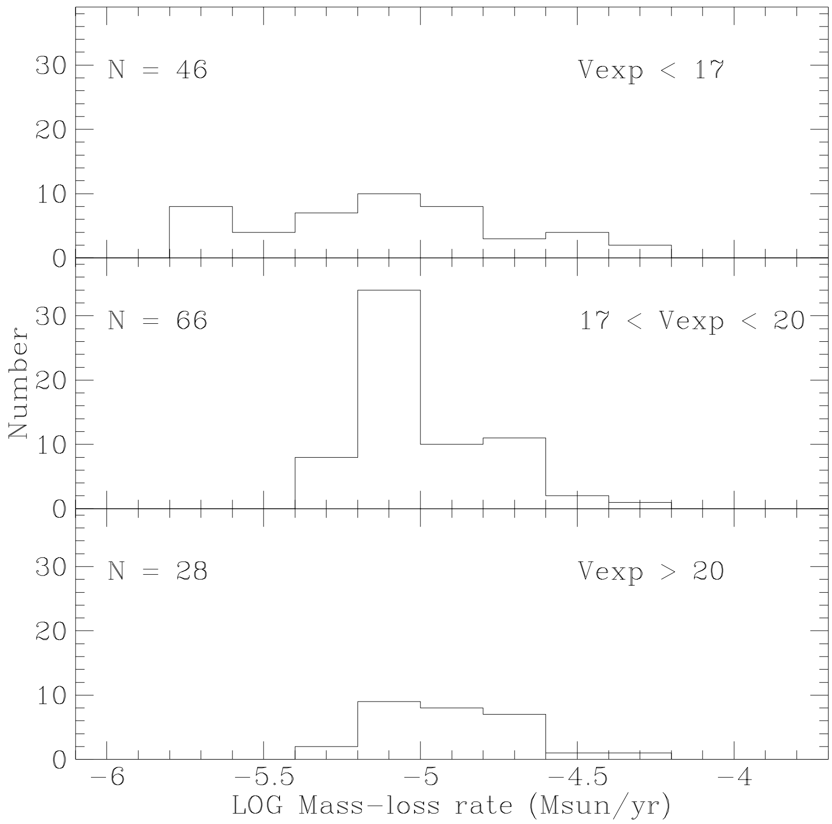

Figure 7.9 BH83 OH maser mass-loss rate distribution for three different groups of v_{exp}; low expansion velocity (top, $v_{exp} < 17$ km s^{-1}), high expansion velocity (bottom, $v_{exp} > 20$ km s^{-1}), and a group for which we think a large fraction has a common origin (middle, $17 < v_{exp} < 20$ km s^{-1})

OH maser photons (assumed to be relatively constant in the BH83 calculation, see below). A larger deviation thus can be interpreted as a lower metallicity, conform the location away from the line for the LMC OH/IR stars. It is then very attractive to extrapolate (dashed line) the low metallicity and luminous LMC OH/IR stars toward the cluster of low mass-loss rate stars. It predicts that these stars are very metal poor low mass stars, and thus very old. However, the dynamical mechanism of mass segregation, in combination with the very concentrated location toward Sgr A* contradicts with this view.

Knowing that the environment of the very center might be very hostile for large and expanding circumstellar envelopes, instead we suspect that these stars have a very different OH masing environment. The fact that $\sim$ 90% of GC stars have a remarkably higher $v_{\rm exp}$ means that this is a very localised phenomenon. For example, a high local particle density could suppress the expansion of the envelope, resulting in slower outflow and less mass lost per unit time, but still with a maser efficiency comparable to the other weaker OH masing objects. Also, locally the interstellar radiation field can be very intense, penetrating deeper into the envelope and photo-dissociate H_2O into OH in the region where the acceleration of particles still takes place. Then, besides a lower value of what we think is the terminal velocity $v_{\rm exp}$, less velocity coherence of OH molecules would result in lower maser efficiencies. It explains why we do not see many stars with low $v_{\rm exp}$ at higher OH maser flux. Finally, we cannot exclude that the cluster consists of low-mass Miras (that generally have low $v_{\rm exp}$ and low OH maser intensities). The cluster is then explained as an statistical artifact of the increased number density of such stars in the very center (extrapolated from the near-infrared surface intensity; e.g. Serabyn & Morris 1996).

7.4.3 Expansion velocity groups

In Fig. 7.7a, the peak of the mass-loss distribution at $\approx 10^{-5}$ $M_\odot$ yr^{-1} finds its origin in the fact that a large fraction of the stars has roughly the same OH maser flux and expansion velocity, in particular $17 \lesssim v_{\rm exp} \lesssim 20$ km s^{-1}. In Ch 6, we hypothesise that a large fraction of the GC OH/IR stars with $17 \lesssim v_{\rm exp} \lesssim 20$ km s^{-1} have the same metallicity and a similar $M_{\rm bol}$; they have a common origin in an epoch of enhanced star formation.

Figure 7.9 displays the mass-loss distribution for this group compared to the mass-loss distributions of OH/IR stars in the GC with lower $v_{\rm exp}$ (top frame), and with higher $v_{\rm exp}$ (bottom frame). Clearly all distributions have an overall flat distribution because of a general mixture of stars with different properties (metallicity, bolometric luminosity) at different stages in their mass-loss evolution. Note the number of stars for each distribution, and that the lowest mass-loss rates only appear in the low $v_{\rm exp}$ group. Striking, but not completely unexpected, there is a clear excess of stars with an equal mass-loss rate in the group with $17 \lesssim v_{\rm exp} \lesssim 20$ km s^{-1}. We find this a strengthening argument for the hypothesis of a common origin for these stars.

7.5 Conclusions

From the OH maser lines from a new sample of OH/IR stars in the GC, we confirm earlier findings that groups of OH/IR stars with high and low expansion velocity form distinct kinematical samples. We support the hypothesis for a third group, based on the distribution of mass-loss rates, in particular for the group with $17 < v_{\rm exp} < 19$ km s^{-1}. Furthermore, we reveal a cluster of stars, within $4'$ of Sgr A*, that has an extremely low mass-loss rate. We suggest that this is caused by the special conditions in the central 10 pc of Sgr A*. We suspect that the stronger OH masers, in particular the group with low expansion velocities, might be biassed toward sources close, but in front of the GC.

References

Baud B., Habing H.J. 1983, A&A 127, 73

Blommaert J.A.D.L., van der Veen W.E.C.J., van Langevelde H.J., Habing H.J., Sjouwerman L.O. 1997, accepted for publication in *Astronomy & Astrophysics*

Chengalur J.N., Lewis B.M., Eder J., Terzian Y. 1993, ApJS 89, 189

David P., Le Squeren A.M., Sivagnanam P. 1993, A&A 277, 453

Habing H.J. 1996, A&AR 7, 97

Habing H.J., Olnon F.M., Winnberg A., Matthews H.E., Baud B. 1983, A&A 128, 230

Herman J., Habing H.J. 1985, A&AS 59, 523

Iben I. 1991, ApJS 76, 55 Gensheimer P.D. 1991, A&A 242, 211

Jones T.J., McGregor P.J., Gehrz R.D., Lawrence G.F. 1994, AJ 107, 1111

Justtanont K., Tielens A.G.G.M. 1992, ApJ 389, 400

Lindqvist M., Winnberg A., Habing H.J., Matthews H.E. 1992a, A&AS 92, 43

Lindqvist M., Habing H.J., Winnberg A. 1992b, A&A 259, 118

Lindqvist M., Winnberg A., Habing H.J. 1997, *in preparation*

Menten K.M., Reid, M.J., Eckart A., Genzel R. 1997, ApJ 475, L111

Netzer N., Knapp G.R. 1987, ApJ 323, 734

Olofsson H. 1993, in "Mass Loss on the AGB and Beyond", H.E. Schwarz (ed.), ESO Conference and Workshop Proceedings #46, p. 330

Olnon F.M., Winnberg A., Matthews H.E., Schultz G.V. 1980, A&AS 42, 119

Reid M.J. 1993, ARAA 31, 345

Serabyn E., Morris M. 1996, Nat 382, 602

Shiki S., Ohishi M., Deguchi S. 1997, ApJ 478, 206

van der Veen W.E.C.J. 1989, A&A 210, 127

van der Veen W., Olofsson H. 1990, in "From Miras to Planetary Nebulae", M.O. Mennessier, Omont A. (eds.), Editions Frontieres, Gif sur Yvette, p. 139

van Langevelde H.J., van der Heiden R., van Schooneveld C. 1990, A&A 239, 193

van Langevelde H.J., Janssens A.M., Goss W.M., Habing H.J., Winnberg A. 1993, A&AS 101, 109

van Paradijs J., Spruit H.C., van Langevelde H.J., Waters L.B.F.M. 1995, A&A 303, L25

Whitelock P., Menzies J., Feast M., Marang F., Carter B., Roberts G., Catchpole R., Chapman J. 1994, MNRAS 267, 711

Winnberg A., Baud B., Matthews H.E., Habing H.J., Olnon F.M. 1985, ApJ 291, L45

Wood P.R., Whiteoak J.B., Hughes S.M.G., Bessel M.S., Gardner F.F., Hyland R. 1992, ApJ 397, 552

Speech

Actually, I do not know precisely who has been responsible for this 'opportunity of a lifetime', but Harm Habing, Anders Winnberg and Huib Jan van Langevelde must have formed an excellent team in initialising and realizing this mixed Swedish-Dutch PhD 'adventure'. For that I shall remember them equally grateful. To Susanne: thanks for the tip!

Over the years, it has been a pleasure (and also a great 'adventure') to discuss work and have fun with Huib Jan, Joris, Michael, Peter, Richard, Phil, Paul, Aage, Wil, Ian, Marco, John, Roland, Per & Susanne & Henrik, Roel, Cathy, Enrico, Tommy, Garrelt, Ylva, Ola, Max, Celeste and all other friends and colleagues. I admire the continuous efforts of the secretaries and whiz-kids/digiware specialists of Sterrewacht Leiden and Onsala Rymdobservatorium, as well as all landlords and landladies, for helping me out for whatever I needed, or thought I needed.

In het bijzonder gaat mijn waardering uit naar mijn Leidse "wat je wilt" maatje voor hand- en spandiensten, alle denkbare soorten van communicatie en de op z'n tijd o-zo-nodige borrel(praat) en aanstekelijk brede glimlach: miss Maartje 7*.

Lex en mijn moeder hielden mij mobiel door mede de auto te onderhouden, ook al poogden vele sneeuwstormen, ijzel en vorstaanvallen, alsmede gekke mede-weggebruikers mij van mijn bureau, giga-bytes en e-mail weg te houden.

Ed, nooit gedacht dat een stilzwijgend, simpel strategisch pact op een drijvend matje tot zo'n toffe vriendschap zou leiden. Dat maakte dat ik in de afgelopen jaren niet alleen sterrenkunde leerde. Van hier wens ik je alle goeds in je allernieuwste pact, met Lilis: Selamat berbahagia kepada kedua mempelai!

LSD hielp me meermalen wankelend op de been. Ik dank dan ook alle vrienden van de Leidse Studenten Duikvereniging met wie ik onder èn boven water zwevend de mooiste tijd van de laatste jaren heb beleefd. Detsamma skulle jag kunna säga om CDK, om vattnet inte hade varit så kallt! Icke desto mindre var (är) det mycket roligt på dykhelgerna och i klubblokalen med mina svenska parkompisar. När jag var medlem av Chalmers dykarklubb träffade jag många typiska svenska sjödjur vars namn jag inte kan uttala och – jag beklagar – också har glömt.

Tim, don't forget our appointment in 'Valhalla', after we have used up our awarded time on 'Klotet'. You, and Andreas and Stefan – die glücklicherweise auch Englisch lesen können – have been the best friends one can wish for when one wants to work on one's physical, social and 'spirituous' health in Sweden.

Ett stort tack till Elisabeth, för att du lärde mig lite svenska. Det har varit mycket användbart. Jag hoppas du vill hjälpa mig igen om jag skulle behöva fler lektioner.

I am very much indebted to my co-authors, Huib Jan van Langevelde, Michael Lindqvist, Harm Habing, Anders Winnberg, Phil Diamond and Joris Blommaert, for their help, support, advice, and – very important – their patience.

Because of the character of this 'adventure', occasionally balancing on the edge of 'technicalities', I often had – and thankfully was able – to call on external institutes and foundations, that for the successful continuation of the project and after the necessary investments taken at our side, seemed to allocate the requested – in my eyes usually huge – amounts of observing time and cases with money, without any trouble. I pay my respects to the hospitality and to the open policy for using the facilities of Sterrewacht Leiden, Onsala Rymdobservatorium, National Radio Astronomy Observatory, Australia Telescope National Facility, and the European VLBI Network. For financial support, in whatever form or amount during this 'adventure', I gratefully acknowledge all the contributions of Sterrewacht Leiden, Svenska Institutet, Onsala Rymdobservatorium, IAU Colloquium 153, 22nd IAU General Assembly, het NWO Stimuleringsfonds voor AIO/OIO's, het Leids Kerkhoven-Bosscha Fonds, het Leids Sterrewacht Fonds, Chalmers Tekniska Högskola, JIVE/EVN 2nd Annual Symposium, de Dienst Uitvoering Ontslaguitkeringen van het ministerie van Binnenlandse Zaken and the Swedish National Research Council (NFR),

és végül egy külön köszönet az életem legdrágább hölgyeinek, Anyunak és Nagyinak, akik nem kérdezgettek, nem vontak felelöségre.
En Zsas, dat geldt voor jou natuurlijk ook!

Köszönök nektek mindent nagyon szépen.

At the age of 30, time has come to begin a new 'adventure'..

JIVE-ing the Dwingeloo moor.

Thanks, bedankt, köszönem, och ett stort tack till alla!

Onsala, August 1997; Loránt Olivér Sjouwerman, 661223-2196